HAL
open science

The role of galactic winds in the galaxy formation and evolution using 3D spectroscopy

Ilane Schroetter

To cite this version:

Ilane Schroetter. The role of galactic winds in the galaxy formation and evolution using 3D spectroscopy. Astrophysics [astro-ph]. Université Toulouse 3 Paul Sabatier, 2016. English. NNT : . tel-01480054

HAL Id: tel-01480054

https://theses.hal.science/tel-01480054v1

Submitted on 13 Mar 2017

HAL is a multi-disciplinary open access archive for the deposit and dissemination of scientific research documents, whether they are published or not. The documents may come from teaching and research institutions in France or abroad, or from public or private research centers.

L'archive ouverte pluridisciplinaire **HAL**, est destinée au dépôt et à la diffusion de documents scientifiques de niveau recherche, publiés ou non, émanant des établissements d'enseignement et de recherche français ou étrangers, des laboratoires publics ou privés.

THÈSE

En vue de l'obtention du

DOCTORAT DE L'UNIVERSITÉ DE TOULOUSE

Délivré par : *l'Université Toulouse 3 Paul Sabatier (UT3 Paul Sabatier)*

Présentée et soutenue le *05/01/2017* **par :**

Ilane SCHROETTER

La formation et l'évolution des galaxies grâce à la spectroscopie 3D : le rôle des vents

---

JURY

Roser PELLO	Astronome	Présidente du Jury
Frédéric BOURNAUD	Ingénieur chercheur	Rapporteur
Daniel SCHAERER	Professeur adjoint	Rapporteur
Philippe AMRAM	Professeur	Examinateur
Nicolas BOUCHE	Chargé de recherche	Directeur de thèse
Thierry CONTINI	Directeur de recherche	Co-directeur de thèse

École doctorale et spécialité :
SDU2E : Astrophysique, Sciences de l'Espace, Planétologie
Unité de Recherche :
Institut de Recherche en Astrophysique et Planétologie (UMR 5277)
Directeur(s) de Thèse :
Nicolas BOUCHE et *Thierry CONTINI*
Rapporteurs :
Frédéric BOURNAUD et *Daniel SCHAERER*

Acknowledgments

Abstract

0.1 French version

Le modèle cosmolgique standard Λ-CDM est celui qui connaît le plus grand succès dans la cosmologie moderne. Pourtant, malgré sa capacité à expliquer la domination de la matière noire sur la structuration de l'univers à grande échelle, il échoue, parfois dramatiquement, lorsque la physique complexe de la matière baryonique entre en jeu. En particulier, l'une des plus grandes questions restant encore sans réponse concerne la différence importante entre la quantité de matière baryonique prédite et celle réellement observée dans les halos de galaxies de faible et de grande masse (e.g. Behroozi et al., 2013b). Les modèles théoriques prédisent beaucoup trop de masse comparé à ce qui est véritablement observé, ce qui mène à la conclusion qu'il éxiste des mécanismes permettant d'éjecter une partie du réservoir de matière baryonique des galaxies, ce qui affectera donc leur évolution. En d'autres termes, si nous voulons comprendre l'évolution des galaxies, il est essentiel de comprendre de manière précise comment ces galaxies perdent une partie de leur matière baryonique.

Pour les galaxies de faibles masses, un ingrédient clé est contenu dans les vents produits par les explosions de supernovae (Dekel & Silk, 1986). Non seulement ces vents peuvent être efficaces pour éjecter le gaz et les métaux du disque galactique, pour enrichir le milieu inter-galactique en éléments lourds (Oppenheimer et al., 2010), mais ils sont aussi observés dans presque toutes les galaxies à formation d'étoiles (Veilleux et al., 2005a), ce qui donne à ces vents un rôle important concernant le cycle de la matière dans les galaxies. Notre connaissance incomplète concernant les relations entre la galaxie et les propriétés du gaz qu'elle éjecte, comme le lien entre le taux de formation stellaire (SFR) et la quantité de masse éjectée $\dot{M}_{\rm out}$, limite notre capacité à produire des simulations numériques précises sur l'évolution des galaxies.

L'objectif de cette thèse est de quantifier les propriétés des vents galactiques en utilisant des quasars en arrière plan et la spectroscopie 3D. Afin d'y parvenir, nous utiliserons une quantité importante de données provenant de plusieurs instruments (SDSS, LRIS au Keck, SINFONI, UVES et MUSE au VLT). Grâce à cette nouvelle stratégie d'observation et l'utilisation d'instruments de pointe, nous avons pu

augmenter l'échantillon d'un ordre de grandeur et ainsi obtenir de bien meilleures contraintes sur les propriétés du gaz qui s'échappe des galaxies de faible masse.

0.2 English version

The Λ-CDM model is one of the most resounding triumphs of modern cosmology. Yet, even though it is immensely successful at explaining the dark matter dominated large scale structures, it fails, sometimes dramatically, when the complex physics of baryonic matter comes into play. In particular, one of the major remaining discrepancies is between the observed and predicted baryonic densities of the dark matter halos of galaxies both in the high mass and low mass regimes (e.g. Behroozi et al., 2013b). Theoretical models predict much more mass than is actually observed, leading to the conclusion that there are mechanisms at play ejecting part of the baryonic matter reservoir from galaxies and therefore affecting their evolution. In other words, if we want to understand the evolution of galaxies, it is essential to understand precisely how galaxies lose a fraction of their baryonic matter.

For low mass galaxies, a key part of the solution lies on supernovae-driven outflows (Dekel & Silk, 1986). Not only can such outflows efficiently expel gas and metals from galactic disks, enriching the inter-galactic medium (Oppenheimer et al., 2010), they are also observed in almost every star-forming galaxy (Veilleux et al., 2005a), making them an important part of the matter cycle of galaxies in general. Our incomplete knowledge of scaling relations between galaxies and the properties of their outflowing material, such as between the star formation rate (SFR) and the ejected mass rate $\dot{M}_{\rm out}$, limits our ability to produce accurate numerical simulations of galaxy evolution.

The objective of this thesis is to quantify galactic wind properties using background quasars and 3D spectroscopy. In order to achieve our goal, we use large data sets from several instruments (SDSS, LRIS at Keck, SINFONI, UVES and MUSE on VLT).

After developing observational strategies in order to have the largest data set possible with this technique, we increased the number of observations by 1 order of magnitude which resulted in better constraints on the outflowing materials for the low mass galaxies.

Contents

Acknowledgments **i**

Abstract **iii**
0.1 French version . . . iii
0.2 English version . . . iv

Introduction **xxiii**
0.3 French version . . . xxiii
0.4 English version . . . xxvi

1 General context **1**
1.1 Galaxy formation and evolution . . . 2
1.1.1 What is a galaxy? . . . 2
1.1.2 Galaxy spectrum . . . 2
1.1.3 Star formation in galaxies . . . 4
1.2 Galaxy and cosmology fundamentals . . . 8
1.2.1 Cosmology fundamentals . . . 8
1.2.2 Galaxy fundamentals . . . 10
1.2.3 The Tully-Fisher relation and other mass estimator . . . 15
1.2.4 The galaxy "main sequence" . . . 15
1.2.5 What is a quasar? . . . 17
1.2.6 The low efficiency of galaxy formation . . . 17
1.3 Galactic winds "state of the art" . . . 19
1.3.1 Galactic winds are multi-phased and collimated . . . 19
1.3.2 Wind properties in emission . . . 23
1.3.3 Wind properties in absorption . . . 24
1.3.4 Wind properties using background sources . . . 26
1.3.5 Perspective from numerical simulations . . . 26

2 Observational strategy and sample selection **29**
2.1 The background quasar methodology . . . 30
2.1.1 Observational strategies . . . 30
2.1.2 Why do we need integral field spectroscopy? . . . 31
2.1.3 Critical parameters derived from IFUs . . . 32
2.1.4 A 3D fitting tool: GalPaK^{3D} . . . 33
2.2 The SINFONI Mg II Program for Line Emitters (SIMPLE) sample . . . 33
2.2.1 Selection criteria . . . 34
2.2.2 Sample description . . . 34
2.3 The MUSE GAs Flow and Wind (MEGAFLOW) survey . . . 35
2.3.1 Selection criterion . . . 35
2.3.2 Sample description . . . 35

3 Data acquisition and reduction **39**
3.1 SIMPLE observations and data reduction . . . 40
3.2 MUSE observations and data reduction . . . 41
3.2.1 GTO observations . . . 41
3.2.2 Pre-processing data reduction . . . 41
3.2.3 Science reduction . . . 43
3.2.4 Post-processing reduction . . . 44
3.2.5 Exposures combination . . . 46
3.2.6 Sky emission lines removal . . . 46

4 Data analysis **47**
4.1 Methodology . . . 48
4.1.1 Estimate of Star Formation Rate (SFR) . . . 48
4.1.2 A simple cone model for galactic winds . . . 49
4.2 SIMPLE sample . . . 53
4.2.1 Morpho-kinematics from GalPaK^{3D} . . . 53
4.2.2 Galaxy-quasar pairs classification . . . 54
4.2.3 Outflow properties . . . 55
4.3 MEGAFLOW survey . . . 60
4.3.1 Survey status . . . 60
4.3.2 Morpho-kinematics from GalPaK^{3D} . . . 60
4.3.3 Galaxy-quasar pairs classification . . . 66
4.3.4 Outflow properties . . . 67

5 Combining both samples: galactic wind properties as a function of galaxy properties **75**
5.1 Basic properties of the sampled galaxies . . . 76

5.1.1 Galaxy redshift distribution 76
5.1.2 Galaxy stellar mass measurement 77
5.2 How far do winds go? 81
5.3 Do winds escape? 83
5.4 Wind scaling relations 85
5.4.1 Previous studies on galactic winds 85
5.4.2 Scaling relations involving $V_{\rm out}$ 88
5.4.3 Scaling relations involving $\dot{M}_{\rm out}$ 89
5.4.4 Scaling relations on loading factor η 92
5.5 What mechanisms drive galactic winds? 94

6 Conclusions and perspectives 99
6.1 French version 100
6.1.1 Conclusions de thèse 100
6.1.2 Perspectives 102
6.2 English version 103
6.2.1 Thesis conclusions 103
6.2.2 Perspectives 105

A Schroetter et al. 2015: The SINFONI Mg II Program for Line Emitters (SIMPLE) II: background quasar probing z∼1 galactic winds 113

B Schroetter et al. 2016: MusE GAs FLOw and Wind (MEGAFLOW): first MUSE results on background quasars 133

Last note 155

List of Tables

4.1 Kinematic and morphological parameters for the 10 SIMPLE galaxy-quasar pairs. 54
4.2 Results for galaxies J0448+0950, J2357-2736, J0839+1112. 57
4.3 MEGAFLOW survey status. 62
4.4 GalPaK^{3D} results on 26 MEGAFLOW galaxies with reliable morpho-kinematic parameters. 65
4.5 Results on outflow properties for MEGAFLOW galaxies. 72

5.1 Summary of other wind studies 85

List of Figures

1 Scheme of the fraction of baryons versus galaxy halo mass. The predicted amount is represented by the dashed black curve whereas the observations are represented by the green one. We can see the two major problems : the global shift between observations and theory as well as the two cutoffs at low and high mass regimes. The two phenomena invoked to explain these cutoffs are Active Galactic Nuclei (AGN in blue) for the high mass regime and galactic winds (in red) for low mass galaxies. xxv

1.1 Scheme of electron excitation. A coming photon (on left) will: (1) give energy to the electron (represented in dark gray). The electron will go to the next atomic level (2) in an excited state (top right). It will then unleash the excess energy as an emitted photon (bottom right) and come back to its initial atomic level. 3

1.2 Representation of three types of galaxy spectra with the principle emission lines: the red spectrum at the bottom represents an early-type galaxy spectrum with no emission lines, as this type of galaxy does not form stars anymore. We can see the Lyman break (at $\sim$ 1200 Å) as well as the Balmer break ($\sim$4000 Å). The middle spectrum (in blue) represents a late-type galaxy: this type of galaxy is still forming stars and has a bright blue continuum as well as emission lines. The top spectrum represents a low-mass galaxy spectra, it does not have a continuum but we clearly see the main emission lines tracing star formation: Lyα(λ1216), C III](λ1909), [O II] ($\lambda\lambda$3727, 3729), Hδ (λ4102), Hβ (λ4862), [O III] ($\lambda\lambda$4960, 5008), [N II] ($\lambda\lambda$6549, 6585), Hα (λ6564) and [S II] (λ6718). 5

1.3 Scheme of the Doppler effect: The observer is represented by telescopes on the left. *The top row* represents a galaxy emitting at a wavelength in green. This galaxy is not moving so the observed wavelength is the same as the emitted wavelength. *The middle row* shows a galaxy moving towards the observer and thus the observed wavelength is compressed as compared to the emitted one, we call that shift a blue-shift. *The bottom row* represent a galaxy moving away from us and thus the observed wavelength is diluted as compared to the emitted one, the wavelength is thus red-shifted. 6

1.4 The star formation rate density (SFRD) as a function of redshift. We can see that the SFRD increases from high redshift to peak at redshift $z \sim 2-3$ and then drops to redshift $z = 0$. This figure is from Madau & Dickinson (2014). 8

1.5 The anisotropies of the Cosmic microwave background (CMB) as observed by Planck. The CMB is a snapshot of the oldest light in our Universe, imprinted on the sky when the Universe was just 380 000 years old. It shows tiny temperature fluctuations that correspond to regions of slightly different densities, representing the seeds of all future structure: the stars and galaxies of today. Copyright: ESA and the Planck Collaboration. 9

1.6 Scheme of Hubble classification for galaxy morphologies. 11

1.7 Scheme of a galaxy in rotation. The galaxy is in black and is represented on the sky plane x, y (y representing the celestial north). This galaxy has a position angle PA which is the angle between the celestial north and the major axis of the galaxy. At the bottom, we can see 3 Gaussians on a wavelength axis (λ) corresponding to emission lines in 3 different regions of the galaxy. The left part of the galaxy is moving towards us, so its emission line is blue-shifted, its middle do not move with respect to its systemic velocity and the right part is moving away from us, so its emission line is red-shifted. 13

1.8 SDSS transmission curves for the different filters. 14

1.9 Scheme of the galaxy "main sequence" in blue as well as outliers: starbursts above this main sequence (purple) and red or dead (not forming stars anymore) galaxies (red). Space between the main sequence and red galaxies is called the green valley. 16

1.10 Scheme of a typical quasar spectrum. 17

1.11 Figure from Papastergis et al. (2012). The ratio of galactic stellar mass to halo mass as a function of host halo mass ($M_*/M_h - M_h$ relation). The thick yellow line shows Papastergis et al. (2012) main result, obtained from abundance matching the stellar mass function of optically-selected sample with the halo mass function including sub-haloes. The dotted-dashed horizontal line shows the cosmic baryon fraction $f_b \approx 0.16$. 18
1.12 The galaxy M82 in visible wavelength, taken with HST. We can see that this galaxy is almost edge-on, in white we see the stars and gas contributions and the dust is shown in dark filaments along the galaxy. 20
1.13 On left panel, the galaxy M82 in B,V (blue and visible) combined with Hα, taken with the Subaru telescope. Like Figure 1.12, we see the disk of the galaxy (B and V filters) in white. In addition, the Hα is represented in red. We see the presence of this ionized gas perpendicular to the galactic disk. Hence, these outflows appear to be collimated in a cone. This gas is a direct imaging of galactic winds. On right panel, the galaxy M82 in X-ray, taken with the Chandra telescope. Unlike Figure 1.12 and left panel of this figure, we do not see the disk of the galaxy. We can, however, see the hot gas at almost the same location where we see the Hα gas on left panel. Again, we can see the conical structure of these outflows. 21
1.14 Other examples of galactic outflows seen in emission in local galaxies NGC 253, NGC 1482 and NGC 3079. On each of these galaxies we have a zoom of their center which clearly show the presence of outflows. Like M82, these outflows are ejected perpendicular to the galactic disk. Hence, we clearly see (especially for NGC 1482 and 3079) that galactic winds are likely collimated in a cone. 22
1.15 Scheme of the blue-shifted component for Hα and [N II] produced by galactic outflows. The green Gaussian correspond to the systemic (narrow) component and the broad component is shown in blue. The velocity difference (corresponding to the outflow velocity) between the two components is shown by the label ΔV. 23
1.16 Outflow absorption lines seen in a galaxy spectrum from Heckman et al. (2015). This absorption is blue-shifted with respect to the galaxy systemic velocity. We can also see that the different absorption lines have the same absorption behavior like their asymmetry. 25
1.17 Loading factor as a function of galaxy rotational velocity (bottom x axis) and halo mass (top x axis) assumed by theoretical/empirical models. 27

2.1 Scheme of an 3D IFU cube: the foreground image represents a white-light image of the cube and the extracted image represents a slide of the cube at a given wavelength. On this extracted image one can see only one galaxy which is emitting at the extracted wavelength. 31

2.2 Scheme geometry configuration: the quasar LOS, represented by the yellow star, is crossing galactic outflows represented by the red crosses getting out of the galaxies. The Azimuthal angle is represented by the blue cross going from the galaxy major axis to the quasar LOS. b represents the impact parameter for the galaxy−quasar pair, represented by the light green cross showing the distance between the galaxy center and the quasar LOS. 32

2.3 $W_r^{\lambda 2796}$ as a function of impact parameter b for galaxy-quasar pairs classified as wind-pairs. The red colored area shows the selection criterion of the SIMPLE sample ($W_r^{\lambda 2796} > 2.0\mathring{A}$). 34

2.4 Scheme of our target strategy: the quasar LOS, represented by the yellow arrow heading toward the telescope, is crossing two galactic outflows represented by the red arrows getting out of the galaxies. These galactic outflows are absorbing a portion of the quasar spectra which gives the two Mg II absorption systems at two different redshifts. b represents the impact parameter for one galaxy−quasar pair. 36

2.5 $W_r^{\lambda 2796}$ as a function of impact parameter b for galaxy-quasar pairs classified as wind-pairs. Horizontal dashed black lines shows the $W_r^{\lambda 2796} >$ 0.5Å and $W_r^{\lambda 2796} > 0.8$Å selection criteria. 37

2.6 Redshift distribution of MEGAFLOW galaxies. 38

3.1 Association map for the basic science data reduction. This diagram shows the part of the pipeline that operates on the basis of a single IFU. 42

3.2 Association map for the second part of the science data reduction. This part of the pipeline deals with data of all 24 IFUs simultaneously. 45

4.1 Representation of a galaxy position angle (PA) and inclination (i). *Top left:* sky plane (x, y) representation of the PA of a galaxy. This angle is defined to be the angle between the "y" axis (pointing the North) and the galaxy major axis. The galaxy PA is usually given positive towards the East. *Bottom right:* side view (y, z) of a galaxy inclined with the i angle. The inclination of a galaxy is defined to be the angle between the disk plane (y, z) and the sky plane (y, x). The telescope on the left is to better illustrate the side view: the black arrow pointing to the telescope represents the line of sight, the z axis represents the depth. 50

4.2 Wind model principle description. On the left side one can see a geometric representation of a galaxy-quasar system. The observer is on the left, the background quasar is represented by the yellow star labeled "QSO". The quasar LOS is crossing galactic outflows (red). We fill particles inside the cone with a constant radial velocity $V_{\rm out}$ (blue arrows). We project the velocities on the quasar LOS to end up with a simulated profile (absorption profile on the top right side). We compare this profile with the data (bottom absorption profile, UVES data), and we fit the data by changing $V_{\rm out}$ or the cone opening angle ($\theta_{\rm max}$). For this case, $V_{\rm out} = 115 \pm 10$ km s^{-1} and $\theta_{\rm max}= 40 \pm 5°$. . . 51

4.3 Examples of simulated absorption profiles with different galaxy inclinations (i), opening angle (θ) and wind velocities ($V_{\rm out}$): while each of the simulated profiles has the same number of particles, the apparent depth decreases as each parameter increases due to larger velocity projections for i and θ, and larger range of velocities for $V_{\rm out}$. *Top row*: absorption profiles for galaxies inclined at 30, 60 and 90 degrees with $V_{\rm out}$= 100 km s^{-1}and θ= 30°. The noise effect is due to the Monte Carlo distribution of particles. *Middle row*: absorption profiles for wind cones with opening angles of 30, 40 and 45 degrees with $V_{\rm out}$= 100 km s^{-1}and i=45°. *Bottom row*: absorption profiles with wind velocities of 50, 100 and 150 km s^{-1}with i= 45 degrees and θ= 30°. Each simulated profile has the same amount of particles but show a larger velocity range due to the increasing gas speed, hence the varying apparent depths. 52

4.4 Zoom of QSO-subtracted Hα maps of the 10 SIMPLE galaxies: quasar LOS is represented by the white contours if present or pointed out with a white arrow. The 4 wind-pairs are framed with a black rectangle. . 55

4.5 Galaxy inclinations for the SIMPLE sample as a function of the azimuthal angle α. Note there are three types of galaxies in this sample: the wind-pairs which have an azimuthal angle larger than 60±10°, the inflow-pairs with α lower than 60±10° and pairs that are ambiguous due to uncertainty on α. It is difficult to derive the azimuthal angle for a nearly face-on galaxy. The wind-pair and inflow-pair classes describe the fact of having the quasar absorptions tracing outflows and inflows, respectively. 56

4.6 *Left column:* from top to bottom: simulated absorption profiles with r_0=1,5,10 kpc. Notice that the asymmetry changes as r_0 increases, it goes from outward to inward asymmetry. *Right column:* The velocity profile corresponding to the associated simulated profile to the left where the turn over radius of the velocity profile (r_0) varies, from top to bottom: r_0=1,5,10 kpc. The red dashed line represents the distance between the galaxy and the quasar LOS ($b/\sin(\alpha)/\sin(i)$), corrected for the inclination i. 58

4.7 Wind models for the three wind-pairs. The bottom row corresponds to UVES quasar Mg I λ2852 absorption lines for the three fields: J0448+0950, J0839+1112 and J2357−2736 from left to right. The upper row shows the resulting simulated profiles for each case. One can see that we reproduce the equivalent widths and the profile asymmetries for each galaxy. Note that we do not reproduce the depth as the simulated profile is normalized 'by hand'. On each simulated profile, the red lines correspond to the wind contribution only whereas the black part corresponds to the galaxy component. 59

4.8 Comparison of predicted mass loading factors from theoretical/empirical models (curves) with values derived from observations (dots and triangles) as a function of the maximum rotational velocity. The results from the SIMPLE sample are represented by the cyan circles (Schroetter et al., 2015). The red circle shows the mass loading factor for a $z \sim 0.2$ galaxy (Kacprzak et al., 2014). The triangles show the results for $z \sim 0.2$ galaxies from Bouché et al. (2012). The gray triangles show the galaxies with quasars located at >60kpc where the mass loading factor is less reliable due to the large travel time needed for the outflow to cross the quasar LOS (several 100 Myr) compared to the short time scale of the Hα derived SFR ($\sim$ 10Myr). The upper halo mass axis is scaled on $V_{\rm max}$ at redshift 0.8 from Mo & White (2002). . . . 61

4.9 Results for 10 MEGAFLOW galaxies: Each set of result for a galaxy is composed of 3 maps: *left:* zoom of QSO-subtracted [O II] maps. On each of these maps, on top of them is indicated the redshift of the galaxy and at the bottom the quasar field name. *Middle:* zoom of QSO-subtracted Camel velocity map. *Right:* Zoom of QSO-subtracted GalPaK^{3D} PSF-deconvolved velocity map. Wind-pairs are framed with a red rectangles for Camel and GalPaK^{3D} velocity maps. 63
4.10 Same as Figure 4.9 for the 10 next galaxies. 64
4.11 Same as Figure 4.9 for the last 6 galaxies. 64
4.12 Galaxy inclination as a function of azimuthal angle α for 26 galaxies with reliable morpho-kinematic parameters detected in the MUSE fields. The dashed areas correspond to azimuthal angle ranges for which we classify pairs as inflow-pairs (blue and narrow dashes) or wind-pairs (green and wider dashes). These areas stop for face-on galaxies as uncertainty on position angles are too large. It is thus difficult to determine α and to classify galaxy-quasar pairs in this area. We note that 11 galaxies are classified as wind-pairs. 66
4.13 Azimuthal angle α distribution for 26 galaxies with reliable morpho-kinematic parameters detected in the MUSE fields. We note that 11 galaxies are classified as wind-pairs and that there is a bimodal distribution of α. There are more galaxy-quasar pairs in a configuration favorable for wind study.. This is probably due to the fact that we select only strong Mg II REW in the quasar spectra and the largest $W_r^{\lambda 2796}$ tend to be associated with outflows (e.g. Kacprzak et al., 2011; Lan et al., 2014a). 67
4.14 Representation of simulated profile and quasar spectrum associated with the J0014−0028 galaxy. Simulated wind profile (top) reproducing the Mg I absorption profile (centered at $z = 0.8343$) from UVES (bottom). This outflow has a $V_{\rm out}$ of 210 ± 10 km s^{-1} and an opening angle $\theta_{\rm max}$ of $25 \pm 5°$. 69
4.15 Same as Figure 4.14 but for the J0937+0656 galaxy at redshift $z \approx 0.9340$. This outflow has a $V_{\rm out}$ of 150 ± 10 km s^{-1} and an opening angle $\theta_{\rm max}$ of $30 \pm 5°$ for the galaxy at redshift $z = 0.9340$. 70
4.16 Same as Figure 4.14 but for the J1039+0714 galaxy at redshift $z \approx 0.9495$. This outflow has a $V_{\rm out}$ of 65 ± 10 km s^{-1} and an opening angle $\theta_{\rm max}$ of $30 \pm 5°$ for this galaxy. 70
4.17 Same as Figure 4.14 but for the J1314+0657 galaxy at redshift $z \approx 0.9867$. This outflow has a $V_{\rm out}$ of 95 ± 10 km s^{-1} and an opening angle $\theta_{\rm max}$ of $20 \pm 5°$ for this galaxy. 71

4.18 Same as Figure 4.14 but for the J1236+0725 galaxy at redshift $z \approx 0.6342$. This outflow has a $V_{\rm out}$ of 60 ± 10 km s^{-1} and an opening angle $\theta_{\rm max}$ of $35 \pm 5°$ for this galaxy. 71

4.19 Same as Figure 4.14 but for the J0131+1303 galaxies at redshift $z \approx 1.0106$. For this case, because two galaxies were detected at the absorber redshift, we needed to run wind models for both of them (at redshift 1.0106 and 1.0108) in order to reproduce the absorption lines in red. The outflow in green has a $V_{\rm out}$ of 205 ± 10 km s^{-1} and an opening angle $\theta_{\rm max}$ of $35 \pm 5°$ for the galaxy at redshift $z = 1.0108$. The outflow in black has a $V_{\rm out}$ of 80 ± 10 km s^{-1} and an opening angle $\theta_{\rm max}$ of $35 \pm 5°$ and $\theta_{\rm in}$ of $8 \pm 2°$ for the galaxy at redshift $z = 1.0106$. 72

4.20 Same as Figure 4.19 but for the J0937+0656 galaxies at redshift $z \approx 0.7024$. The outflow in green (the positive absorption component) has a $V_{\rm out}$ of 100 ± 10 km s^{-1} and an opening angle $\theta_{\rm max}$ of $30 \pm 5°$ for the galaxy at redshift $z = 0.7022$ (this pair has an azimuthal angle α of 55°). The outflow in black (the negative absorption components) has a $V_{\rm out}$ of 120 ± 10 km s^{-1} and an opening angle $\theta_{\rm max}$ of $35 \pm 5°$ and $\theta_{\rm in}$ of $8 \pm 2°$ for the galaxy at redshift $z = 0.7024$ (his pair has an azimuthal angle α of 84°). Results on these two pairs are shown in Tables 4.4 and 4.5. 73

4.21 Same as Figure 4.14 but for the J1107+1757 galaxy at redshift $z \approx 1.1620$. This outflow has a $V_{\rm out}$ of 150 ± 10 km s^{-1} and an opening angle $\theta_{\rm max}$ of $30 \pm 5°$ and $\theta_{\rm in}$ of $20 \pm 2°$ for this galaxy. 73

4.22 Same as Figure 4.14 but for the J1314+0657 galaxy at redshift $z \approx 0.9085$. This outflow has a $V_{\rm out}$ of 210 ± 10 km s^{-1} and an opening angle $\theta_{\rm max}$ of $30 \pm 5°$ and $\theta_{\rm in}$ of $7 \pm 2°$ for this galaxy. 74

4.23 Same as Figure 4.14 but for the J2152+0625 galaxy at redshift $z \approx 1.3185$. This outflow has a $V_{\rm out}$ of 150 ± 10 km s^{-1} and an opening angle $\theta_{\rm max}$ of $20 \pm 5°$ and $\theta_{\rm in}$ of $7 \pm 2°$ for this galaxy. 74

5.1 Redshift distribution of the 36 galaxies from SIMPLE and MEGAFLOW. 76

5.2 V/σ distribution of all the galaxies from both surveys. Orange colored bar represents dispersion-dominated galaxies ($V/\sigma < 1$). 78

5.3 Galaxy stellar mass as a function of the $S_{0.5}$ parameter for HDFS, SINS and MASSIV data. The dashed red line represent a fit with coefficients shown in the legend. 79

5.4 Star formation rate as a function of galaxy stellar mass (bottom x-axis) and $S_{0.5}$ (top x-axis) for our surveys. MUSE-HDFS observation from Contini et al. (2016) has been added in order to place our survey in a more general context. Galaxies with $1.0 < z < 1.5$ are represented in red for our surveys. The two dashed lines represent the empirical relations between SFR and stellar mass for different redshifts between $0.5 < z < 1.5$ from Whitaker et al. (2014). 80

5.5 Azimuthal angle distribution of all the galaxies from SIMPLE and MEGAFLOW. We note the bimodal distribution of the whole survey. 81

5.6 Mg II (λ2796) rest equivalent width as a function of impact parameter b for galaxy-quasar pairs classified as wind-pairs. Horizontal dashed black lines shows the $W_r^{\lambda 2796} > 0.5$Å and $W_r^{\lambda 2796} > 0.8$Å selection criteria. The thick black dashed line represent a fit to the data. Fitting coefficients are shown in the legend. Errors on $W_r^{\lambda 2796}$ are typically $\sim 10^{-3}$ Å and ~ 0.5 kpc for b. 82

5.7 *Left:* Mg II (λ2796) rest equivalent width as a function of impact parameter b for galaxy-quasar pairs classified as inflow-pairs. *Right:* same as left panel with the $W_r^{\lambda 2796}$ normalized by the disk path length $X = X_0/\cos(i)$ where i is the galaxy inclination and X_0 is a normalization factor, taken as $X_0 = \cos(60°)$. The thick black dashed line represent a fit to the data. Fitting coefficients are shown in the legend. Errors on $W_r^{\lambda 2796}$ are typically $\sim 10^{-3}$ Å and ~ 0.5 kpc for b. 83

5.8 $V_{\rm out}/V_{\rm esc}$ as a function of $S_{0.5}$ (bottom x-axis) and $M_\star$ (top x-axis). Yellow triangles are from Bouché et al. (2012), cyan and red circles are from Schroetter et al. (2015) and Schroetter et al. (2016) respectively. The horizontal line corresponds to $V_{\rm out} = V_{\rm esc}$. The dashed black line corresponds to a fit with coefficients shown in the legend. 84

5.9 Scheme of the two main technique to study outflowing materials in absorption. On the right part of this scheme, we can see a star-forming galaxy (in black) ejecting gas in a cone (represented by the two red arrows). The horizontal dark blue arrow represents the LOS as used in Heckman et al. (2015). In this LOS type observation, the galaxy is face-on and the outflowing gas creates blue-shifted absorption lines in the galaxy spectrum. This absorption profile is represented on top of the telescope on the left in dark blue. We can see that this absorption profile is asymmetric, only blue-shifted (on the left of the systemic velocity, represented by the 0 vertical dashed line) and with an outflow velocity corresponding to where the absorption crosses the galaxy continuum. On the right part of this figure, the light blue vertical arrow represent a quasar (the yellow star labeled "QSO") LOS crossing the outflowing material of the same galaxy. This configuration represent our background quasar technique and the galaxy is seen as edge-on. The projected velocities onto this LOS creates an absorption profile represented in light blue at the bottom of the figure. This absorption profile is symmetric and centered on the galaxy systemic velocity. 87

5.10 $V_{\rm out}$ as a function of SFR for both surveys (MEGAFLOW and SIMPLE) as well as observations from Bouché et al. (2012) and Heckman et al. (2015). The dashed black line show a fit ($\log V = (0.35 \pm 0.06)\log(\mathrm{SFR}) + (1.56 \pm 0.13)$) from Martin (2005). Errors on Heckman et al. (2015) observations are 0.2 dex for SFR and 0.05 dex for $V_{\rm out}$. 90

5.11 Ejected mass rate as a function of star formation rate (left) and star formation rate by surface area ($\Sigma_{\rm SFR}$, right) for both surveys (MEGAFLOW and SIMPLE) as well as observations from Bouché et al. (2012). On left panel, the dashed red line shows a prediction $\dot{M}_{\rm out} \propto \mathrm{SFR}^{0.7}$ from Hopkins et al. (2012) model. On left panel, the black line shows $\dot{M}_{\rm out} \propto \mathrm{SFR}^{1.11}$ from Arribas et al. (2014). the blue dotted line correspond to a loading factor ($\dot{M}_{\rm out}/\mathrm{SFR}$) equals 2. Errors for Heckman et al. (2015) are 0.25 dex for $\dot{M}_{\rm out}$ and 0.2 dex for SFR and $\Sigma_{\rm SFR}$. 91

5.12 η as a function of SFR (left) and $\Sigma_{\rm SFR}$ (right) for both surveys (MEGAFLOW and SIMPLE) as well as observations from Bouché et al. (2012) and Heckman et al. (2015). On left panel, the dashed red line shows a fit $\eta \propto {\rm SFR}^{-0.3}$ from Hopkins et al. (2012) and the black line shows a fit $\eta \propto {\rm SFR}^{0.11}$ from Arribas et al. (2014). On right panel, the dashed red line shows a fit $\eta \propto \Sigma_{\rm SFR}^{-1/2}$ from Hopkins et al. (2012) and the black line shows a fit $\eta \propto \Sigma_{\rm SFR}^{0.17}$ from Arribas et al. (2014). Again, errors for Heckman et al. (2015) are 0.2 dex for SFR (and $\Sigma_{\rm SFR}$) and 0.45 dex for η. 93
5.13 η as a function of $S_{0.5}$ for both surveys (MEGAFLOW and SIMPLE) as well as observations from Bouché et al. (2012) and Heckman et al. (2015). The dashed red line shows a fit $\eta \propto S_{0.5}^{-1.2}$ from Hopkins et al. (2012). The black line shows $\eta \propto V^{-2}$. Errors on Heckman et al. (2015) are 0.45 dex for η and 0.1 dex for $V_{\rm max}$. 95
5.14 Comparison of mass loading factors assumed by theoretical/empirical models (curves) with values derived from background quasar observations (dots and triangles) as a function of the maximum rotational velocity. MEGAFLOW results are represented by the blue squares. The result from Schroetter et al. (2016) is represented by the red circle. Arrows represent the loading factors of the galaxies with the subtracted mass from the inner cone models. The cyan circles show the results for galaxies at $z \approx 0.8$ from Schroetter et al. (2015). The green square shows the mass loading factor for a $z \approx 0.2$ galaxy (Kacprzak et al., 2014). The triangles show the results for $z \approx 0.2$ galaxies from Bouché et al. (2012). The gray triangles and squares show the galaxies with quasars located at >60kpc where the mass loading factor is less reliable due to the large travel time needed for the outflow to cross the quasar LOS (several 100 Myr) compared to the short time scale of the Hα derived SFR ($\sim$ 10Myr). The upper halo mass axis is scaled on $V_{\rm max}$ at redshift 0.8 from Mo & White (2002). 96

Introduction

0.3 French version

Certains évoquent que nous serions des manifestations de l'univers essayant de se comprendre.

Ainsi, depuis la nuit des temps, l'Homme porte un regard fasciné vers le ciel, contemplant ces objets brillants que sont les étoiles, galaxies, planètes et autres éléments cosmiques.

Cette contemplation activera rapidement la curiosité et l'envie, voire même le besoin, de comprendre comment tout cela fonctionne. Afin d'y répondre, l'Homme fera preuve de génie et inventera des instruments de plus en plus complexes et performants. Des instruments qui nous permettent d'observer le ciel en détail et même de remonter le temps, de plus en plus loin, en quète de l'origine de l'univers.

La majorité des informations que nous avons sur l'Univers vient de la lumière qui nous permet d'accéder à la connaissance de propriétés telles que la distance à laquelle se situe un objet astrophysique, sa vitesse de rotation, sa taille et bien plus encore.

Toutefois aujourd'hui, malgré les grandes avancées dans la compréhension de notre univers, force est de constater notre manque de connaissances concernant la "machine" galaxie. Les galaxies, appelées autrefois nébuleuses, se forment et évoluent suite à de nombreux mécanismes physiques, comme la formation des étoiles, les fusions, l'accrétion de matières ou son éjection... pour n'en citer que quelques-uns.

Pour comprendre et contraindre ces mécanismes, deux voies principales sont utilisés : les observations et les simulations.

Les observateurs vont regarder directement le ciel comme nous pouvons le faire avec nos yeux mais via de grands téléscopes ayant une surface collectrice de lumière beaucoup plus importante. Ces téléscopes sont situés sur Terre comme au Chili (Very Large Telescope, VLT) ou bien dans l'espace comme le Hubble Space Telescope (HST).

Les simulations, quant à elles, vont tenter de re-créer notre univers, c'est à dire qu'elles vont essayer de reproduire les observations en se basant sur des modèles cosmologiques, simulant de la matière en la faisant intéragir en utilisant des mécanismes

physiques complexes. Actuellement, les simulations utilisant le modèle cosmologique standard marchent plutôt bien car elles réussissent à reproduire l'univers que nous observons à tel point qu'on ne peut plus faire la différence entre une simulation et une observation si l'on regarde à grande échelle. Ces simulations arrivent même à reproduire les morphologies des galaxies que nous observons si les bons paramètres initiaux sont utilisés.

Le modèle cosmologique standard se base sur l'hypothèse d'un univers composé de matière collisionnelle (que l'on appele matière baryonique, celle que nous voyons, qui nous constitue et constitue les objets qui nous entourent) et d'une matière non collisionnelle : la matière noire, que nous ne voyons pas, mais qui agit gravitationnelement. Ces deux matières (baryonique et noire) sont supposées en proportions constantes, la quantité de matière noire étant beaucoup plus importante que la quantité de matière baryonique (environ six fois plus abondante). Malgré les succès de ce modèle cosmologique standard, un problème important reste à éclaircir : beaucoup trop peu de baryons se retrouvent dans les galaxies comparé à la théorie. Trop peu voulant dire que l'on observe au maximum 20% de ces baryons dans les galaxies de masse intermédiaire (masse intermédiaire correspondant à la masse de notre galaxie).

La faible quantité de baryons observée par rapport aux prédictions des simulations est une chose, mais ce qui est le plus perturbant est le fait que cette quantité diminue pour les galaxies de haute et de faible masse. La question qui se pose ici est de savoir où sont passés les baryons. La Figure 1 représente ce problème.

Afin de répondre à cette question, deux hypothèses de mécanismes permettant d'éjecter les baryons en dehors de la galaxie ont été proposées, une pour les galaxies de faible masse, une pour les galaxies de grande masse. Concernant ces dernières, le principal mécanisme serait que le noyau actif de la galaxie éjecte de manière fortement collimaté de la matière s'accrétant autour du trou noir central. De plus, ces jets peuvent s'avérer efficace pour entraîner et pousser la matière hors de la galaxie (en plus de la matière passant par le disque d'accrétion du trou noir).

Le principal mécanisme invoqué pour éjecter les baryons des galaxies de faible masse est ce que l'on appelle les vents galactiques. Ces vents sont principalement produits par accumulation d'éjection de supernovae. Ce phénomène est maintenant bien connu par la communauté astrophysique car on l'observe dans presque toutes les galaxies de faible masse à forte formation d'étoiles. Le principal problème est que ce mécanisme est peu contraint par les observations. En effet, le gaz éjecté par les vents n'est pas assez dense pour qu'on puisse l'observer en émission mais il peut absorber tout de même une partie de la lumière émise par une source brillante en arrière plan. Les vents galactiques sont donc contraints par la lumière qu'ils absorbent.

La source de cette lumière peut être la galaxie hôte de ces vents mais l'absorption dépend de l'orientation de la galaxie et est souvent très faible. C'est pourquoi une méthode consiste à additionner des spectres de galaxies, ayant les mêmes propriétés,

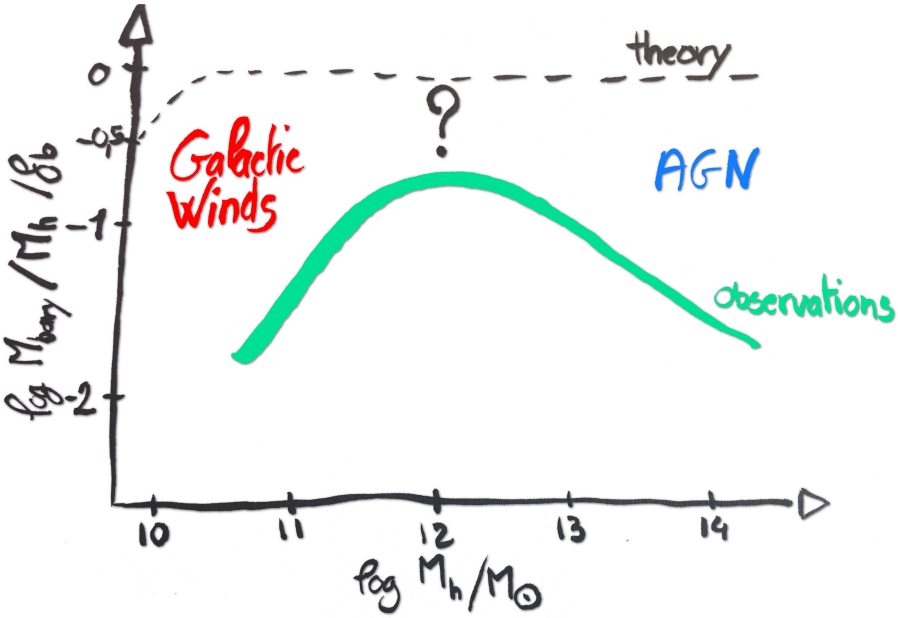

Figure 1: Scheme of the fraction of baryons versus galaxy halo mass. The predicted amount is represented by the dashed black curve whereas the observations are represented by the green one. We can see the two major problems : the global shift between observations and theory as well as the two cutoffs at low and high mass regimes. The two phenomena invoked to explain these cutoffs are Active Galactic Nuclei (AGN in blue) for the high mass regime and galactic winds (in red) for low mass galaxies.

afin de contraster cette absorption. En essayant de reproduire cette absorption par des modèles de vents, les propriétés telles que la vitesse d'éjection ou la quantité de masse éjectée peuvent être caractérisées. Cependant, en utilisant cette technique, nous ne connaissons pas la distance à laquelle se situe le gaz éjecté, ce qui engendre des erreurs de plusieurs ordres de grandeur.

Une autre méthode est d'utiliser un quasar en arrière plan afin de contraindre ces vents galactiques. Le quasar est une galaxie à noyau actif extrêmement brillant. La lumière émise par le quasar en arrière plan traverse donc le gaz éjecté par la galaxie. Comme mentionné précédemment, ce gaz va absorber une partie de la lumière du quasar et ainsi créer ce qu'on appelle des raies d'absorption. En simulant ces raies d'absorption, tout comme la méthode précédente, les propriétés des vents peuvent être estimées avec comme avantage principal de connaître la position du gaz que nous détectons. L'inconvénient de cette méthode est qu'elle nécéssite d'avoir un quasar dont la ligne de visée traverse l'environnement d'une galaxie en avant plan, et cette configuration est rare.

L'objectif principal de cette thèse est de placer des contraintes fortes sur les propriétés des vents galactiques, et plus particulièrement en utilisant la méthode des quasars en arrière plan. Comme énoncé précédemment, la configuration requise étant rare, contraindre les propriétés des vents galactiques nécéssite une stratégie d'observation spécifique afin d'optimiser le nombre de paires galaxie-quasar.

Tout au long de ma thèse, nous avons utilisé des observations venant d'instruments localisés sur le plus grand téléscope du monde (le VLT au Chili), principalement UVES, SINFONI et MUSE. Grâce à ces instruments, nous avons pu construire des stratégies d'observation, les tester et ainsi amener à une meilleure contrainte des propriétés des vents galactiques.

0.4 English version

Some evoke that we would be the Universe made manifest, trying to understand itself. Thus, since dawn of time, mankind looks, fascinated, skyward contemplating these shiny objects that are stars, galaxies, planets and other cosmic objects.

This contemplation quickly activates curiosity and desire, even the need to understand how it all works. To answer this, man will demonstrate engineering and invent instruments of increasing complexity and performance. Instruments that allow us to observe the sky and even look back in time, further and further in quest of the origin of the Universe.

The majority of information we have about the universe comes from light that allows us to access to knowledge of properties such as the distance of an astrophysical object, its speed, size and many more. However today, despite major advance in the understanding of our universe, it is important to note our lack of knowledge about the galaxy "machinery". Galaxies, formerly called nebulae form and evolve through many physical mechanisms such as star formation, mergers, accretion of materials or ejection...to name a few. To understand these mechanisms and force, two main paths are available: observations and simulations.

Observations will directly look to the sky like we do with our eyes but via large telescopes having huge light-collectible surface. These telescopes are located on Earth like in Chile (Very Large Telescope, VLT) or in space like the Hubble Space Telescope (HST).

Simulations, meanwhile, will try to re-create our universe, that is, they will try to reproduce the observations based on cosmological models , matter simulation and interaction of the latter using complex physical mechanisms. Currently, simulations using the standard cosmological model have great success because they manage to reproduce the universe we observe such that we can not make the difference between simulation and observation if one looks at large scale. These simulations even manage

to reproduce galaxy morphologies that we see if good initial parameters are used. The standard cosmological model hypothesis is based on a universe composed of collisional matter (which is called baryonic matter, which we see, which constitutes us and objects around us) and a non collisional matter: black matter that we do not see but which interacts gravitationally. Both matters (baryonic and dark) are assumed to be in constant proportions, the amount of dark matter being much higher than the amount of baryonic one (about six times more abundant). Despite the success of this standard cosmological model, an important problem remains: far too few baryons are found in galaxies compared to theory. Too few meaning that we observe only 20% at maximum of these baryons in intermediate galaxies (intermediate corresponding to the mass of our galaxy).

The low amount of baryons observed compared to simulation predictions is one thing, but what is most disturbing is the fact that this amount decreases for high and low-mass galaxies. The question that arises here is: where are the baryons? Figure 1 represents this problem.

To answer this question, two main mechanisms to eject baryons outside the galaxy have been proposed, one for low-mass galaxies and one for the high-mass galaxies. Regarding the latter, the main mechanism should be that the active core of the galaxy ejects, highly-collimated, the material accreting around the central black hole. Furthermore, these jets can be effective in driving and pushing off the matter out of the galaxy (in addition to the material through the accretion disk of the black hole).

The main mechanism invoked to eject baryons for low-mass galaxies is what we call galactic winds. These winds are mainly produced by accumulation of supernovae explosions. This phenomenon is now well known by the astrophysics community as it is observed in almost all low-mass galaxies with high star formation. The main problem is that mechanism is somewhat constrained by observations. Indeed, the gas ejected by winds is not dense enough to be observed in emission but can absorb a part of the light emitted from a bright source in the background. The galactic wind properties are thus constrained by the light they absorb.

The source of this light can be the host galaxy of the winds but the absorption depends on the orientation of the galaxy and this absorption is often very weak. This is why one method consists in stacking galaxy spectra having the same properties to contrast this absorption. Trying to reproduce the absorption wind patterns, properties such as the outflow velocity or the amount of ejected mass may be constrained. However, using this technique, we do not know the distance where we probe the ejected gas, which generates errors by several orders of magnitude.

Another method is to use a background quasar in order to constrain these galactic winds. The quasar is an active galaxy nucleus and is extremely bright. The light emitted by the background quasar crosses the eject gas by the galaxy. As mentioned previously, this gas will absorb a part of the light of the quasar and thus create what

is called absorption lines. By simulating these absorption lines, like the previous method, the wind properties can be constraints with the main advantage of knowing the position of the gas we detect. The drawback of this method is that it requires having a quasar whose line of sight is passing through the environment of a foreground galaxy, and this configuration is rare.

The main objective of this thesis is to put strong constraints on galactic wind properties, especially using the method of background quasars. As stated previously, the required configuration is rare, thus constraining outflow properties requires a specific observational strategy to maximize the number of galaxy-quasar pairs. Throughout my thesis , we used observations from instruments located on the largest telescope in the world (the VLT in Chile), mainly UVES , SINFONI and MUSE. With these instruments, we were able to build observing strategies, test them and thus lead to a better constraints on galactic wind properties.

Chapter 1

General context

Contents

1.1 Galaxy formation and evolution . . . 2
1.1.1 What is a galaxy? . . . 2
1.1.2 Galaxy spectrum . . . 2
1.1.3 Star formation in galaxies . . . 4
1.2 Galaxy and cosmology fundamentals . . . 8
1.2.1 Cosmology fundamentals . . . 8
1.2.2 Galaxy fundamentals . . . 10
1.2.3 The Tully-Fisher relation and other mass estimator . . . 15
1.2.4 The galaxy "main sequence" . . . 15
1.2.5 What is a quasar? . . . 17
1.2.6 The low efficiency of galaxy formation . . . 17
1.3 Galactic winds "state of the art" . . . 19
1.3.1 Galactic winds are multi-phased and collimated . . . 19
1.3.2 Wind properties in emission . . . 23
1.3.3 Wind properties in absorption . . . 24
1.3.4 Wind properties using background sources . . . 26
1.3.5 Perspective from numerical simulations . . . 26

In this chapter, we describe our knowledge on galaxy formation and evolution, unresolved mechanisms as well as proposed solutions.

1.1 Galaxy formation and evolution

The ultimate aim of extragalactic astrophysics is to understand how galaxies form and evolve from the quantum initial conditions to the Universe we observe today. Two approaches to achieve that goal are via observations and simulations. Both approaches are directly connected as they both need each other to make progress in our understanding of the Universe.

1.1.1 What is a galaxy?

Before jumping into complex mechanisms and problems we face in astrophysics, it is important to begin with some definitions. As mentioned in this thesis title, we will talk about galaxies. What is a galaxy? By definition, a galaxy is assumed to be composed of stars, dust of the interstellar medium (ISM), gas (mostly hydrogen) and dark matter (non collisional matter). Each of these components will contribute to the galaxy luminosity (apart for the dark matter which is non collisional and thus does not emit light), each with different intensities, stars being the main light source of a galaxy. These light contributions will form what we call a galaxy spectrum.

1.1.2 Galaxy spectrum

As mentioned just before, stars are the main light component of a galaxy. Hot stars are mainly emitting in ultra-violet (UV) whereas "cold" stars will emit in infra-red (IR). Adding all different populations of stars contributions in a galaxy, it will lead to the stellar component of a galaxy spectrum. In addition, stars, beaming photons, will ionize and excite their surrounding ISM gas. But what does it mean to ionize and excite a gas?

To ionize a gas is mainly to give enough energy to free an electron from an atom or a molecule. The gas around stars will stay in an ionized state mainly due to stars heating it. In order to clearly understand the excitation process, let us go back to elementary physics.

Gas excitation process

A gas is composed with molecules and/or atoms. Each atom has a specific number of electrons rotating around them. These electrons are not orbiting freely around the atom, indeed, they are forced to move following specific orbitals. These orbitals are

quantified, which means that only some orbitals are allowed for electrons to rotate on. These allowed orbitals are called atomic levels (these orbitals or atomic levels are represented by the dashed gray circles on left part of Figure 1.1). Giving a specific amount of energy to an electron is, by definition, exciting it. With this energy, this electron will move to an upper atomic level. This electron is then in an excited state. It means that the electron is not stable because it has too much energy and needs to unload this excess energy. This excess energy is unleashed by the electron as a photon, the electron is then going back to its initial atomic level. All these processes are represented in Figure 1.1.

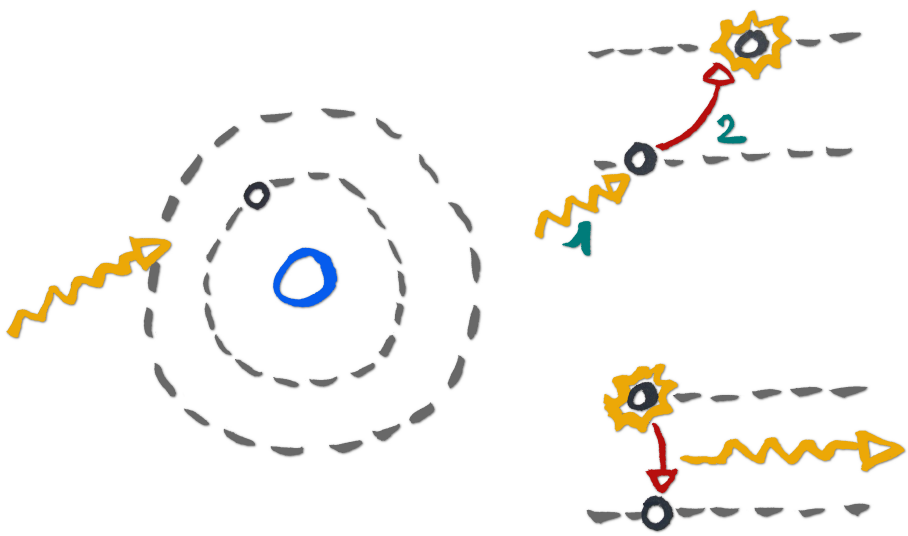

Figure 1.1: Scheme of electron excitation. A coming photon (on left) will: (1) give energy to the electron (represented in dark gray). The electron will go to the next atomic level (2) in an excited state (top right). It will then unleash the excess energy as an emitted photon (bottom right) and come back to its initial atomic level.

Coming back inside a galaxy, the stars will ionize and excite the surrounding ISM, and by unleashing the excess energy, the ionized gas will emit radiations which will be detected as narrow emission lines in a galaxy spectrum. In addition, dust in the ISM will be "heated" by short-wavelength stellar photons (mostly UV photons) and then emit at larger wavelength, typically in the IR. This dust has a tendency to absorb UV and we talk of spectrum reddening. This reddening depends on the amount of dust grains in the ISM. In some cases, a galaxy is not detected in visible wavelength domain but is detected in IR.

A galaxy is something which is alive. Indeed, it evolves, feed on gas to grow, forms stars and also accretes and ejects matter.

1.1.3 Star formation in galaxies

As just mentioned, a galaxy is alive and forms stars. A galaxy which forms stars is called a star-forming galaxy (SFG). SFGs are characterized by the amount of stars they form per year. The amount of stars a galaxy forms per year is called the star formation rate (SFR), given in solar mass per year ($M_\odot\,yr^{-1}$).

Star formation rate

To estimate the amount of stars a galaxy forms, we relate mainly on specific emission lines and photometry. There are several ways of deriving galaxy SFRs depending on the type of galaxy we study, the available emission lines observed, etc...

We detect the signatures of star formation by looking at ionized gas in the galaxy. Indeed, young massive stars produce strong UV radiations that ionize the surrounding gas. This ionized gas recombines, emitting photons with the energy corresponding to the atomic level transition. Lyα (λ1216) and Hα (λ6564) are, for instance, atomic transitions tracing this radiation. If one assumes a mass distribution of the stars in the galaxy (called a mass function), we can convert this UV radiation into a global SFR. Figure 1.2 represents different types of galaxy spectra and shows the main bright emission lines used to trace the SFRs. Correct estimates of SFRs are made from hydrogen emission lines (mainly Hα and Hβ). Other "collision" lines (like [O II]) are less reliable as their intensities depend also on gas physical properties (i.e. degree of ionization, metallicity, etc...).

Another method to estimate SFRs is to reproduce the observed galaxy continuum using a Spectral Energy Distribution (SED) fitting algorithm. The SED fitting method generates a galaxy spectrum using template spectra from well known galaxies and, depending on a large number of parameters, like a specific Initial Mass Function (IMF), dust content of the galaxy, its age, a constant SFR... one can derive the star formation history of a galaxy. This method is more complex than the emission line calibration and can give SFRs on a different time scale. To measure the SFR over longer periods of time, the ultraviolet is the tracer of choice as it is sensitive to stars living up to a few 100 Myrs. Unfortunately, simple recipes to measure the SFR from the UV can be severely affected by degeneracies (e.g., is a galaxy red because it is star–forming but dusty, or is it rather because it has stopped forming stars?) and contamination by long–lived stars (e.g. Boquien et al., 2016). New models making use of data from the far–ultraviolet (FUV) to the far–infrared (FIR), such as CIGALE (Noll et al. (2009a), Boquien et al. in prep.) now allow to have more reliable measurements of the SFR over timescales of 100 Myr. This coverage is not always available, as far-UV and far-IR observations cannot be obtained with ground-based telescopes due to the atmospheric absorption.

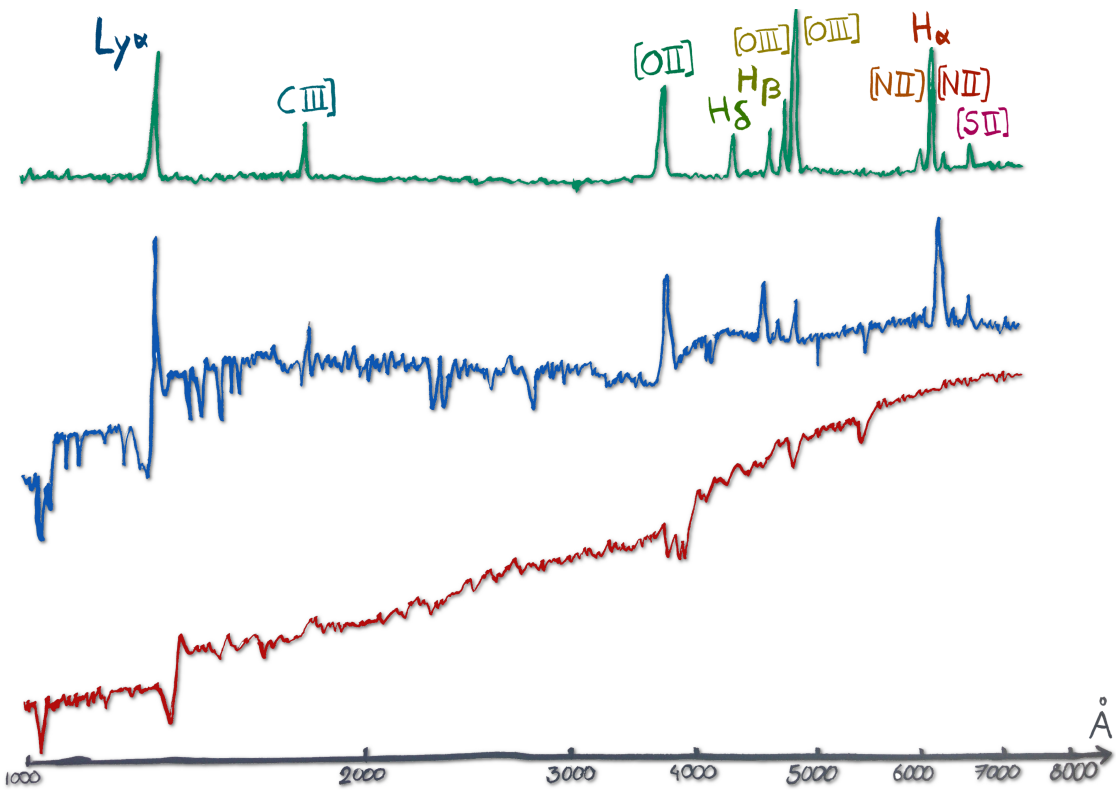

Figure 1.2: Representation of three types of galaxy spectra with the principle emission lines: the red spectrum at the bottom represents an early-type galaxy spectrum with no emission lines, as this type of galaxy does not form stars anymore. We can see the Lyman break (at ~ 1200 Å) as well as the Balmer break ($\sim$4000 Å). The middle spectrum (in blue) represents a late-type galaxy: this type of galaxy is still forming stars and has a bright blue continuum as well as emission lines. The top spectrum represents a low-mass galaxy spectra, it does not have a continuum but we clearly see the main emission lines tracing star formation: Lyα(λ1216), C III](λ1909), [O II] ($\lambda\lambda$3727, 3729), Hδ (λ4102), Hβ (λ4862), [O III] ($\lambda\lambda$4960, 5008), [N II] ($\lambda\lambda$6549, 6585), Hα (λ6564) and [S II] (λ6718).

Another useful parameter is called the star formation density (see further in the text), and more importantly, its evolution with the redshift. In order to describe this parameter, we first need to define what we call the redshift.

Redshift

Other galaxies than our Milky-way are located far away from us. This distance is usually characterized by what we call the redshift. We all know that the Universe is in expansion. This was observed for the first time by G. Lemaitre in 1927 (and after by E. Hubble in 1929) who calculated distances of galaxies and found that they

were moving away from each other, like in an expanding box. If one observes an astrophysical source, the observed wavelength of this object is shifted from its emitted wavelength. This shift in observed versus emitted wavelength is a consequence of motion (this is the Doppler effect): blueshift when moving towards the observer and redshift when moving away from the observer (see Figure 1.3). In an expanding universe, objects like galaxies, at rest, are redshifted due to the expansion of space. The redshift also corresponds to a distance.

The redshift z of an object is defined by the following equation:

$$1 + z = \frac{\lambda_o}{\lambda_e} \tag{1.1}$$

where λ_o is the observed wavelength and λ_e is the emitted wavelength.

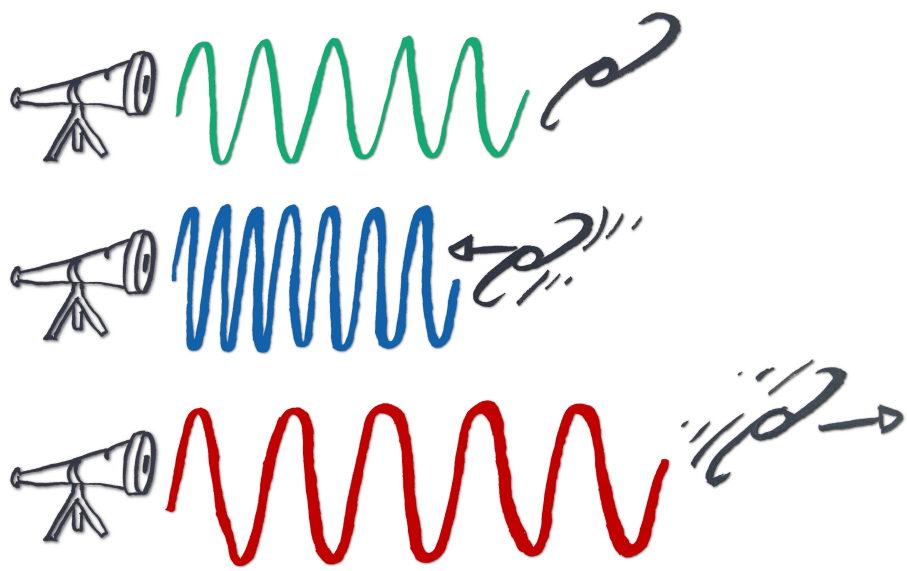

Figure 1.3: Scheme of the Doppler effect: The observer is represented by telescopes on the left. *The top row* represents a galaxy emitting at a wavelength in green. This galaxy is not moving so the observed wavelength is the same as the emitted wavelength. *The middle row* shows a galaxy moving towards the observer and thus the observed wavelength is compressed as compared to the emitted one, we call that shift a blue-shift. *The bottom row* represent a galaxy moving away from us and thus the observed wavelength is diluted as compared to the emitted one, the wavelength is thus red-shifted.

There are two ways to measure redshifts: from photometric data and from spec-

troscopic data. The photometric redshift (photo-z) is mainly derived from SED fitting. The principle of SED fitting, as described above, is to reproduce the object photometry from the different broad band filters magnitudes. This fitting correlates against a set of templates (typical galaxy spectra with various properties). SED fitting can also provide the stellar mass of a galaxy, its SFR, age, etc... using the same process. Photometric redshifts can be accurate (typically $\sim 3-5\%$, $dz \sim 0.05(1+z)$) if one have enough wavelength coverage on an object. However, it can also lead to catastrophic redshift errors if the number of available magnitudes for an object is not enough.

The spectroscopic redshift, on the other hand, is very accurate ($dz \sim 0.001$). Indeed, the principle is to identify observed spectral features to rest-frame known features such as emission/absorption lines (if the spectral resolution of the instrument is high enough and the observation is deep enough).

Spectroscopy with a resolution of 3000 can identify spectral features with an accuracy of 10^{-4}, hence, a redshift accuracy of 10^{-4}. Multi-band photometry with typical resolution of 50 to maybe 500 (when there are many filters) only have accuracy of a few percents.

These two methods of redshift determination are complementary but differs in their accuracy.

Star formation rate density

In order to have a bigger picture on the evolution of the SFR over time, lots of studies have estimated SFR as a function of redshift (e.g. Lilly et al., 1996; Madau et al., 1996; Behroozi et al., 2013a, to cite a few). This correlation usually involves the star formation rate by unit volume. This quantity is called the star-formation rate density (SFRD, given in $\mathrm{M_{\odot} yr^{-1} Mpc^{-3}}$). Its redshift evolution shows an increase from redshift $z \sim 7$ to peak at redshift $z \sim 2-3$ and then a decrease to the local universe ($z = 0$). A representation of SFRD as a function of redshift is shown in Figure 1.4 from Madau & Dickinson (2014).

Work on understanding the SFRD evolution is still taking place but we can briefly summarize the emerging picture presented in Madau & Dickinson (2014). The Universe was much more active in the past. Stars formed around nine times higher than seen today. Approximatively 25% of the stellar mass density formed at $z > 2$, before the SFRD peak. Another 25% formed since $z = 0.7$ i.e. over half of the Universe's age. From $z = 2$, where the SFRD peaks, to the present day, most stars formed in galaxies following the SFR-$M_\star$ correlation. The evolution of these "main sequence"

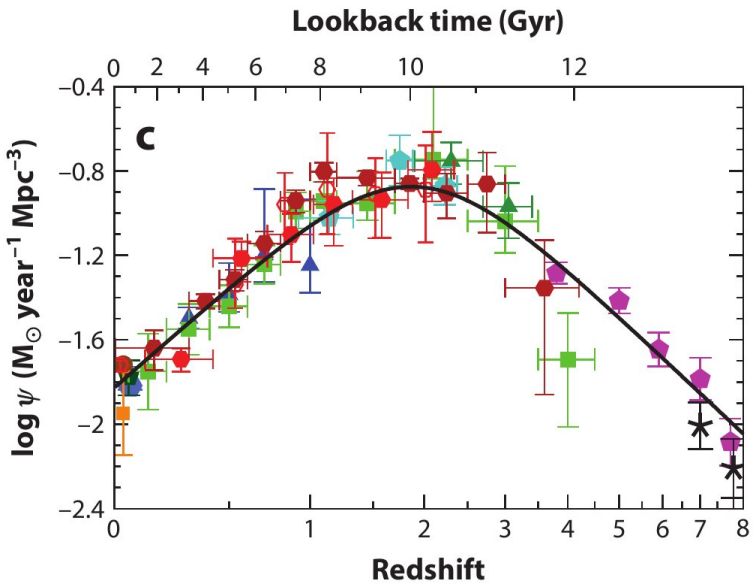

Figure 1.4: The star formation rate density (SFRD) as a function of redshift. We can see that the SFRD increases from high redshift to peak at redshift $z \sim 2-3$ and then drops to redshift $z = 0$. This figure is from Madau & Dickinson (2014).

(described later in this chapter) galaxy population suggests that the star formation history is mostly determined by a balance between accretion and feedback processes. Before going further, it is essential to place the cosmological context in which modern astrophysics evolve.

1.2 Galaxy and cosmology fundamentals

1.2.1 Cosmology fundamentals

To date, one of the most famous and successful cosmological model is the Cold Dark Matter (CDM) model. In this model, seconds after the Big Bang (a rapid expansion), the Universe was composed of baryonic (collisional) matter, dark matter (DM) and light. The Universe was extremely dense and in thermal equilibrium. Through expansion, its temperature began to decrease and around 300 000 years after the Big Bang, photons could move freely and radiance of this epoch is still visible and is called the Cosmic Microwave Background (CMB). A picture of the observed CMB is represented in Figure 1.5. The CMB shows temperature fluctuations which are linked with density fluctuations.

Through these density fluctuations, matter agglomerated via filamentary struc-

ture, forming DM haloes in the center of nodes. Gas collapsed via cooling and fragment into small structures such as stars or galaxies. These galaxies, through merger events and gas accretion, grow and evolve to finally form the observed galaxies.

On large scales (100s of Mpc), galaxy distribution is described by a power spectrum which comes from the probability of finding a galaxy in a volume at a certain distance from another galaxy (more details on this power spectrum is given in the next framed text on simulations). This power spectrum is usually the starting point of cosmological simulations.

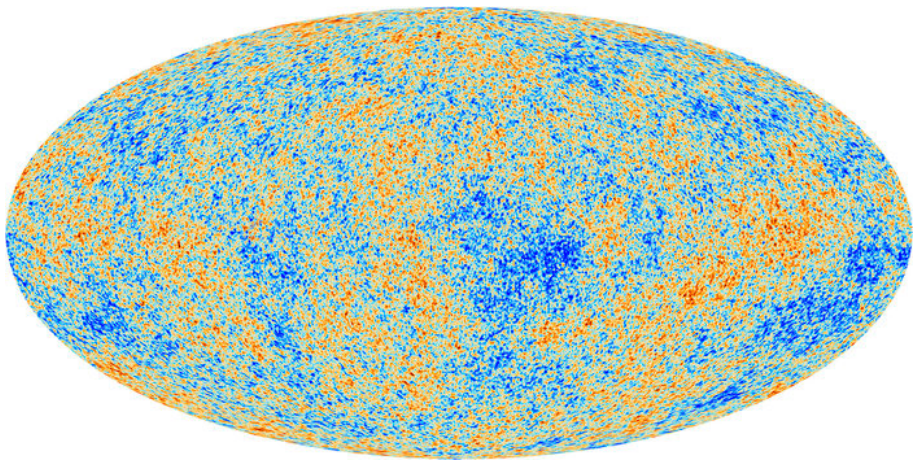

Figure 1.5: The anisotropies of the Cosmic microwave background (CMB) as observed by Planck. The CMB is a snapshot of the oldest light in our Universe, imprinted on the sky when the Universe was just 380 000 years old. It shows tiny temperature fluctuations that correspond to regions of slightly different densities, representing the seeds of all future structure: the stars and galaxies of today. Copyright: ESA and the Planck Collaboration.

In simulations, we need a power spectrum to begin with. This power spectrum is found from a two point correlation function which will quantify the clustering of galaxies later in the simulation. This correlation function is the probability to find an object (i.e. a galaxy) at a distance r from another object. This function is defined as follows:

$$\xi(r) = 1 + \frac{\langle N(r + \mathrm{dr})\rangle}{N_{\mathrm{Poisson}}(r + \mathrm{dr})} \tag{1.2}$$

This function is defined as a measure of the excess probability dP of finding a galaxy in a volume element dV at a separation r from another galaxy:

$$dP = n[1 + \xi(r)]dV \tag{1.3}$$

Where n is the mean number of the galaxy sample (Peebles, 1980). The Fourier transform of $\xi(r)$ gives the power spectrum which is used to describe density fluctuations observed in the Cosmic Microwave Background (CMB) (see Figure 1.5).

In most simulations, we need sub-grid physics in order to make the universe evolve and this usually ask for huge computational resources.

Look-back time

From this standard model, lots of cosmological parameters help us deriving astrophysical objects properties. In particular, it is important to define what we call the look back time. We define the look-back time as the time it takes for the light to come to us from an object at redshift z. The look-back time of an object is the difference between the age of the Universe now (at observation) and the age of the Universe when the photons of the object were emitted.

Cosmological simulations try to reproduce the observed universe. They start from a certain amount of matter, initial conditions and make them evolve and form structures with time to afterwards compare with what we observe. Simulations are based on several ingredients and physical mechanisms:

- Initial conditions which mainly comes from observations from WMAP or Planck, providing a starting environment for the Universe to evolve from,

- Physics of collisionless fluid for Dark Matter (DM) and star particles,

- Physics of collisional fluid for gas heated and cooled radiatively (atomic and molecular),

- "Galaxy physics" for star formation and feedback on the surrounding gas (supernovae, turbulence, black hole growth, jets, chemistry of heavy elements, dust...).

1.2.2 Galaxy fundamentals

At galaxy scale (scale of kpc), several properties can be derived from observation of galaxies such as apparent magnitude and the galaxy morphology. From these direct measurements, several indirect ones can be made such as relative velocities, velocity fields, physical sizes, absolute luminosities, stellar masses, star formation rate, age, metallicity, dust...

Apparent magnitude, flux and galaxy morphology

Once objects are identified, we get the total observed flux on an image to derive the apparent magnitude (Eq. 1.4) using calibrated reference sources.

$$m = -2.5 \log(Flux) + C \tag{1.4}$$

where m is the apparent magnitude and C is a normalized constant derived from the reference source.

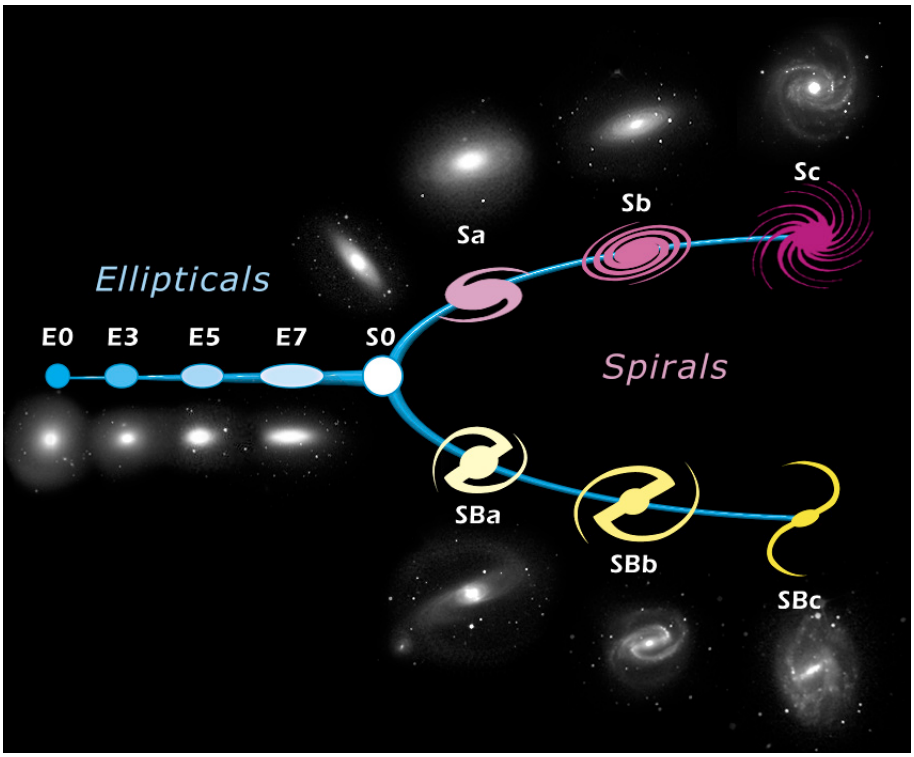

Figure 1.6: Scheme of Hubble classification for galaxy morphologies.

The Hubble sequence

From the apparent shape of a galaxy, one can classify them following the Hubble sequence. This sequence classifies galaxies by their morphology (see Figure 1.6). In order to classify galaxies, one can fit their morphology using models to represent the galaxy in 2 dimensions. We usually use a Sersic (Sérsic, 1963) profile to fit the flux distribution of a galaxy as a function of its radius:

$$I(r) = I_0 \exp(-kr^{1/n}) \tag{1.5}$$

and thus:

$$\ln I(r) = \ln I_0 - kr^{1/n} \tag{1.6}$$

Where $I(r)$ is the intensity at radius r, n being the Sersic index.

A typical flux profile for spiral galaxies is an exponential flux distribution (Sersic index $n = 1$), whereas an elliptical galaxy is best fitted by a de Vaucouleurs profile ($n = 4$).

This method offers a basis to automated classification of galaxy morphology. However, it becomes complicated for galaxies at $z > 1$ mainly due to the fact that they become mostly irregular. Hence, these "high redshift" galaxies are usually not resolved and it is thus difficult to classify them on the Hubble sequence.

It is important to define "red early-type" and "blue star-forming" galaxies. A red early-type galaxy is usually an elliptical galaxy. These galaxies starved of star-forming gas at high redshift and thus do not form stars anymore (or their SFR is very low). They appear yellow-red because of old star population they are composed of, as compared to the blue star-forming galaxies which are usually spirals and appear blue due to the young and hot stars in their spiral arms. The blue star-forming galaxies are also called late-type galaxies as they are still forming stars.

Relative velocities

In galaxies, one can derive their rotational velocities and their redshifts. For deriving the velocity field of a galaxy, i.e to determine which part of a galaxy is moving toward us and which part away from us, we basically need to look at this galaxy spectrum. Emission lines from this galaxy will blue/red shift from its systemic velocity (usually located at the center of this galaxy). We can see a representation of this effect on Figure 1.7. On this figure, the right part of the galaxy arm will have an emission red-shifted compared to its center, whereas the left end arm will have its emission blue-shifted. Mapping all the galaxy will lead to building the velocity field of this galaxy.

Physical sizes

The aim is to transform the observed angular size to physical dimension of the source. In order to do this, we use a cosmological model (the ΛCDM is the most popular to date). We use Equation 1.7 to derive the angular diameter distance for a source at redshift z.

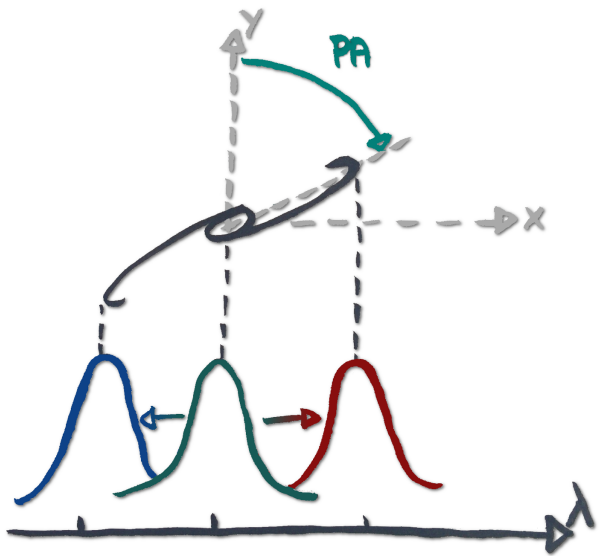

Figure 1.7: Scheme of a galaxy in rotation. The galaxy is in black and is represented on the sky plane x, y (y representing the celestial north). This galaxy has a position angle PA which is the angle between the celestial north and the major axis of the galaxy. At the bottom, we can see 3 Gaussians on a wavelength axis (λ) corresponding to emission lines in 3 different regions of the galaxy. The left part of the galaxy is moving towards us, so its emission line is blue-shifted, its middle do not move with respect to its systemic velocity and the right part is moving away from us, so its emission line is red-shifted.

$$d_a = \frac{S_k(r)}{1+z} \tag{1.7}$$

where $S_k(r)$ is the FLRW (Friedmann-Lemaître-Robertson-Walker) coordinate defined as:

$$S_k(r) = \begin{cases} \sin(\sqrt{-\Omega_k} H_0 r)/(H_0\sqrt{|\Omega_k|}), & \text{if } \Omega_k < 0 \\ r, & \text{if } \Omega_k = 0 \\ \sinh(\sqrt{\Omega_k} H_0 r)/(H_0\sqrt{|\Omega_k|}), & \text{if } \Omega_k > 0 \end{cases} \tag{1.8}$$

where d_a is the angular diameter distance, Ω_k the curvature density z is the redshift of the object, r the comoving distance and H_0 is the Hubble constant.

Absolute luminosities

From apparent magnitude, we can derive the absolute magnitude using Equation 1.9.

$$M = m - 5\log_{10}(\frac{D_L}{10\text{pc}}) - K \tag{1.9}$$

where M is the absolute magnitude, m is the apparent magnitude, D_L is the luminosity distance of the object and K is a correction factor for the redshift effect on object outside our galaxy. This K correction depends on filter used to make the observation and the shape of the object spectrum. If one have access to all the light in all wavelength of an object or if the light is measured in an emission line, the K correction is not needed. However, if one has access only to a filter (only see a fraction of the object spectrum) and want to compare measurements with different objects at different redshifts in this filter, estimation of this K correction is needed. An example of filters for the Sload Digital Sky Survey (SDSS) is shown in Figure 1.8.

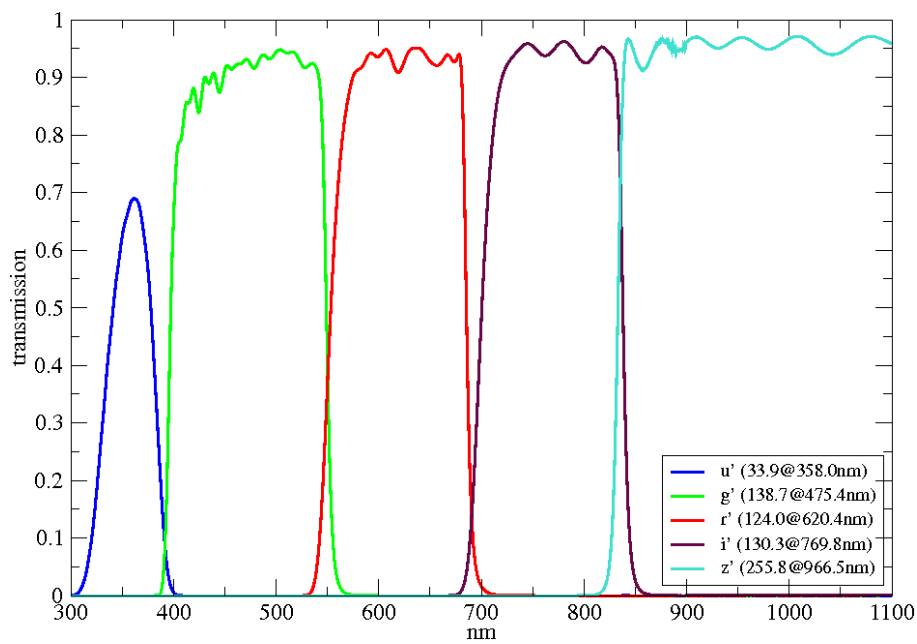

Figure 1.8: SDSS transmission curves for the different filters.

Stellar masse, star formation rate, age, dust...

These quantities are usually derived from SED fitting method. The stellar population add up to produce a galaxy luminosity and colors. The stellar population

synthesis models aim at reproducing the observed stellar light from galaxies, these models include changes with age, metallicity and extinction law from dust. It is difficult to be confident in results from these models as lots of degeneracies occur (i.e. age and metallicity, IMF and SFR laws...).

1.2.3 The Tully-Fisher relation and other mass estimator

A very popular relation is the Tully-Fisher relation (TFR, Tully & Fisher, 1977; Miller et al., 2011, 2014; Vergani et al., 2012; Simons et al., 2015, to cite a few). This empirical relation is linking the galaxy rotational velocity with the intrinsic luminosity of the galaxy and thus its stellar mass. Indeed, the stellar mass of a galaxy is directly proportional to the amount of stars within, and the amount of stars is directly linked to the galaxy luminosity. The TFR applies for rotation-dominated galaxies, where the dispersion velocity of the galaxy is negligible compared to the rotational velocity.

Another mass estimator which include a combination of the galaxy dispersion velocity σ and the rotational velocity $V_{\max}$ can be used. Weiner et al. (2006); Kassin et al. (2007) and Price et al. (2016) argued that the quantity $S_K^2 = K \times V_{\max}^2 + \sigma^2$, where K is a constant, can be used as a dynamical mass estimator as it combines dynamical support from ordered motion ($V_{\max}$) and disordered motions (σ). This mass estimator will be used in § 5.1.2. In order to clearly understand on which type of galaxies these mass estimators work with, it is important to define the galaxy "main sequence" as well as some type of galaxies we will later encounter.

1.2.4 The galaxy "main sequence"

Like stars, there is what we call a galaxy "main sequence". If one investigates the relation between galaxy SFR and stellar mass, one can see that most of galaxies lie along a scattered line. This line is called the galaxy "main sequence". However, even if most galaxies lie on this line, some galaxies are outliers. These outliers are above (starbursts) or under (red) the main sequence. Figure 1.9 shows a representation of this main sequence as well as outliers categories. We will quickly describe galaxies located above the main sequence: starburst galaxies.

Star-burst galaxies

It is important for us to define this type of galaxies. Indeed, further in this manuscript, we will encounter such type of galaxies used in other studies to compare with ours. The galaxy M82 for instance (presented in § 1.3), is the starburst archetype. This galaxy has high SFR and therefore lots of supernovae which leads to galactic winds.

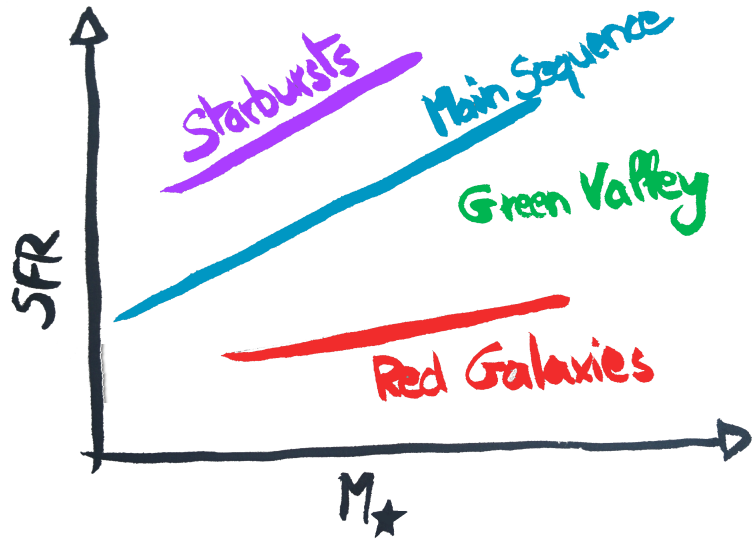

Figure 1.9: Scheme of the galaxy "main sequence" in blue as well as outliers: starbursts above this main sequence (purple) and red or dead (not forming stars anymore) galaxies (red). Space between the main sequence and red galaxies is called the green valley.

As mentioned earlier, starburst galaxies have higher SFR (above the main sequence) compared to other galaxies for the same stellar mass. The rate of star formation is so large in starbursts that they will consume almost all their gas reservoir used to form stars in a shorter timescale compared to "main sequence" galaxies. There are different types of starburst galaxies, and within these types, a popular one is the Ultra Luminus Infra Red Galaxy (ULIRG).

U/LIRGs

ULIRGs are generally extremely dusty objects. As their name tells us, these galaxies are emitting in IR. Indeed, as mentioned before, the dust is absorbing UV photons produced mainly by star formation and re-emit them in larger wavelength, typically in IR. This could explain the red color associated with ULIRGs.

In addition, these galaxies are extreme cases of starbursts. They are often galaxies in major interactions or even in advanced merging process. ULIRGs can form a huge amount of stars (SFR$\sim$100 to 1000 $M_\odot\,yr^{-1}$). However, due to their extreme properties, these galaxies are rare.

1.2.5 What is a quasar?

Another type of astrophysical objects we will largely encounter and use during this thesis are quasars. A quasar is among the most energetic and luminous type of object in the universe. They belong to the class of object called Active Galactic Nuclei (AGN) and are the most luminous and distant objects of this class. An AGN is a compact region in the center of galaxies. Quasars are thus powered by a super massive black hole and are active galaxies. A typical quasar spectrum is represented in Figure 1.10.

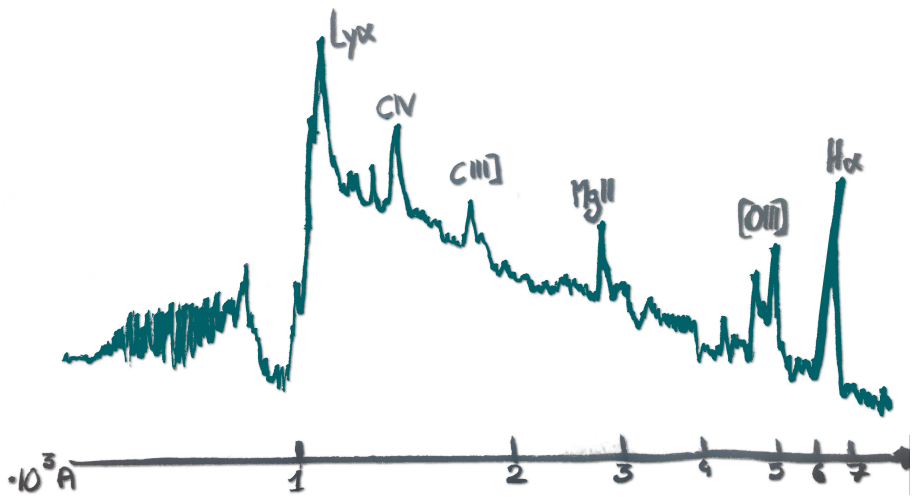

Figure 1.10: Scheme of a typical quasar spectrum.

1.2.6 The low efficiency of galaxy formation

It is important to remind the reader that galaxies are not only isolated astrophysical objects living their life without interacting. Indeed, they have gas flows, inflowing and outflowing gas which play an important role in galaxy evolution.

In order to introduce the main question we want to address in this thesis, we first need to present the baryonic mass function. The baryonic mass function is built from the sum of the stellar mass function and the gas mass function, i.e. it represents the baryon budget locked into galaxies. The stellar mass function is derived from the conversion of the luminosity function and requires a mass-to-light ratio for the stellar populations. This ratio usually depends on galaxy type, age and metallicity.

Concerning the gas mass function, the principle is to estimate the total cold mass density. It corresponds to the sum of atomic (H I) and molecular (H_2) hydrogen gas content of galaxies. Large samples of atomic hydrogen H I gas (e.g. the Australian

HIPASS survey Koribalski et al. (2004)) allowed to derive a gas mass function (e.g. Zwaan et al., 2003) for galaxies in the local universe. The molecular hydrogen reservoir, however, is difficult to constrain due to the lack of electric dipole moment in the H_2 molecule, which is the main component in molecular clouds. In order to derive the molecular gas content of a galaxy, one needs a tracer which is robust and directly linked to the molecular hydrogen density. Keres et al. (2003) derived a molecular gas mass function of galaxies using CO as a proxy for H_2 because CO is abundant and easily excited by collision with H_2.

Summing the stellar mass and gas mass functions, one can obtain the baryonic mass function of galaxies. Papastergis et al. (2012) derived this baryonic mass function and compared it with the predicted amount from the CDM model (see Figure 1.11).

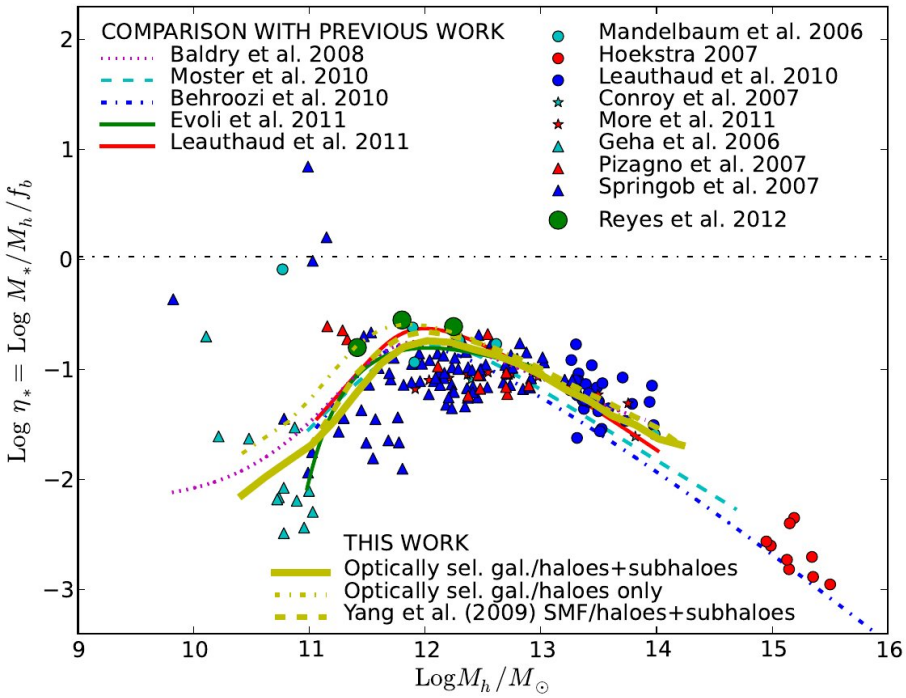

Figure 1.11: Figure from Papastergis et al. (2012). The ratio of galactic stellar mass to halo mass as a function of host halo mass ($M_*/M_h - M_h$ relation). The thick yellow line shows Papastergis et al. (2012) main result, obtained from abundance matching the stellar mass function of optically-selected sample with the halo mass function including subhaloes. The dotted-dashed horizontal line shows the cosmic baryon fraction $f_b \approx 0.16$.

The main results from this baryonic mass function are that in low and high mass

haloes ($\log(M_h/M_\odot) < 12$ and $\log(M_h/M_\odot) > 12$ respectively), there are huge differences between observations (yellow thick curve) and the cosmic value of baryon fraction $f_b \approx 0.16$ (black dotted-dashed horizontal line). Indeed, we only observe a few percents of the baryonic matter and there are even less matter in low and high mass regimes (see yellow curve as compare to the horizontal dotted line in Figure 1.11). These differences lead to the conclusion that there must be mechanisms responsible for this lack of observed matter. Feedback is therefore needed in order to expel baryons out of galaxies for low and high mass galaxies.

In the high-mass galaxy regime, feedback from Active Galactic Nuclei is invoked as an efficient mechanism to expel baryons out of the galaxy halo, but we will not detail this mechanism here. From now on, we will focus on low mass galaxies since this thesis is focused on these objects. Low-mass galaxies need feedback mechanisms such as baryons blown out by supernova explosions and these mechanisms must be very efficient in pushing away gas out of the galaxy. This mechanism is called galactic winds and our scientific goal is to constrain properties of this phenomenon such as the ejected mass rate, the outflowing velocity or the ability for the gas to leave the galaxy halo.

1.3 Galactic winds "state of the art"

As described in the previous section, and in spite of successes of the ΛCDM cosmological model, a major discrepancy remains between the predicted baryonic density of dark matter haloes and the observed ones in the low-mass galaxy regime ($L < L_*$) (Behroozi et al., 2013b). This fundamental problem is usually explained by supernovae(SN)-driven outflows (Dekel & Silk 1986) which expel baryons out of the galactic disk. Indeed, these galactic outflows are observed in almost every star-forming galaxy (SFG) (Veilleux et al., 2005a) and are a viable mechanism to enrich the inter-galactic medium (Oppenheimer et al., 2010).

Various observational techniques are used to study galactic outflows. In order to better understand the main geometrical properties of galactic winds, one can observe SFGs in the local universe at $z = 0$.

1.3.1 Galactic winds are multi-phased and collimated

Messier 82 (or M82) is a famous local galaxy. This galaxy can be observed in the night sky using a personal telescope. However, in order to see the details of this galaxy, one needs a large telescope and a wide wavelength coverage. This galaxy has been observed in lots of different wavelengths with several instruments.

Galactic winds geometry

Figure 1.12 shows the galaxy M82 taken with the Hubble Space Telescope (HST), in visible. On this figure, we can see the disk of the galaxy as well as the dust in dark filaments. This galaxy has the advantage of being almost edge-on, which means that we have a side view of the galaxy. If we look closer at this image, we can see the presence of gas perpendicular to the galactic disk, but this is not obvious in these wavelengths. If we observe this same galaxy with a different wavelength filter, we will see that this galaxy does not only have a disk.

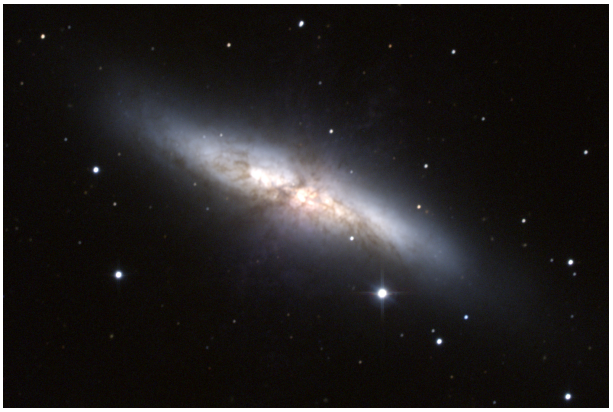

Figure 1.12: The galaxy M82 in visible wavelength, taken with HST. We can see that this galaxy is almost edge-on, in white we see the stars and gas contributions and the dust is shown in dark filaments along the galaxy.

Left panel of Figure 1.13 shows a combined picture of this galaxy from different filters: B (blue, in blue), V (visible, in white) and Hα (in red). We can clearly see the presence of a gas perpendicular to the galactic plane. The Hα filter detects the presence of ionized gas. This ionized gas is ejected from the galaxy with a direction perpendicular to its plane. This ejected gas is a direct observation of galactic winds in emission.

Again, looking at a different wavelength, and in X-ray to be precise, one can trace the hot gas of this galaxy. Right panel of Figure 1.13 shows the same galaxy observed in X-rays by the space telescope called Chandra. We do not see the galactic disk anymore but only the hot gas ejected from the galaxy. This hot gas is located at the same place as the red ionized gas seen in Figure 1.13. Here, we are tracing the hot phase of galactic winds.

Through a simple example, we already seen major properties about galactic winds. Indeed, we saw that they are located perpendicular to the galactic plane and are multi-phased. The hot phase of the gas, directly connected to supernovae explosions,

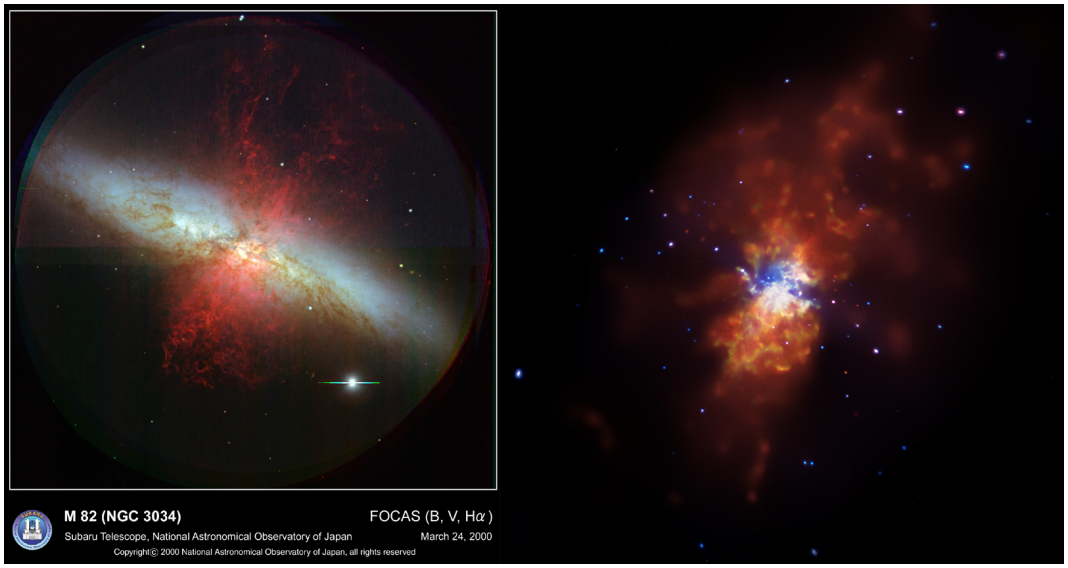

Figure 1.13: On left panel, the galaxy M82 in B,V (blue and visible) combined with Hα, taken with the Subaru telescope. Like Figure 1.12, we see the disk of the galaxy (B and V filters) in white. In addition, the Hα is represented in red. We see the presence of this ionized gas perpendicular to the galactic disk. Hence, these outflows appear to be collimated in a cone. This gas is a direct imaging of galactic winds. On right panel, the galaxy M82 in X-ray, taken with the Chandra telescope. Unlike Figure 1.12 and left panel of this figure, we do not see the disk of the galaxy. We can, however, see the hot gas at almost the same location where we see the Hα gas on left panel. Again, we can see the conical structure of these outflows.

is pushing the cold gas out of the galaxy. The hot gas is supposed to hold most of the outflow energy with low mass and flux whereas the cold gas is believed to hold most of the outflowing flux and mass.

Bi-conical outflows

In addition to these properties, we can also see that galactic winds appear to be collimated in a cone. We talk of bi-conical outflows as they are ejected in both directions perpendicular to the galaxy. These properties are confirmed if we look at other local star-forming galaxies like in Figure 1.14.

However, even if we can directly see these geometrical properties for local galaxies, direct imaging of galactic winds is not yet possible for $z > 0$ galaxies. Indeed, the outflowing gas has a very low surface brightness compared to its host galaxy and other observational techniques are needed in order to derive outflow geometrical properties.

The outflowing gas is thus not visible in emission for $z > 0$ galaxies, but the

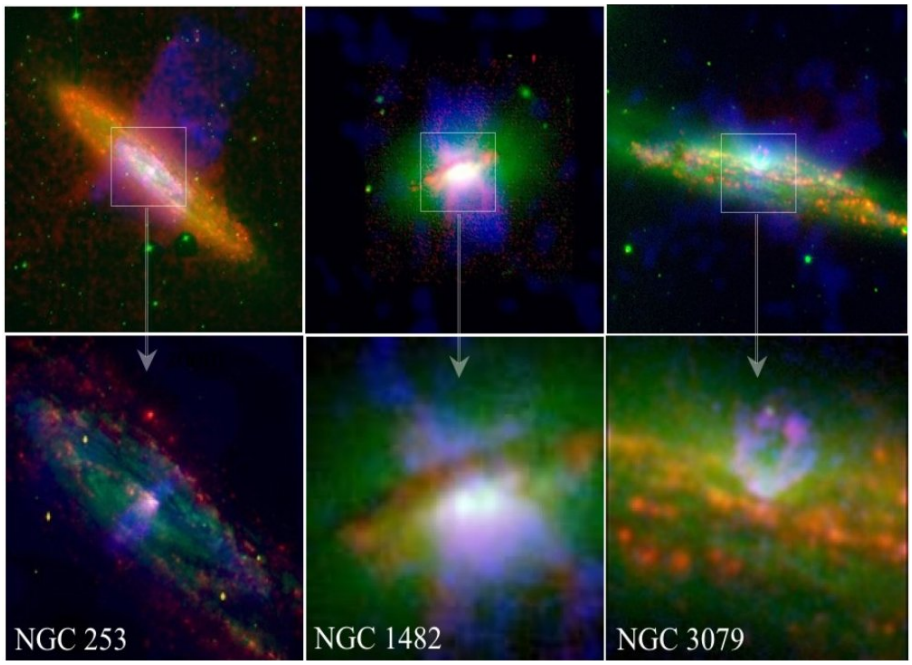

Figure 1.14: Other examples of galactic outflows seen in emission in local galaxies NGC 253, NGC 1482 and NGC 3079. On each of these galaxies we have a zoom of their center which clearly show the presence of outflows. Like M82, these outflows are ejected perpendicular to the galactic disk. Hence, we clearly see (especially for NGC 1482 and 3079) that galactic winds are likely collimated in a cone.

circum-galactic gas can be observed in absorption. Several studies have shown that galactic outflows are collimated using stacked background galaxy spectra (Bordoloi et al., 2011, 2014; Rubin et al., 2014) and using background quasars passing near star-forming galaxies (Bouché et al., 2012; Lan et al., 2014b). These studies showed that galactic winds are collimated within a cone[1] of $\approx 30°$ to $40°$ from the minor axis of the host galaxy.

The main outflow properties which need to be constrained are the outflowing velocity $V_{\rm out}$, the ejected mass rate $\dot{M}_{\rm out}$ and the loading factor η which is the ratio between the ejected mass rate and the host galaxy SFR. There are several techniques to constrain these outflow properties. The three main techniques are: (1) studying winds in emission using a broad blue-shifted component in the galaxy spectrum, (2) using the absorption profiles in galaxy spectra and (3) using background sources having their line of sight (LOS) passing through the circum-galactic gas of a foreground galaxy.

[1]A cone opening angle $\theta_{\rm max}$, where $\theta_{\rm max}$ is defined from the central axis, and the cone subtends an area Σ of $\pi \cdot \theta^2_{\rm max}$.

1.3.2 Wind properties in emission

Unlike local galaxies, wind study of further away galaxies is not possible in emission via imaging. However, if one takes a galaxy spectrum, and this galaxy happens to be nearly face-on (seen from above), the outflowing gas is ejected toward the observer and we can see its signature. Indeed, this outflowing gas will contribute to the galaxy spectrum with a blue-shifted emission line component with respect to the systemic velocity. This behavior is represented in Figure 1.15.

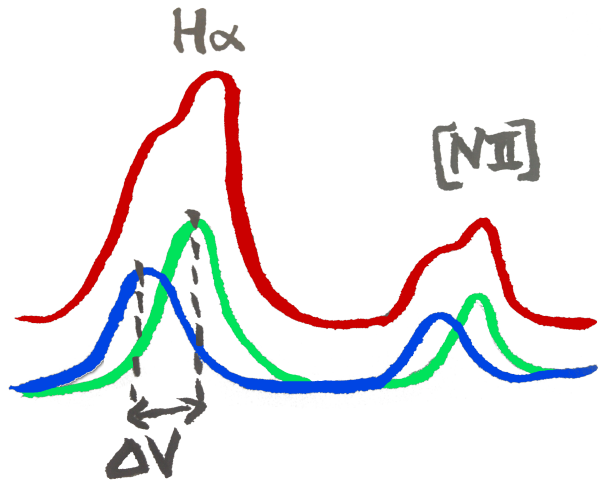

Figure 1.15: Scheme of the blue-shifted component for Hα and [N II] produced by galactic outflows. The green Gaussian correspond to the systemic (narrow) component and the broad component is shown in blue. The velocity difference (corresponding to the outflow velocity) between the two components is shown by the label ΔV.

Studies like Genzel et al. (2011a), Newman et al. (2012) or Arribas et al. (2014) (to cite a few) used this technique in order to constrain outflow properties. Together with theoretical prediction (e.g. Hopkins et al., 2012), Newman et al. (2012) found that:

- the loading factor η correlates with galaxy size and inclination.
- Argue for strong dependence of the loading factor with SFR per unit area ($\Sigma_{\rm SFR}$).
- That galaxies should have a SFR per unit area larger than $1 M_\odot yr^{-1} kpc^{-2}$ in order to be able to show the presence of galactic winds.
- And it is harder for a massive galaxy to launch winds.

These results are based on SINFONI[2] data of $z \sim 2$ star-forming galaxies from the SINS and zC-SINF surveys (e.g. Förster Schreiber et al., 2004). They used the broad emission lines component (without stacking) as in Shapiro et al. (2009) and Genzel et al. (2011b) in order to put outflowing gas constraints.

Work of Arribas et al. (2014) study 58 local (low-z) (Ultra) Luminous Infra-Red Galaxies (U/LIRG) using the Visible Multi Object Spectrograph (VIMOS, Le Fèvre et al., 2003) and INTEGRAL (Arribas et al., 1998) instruments. In their work, they also use the blue-shifted broad component of several emission lines like Hα and [N II] in order to derive the outflow velocity. This velocity is derived by fitting a Gaussian profile to this blue-shifted broad component (see Figure 1.15). In their paper, they assume impact parameters[3] b of 0.7 kpc and find that:

- the outflow velocity is proportional to the SFR ($V_{\rm out} \propto {\rm SFR}^{0.24}$),
- that high-z galaxies also require SFR per unit area larger than 1 ($\Sigma_{\rm SFR} > 1$) for launching strong outflows (as in Newman et al., 2012).
- The mass loading factor is correlated with SFR per unit area ($\eta \propto \Sigma_{\rm SFR}^{0.17}$).

1.3.3 Wind properties in absorption

The second technique is to use the absorption lines produced by the outflowing gas in the galaxy spectrum (see Figure 1.16 for an example).

Because galaxies with redshifts larger than 0.5 are usually fainter, it can be difficult to see the absorption lines produces by outflowing gas in the spectrum of these galaxies. Therefore, a number of investigations on intermediate redshift ($0.5 < z < 1.5$) SFGs (e.g. Weiner, 2009; Martin et al., 2012; Bordoloi et al., 2014; Rubin et al., 2014) used stacked galaxy spectra. This method consists in stacking strong absorption lines like the Mg II λ2796 doublet of galaxies with similar properties and constrain outflows for a specific type of galaxy. The recent study of Heckman et al. (2015) uses the absorption technique but does not use stacked galaxy spectra as they have enough signal to noise ratio (SNR) to characterize the outflows in individual galaxies.

In the paper of Heckman et al. (2015), they assume impact parameters of 5 kpc for a sample of 39 low-z galaxies. They study two samples of low-z starburst galaxies. The first sample is composed of 19 galaxies observed by Far Ultraviolet Spectroscopic Explorer (FUSE) (previously analysed by Grimes et al. (2009) and Heckman et al. (2001)). The second sample they use is composed of 21 Lyman break analogs (LBAs) observed with Cosmic Origin Spectrograph (COS) on HST and previously analysed by Alexandroff et al. (2015). These galaxies are starburst galaxies, which means that

[2]SINFONI is an Integral Field Unit (IFU, described in § 2.1.2) instrument on the Very Large Telescope (VLT) in Chile.

[3]The impact parameter corresponds to the distance where the outflowing gas is probed from the host galaxy.

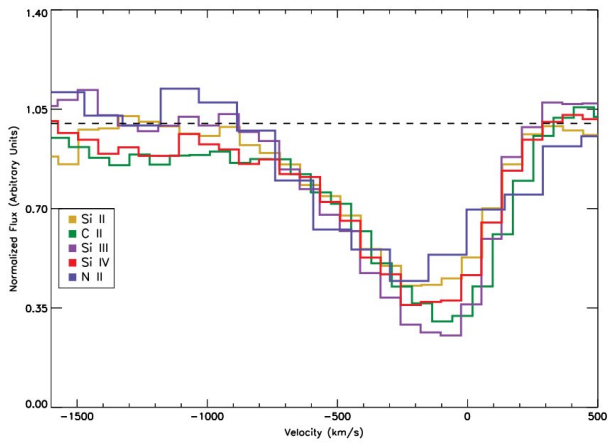

Figure 1.16: Outflow absorption lines seen in a galaxy spectrum from Heckman et al. (2015). This absorption is blue-shifted with respect to the galaxy systemic velocity. We can also see that the different absorption lines have the same absorption behavior like their asymmetry.

they have high SFRs and thus are likely to have galactic winds. In order to derive outflow velocities, they used the absorption lines produces by the outflowing gas but without stacking different galaxy spectra as they have enough SNR to analyze almost each galaxy individually. To estimate $V_{\rm out}$, they used the value corresponding to 80% of the absorption profile in order to avoid instrumental noise seen in the galaxy continuum. Using these blue-shifted absorption lines, they found that:

- the outflow velocity correlates weakly with the galaxy stellar mass and its maximum rotational velocity.
- That there is strong correlation between the outflow velocity and SFR (and also with SFR per unit area ($\Sigma_{\rm SFR}$)).
- And the mass loading factor is not correlated with the outflow velocity (compared to Hopkins et al. (2012)).

In summary they claim that the outflowing gas should be accelerated by the combined force due to gravity and momentum flux from starburst.

This technique has the advantage of having lots of observations since it mainly needs a face-on SFG. However, estimates of ejected mass rates and thus loading factors are uncertain by order of magnitude and are therefore mostly indicative. The major cause of these uncertainties is the lack of knowledge on the outflowing gas location. Indeed, as they look at face-on galaxies, the outflowing gas is directed towards the observer and the probed outflowing gas can be at 1 parsec (pc), 10 pc or even 10 kiloparsecs (kpc) away from the host galaxy. To bypass this problem,

another technique is the use of background sources to probe the surrounding gas of a galaxy.

1.3.4 Wind properties using background sources

Two kinds of background sources can be used in order to probe the outflowing gas and therefore knowing the gas location. These background sources can be either a galaxy or a quasar. Background quasars studies showed galactic winds are indeed collimated in a bi-conical shape (i.e. Bouché et al., 2012; Lan et al., 2014b). To date, star-forming galaxies having a background quasar LOS passing near is rare and building large samples is therefore difficult. Thus, it requires specific observational strategies. Increasing the number of galaxy-quasar pairs is one of this thesis objective.

From results of various techniques we just presented, the correlation between the loading factor and the galaxy SFR must be taken with caution as plotting y/x vs. x can lead to non physical correlations (and it is the same with $\Sigma_{\rm SFR}$). As there is a peak in star-formation density at redshift 2-3 (Lilly et al., 1996; Madau et al., 1996; Behroozi et al., 2013a), if η correlates with SFR, one can expect a correlation between η and redshift. The result from Heckman et al. (2015) on the non correlation between η and $V_{\rm out}$ makes sense as there is no specific reason for a galaxy to eject more gas if this gas velocity changes.

Other constraints on galactic winds are thus needed in order to find what drives winds out of the galaxy and this is exactly what we intended to during this thesis. With the background quasar methodology (described in § 2.1), we intend to estimate galactic wind properties with higher accuracy (as we know where we are probing the outflowing gas).

1.3.5 Perspective from numerical simulations

As mentioned earlier, concerning numerical simulations, the incomplete knowledge on scaling relations between a galaxy and its outflowing material properties, such as between the ejected mass rate $\dot{M}_{\rm out}$ and the star formation rate (SFR), limits our ability to produce accurate numerical models. In simulations, outflows are usually implemented with sub-grid prescriptions (e.g. Schaye et al., 2010; Oppenheimer et al., 2010; Vogelsberger et al., 2014). A popular sub-grid recipe is to set the loading factor η be a function of galaxy circular velocity V_c (Oppenheimer et al., 2010) (and thus the galaxy (halo) mass). These relations are usually set to $\eta \propto V_c^{-1}$ for momentum-driven winds and $\eta \propto V_c^{-2}$ for energy-driven winds. An alternative way to implement the collective effect of SN explosions is the (stochastic) implementation of thermal feedback. Using this method, galactic winds develop without imposing any input outflow velocity nor mass loading factor. This method is used by popular

simulations such as the EAGLE simulations (e.g. Schaye et al., 2015), the FIRE simulations (Hopkins et al., 2014; Muratov et al., 2015), and the multi-phase scheme of Barai et al. (2015).

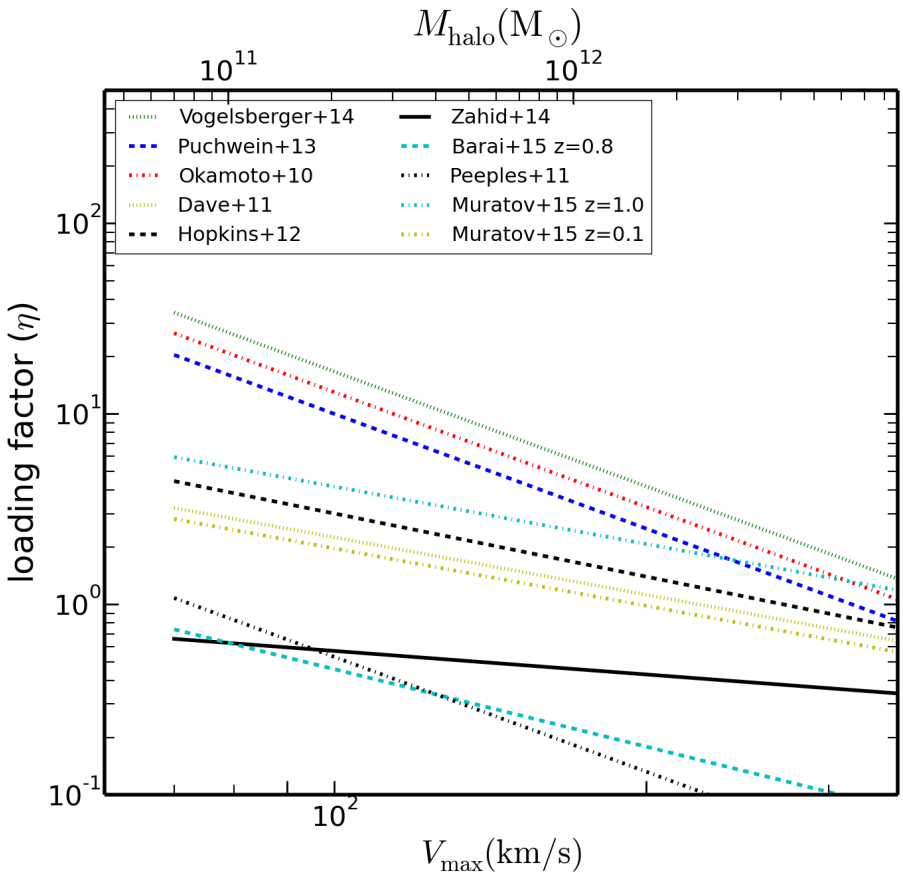

Figure 1.17: Loading factor as a function of galaxy rotational velocity (bottom x axis) and halo mass (top x axis) assumed by theoretical/empirical models.

Figure 1.17 shows assumed loading factors ($\eta = \dot{M}_{\rm out}/\rm SFR$) as a function of the galaxy rotational velocity (and halo mass) by theoritical/empirical models. We clearly see on this figure that there is absolutely no consensus about the loading factor behavior on the galaxy halo mass. Thus, we definitely need observational constrains on outflow properties.

Chapter 2

Observational strategy and sample selection

Contents

2.1 The background quasar methodology 30
2.1.1 Observational strategies 30
2.1.2 Why do we need integral field spectroscopy? 31
2.1.3 Critical parameters derived from IFUs 32
2.1.4 A 3D fitting tool: GalPaK^{3D} 33
2.2 The SINFONI Mg II Program for Line Emitters (SIMPLE) sample . . 33
2.2.1 Selection criteria 34
2.2.2 Sample description 34
2.3 The MUSE GAs Flow and Wind (MEGAFLOW) survey 35
2.3.1 Selection criterion 35
2.3.2 Sample description 35

In this chapter, we present the methodology we use to constrain galactic outflow properties as well as observational strategies aiming to build a statistical sample.

2.1 The background quasar methodology

Contrary to the stacked spectra technique, background quasars have 3 main advantages. (1) We know the location of the outflowing gas we are tracing with the impact parameter b, which is the distance between the quasar LOS and the galaxy center. (2) We know the galaxy redshift without knowing its position at first by looking at the absorber redshift in the quasar spectrum. (3) The quasar gives a direct information of the Point Spread Function (PSF).

The only drawback of this technique is the number of galaxy-quasar pairs. Indeed, this technique needs a galaxy-quasar pair in the right geometrical configuration allowing to study the outflowing materials. In order to have a maximum number of galaxy-quasar pairs and thus have a statistical sample, we need to build observational strategies.

2.1.1 Observational strategies

We use a background quasar as a probe for constraining properties of the surrounding gas of galaxies, also known as circum-galactic medium (CGM). This CGM will absorb a part of the background quasar light which will create absorption lines in the quasar spectrum. Our observational strategy will be first to identify and select these absorption lines, in particular the Mg II ($\lambda\lambda 2796, 2802$) doublet. This Mg II doublet has the advantages of being strong and being a doublet, which facilitates its identification.

A first strategy to gather galaxy-quasar pairs was to select blue $z \sim 0.1$ SFGs near higher redshift quasars from the SDSS database. Together with observations from the blue sensitive spectrograph (Keck Low Resolution Imaging Spectrometer (LRIS Oke et al., 1995) and the double imaging spectrograph (DIS) at the Apache Point Observatory (APO)), one can identify the Mg II low-ionization lines at low redshift $z \sim 0.1 - 0.3$. The slit of LRIS was placed to get both the quasar and the galaxy spectra. The slit of DIS was placed on the galaxy major axis to get its Hα ($\lambda 6564$) flux. We then looked for Mg II absorptions in the quasar spectrum as well as in the galaxy one. The detection rate was around 30% and one galaxy-quasar pair is presented in Kacprzak et al. (2014).

In order to have a large sample composed of galaxy-quasar pairs suitable for wind study, we need to look at already observed quasars spectra to search for absorption lines. One of the largest quasar surveys is the SDSS-III Baryon Oscillation Spectroscopic Survey (BOSS) (Alam et al., 2015). Catalogs such as Ménard & Chelouche

(2009) directly gives detected absorption lines and their properties (i.e. absorber redshift, Rest Equivalent Width (REW)) for a large number of quasar spectra.

Looking at the Mg II REW in the quasar spectrum, the host galaxy can be located far away from the quasar LOS. Depending on the available instrument, we need to select strong Mg II absorbers, strong being $W_r^{\lambda 2796} > 0.3 - 0.5$ Å as in Nestor et al. (2005). This selection criteria is indeed dependent of the Integral Field Unit (IFU) instrument we want to use and can differ. Using this method, we thus need powerful instrument in order to detect galaxies responsible for the absorptions seen in quasar spectra.

2.1.2 Why do we need integral field spectroscopy?

We select strong Mg II absorbers in background quasar spectra. By doing that, we know the host galaxy redshift without knowing its position. We therefore need an IFU in order to detect and identify the host galaxy.

An IFU has the particularity to have a FOV in which every pixel has a spectrum (see an example in Figure 2.1). This avoids the pre-selection of SFGs as we can search for host galaxies all around the quasar LOS.

After observing a quasar field with an IFU, we then search for galaxies responsible for the Mg II absorption lines at a specific redshift around the quasar LOS. When the host galaxy is detected, we need its morpho-kinematic properties and geometrical configuration with respect to the background quasar.

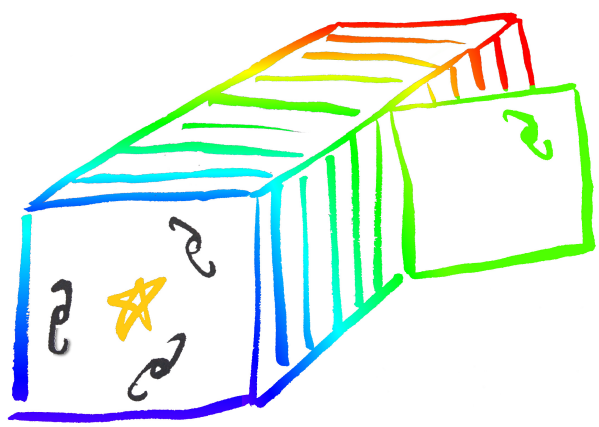

Figure 2.1: Scheme of an 3D IFU cube: the foreground image represents a white-light image of the cube and the extracted image represents a slide of the cube at a given wavelength. On this extracted image one can see only one galaxy which is emitting at the extracted wavelength.

2.1.3 Critical parameters derived from IFUs

In order to constrain galactic outflows, we first need to classify the galaxy-quasar pairs depending on their geometrical configurations. Indeed, one drawback of galaxy-quasar pairs is that the quasar LOS can go through gas associated with several mechanisms depending on the inclination of the galaxy with respect to the LOS. If the quasar is aligned with the galaxy major axis, it is likely probing inflowing or galactic disk material. If the quasar LOS is aligned with the galaxy minor axis, then it is likely probing the outflowing material from the galaxy. Hence, in order to study outflows, we need to untangle these geometrical effects.

We can sort out the geometry ambiguity by classifying pairs in two classes ("wind-pair" and "inflow-pair") using the azimuthal angle α, defined as the angle between the galaxy major axis and the quasar LOS. If $60° < \alpha < 90°$, then the galaxy quasar pair is classified as a "wind-pair", as it is likely to probe galactic outflows. However, if $0° < \alpha < 30°$, then we classify this galaxy-quasar pair as an "inflow-pair", as the quasar LOS is likely probing inflowing material or galactic disk component. Figure 2.2 shows the geometrical configuration of a galaxy-quasar system.

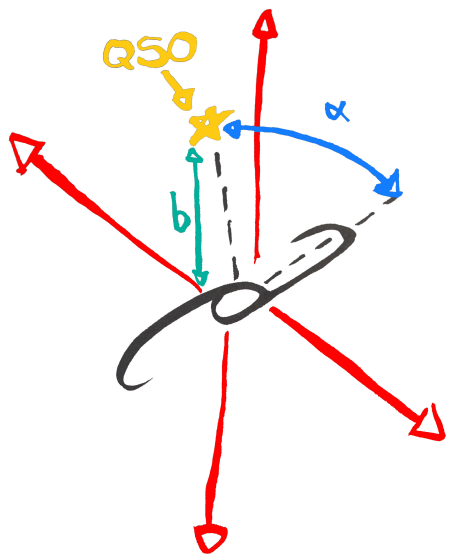

Figure 2.2: Scheme geometry configuration: the quasar LOS, represented by the yellow star, is crossing galactic outflows represented by the red crosses getting out of the galaxies. The Azimuthal angle is represented by the blue cross going from the galaxy major axis to the quasar LOS. b represents the impact parameter for the galaxy−quasar pair, represented by the light green cross showing the distance between the galaxy center and the quasar LOS.

In order to determine α, we need to measure/determine the galaxy major-axis. The galaxy major axis can be determined by directly looking at the morphology

of the galaxy or better by looking at the kinematics and morphology. The galaxy morpho-kinematical properties are derived with the 3D fitting tool called GalPaK^{3D} (Bouché et al., 2015).

2.1.4 A 3D fitting tool: GalPaK^{3D}

From IFU data, it is customary to extract moment maps (e.g. flux, velocity and dispersion maps) from the emission line(s) spectra. This is usually done on a pixel by pixel basis, as most algorithms treat the spaxels to be independent (e.g. Law et al., 2007, 2009; Förster Schreiber et al., 2004; Cresci et al., 2009; Epinat et al., 2009), a condition that requires high quality data with a high signal-to-noise ratio (SNR) in each spaxel[1], in order to constrain the width and centroid of the emission lines. Here, we avoid shortcomings of the traditional techniques by comparing the three-dimensional data cubes directly to a three-dimensional galaxy disk model using the GalPaK^{3D} tool. GalPaK^{3D} uses a disk parametric model with 10 free parameters and a MCMC algorithm with non-traditional sampling laws in order to efficiently probe the parameter space. The algorithm also uses a 3-dimensional kernel to convolve the model with the instrument PSF and line spread function (LSF), and thus returns the intrinsic (free of the PSF) galaxy properties (such as half-light radius, inclination, and maximum rotation velocity). Other parameters include the major-axis position angle, the galaxy flux, position, redshift and intrinsic velocity dispersion. Extensive tests presented in Bouché et al. (2015) show that the algorithm requires data with a $\mathrm{SNR}_{\mathrm{max}} > 3$ in the brightest pixel. For high SNR, all parameters can be well recovered, but in low SNR data, degeneracies can appear: for instance between turn-over radius and V_{max}.

Once galaxy parameters are derived, we can classify them into the previously defined categories : wind-pairs or inflow-pairs depending on their azimuthal angle. We will now describe galaxy-quasar samples we obtained.

2.2 The SINFONI Mg II Program for Line Emitters (SIMPLE) sample

The SINFONI Mg II Program for Line Emitters (SIMPLE) sample (Bouché et al., 2007) is built by a combination of VLT/SINFONI and VLT/UVES (Dekker et al., 2000) data.

[1] A spaxel being a pixel on the sky containing a whole spectrum.

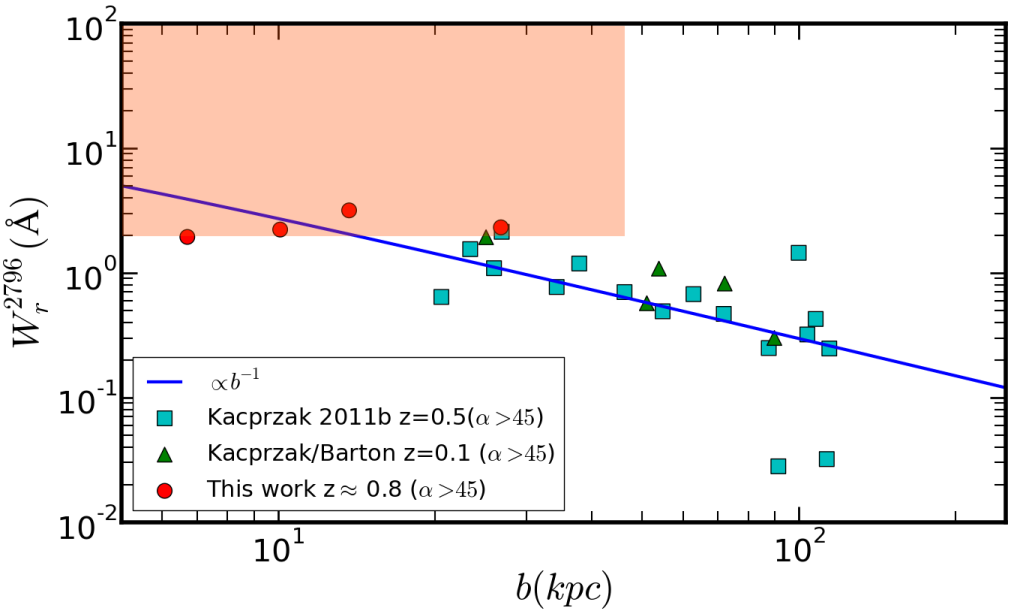

Figure 2.3: $W_r^{\lambda 2796}$ as a function of impact parameter b for galaxy-quasar pairs classified as wind-pairs. The red colored area shows the selection criterion of the SIMPLE sample ($W_r^{\lambda 2796} > 2.0\AA$).

2.2.1 Selection criteria

As mentioned before, we select quasar fields based on Mg II absorption lines in the quasar spectrum. SINFONI is a near infra-red (IR, $1.1 - 2.45\mu m$) IFU and to detect a SFG, this galaxy must have emission lines falling into this wavelength range. We thus select Mg II absorption lines having a redshift between 0.8 and 1.0 in order to detect the galaxy Hα (λ6564) emission line in SINFONI J band. Given the SINFONI field of view ($\sim 8'' \times 8''$), it is important to ensure that the galaxy will fall inside the field of view. For this purpose, we used the anti-correlation between b and equivalent width (e.g. Lanzetta & Bowen, 1990; Steidel, 1995; Bouché et al., 2006; Ménard & Chelouche, 2009; Chen, 2012) (see Figure 2.3) and select absorbers with $W_r^{\lambda 2796} > 2$ Å.

For this sample, the Mg II REW ($W_r^{\lambda 2796}$) has to be at least 2 Å.

2.2.2 Sample description

This sample was observed in two major steps:

First, 21 quasar fields were observed using SINFONI GTO time in which 14 host

galaxies were detected (Bouché et al., 2007)[2]. These observations were shallow with exposure times ≤ 40 min and seeing conditions $\geq 0.8''$. Then, in order to compare the host galaxy kinematics with the kinematics of the absorbing materials, 10 fields were re-observed both with SINFONI and UVES in open time.

These 10 re-observed pairs were aquired under SINFONI GO time[3]. This subsample was selected to have the highest initial Hα host galaxy fluxes and was re-observed with longer integration times (2-3 hr) and in better seeing conditions ($\leq 0.8''$). Details on these observations are given in Schroetter et al. (2015).

2.3 The MUSE GAs Flow and Wind (MEGAFLOW) survey

We seek to increase the sample size by almost an order of magnitude in order to allow for statistical analysis between the absorption properties with the galaxy properties. Thanks to the large wavelength range of MUSE, having a sample of 80–100 pairs is now within reach in only 20–25 quasar fields with multiple metal absorption lines. The MUSE GAs Flow and Wind (MEGAFLOW) survey is composed of VLT/MUSE (Bacon et al., 2006) and UVES data.

2.3.1 Selection criterion

The selection principle is similar to the SIMPLE sample : we select quasar fields with Mg II $\lambda 2796$ absorption lines. To select quasar fields, we search for multiple (three, four or five) Mg II absorbers (see Figure 2.4) in the quasar catalog from the Sloan Digital Sky Survey (SDSS) data release (DR12, Ross et al., 2012; Alam et al., 2015). These Mg II absorption lines should have redshifts between 0.4 and 1.4 such that the [O II] ($\lambda\lambda 3727, 3729$) galaxy emission lines fall into the MUSE wavelength range (4800Å to 9300Å). We used the Zhu and Ménard catalog[4] (Zhu & Ménard, 2013). MUSE having a larger FOV compared to SINFONI ($1' \times 1'$ compared to $8'' \times 8''$), we thus lower the REW ($W_r^{\lambda 2796}$) criterion from 2 Å to 0.8 Å. This limit corresponds to $b \sim 100$ kpc.

2.3.2 Sample description

Our MEGAFLOW survey is composed (at the time of writing) of 22 quasar fields. 19 of these 22 fields have been observed with MUSE and 15 of them have UVES followed up data. Out of these 19 quasar fieds, two (J2137+0012 and J2152+0625) are published in Schroetter et al. (2016, submitted to ApJ). Figures 2.5 and 2.6 show

[2]under program IDs 077.A-0576, 078.A-0600, 078.A-0718 and 079.A-0600.
[3]Under program 080.A-0364(A) 080.A-0364(B) and 079.A-0600(B).
[4]This catalog can be found at http://www.pha.jhu.edu/∼gz323/Site/Download_Absorber_Catalog.html

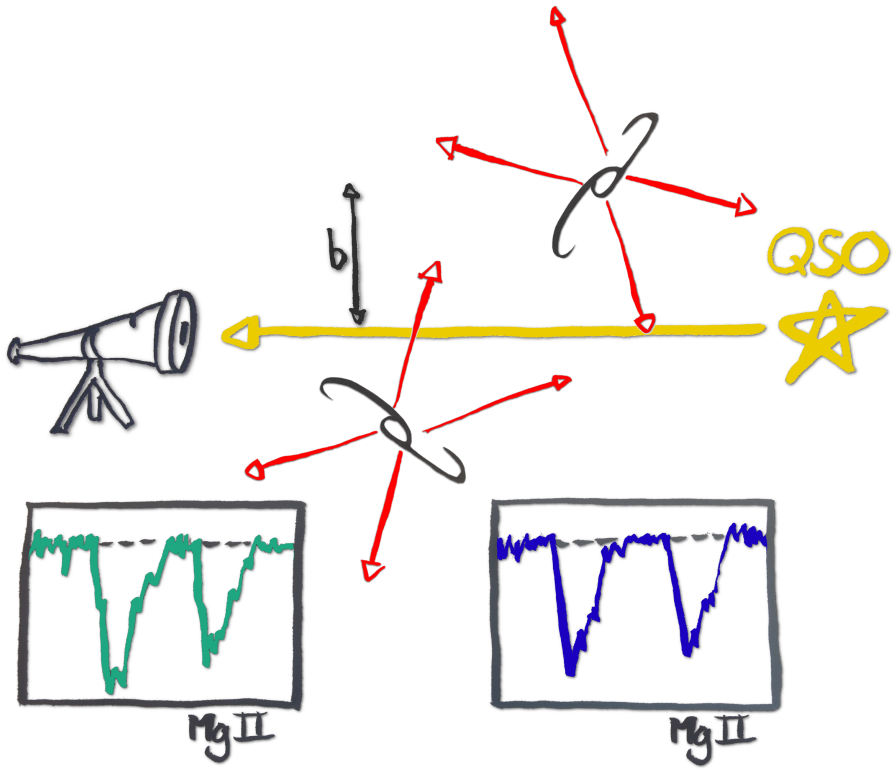

Figure 2.4: Scheme of our target strategy: the quasar LOS, represented by the yellow arrow heading toward the telescope, is crossing two galactic outflows represented by the red arrows getting out of the galaxies. These galactic outflows are absorbing a portion of the quasar spectra which gives the two Mg II absorption systems at two different redshifts. b represents the impact parameter for one galaxy−quasar pair.

the $W_r^{\lambda 2796}$ as a function of impact parameter (for galaxies with their associated quasar roughly aligned with their minor axis) and the redshift distribution of host galaxies respectively.

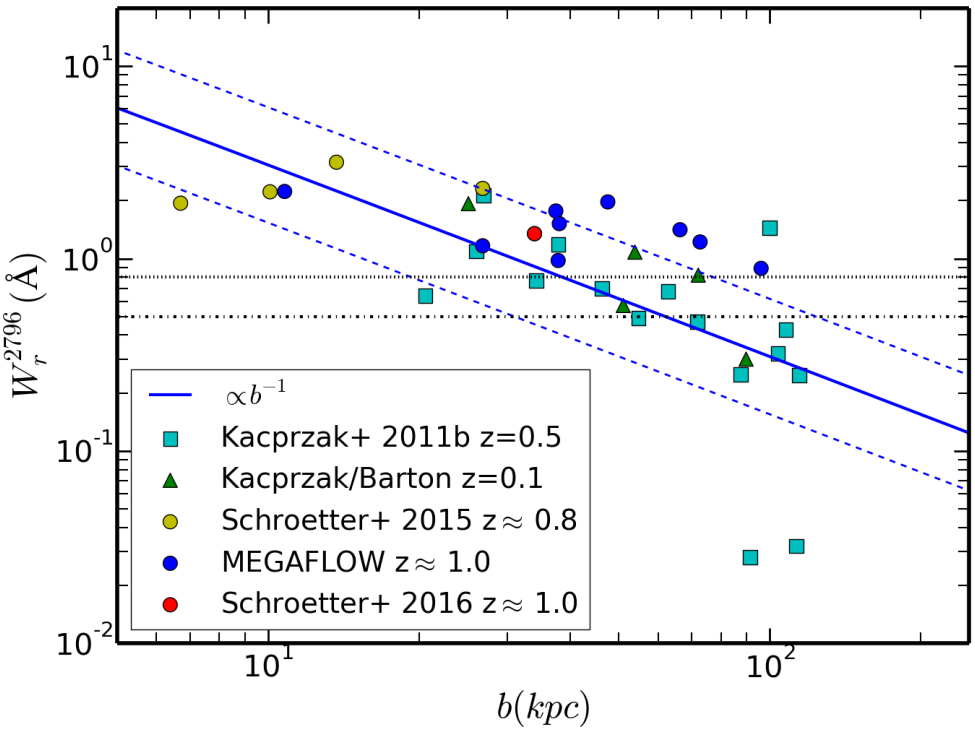

Figure 2.5: $W_r^{\lambda 2796}$ as a function of impact parameter b for galaxy-quasar pairs classified as wind-pairs. Horizontal dashed black lines shows the $W_r^{\lambda 2796} > 0.5$Å and $W_r^{\lambda 2796} > 0.8$Å selection criteria.

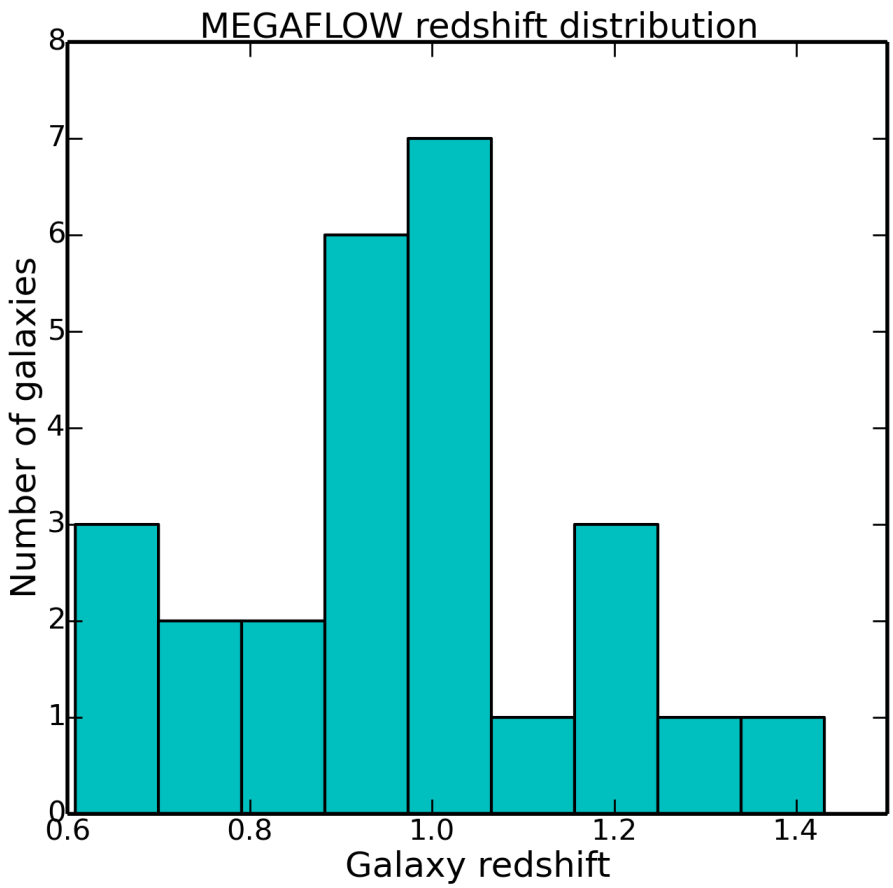

Figure 2.6: Redshift distribution of MEGAFLOW galaxies.

Chapter 3

Data acquisition and reduction

Contents

3.1 SIMPLE observations and data reduction 40

3.2 MUSE observations and data reduction 41

3.2.1 GTO observations 41

3.2.2 Pre-processing data reduction 41

3.2.3 Science reduction 43

3.2.4 Post-processing reduction 44

3.2.5 Exposures combination 46

3.2.6 Sky emission lines removal 46

In this chapter, we describe how the data were observed and focus on data reduction.

3.1 SIMPLE observations and data reduction

SINFONI observations, obtained in service mode, were optimized by adopting a 'on source' dithering strategy designed to ensure a continuous integration at the host location.

SINFONI data reduction was performed as in Bouché et al. (2007); Förster Schreiber et al. (2009); Bouché et al. (2012), using the SINFONI pipeline (SPRED, Schreiber et al., 2004; Abuter et al., 2006) complemented with custom routines such as the OH sky line removal scheme of Davies (2007) and the Laplacian edge cosmic ray removal technique of van Dokkum (2001).

Regarding the wavelength calibration, we emphasize that we applied the heliocentric correction to the sky-subtracted frames. Each frame was associated with a single reference frame by cross-correlating each of the science frames spectrally against the reference frame (the first science exposure). For each observing block, we use the quasar continuum to spatially register the various sets of observations. Finally, we created a co-added cube from all the individual sky-subtracted 600s exposures using a median clipping at 2.5σ.

Flux calibration was performed on a night-by-night basis using the broadband magnitudes of the standards from 2MASS. The flux calibration is accurate to $\sim 15\%$. Finally, the atmospheric transmission was calibrated out by dividing the science cubes by the integrated spectrum of the telluric standard.

UVES data were taken in both visitor mode and service mode. These data were reduced using version 3.4.5 of the UVES pipeline in MIDAS. Master bias and flat images were constructed using calibration frames taken closest in time to the science frames. The science frames were extracted with the optimal option. The blue portion of the spectra was checked order by order to verify that all were properly extracted. The spectra were then corrected to the vacuum heliocentric reference frame. The resulting spectra were combined, weighting each spectrum with its signal-to-noise ratio. To perform absorption line analysis, the spectra were normalized using cubic spline functions of the orders of 1–5 as the local continuum. Note that UVES and SINFONI data have their wavelength calibrations made in vacuum.

3.2 MUSE observations and data reduction

3.2.1 GTO observations

Our MUSE data were taken from September 2014 in visitor mode during Guaranteed Time Observations (GTO) runs[1]. We first point the telescope towards a quasar and then offset the first exposure by $\approx 4 - 5''$ in Right Ascension (RA) and Declination (DEC). Observing Blocks (OBs) were composed of four exposures of 900 seconds (or 2× 1500s) with a rotation of 90° between each exposure. Each OB has 1 hour exposure time and each field is observed for 2 hours (so 8 or 4 exposures). This observation strategy is used to minimize the slice pattern which appears during image reconstruction. Some observations were composed of two exposures of 1500 seconds with the same 90° rotation between the two exposures. The two-exposure OBs were used to reduce the overheads produced mainly by CCD readout and rotations between exposures. Prolonging the exposure time of one exposure leads to better chance of seeing fluctuation and thus lower guiding accuracy. We used this strategy when the quasar field happens to have at least one star falling in the Slow Guiding System (SGS) of MUSE so the guiding is more accurate and thus allows for longer exposure time.

3.2.2 Pre-processing data reduction

These first steps of the data reduction build up all the needed files for the science reduction. The calibration recipes are executed on the basis of single CCDs on an IFU per IFU basis. Figure 3.1 shows a basic science MUSE data reduction diagram.

We combine the raw bias frames into one master–bias which will be used for the reductions. These raw bias frames are separate images that contains pixels values of the raw bias exposures. The recipe trims the raw data and record the overscan statistics used to correct the data levels and combine the exposures using the input method parameters such as the type of image combination (sigma clipping, median, average...) or the way of rejecting values for instance. The read-out noise is computed for each quadrant of the raw images and stored as Quality Control (QC) parameter, so we can control the quality of combined data. Every output frame has a variance extension which is filled with initial values according to the read-out noise before image combination. Additionally, bad columns are searched for and marked in the data quality extension. One has to take into account the weather temperature (which is found in the header of each raw frame) of each exposure and reject the ones with large temperature difference compared to the other frames. A double check the mean bias value of each IFU is also needed in order to continue the reduction.

[1] program IDs 096.A-0164, 096.A-0609, 095.A-0365, 094.A-0211

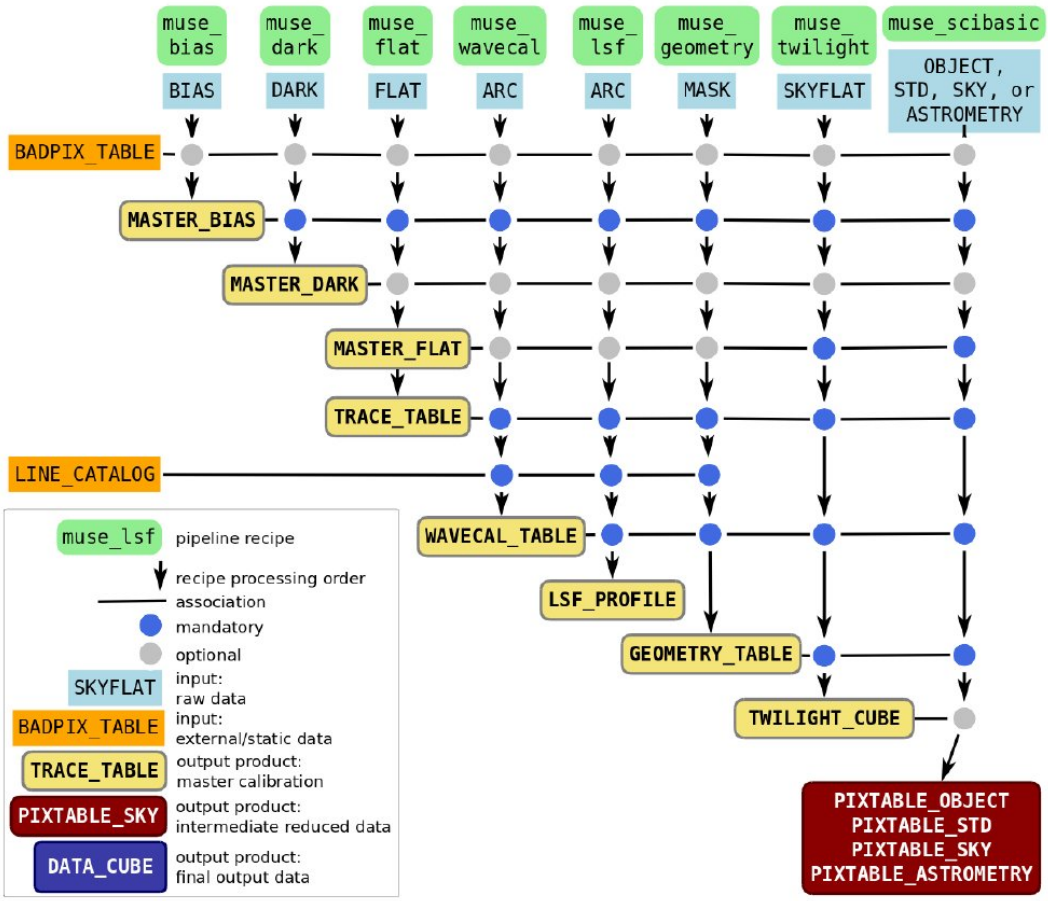

Figure 3.1: Association map for the basic science data reduction. This diagram shows the part of the pipeline that operates on the basis of a single IFU.

The second step should be to combine raw dark frames. Since modern CCDs have a very small dark current, master dark frames are not used further in the data reduction. This recipe trims the raw data and, like the bias recipe, records the overscan statistics, subtracts the bias, scales the pixel count according to their exposure time and combines them using input parameters (we used the sigma-clipping method, which is the default parameter).

The next step is to combine separate flat-field images into one master flat-field, trace the location of the slices on the CCD and locate dark pixels. To trace the position of the slices on the CCD, their edges are located using a threshold method. At given interval, the edge detection is repeated tracing the central position and width of each slit vertically across the CCD. A polynomial fitting is then applied to

all positions measured for one slice and saved in an output trace table.

Once we obtained master files for bias, flat-field (dark is optional) and the trace table, we can run the wavelength calibration recipe ("muse_wavecal" recipe in Figure 3.1). This recipe will reduce the arc frames to detect arc emission lines and also to determine a wavelength solution for each file. To ensure a wavelength solution across the entire range, three lamps are combined. For a complete wavelength coverage, one should aim for at least one arc frame per lamp or a frame with all lamps on. This recipe can, in addition to the other recipes described before, optionally subtract the dark and the lamp frame can be divided by the flat-field. This option is, however, not recommended. At first, the data is combined using input parameters into separate images for each lamp. These separate lamp exposures are then summed (by sigma clipping) to create a single combined master arc. As for the wavelength solution, arc lines are detected at the center of each slice and subsequently assigned wavelengths. This is done using pattern matching to identify lines from the input line catalog given by the pipeline package. Each line is traced to the edge of the slice using a Gaussian centering in each CCD column. In each arc line, a polynomial fit is done to detect deviant fits and reject them. The two-dimensional fit uses all lamps positions, their wavelengths and the given polynomial orders to compute the final wavelength solution for each slice.

3.2.3 Science reduction

In addition to the flat-field, observations usually include twilight sky flat-fields. The next step is to combine these twilight sky flat-fields into a three-dimensional illumination correction ("muse_twilight" recipe in Figure 3.1). This processing handles each raw input image separately. It trims the raw data, records the overscan statistics, subtract bias, dark, divides by the flat-field and combines all the exposures using input parameters. The geometry table, trace table and wavelength calibration table are used to assign 3D coordinates to each CCD-based pixel. It creates a pixel-table from the master sky-flat. Pixel-tables are then cut in wavelength using the input parameters. Integrated flux in each IFU is saved in the pixel table header to be used later as estimate for the relative throughput of each IFU. An additional correction can be applied if an ILLUM file is given as an input to correct relative illumination between all slices of one IFU. This ILLUM file is an additional illumination exposure taken between each OB or when the weather temperature changes more than 1.5°. The data in each slice within the pixel-table of each IFU is multiplied by the normalized median flux of that slice in the ILLUM exposure. Pixel-tables of all 24 IFUs are then merged, using the integrated flux as inverse scaling factors, leading to a reconstructed skyflat cube. A white-light image is also created from this cube and the skyflat cube is then saved to disk with the white-light image as an extension.

The last step in the basic reduction phase is the removal of the instrumental signature from the data of each CCD and convert them into pixel-table ("muse_scibasic" recipe in Figure 3.1). This processing handles each raw input image separately, as above, trims the raw data and record the overscan statistics, subtracts bias, can detect cosmic rays (if the input setting is set), subtract dark, divides by the flat-field and optionally propagates the integrated flux value from the twilight-sky cube. The input calibrations (geometry table, trace table and wavelength calibration table) are used to assign 3D coordinates to each CCD-based pixel, creating a pixel table for each exposure. If an ILLUM exposure is given as input, it is used to correct the relative illumination between all slices of one IFU. Since ILLUM exposures are taken every hour and every time the temperature changes more than 1.5°C, it is best to use this additional exposure for every set of data we reduce. The last step of this recipe is to divide the data by the normalized twilight cube using the 3D coordinates of each pixel in the pixel table to interpolate the twilight correction onto the data. For each exposure, the pre-reduced pixel-table is saved to disk.

3.2.4 Post-processing reduction

Figure 3.2, like Figure 3.1, shows a diagram of the post-processing steps of the data reduction.

The first post-processing step is to create a flux response curve from a standard star exposure ("muse_standard" recipe in Figure 3.2). This processing merges the pixel tables of standard star from all IFUs and corrects for atmospheric refraction. To derive the flux response curve, this recipe integrates the flux of all objects detected within the FOV using the given profile. It then select one object as the standard star (either the brightest or the nearest object, depending on input parameter) and compare its measured fluxes to tabulated fluxes to derive the sensitivity over wavelength. The final response curve is then linearly extrapolated to the largest possible MUSE wavelength range and smoothed depending on input parameter.

One of the last step before combining exposures is to prepare reduced and combined science products ("muse_scipost" recipe in Figure 3.2). The processing merges the pixel tables from all IFUs of each exposure. If a previously processed response curved is given, then the flux calibration is carried out. One can use a sky subtraction method at this point but the results show that it does not seem to work properly with the version we used at the time of our data reduction. We therefore do not use this method to remove sky emission lines. Afterwards the data is corrected for the radial velocity of the observer before the input (or a default) astrometric solution is applied. Finally (if the "save" parameter of the recipe contains "cube"), the data is resampled into a datacube. The extent and orientation of the cube is computed from the data itself and as a last step, the computed cube is integrated over all filter

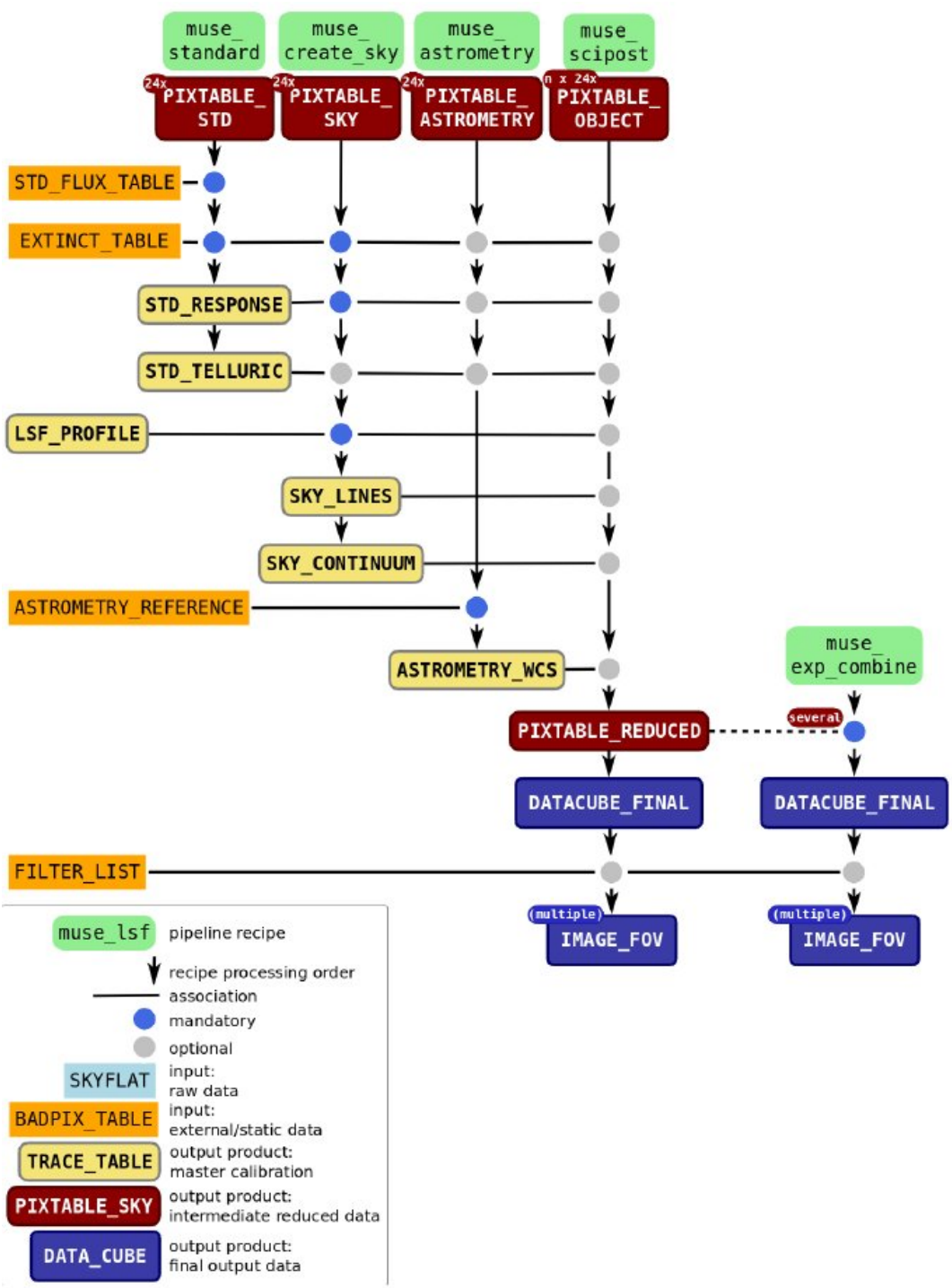

Figure 3.2: Association map for the second part of the science data reduction. This part of the pipeline deals with data of all 24 IFUs simultaneously.

function given in the input "filter" parameter.

Once pixel-tables are reduced by exposure, we need to combine them.

3.2.5 Exposures combination

In order to combine all exposures into one final data cube, we first need to compute the offsets between them. To do so, one can either compute them by hand, or using a recipe. The recipe computes the coordinate offset for each input FOV image with respect to a reference. When this offset table is created, we combine the different exposures giving the pixel table locations we want to combine with the corresponding offsets. This creates a final combined data cube.

One last step we need to finally exploit the science data is the sky emission lines removal that we skipped before.

3.2.6 Sky emission lines removal

On the combined data cube, we perform the sky subtraction with ZAP (Zurich Atmosphere Purge), an algorithm developed by Soto et al. (2016). ZAP first operates by subtracting baseline sky level, found by calculating the median per spectral plane and then uses principal component analysis. This principal component analysis determines the minimal number of eigenspectra.

Chapter 4

Data analysis

Contents

4.1 Methodology **48**
4.1.1 Estimate of Star Formation Rate (SFR) 48
4.1.2 A simple cone model for galactic winds 49
4.2 SIMPLE sample **53**
4.2.1 Morpho-kinematics from GalPaK^{3D} 53
4.2.2 Galaxy-quasar pairs classification 54
4.2.3 Outflow properties 55
4.3 MEGAFLOW survey **60**
4.3.1 Survey status 60
4.3.2 Morpho-kinematics from GalPaK^{3D} 60
4.3.3 Galaxy-quasar pairs classification 66
4.3.4 Outflow properties 67

In this chapter, we describe and detail the analysis of all the data acquired to study gas flows with galaxy-quasar pairs.

4.1 Methodology

With the aim of constraining galactic outflow properties, the methodology we use is made of the following steps. We first need to detect the host galaxy(ies) in the IFU FOV responsible for the Mg II absorption lines. Once detected, we run the GalPaK^{3D} algorithm to constrain their morpho-kinematics.

Each galaxy-quasar pair is then classified as wind-pair or inflow-pair based on azimuthal angles α (defined in § 2.1.3). We focus on wind-pairs in order to constrain their loading factors. This loading factor is defined to be the ratio between the ejected mass rate $\dot{M}_{\rm out}$ and the star formation rate (SFR) of the host galaxy (described in § 4.1.1).

The ejected mass rate is derived by simulating an absorption profile using a cone model to reproduce the absorption lines in the UVES quasar spectrum. This cone model and the formulas used to derive this ejected mass rate are described later in § 4.1.2.

4.1.1 Estimate of Star Formation Rate (SFR)

A very popular calibration to convert Hα flux into SFR is the Kennicutt (1998) relation (Equation 4.1) which assumes a Salpeter (1955) Initial Mass Function (IMF) because the hydrogen Balmer line Hα is currently the most reliable line to use for deriving SFRs as its luminosity scales directly with the total ionizing flux of the stars.

$$SFR(\mathrm{M}_\odot\ \mathrm{yr}^{-1}) = 7.9 \times 10^{-42}\ \mathrm{L}_{\mathrm{H}\alpha} \tag{4.1}$$

Where $L_{H\alpha}$ is the intrinsic dust-corrected Hα luminosity.

Since this line is not always observable in the visible for 'high' redshift ($z >\sim 0.4$) galaxies, other calibrations, like the one based on [O II] ($\lambda\lambda 3727, 3729$) doublet line fluxes, can be used. Line-based fluxes other than hydrogen for SFR calibration usually depend on other properties like dust reddening or abundance. To derive SFRs based on [O II] fluxes, Kennicutt (1998) also provides a calibration (Equation 4.2) which also assumes a Salpeter (1955) IMF:

$$SFR(\mathrm{M}_\odot\ \mathrm{yr}^{-1}) = (1.4 \pm 0.4) \times 10^{-41}\ \mathrm{L}_{\mathrm{O\,II}}(\mathrm{erg\ s}^{-1}) \tag{4.2}$$

Where $L_{\mathrm{O\,II}}$ is the luminosity of the [O II]($\lambda\lambda 3727, 3729$) doublet. Using a Chabrier (2003) IMF and assuming a mean flux attenuation of $A_V = 1$, which is typical for

$z = 1$ galaxies (e.g. Charlot et al., 2002), gives the same results (within 10%) as Equation 4.2.

Equation 4 in Kewley et al. (2004, hereafter K04) uses also a Salpeter IMF but makes no assumption of reddening. The [O II] doublet is closely linked to the electron temperature and abundance. In K04 paper, they show that using the "average" attenuation correction of 0.3 mag leads to underestimate the high SFR[O II] ($> 1\mathrm{M}_\odot\,\mathrm{yr}^{-1}$) and overestimate the low SFRs. They provide a way of deriving the E(B-V) (Eq.16 and 18 of K04) color excess which leads to a more accurate mean attenuation, assuming that $A_V = 3.1 \times E(B-V)$. We use the following equations (Eq 4.3 and 4.4 from K04) to derive SFRs from [O II] fluxes.

$$SFR(\mathrm{M}_\odot\ \mathrm{yr}^{-1}) = (6.58 \pm 1.65) \times 10^{-42}\ \mathrm{L}([\mathrm{O\,II}])_\mathrm{i}(\mathrm{erg\ s}^{-1}) \tag{4.3}$$

$$L([\mathrm{O\,II}])_i = 3.11 \times 10^{-20}\ L([\mathrm{O\,II}])_o^{1.495} \tag{4.4}$$

Where $L([\mathrm{O\,II}])_o$ is the observed luminosity of the source, $L([\mathrm{O\,II}])_i$ being the intrinsic extinction-corrected luminosity. For our $z \sim 1$ SFGs, we cannot use the SED fitting method (described in § 1.1.3 with MUSE as its wavelength range does not cover FIR and FUV.

After deriving the SFRs for all the wind-pairs classified galaxies, we can move on to the outflowing gas properties. In order to put constraints on galactic outflows, we build a simple cone model to reproduce the absorption lines in the quasar spectrum.

4.1.2 A simple cone model for galactic winds

The cone model is based on the assumption that galactic outflows are collimated inside a bi-conical geometry (e.g. Bordoloi et al., 2011; Bouché et al., 2012; Rubin et al., 2014; Bordoloi et al., 2014; Lan et al., 2014b; Kacprzak et al., 2015, see § 1.3).

To model our cone, we use the geometric parameters (inclination, azimuthal angle α) derived from our IFU data (see § 2.1.4). We create a cone perpendicular to the galaxy disk and fill it with particles, created randomly with a uniform distribution, and assume that the mass flux is conserved. Each particle represents a cold gas cloud being pushed away by a hot medium or radiation pressure. For simplicity, we assign the clouds a constant radial velocity, V_out, i.e. we assume that the LOS intercepts the clouds far from the acceleration region[1]. In addition, a single LOS probes a rather small range of distances from the host galaxy such that a gradient in the outflow velocity would have no significant impact on our results. The only free parameters are V_out and the cone opening angle θ_max.

[1]So far, only in one LOS with an impact parameter less than 10 kpc in Schroetter et al. (2015), we required an accelerated wind profile.

The cone is first built along the x, y, z axes where x and y represent the sky plane and z corresponds to the cone height (see representation in Figure 4.1). We then rotate the cone along the y-axis to match the galaxy's inclination derived from the data and create a simulated absorption profile from the distribution of cloud velocities projected along the quasar LOS (z axis). Particles are grouped by bins of LOS-projected velocities. We typically use $\sim 10^6$ particles inside the cone.

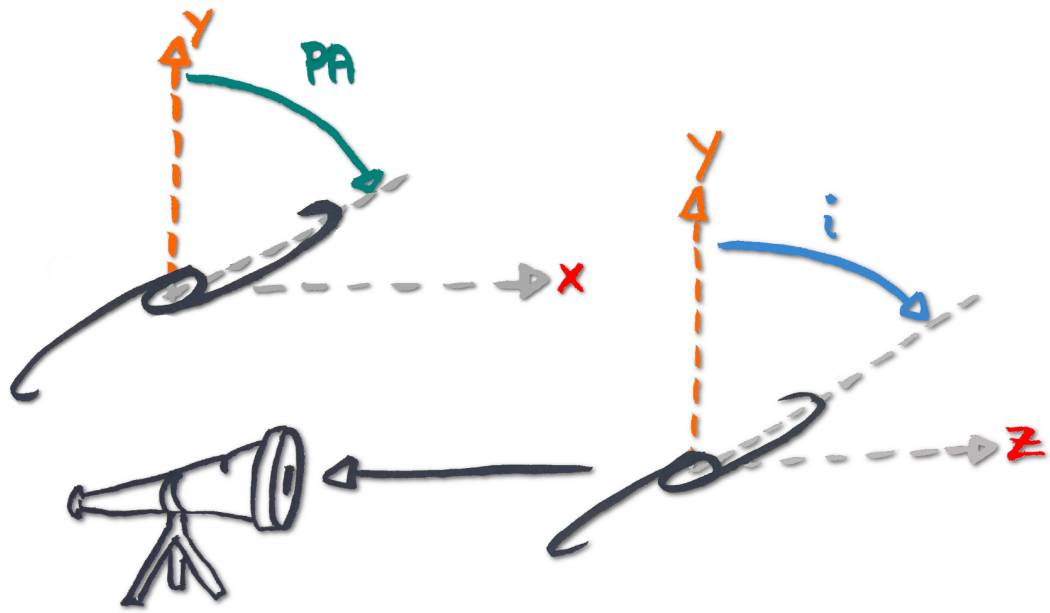

Figure 4.1: Representation of a galaxy position angle (PA) and inclination (i). *Top left:* sky plane (x, y) representation of the PA of a galaxy. This angle is defined to be the angle between the "y" axis (pointing the North) and the galaxy major axis. The galaxy PA is usually given positive towards the East. *Bottom right:* side view (y, z) of a galaxy inclined with the i angle. The inclination of a galaxy is defined to be the angle between the disk plane (y, z) and the sky plane (y, x). The telescope on the left is to better illustrate the side view: the black arrow pointing to the telescope represents the line of sight, the z axis represents the depth.

The quasar LOS is set by the impact parameter (b, the distance between the galaxy center and the quasar LOS) and the azimuthal angle derived from the data. The distribution of the projected velocities gives us a simulated "optical depth $\tau_{\rm v}$", which we turn into an absorption profile $\propto \exp(-\tau_{\rm v})$. The asymmetry of the profile depends of the system geometry. Examples on how the wind model behaves as we change the different parameters can be seen in Figure 4.3. This simulated absorption profile will be compared to the quasar absorption lines, aiming to reproduce the equivalent width and the shape (asymmetry) of the observed absorption lines. To have enough accuracy in the outflow properties, we use high resolution quasar spectra obtained

with the UVES instrument.

Due to the Monte Carlo generation of particles, stochastic effects create noise in the simulated profiles. This noise does not impact the resulting equivalent widths (nor its overall shape/asymmetry) and thus the derived outflow velocities. We then convolve the particle velocity distribution with the UVES instrument resolution. Additionally, in order to simulate the instrument noise, we add a random Poisson noise to the simulated profile. This random Poisson noise has the same level as the data and provides a more meaningful comparison. Figure 4.2 shows the cone model principle, with an example of UVES data fitting.

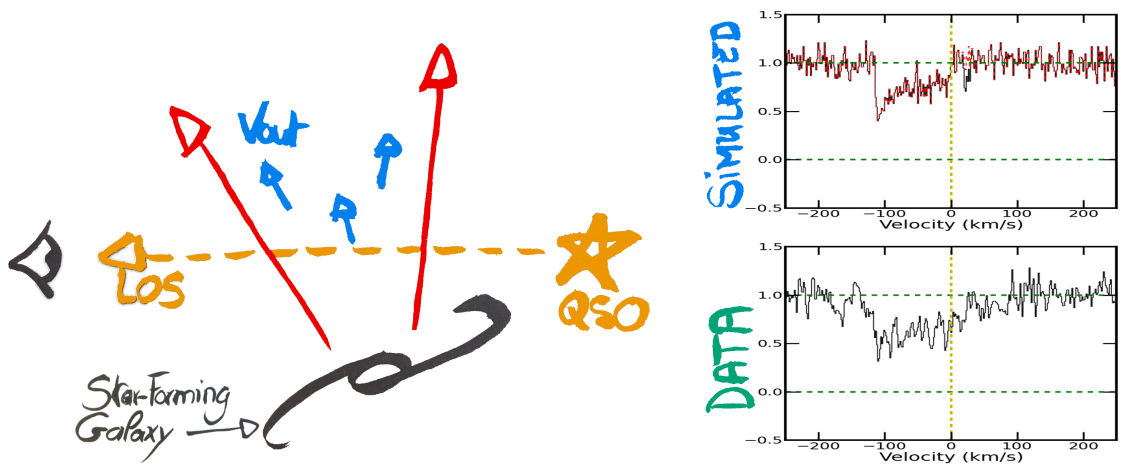

Figure 4.2: Wind model principle description. On the left side one can see a geometric representation of a galaxy-quasar system. The observer is on the left, the background quasar is represented by the yellow star labeled "QSO". The quasar LOS is crossing galactic outflows (red). We fill particles inside the cone with a constant radial velocity $V_{\rm out}$ (blue arrows). We project the velocities on the quasar LOS to end up with a simulated profile (absorption profile on the top right side). We compare this profile with the data (bottom absorption profile, UVES data), and we fit the data by changing $V_{\rm out}$ or the cone opening angle ($\theta_{\rm max}$). For this case, $V_{\rm out} = 115 \pm 10$ km s^{-1} and $\theta_{\rm max}$= $40 \pm 5°$.

Once we have the outflow velocity and the cone opening angle, we almost have everything needed to derive the ejected mass rate $\dot{M}_{\rm out}$ as well as the loading factor of the galaxy. To constrain the ejected mass rate probed by the quasar LOS, we use Equation 4.5 from Bouché et al. (2012) which represents the ejected mass rate for one cone:

$$\dot{M}_{\rm out} \approx \mu \cdot N_{\rm H}(b) \cdot b \cdot V_{\rm out} \cdot \frac{\pi}{2} \cdot \theta_{\rm max} \tag{4.5}$$

$$\frac{\dot{M}_{\rm out}}{0.5 {\rm M}_\odot\,{\rm yr}^{-1}} \approx \frac{\mu}{1.5} \cdot \frac{N_{\rm H}(b)}{10^{19}{\rm cm}^{-2}} \cdot \frac{b}{25{\rm kpc}} \cdot \frac{V_{\rm out}}{200{\rm km\,s}^{-1}} \cdot \frac{\theta_{\rm max}}{30°}$$

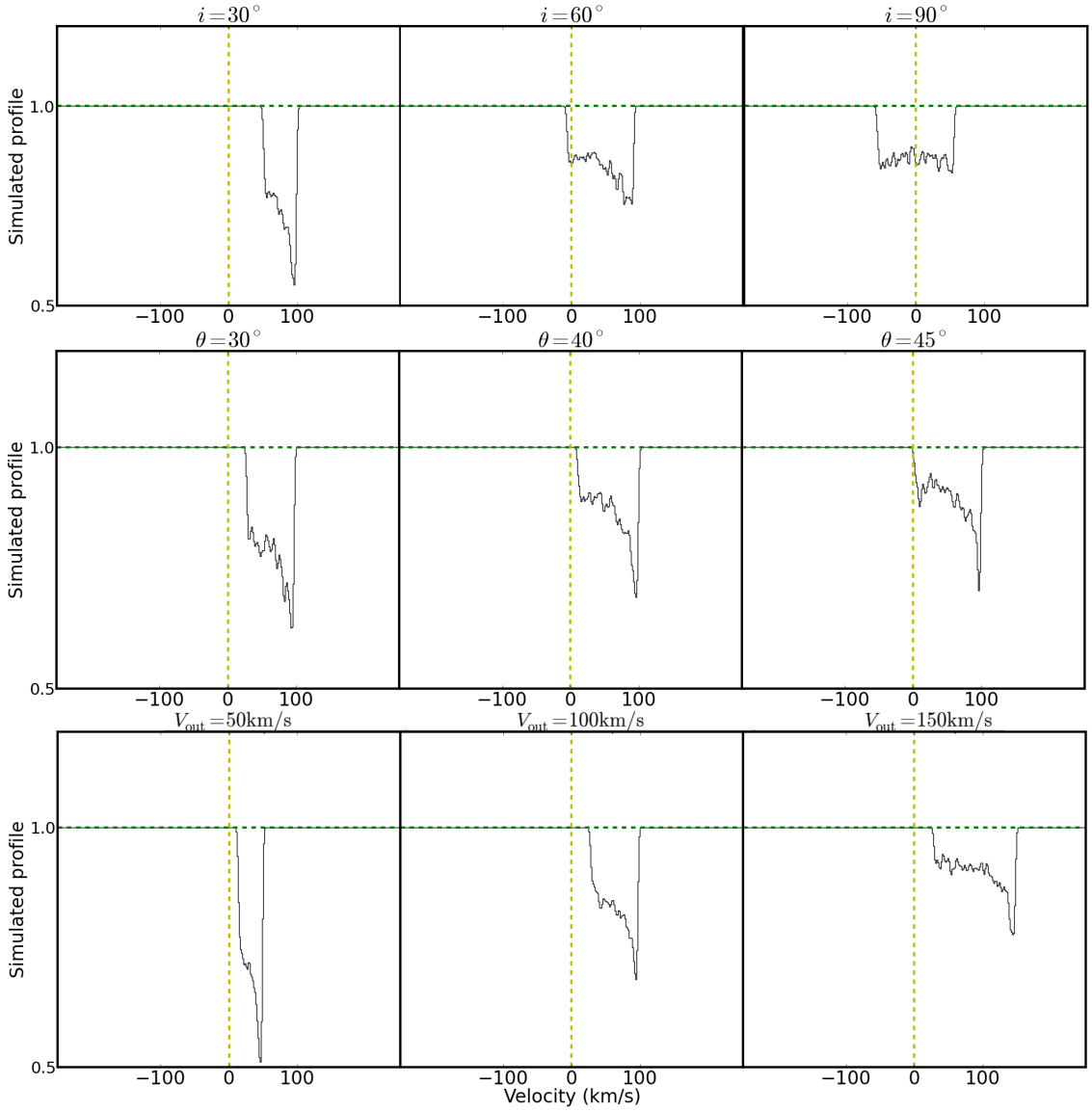

Figure 4.3: Examples of simulated absorption profiles with different galaxy inclinations (i), opening angle (θ) and wind velocities ($V_{\rm out}$): while each of the simulated profiles has the same number of particles, the apparent depth decreases as each parameter increases due to larger velocity projections for i and θ, and larger range of velocities for $V_{\rm out}$. *Top row*: absorption profiles for galaxies inclined at 30, 60 and 90 degrees with $V_{\rm out}$= 100 km s^{-1}and θ= 30°. The noise effect is due to the Monte Carlo distribution of particles. *Middle row*: absorption profiles for wind cones with opening angles of 30, 40 and 45 degrees with $V_{\rm out}$= 100 km s^{-1}and i=45°. *Bottom row*: absorption profiles with wind velocities of 50, 100 and 150 km s^{-1}with i= 45 degrees and θ= 30°. Each simulated profile has the same amount of particles but show a larger velocity range due to the increasing gas speed, hence the varying apparent depths.

Where μ is the mean atomic weight, b the impact parameter, $\theta_{\rm max}$ the cone opening angle[2], $V_{\rm out}$ the outflow velocity and $N_{\rm H}(b)$ is the gas column density at the b distance.

The only parameter which is yet to be constrained is the gas column density $N_{\rm H}(b)$. To do so, we use the empirical relation 4.6 from Ménard & Chelouche (2009) between the neutral gas column density and the Mg II λ2796 REW $W_r^{\lambda 2796}$:

$$N_{\rm HI} = (3.06 \pm 0.55) \times 10^{19} \times (W_r^{\lambda 2796})^{1.7 \pm 0.26}. \tag{4.6}$$

This relation, together with the tight correlation between Mg II equivalent width and dust content (as determined statistically from quasar extinction) from Ménard & Chelouche (2009), leads to a gas-to-dust ratio slightly smaller than that of the Milky Way H I column densities of $\log(N_{\rm H\,I})$ =19.5 and above. Furthermore, the redshift evolution of the dust content of Mg II absorbers, extrapolated to $z = 0$, shows that Mg II–selected absorbers extend the local relation between visual extinction A_V and the *total hydrogen* column $N_{\rm H}$ of Bohlin et al. (1978). This in turn indicates that the ionized gas contribution is negligible in regions with H I columns above $\log(N_{\rm H\,I})$ =19.5, as also argued by Jenkins (2009), and that one can use the correlation between Mg II equivalent width and $N_{\rm H\,I}$ as a proxy for the $N_{\rm H}$ gas column density.

Now that we described the methodology we use in order to constrain galactic outflows, we will now focus on the data analysis from our IFU surveys.

4.2 SIMPLE sample

As mentioned in § 2.2.2, this sample is composed of 10 galaxy-quasar pairs. For each galaxy, we first derive their morpho-kinematic parameters.

4.2.1 Morpho-kinematics from GalPaK^{3D}

Using the GalPaK^{3D} tool, we fit the kinematics and flux distribution (chosen to be exponential or Gaussian in our cases) directly to the data-cubes. Table 4.1 summarizes the morpho-kinematics parameters for each galaxy. We emphasize that the surface-brightness profile breaks the common inclination-$V_{\rm max}$ degeneracy from the axis ratio b/a in kinematic analysis compared to traditional methods fitting the kinematics on velocity field. For every galaxy, we checked that the MCMC chain converged for each of the parameters and estimated the uncertainties from the last 60 percents of the iterations. For J1422−0001, some of the kinematic parameters remain unconstrained, because the rotation curve appears shallow such that the turn-over radius r_t and the circular velocity $V_{\rm max}$ are degenerate The parameters

[2] $\theta_{\rm max}$is defined from the central axis, and the cone subtends an area Σ of $\pi \cdot \theta_{\rm max}^2$.

relevant for wind study for defining the kinematic major axis (position angle (PA)) are well constrained, however.

Table 4.1: Kinematic and morphological parameters for the 10 SIMPLE galaxy-quasar pairs.

Galaxy	inclination ($^\circ$)	PA ($^\circ$)	flux	$V_{\rm max}$	redshift	$r_{\frac{1}{2}}$
(1)	(2)	(3)	(4)	(5)	(6)	(7)
J0147+1258	24.4±3.3	−69±3	$1.63 \cdot 10^{-16}$	241±38	1.0389	7.11 ± 0.20
J0226-2857	47.9±1.0	91±1	$2.01 \cdot 10^{-16}$	50±12	1.0223	2.69 ± 0.04
J0302-3216	30.4±1.5	−37±3	$2.70 \cdot 10^{-16}$	180±15	0.8223	8.99 ± 0.31
J0448+0950	52.0±1.2	31±1	$5.03 \cdot 10^{-16}$	253±10	0.8391	7.85 ± 0.07
J0822+2243	17.9±0.7	168±1	$5.04 \cdot 10^{-16}$	328±14	0.8102	4.14 ± 0.06
J0839+1112	72±5†	139±4	$1.53 \cdot 10^{-16}$	113±20	0.7866	5.65 ± 0.29
J0943+1034	43±5††	140±1	$3.81 \cdot 10^{-16}$	327±10	0.9956	8.73 ± 0.21
J1422-0001	55±5	81±3	$8.93 \cdot 10^{-17}$	130±20†††	0.9096	4.30 ± 0.16
J1441+0443††	···	87±4	$6.62 \cdot 10^{-17}$	···	1.0384	2.99 ± 0.18
J2357-2736	51.6±2.2	109±2	$1.29 \cdot 10^{-16}$	187±15	0.8149	5.53 ± 0.14

(1) Quasar name; (2) Galaxy inclination (degrees); (3) Position Angle (degrees); (4) Integrated Hα flux of the galaxy (erg s^{-1} cm^{-2}); (5) Maximum rotation velocity (km s^{-1}); (6) H$_\alpha$-based redshift; (7) Half-light radius (kpc); † the inclination is determined from the HST data. †† galaxy parameters are derived from 2D fitting (galfit2D). ††† turn-over radius is fixed to $r_t/r_{1/2} = 0.25$.

Once morpho-kinematics of all galaxies are constrained, we need to select galaxy-quasar pairs suitable for wind studies.

4.2.2 Galaxy-quasar pairs classification

Based on azimuthal angles, we classify galaxy-quasar pairs into wind or inflow pairs (see § 2.1.3). For this sample, we classified 4 pairs suitable for wind studies (galaxies framed with black rectangles in Figure 4.4), 4 suitable for accretion studies and 2 are ambiguous cases mainly due to their low-inclination. The low-inclination of a galaxy increase the uncertainty on its position angle (it is difficult for an edge-on galaxy to differentiate the major axis to its minor one) and thus on the azimuthal angle. For our study, we focus on wind-pairs (J0448+0950, J0839+1112, J1441+0443 and J2357-2736). Figure 4.4 shows the 10 galaxies of the SIMPLE sample. Figure 4.5 shows that four galaxies are favorable to study galactic winds properties: J0448+0950, J2357-2739, J0839+1112 and J1441+0443, and are classified as wind-−pairs. J1441+0443 is excluded from subsequent analysis because our SINFONI data does not meet the requirement of SNR$\sim$ 3 imposed by our intensive tests of the GalPaK^{3D} algorithm.

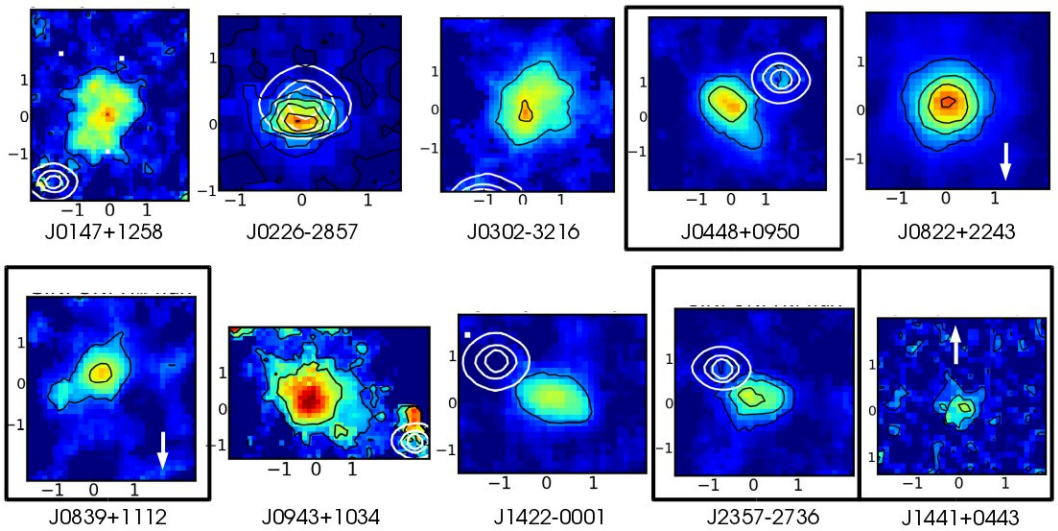

Figure 4.4: Zoom of QSO-subtracted Hα maps of the 10 SIMPLE galaxies: quasar LOS is represented by the white contours if present or pointed out with a white arrow. The 4 wind-pairs are framed with a black rectangle.

4.2.3 Outflow properties

For each of the four galaxy-quasar pairs suitable for wind study, we run our wind model (described in § 4.1.2) with the geometrical parameters derived by GalPaK^{3D}. In UVES quasar spectra, the Mg II λ2796 absorption lines are saturated. We thus use the Mg I λ2852 absorption line which is not saturated. Out of these 4 galaxies, only 3 have well constrained morpho-kinematical parameters (J0448+0950, J0839+1112 and J2357-2736). The J1441+0443 associated galaxy has too low SNR for GalPaK^{3D} to converge.

Since this galaxy-quasar sample consists of pairs with small impact parameters ($b < 20$ kpc) and with moderately-inclined galaxies (from $\sim 18°$ to $\sim 55°$), we improve our wind model by adding galaxy's interstellar medium (ISM) contribution for the galaxy-quasar pairs with the lowest impact parameters such as J2357-2736 and J0448+0950. The procedure is nearly the same as the cone model: we generate particles in a disk with a random exponential distribution from the center with a FWHM corresponding to the galaxy radius previously derived with GalPaK^{3D}. We take the galaxy half light radius derived with GalPaK^{3D} to estimate a realistic contribution from the disk. The thickness of the disk is set to be 0.15 times its radius. We assign the particles a constant circular velocity corresponding to the maximum velocity of the galaxy. We assume that particles have only the maximum rotational velocity of the galaxy since this model simulates the galaxy contribution

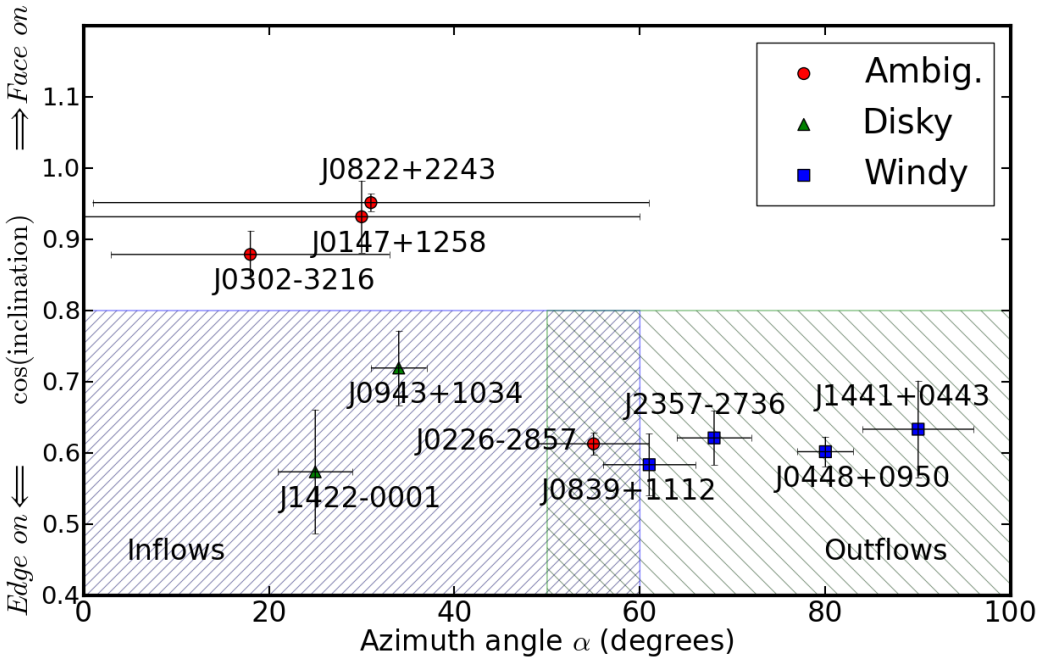

Figure 4.5: Galaxy inclinations for the SIMPLE sample as a function of the azimuthal angle α. Note there are three types of galaxies in this sample: the wind-pairs which have an azimuthal angle larger than 60±10°, the inflow-pairs with α lower than 60±10° and pairs that are ambiguous due to uncertainty on α. It is difficult to derive the azimuthal angle for a nearly face-on galaxy. The wind-pair and inflow-pair classes describe the fact of having the quasar absorptions tracing outflows and inflows, respectively.

at the impact parameter, which is far away from the galaxy center and therefore at this distance, the rotational velocity of the galaxy is considered as constant. The velocity absorption distribution of the disk is naturally strongly dependent on the azimuthal angle with a maximum offset at $\alpha = 0°$ and a distribution centered around $0\ \mathrm{km\,s^{-1}}$ at $\alpha = 90°$.

One "wind" pair has a low impact parameter $b = 6.7$ kpc (J2357−2736). For this galaxy, our assumption of a constant outflow velocity may break down. Indeed, the low-ionization material in momentum-driven winds and energy-driven winds is thought to be accelerated (e.g. Murray et al., 2005; Steidel et al., 2010) by the hot gas, by the radiation pressure, or both. Therefore, instead of using a constant wind speed, we used a generic velocity profile such as $V(r) = V_{\mathrm{out}}\ 2/\pi\ \arctan(r/r_0)$ (e.g. Puech et al., 2008) where r is the distance from the galaxy and r_0 is the characteristic turn-over radius. Behavior of this model can be seen in Figure 4.6. The major impact of the simulated profile using this accelerated wind model is that it affects the asymmetry of the profile when changing r_0.

The accelerated wind model that best describes the data for the J2357−2736 system is using a characteristic turn-over radius r_0 of 10 kpc. In addition, we also included a contribution from the galaxy which appears to account for the bluest components (see left column of Figure 4.7). Figure 4.7 shows the results for the three wind-pairs of the SIMPLE sample. The bottom row shows the UVES data and the upper row the simulated absorption profiles. We can see that we reproduce the equivalent widths of each galaxy-quasar pair as well as the asymmetry in each profile.

If we assume that galactic winds are symmetric with respect to the galactic plane (Figure 2.2), the total ejected mass rate for a galaxy must be increased by a factor of 2. Table 4.2 shows the results for the three wind-pairs.

Table 4.2: Results for galaxies J0448+0950, J2357-2736, J0839+1112.

Galaxy	b (kpc)	$\log(N_{\mathrm{H}}(b))$	V_{out}	θ_{max}	SFR	$\dot{M}_{\mathrm{out}}$	$\frac{V_{\mathrm{out}}}{V_{\mathrm{esc}}}$	η
(1)	(2)	(3)	(4)	(5)	(6)	(7)	(8)	(9)
J0448+0950	13.7	20.30±0.3	115 ± 10	40 ± 5.0	13.6±0.3	$4.6\ ^{+4.9}_{-3.2}$	0.16	0.70
J0839+1112	26.8	20.10±0.3	105 ± 10	30 ± 5.0	3.4±0.2	$3.6\ ^{+3.4}_{-2.2}$	0.43	2.11
J2357−2736	6.7	19.92±0.2	130 ± 10	45 ± 5.0	3.3±0.2	$1.2\ ^{+1.1}_{-0.7}$	0.24	0.75

(1) Galaxy name; (2) Impact parameter (kpc); (3) Gas column density at the impact parameter ($\mathrm{cm^{-2}}$); (4) Wind velocity ($\mathrm{km\,s^{-1}}$); (5) Cone opening angle (degrees) (6) Star Formation Rate ($\mathrm{M_\odot\,yr^{-1}}$); (7) Ejected mass rate for one cone ($\mathrm{M_\odot\,yr^{-1}}$); (8) Ejection velocity divided by escape velocity; (9) Mass loading factor: ejected mass rate divided by star formation rate (for both cones);

In each case, the derived loading factors are around unity and the outflow velocity do not reach the escape velocity so that the outflowing gas is likely to fall back

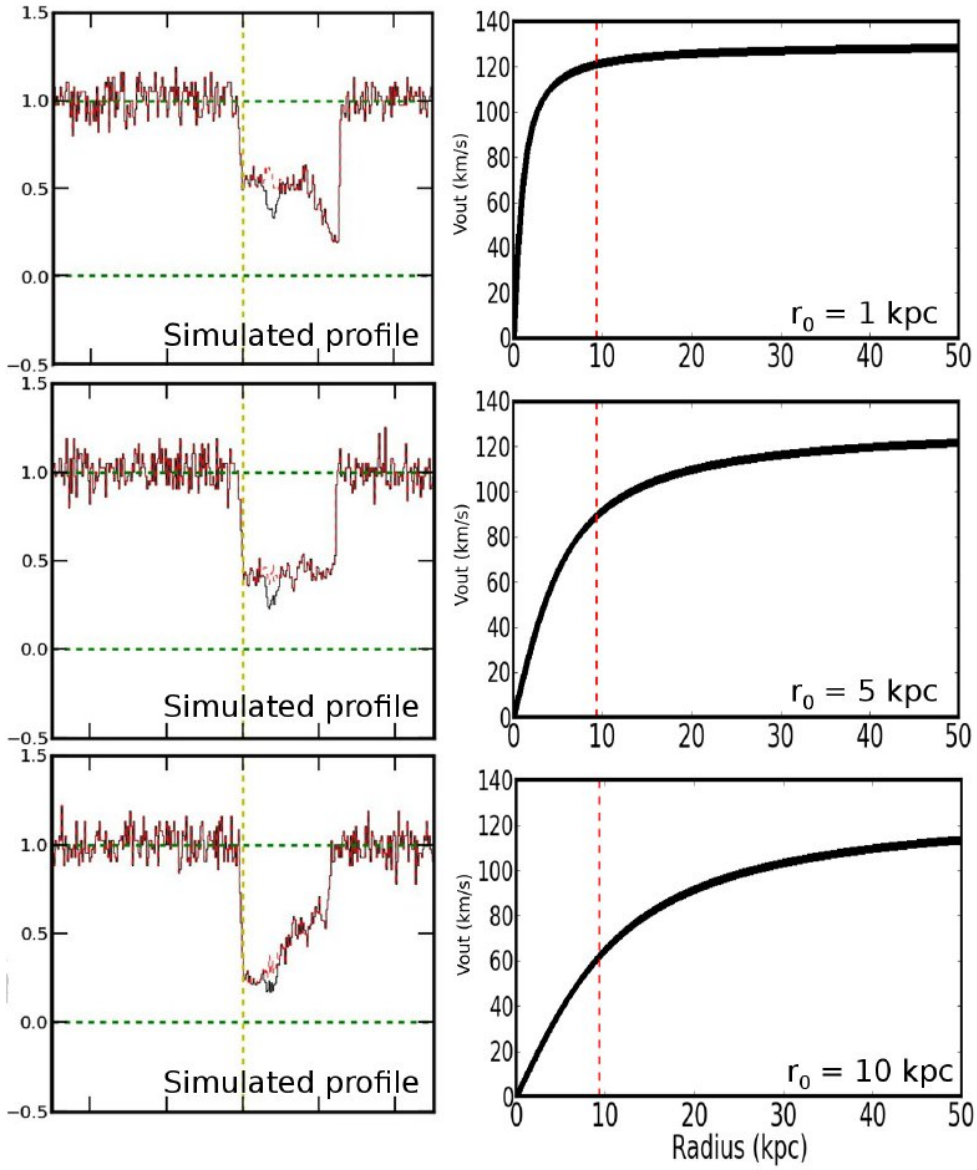

Figure 4.6: *Left column:* from top to bottom: simulated absorption profiles with r_0=1,5,10 kpc. Notice that the asymmetry changes as r_0 increases, it goes from outward to inward asymmetry. *Right column:* The velocity profile corresponding to the associated simulated profile to the left where the turn over radius of the velocity profile (r_0) varies, from top to bottom: r_0=1,5,10 kpc. The red dashed line represents the distance between the galaxy and the quasar LOS ($b/\sin(\alpha)/\sin(i)$), corrected for the inclination i.

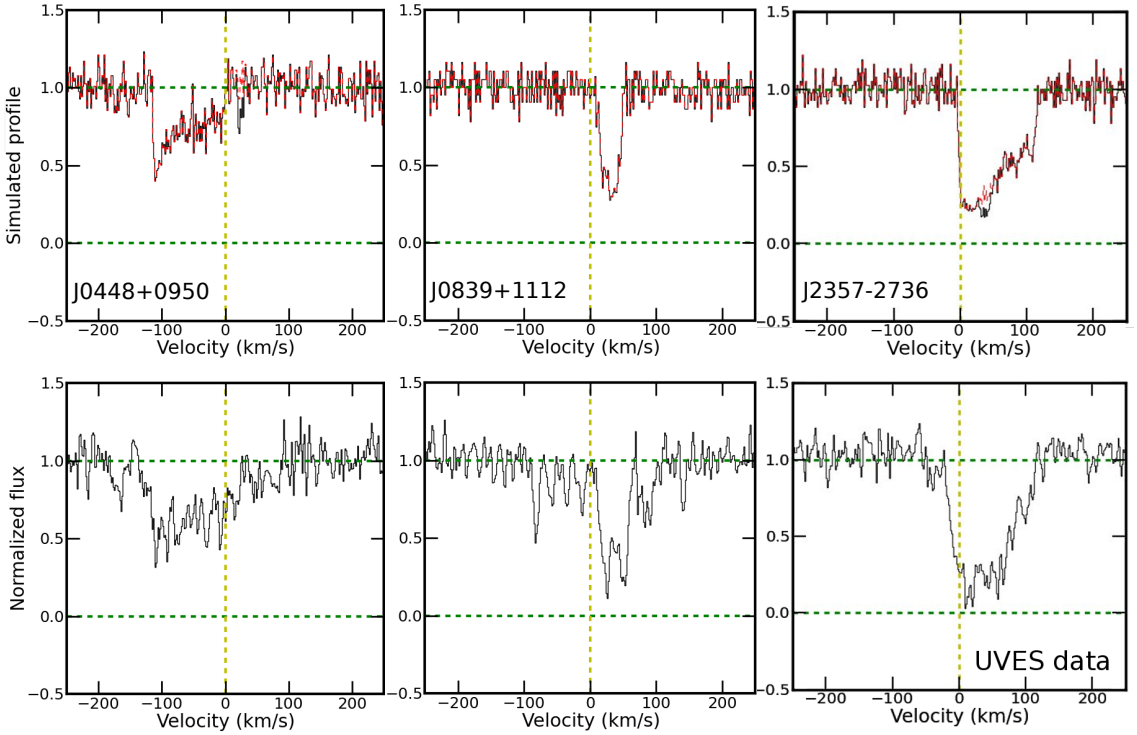

Figure 4.7: Wind models for the three wind-pairs. The bottom row corresponds to UVES quasar Mg I $\lambda 2852$ absorption lines for the three fields: J0448+0950, J0839+1112 and J2357−2736 from left to right. The upper row shows the resulting simulated profiles for each case. One can see that we reproduce the equivalent widths and the profile asymmetries for each galaxy. Note that we do not reproduce the depth as the simulated profile is normalized 'by hand'. On each simulated profile, the red lines correspond to the wind contribution only whereas the black part corresponds to the galaxy component.

onto the galaxy. The resulting loading factors for these 3 wind-pairs are shown in Figure 4.8. In this Figure, the different lines represent theoretical (Okamoto et al., 2010; Davé et al., 2011; Hopkins et al., 2012; Puchwein & Springel, 2013; Vogelsberger et al., 2014; Muratov et al., 2015; Barai et al., 2015) and empirical models (Zahid et al., 2014; Peeples & Shankar, 2011). The parameters of these models are listed in Table 1 of Zahid et al. (2014). It is important to note that the curve from Barai et al. (2015) only includes gas particles with velocities greater than the escape velocity. In addition to this sample, observational constraint include the redshift $z \sim 0.1$ (Bouché et al., 2012, triangles), and Kacprzak et al. (2014) result (square), although very few measurements on individual galaxies exist so far. We raise here the problem of large impact parameters. The loading factor η is, by definition, the ratio between the

ejected mass rate $\dot{M}_{\rm out}$ and the SFR. If the impact parameter is large (typically if $b > 60$ kpc), these two quantities ($\dot{M}_{\rm out}$ and SFR) are on different time scales. Indeed, we derive the ejected mass rate at the quasar LOS, whereas the SFR is derived from emission lines of the host galaxy. For large b, the travel time $b/V_{\rm out}$ is orders of magnitude larger than the time scale of SFR derived from emission lines. SED fitting is a method allowing us to derive SFR on the same time scale than the travel time of the gas to get from the galaxy to the quasar LOS. We took the SED-derived SFRs from the Bouché et al. (2012) sample, given their longer travel times ($b/V_{\rm out}$) to the impact parameters, using UV-to-IR photometry from the Galex+SDSS+Wise surveys and the Code Investigating GALaxy Emission (CIGALE) software (Noll et al., 2009b). The pairs with the largest impact parameters are shown in grey as these mass loading factors can suffer strong biases due to the significant travel time.

4.3 MEGAFLOW survey

As mentionned in § 2.3, the aim of this survey is to increase the number of wind-pairs by 1 order of magnitude in order to allow for statistical analysis.

4.3.1 Survey status

Aiming for 80+ pairs in 20-25 quasar fields, the MEGAFLOW survey is ongoing at the time of writing. As mentioned in § 2.3.2, 19 (out of 25) quasar fields have been observed (as of July 30th 2016) with MUSE as part of GTO time and 17 out of the 25 quasar fields have UVES high resolution quasar spectra follow-up. We do have 15 complete quasar fields with both MUSE and UVES observations. So far, 56 host galaxies have been detected in MUSE data out of 66 candidates (84% detection). Table 4.3 shows MEGAFLOW survey status. The number of detection corresponds to the number of galaxies assumed to be responsible for Mg II absorption lines. In some cases, the number of detected galaxies is larger than the number of absorbers. This means that for one Mg II absorber, more than one galaxy are detected at one absorber redshift and assumed to be the hosts.

4.3.2 Morpho-kinematics from GalPaK^{3D}

As in § 4.2.1, for each detected galaxy we run GalPaK^{3D} in order to derive their morpho-kinematics properties. Every 56 galaxies were GalPaK^{3D}-processed, using default parameters with no assumption. These 56 galaxies were also processed with the 2D fitting tool called Camel[3] in order to cross check the results.

[3]The source code can be found at https://bitbucket.org/bepinat/camel.git

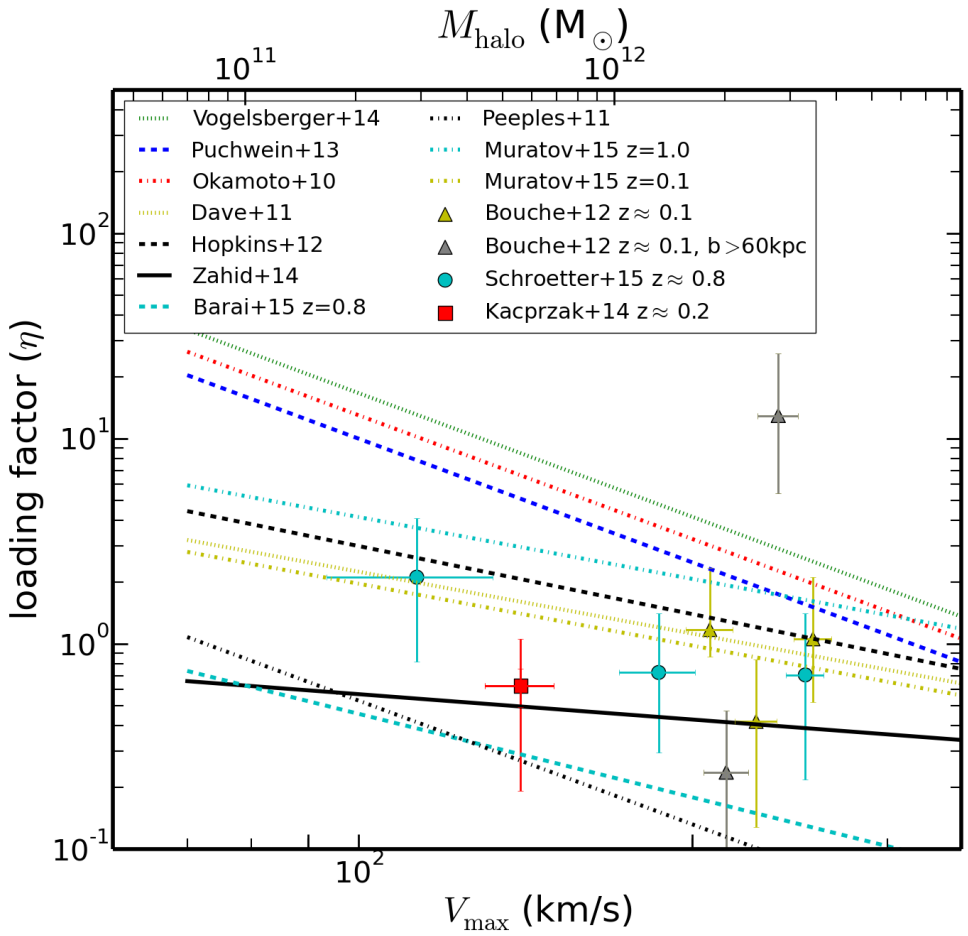

Figure 4.8: Comparison of predicted mass loading factors from theoretical/empirical models (curves) with values derived from observations (dots and triangles) as a function of the maximum rotational velocity. The results from the SIMPLE sample are represented by the cyan circles (Schroetter et al., 2015). The red circle shows the mass loading factor for a $z \sim 0.2$ galaxy (Kacprzak et al., 2014). The triangles show the results for $z \sim 0.2$ galaxies from Bouché et al. (2012). The gray triangles show the galaxies with quasars located at >60kpc where the mass loading factor is less reliable due to the large travel time needed for the outflow to cross the quasar LOS (several 100 Myr) compared to the short time scale of the Hα derived SFR ($\sim$ 10Myr). The upper halo mass axis is scaled on $V_{\rm max}$ at redshift 0.8 from Mo & White (2002).

Table 4.3: MEGAFLOW survey status.

Target name / QSO (1)	Texp (2)	additional Comments (3)	z_{qso} (4)	UVES (5)
SDSSJ001453.19+091217	3.0h / 3.0h	detection 1/3	2.308	1/3OB P96 P97
SDSSJ001453.36−002827	2.0h / 2.0h	detection 3/3	1.924	3/3OB P96
SDSSJ001535.17−075103	2.0h / 2.0h	detection 3/3	0.874	Pending P98
SDSSJ005855.75+011128	1.0h / 2.0h	detection 1/3	1.222	Pending P98
SDSSJ010332.30+133233	2.0h / 2.0h	detection 2/3	1.663	Pending P98
SDSSJ013136.44+130331	2.0h / 2.0h	detection 4/4	1.589	2/2OB P96
SDSSJ013405.70+005109	2.0h / 2.0h	detection 2/4	1.519	Pending P98
SDSSJ014513.10+105626	1.0h / 2.0h	detection 3/3	0.938	1/3OB P96
SDSSJ080004.54+184935	2.0h / 2.0h	detection 3/4	1.292	2/2OB P96
SDSSJ083852.05+025703	2.0h / 2.0h	detection 3/4	1.768	1/1OB P96
SDSSJ093749.58+065656	2.0h / 2.0h	detection 4/4	1.814	3/3OB P96
SDSSJ103936.66+071427	2.0h / 2.0h	detection 3/3	1.532	3/3OB P97
SDSSJ110735.26+175731	2.0h / 2.0h	detection 2/2	2.133	3/3OB P96
SDSSJ110742.70+102126	2.0h / 2.0h	detection 3/5	1.922	2/2OB P96
SDSSJ123624.40+072551	2.0h / 2.0h	detection 2/4	1.605	1/1OB P96
SDSSJ131405.60+065721	2.0h / 2.0h	detection 9/4	1.879	1/1OB P97
SDSSJ135217.67+061433	0.0h / 2.0h	detection ?/3	1.798	1/1OB P97
SDSSJ135809.49+114557	2.0h / 2.0h	detection 3/3	1.716	2/2OB P97
SDSSJ142538.05+120919	1.0h / 2.0h	detection ?/4	1.618	2/2OB P97
SDSSJ150900.12+150634	1.0h / 2.0h	detection ?/4	2.237	2/2OB P97
SDSSJ213748.44+001220	3.0h	really out of spec	1.668	—
SDSSJ213748.44+001220	1.0h	detection 3/4	1.668	P94
SDSSJ215200.03+062516	2.0h / 2.0h	detection 3/4	2.409	P94

(1) Quasar field name; (2) Total exposure time of the field; (3) Number of detected galaxy corresponding to Mg II absorber; (4) Quasar redshift; (5) UVES follow-up observation period.

Out of these 56 galaxies, 26 have converged parameters, based on MCMC chains and comparison with the input data and Camel results. The 30 other galaxies did not converged for several reasons. These reasons are either a low SNR, mergers or the galaxy was too small ($r_{1/2}$ < seeing FWHM).

For mergers, a reason for GalPaK^{3D} not to converge is that the "simple" model of a rotating disk represented with a smooth symmetric light profile is not adapted to complex kinematic of some galaxies, and these galaxies are usually gravitationally interacting or in advance merging process.

For "non-converged" galaxies, some parameters like PA or $V_{\max}$ are still accessible with Camel or GalPaK^{3D} but because lack of time needed to study each of these galaxies forced us to only focus on converged galaxies.

Middle and right columns of each case in Figures 4.9, 4.10 and 4.11 show velocity maps of each galaxy corresponding to the ones presented on left panels. What is important to look at between these two columns is to compare the position angles of

each galaxy as well as the velocity fields (check if the positive and negative velocities areas correspond to each other). We can see that for almost every galaxy, these parameters are in good agreements. Some galaxy like the one at redshift 1.0108 in the J0131+1303 quasar field show a position angle difference of $\sim 60°$.

Table 4.4 show the GalPaK^{3D} results for the 26 galaxies. Figures 4.9, 4.10 and 4.11 show the 26 galaxies of the MEGAFLOW survey as well as wind-pairs which are framed with a red rectangle.

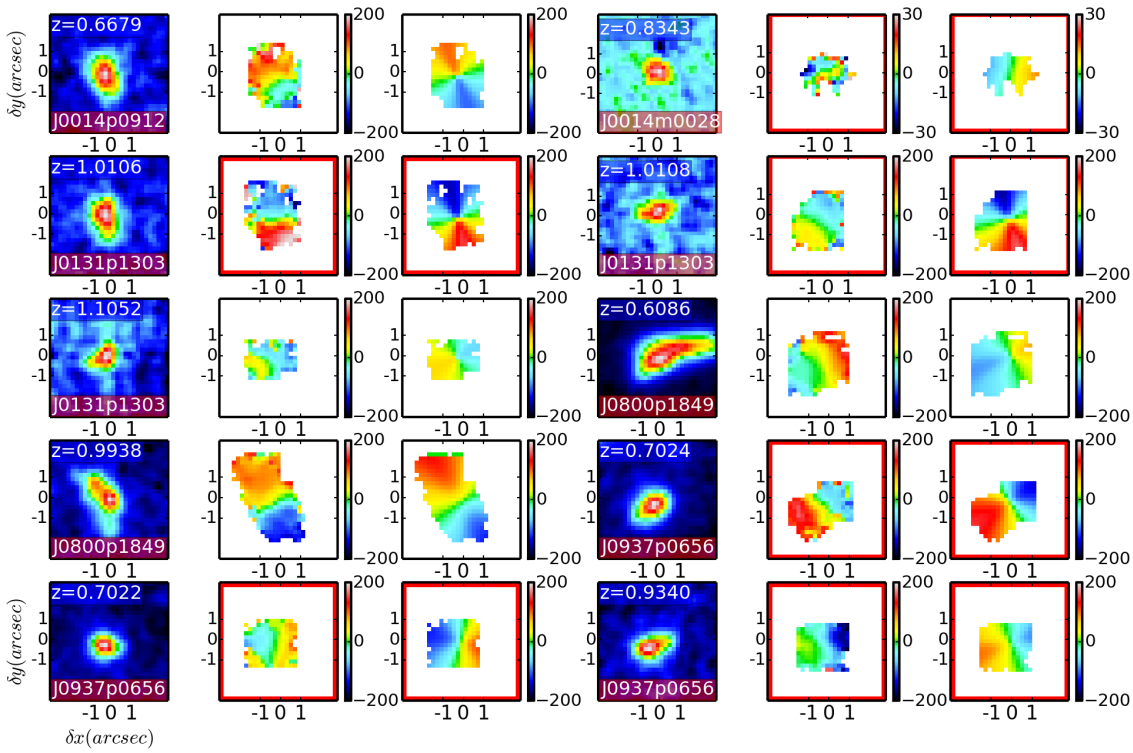

Figure 4.9: Results for 10 MEGAFLOW galaxies: Each set of result for a galaxy is composed of 3 maps: *left:* zoom of QSO-subtracted [O II] maps. On each of these maps, on top of them is indicated the redshift of the galaxy and at the bottom the quasar field name. *Middle:* zoom of QSO-subtracted Camel velocity map. *Right:* Zoom of QSO-subtracted GalPaK^{3D} PSF-deconvolved velocity map. Wind-pairs are framed with a red rectangles for Camel and GalPaK^{3D} velocity maps.

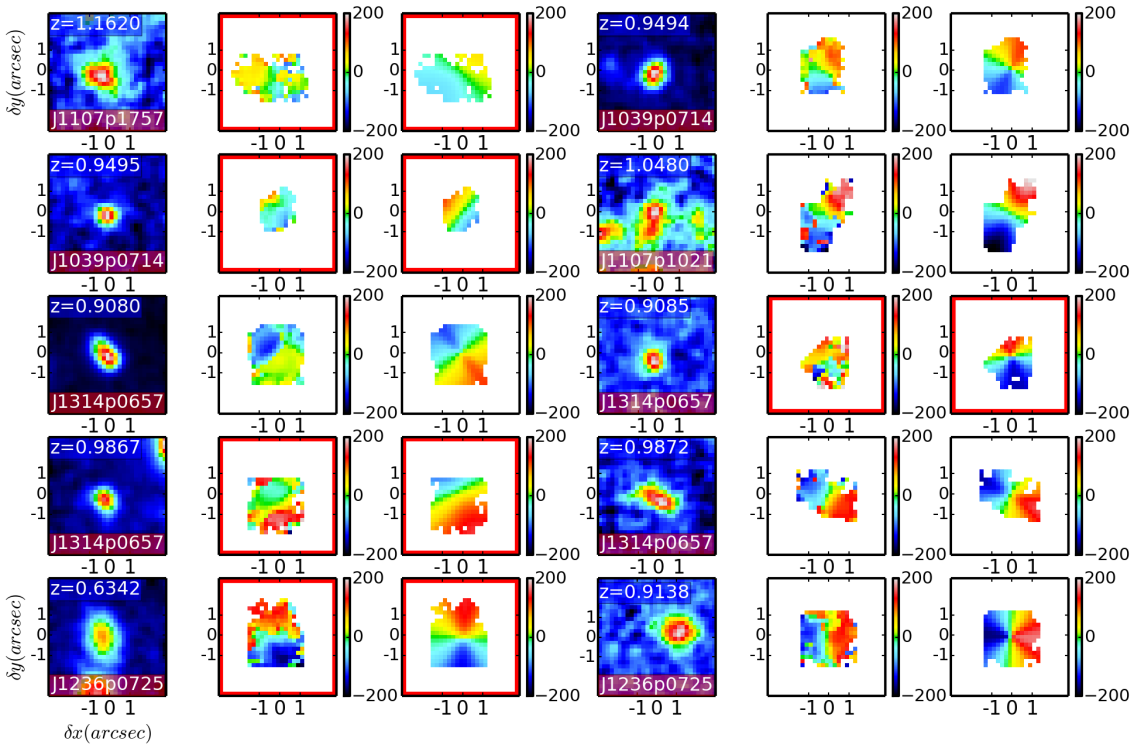

Figure 4.10: Same as Figure 4.9 for the 10 next galaxies.

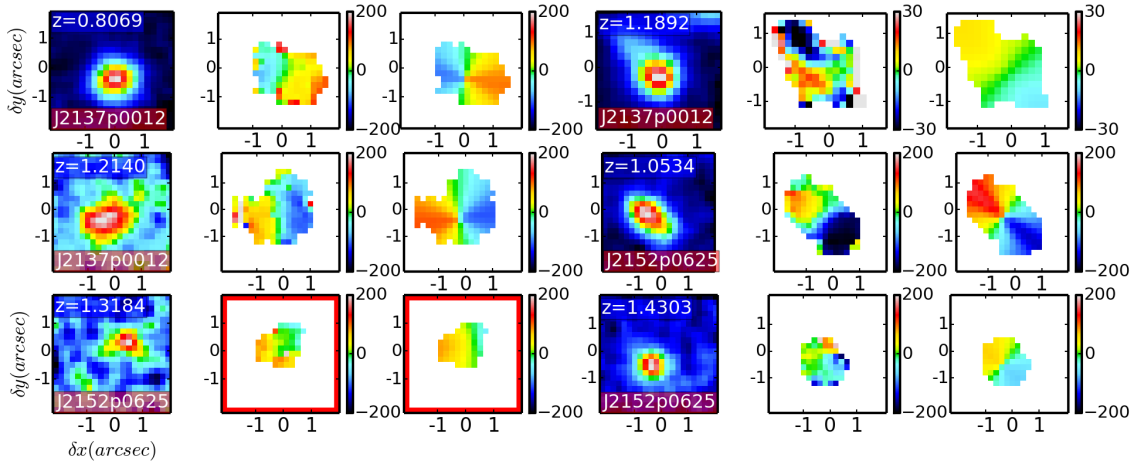

Figure 4.11: Same as Figure 4.9 for the last 6 galaxies.

Table 4.4: GalPaK^{3D} results on 26 MEGAFLOW galaxies with reliable morpho-kinematic parameters.

field name (1)	redshift (2)	α (3)	b (4)	$W_r^{\lambda 2796}$ (5)	PA (6)	incl (7)	$V_{\rm max}$ (8)	$V_{\rm disp}$ (9)	Flux (10)
J0014p0912	0.6679	26± 2	63.5	...	-160 ± 2	61 ± 2	158 ± 15	38 ± 5	2.9×10^{-17}
J0014m0028	0.8343	79± 10	10.8	2.232	78 ± 68	65 ± 5	16 ± 16	40 ± 2	3.2×10^{-17}
J0131p1303_G1	1.0106	76± 1	26.8	1.165	-32 ± 1	50 ± 1	151 ± 17	30 ± 2	3.0×10^{-17}
J0131p1303_G2	1.0108	53± 1	125.8	1.165	16 ± 1	65 ± 2	189 ± 14	27 ± 6	2.1×10^{-17}
J0131p1303_G3	1.1052	60± 2	72.8	1.168	-74 ± 2	78 ± 5	107 ± 26	58 ± 4	2.3×10^{-17}
J0800p1849_G1	0.6085	22± 1	62.3	0.915	112 ± 1	65 ± 1	102 ± 3	40 ± 0.7	6.9×10^{-17}
J0800p1849_G2	0.9937	72± 1	76.8	0.934	-146 ± 1	66 ± 1	174 ± 19	50 ± 1	4.4×10^{-17}
J0937p0656_G1	0.7024	84± 1	37.5	1.767	-56 ± 1	47 ± 1	215 ± 13	64 ± 2	1.4×10^{-16}
J0937p0656_G2	0.7022	55± 1	67.8	1.767	76 ± 1	44 ± 1	203 ± 21	33 ± 2	9.5×10^{-17}
J0937p0656_G3	0.9340	72± 1	38.1	1.519	-71 ± 1	66 ± 1	131 ± 29	47 ± 2	6.9×10^{-17}
J1107p1757	1.1620	72± 3	47.6	1.97	-114 ± 3	61 ± 4	66 ± 5	38 ± 3	6.4×10^{-17}
J1039p0714_G1	0.9493	4± 1	48.7	1.22	152 ± 1	53 ± 1	152 ± 7	54 ± 2	8.5×10^{-17}
J1039p0714_G2	0.9494	66± 4	72.7	1.22	-129 ± 4	69 ± 7	191 ± 65	83 ± 6	2.6×10^{-17}
J1107p1021	1.0479	23± 2	40.9	0.499	151 ± 2	70 ± 4	294 ± 38	33 ± 14	3.5×10^{-17}
J1314p0657_G1	0.9080	35± 1	66.3	0.889	37 ± 1	67 ± 1	135 ± 2	78 ± 1	1.9×10^{-16}
J1314p0657_G2	0.9084	85± 3	96.2	0.889	-168 ± 3	44 ± 2	225 ± 22	11 ± 11	1.4×10^{-17}
J1314p0657_G3	0.9867	89± 4	37.9	0.977	24 ± 4	36 ± 3	330 ± 24	50 ± 2	6.4×10^{-17}
J1314p0657_G4	0.9871	7± 3	104.1	0.977	-30 ± 3	30 ± 15	118 ± 117	39 ± 9	1.4×10^{-17}
J1236p0725_G1	0.6341	77± 2	66.3	1.412	177 ± 2	65 ± 12	168 ± 12	71 ± 5	1.0×10^{-16}
J1236p0725_G2	0.9137	2± 2	18.2	2.24	85 ± 2	47 ± 2	232 ± 12	6 ± 4	6.7×10^{-17}
J2137p0012_G1	0.8069	25± 2	88.1	0.724	74 ± 2	54 ± 2	132 ± 5	39 ± 2	8.3×10^{-17}
J2137p0012_G2	1.1892	71± 10	63.7	0.308	-134 ± 68	52 ± 2	12 ± 12	102 ± 1	1.4×10^{-16}
J2137p0012_G3	1.2139	47± 4	87.2	1.122	-83 ± 4	32 ± 6	203 ± 39	11 ± 7	4.0×10^{-17}
J2152p0625_G1	1.0533	4± 1	45.4	0.522	-128 ± 1	75 ± 1	173 ± 2	2 ± 2	8.7×10^{-17}
J2152p0625_G2	1.3184	88± 10	34	1.347	-87 ± 10	75 ± 9	139 ± 52	29 ± 12	1.3×10^{-17}
J2152p0625_G3	1.4303	72± 3	62.5	1.152	-162 ± 3	28 ± 1	299 ± 25	22 ± 12	3.1×10^{-17}

(1) Quasar field name; (2) Galaxy redshift; (3) Azimuthal angle (α) in degrees; (4) Impact parameter (kpc); (5) Mg II REW (Å); (6) Galaxy position angle (degrees); (7) Galaxy inclination (degrees); (8) Maximum rotational velocity (km s^{-1}); (9) Velocity dispersion (km s^{-1}); (10) [O II] flux (erg s^{-1} cm^{-2});

In the next sections, we only focus on the 26 converged galaxies.

4.3.3 Galaxy-quasar pairs classification

To put constraints on galactic outflows, we first need to select galaxy-quasar pairs suitable for wind studies (wind pairs). To do so, we measure the angle between the galaxy major axis and the apparent quasar location, which is referred to as the azimuthal angle α (see Figure 2.2 and § 2.1.3). Figure 4.12 shows galaxy inclination as a function of quasar azimuthal angle. We can see that 3 pairs are classified as ambiguous whereas 9 are likely to be inflow-pairs and 11 likely to be wind-pairs. Figure 4.13 shows the distribution of azimuthal angles. We note that there is a bimodal distribution of azimuthal angle and there are more galaxy-quasar pairs in a configuration favorable for wind study. This is probably due to the fact that we select only strong Mg II REW in the quasar spectra and the largest $W_r^{\lambda 2796}$ tend to be associated with outflows (e.g. Kacprzak et al., 2011; Lan et al., 2014a).

Now that we classified our galaxy-quasar pairs, we can focus on wind-pairs in order to constrain galactic outflow properties.

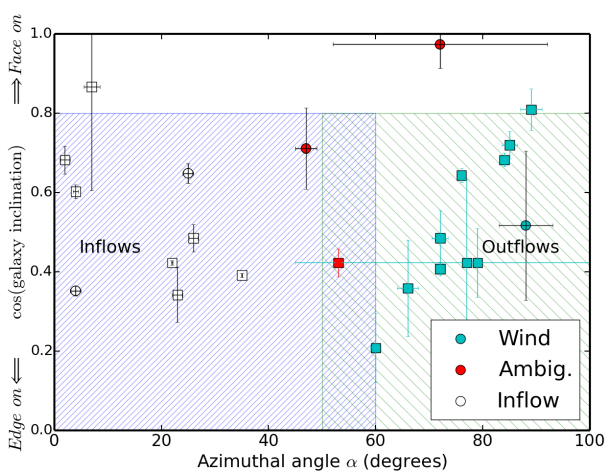

Figure 4.12: Galaxy inclination as a function of azimuthal angle α for 26 galaxies with reliable morpho-kinematic parameters detected in the MUSE fields. The dashed areas correspond to azimuthal angle ranges for which we classify pairs as inflow-pairs (blue and narrow dashes) or wind-pairs (green and wider dashes). These areas stop for face-on galaxies as uncertainty on position angles are too large. It is thus difficult to determine α and to classify galaxy-quasar pairs in this area. We note that 11 galaxies are classified as wind-pairs.

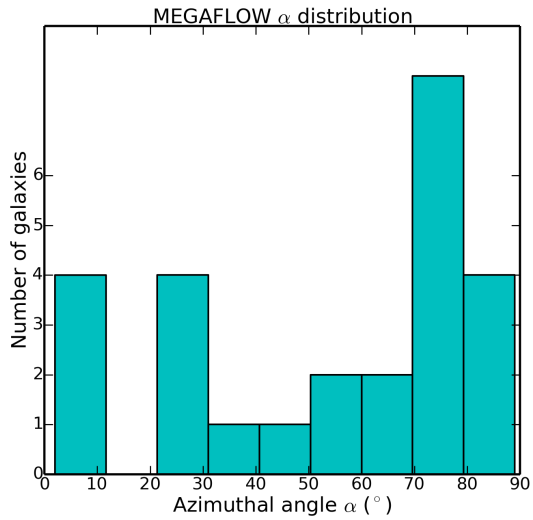

Figure 4.13: Azimuthal angle α distribution for 26 galaxies with reliable morpho-kinematic parameters detected in the MUSE fields. We note that 11 galaxies are classified as wind-pairs and that there is a bimodal distribution of α. There are more galaxy-quasar pairs in a configuration favorable for wind study.. This is probably due to the fact that we select only strong Mg II REW in the quasar spectra and the largest $W_r^{\lambda 2796}$ tend to be associated with outflows (e.g. Kacprzak et al., 2011; Lan et al., 2014a).

4.3.4 Outflow properties

With the 11 wind-pairs we have, we proceed as in § 4.2.3. For each wind-pair, we build our cone model in order to reproduce the absorption lines in the UVES quasar spectra. In some absorption lines (Fe II in Figures 4.19, 4.20 and 4.23, Mg I in Figure 4.21, Mg II in Figure 4.22), we can see a lack of absorption in roughly the middle of a line, and this happens when the quasar LOS is aligned with the galaxy minor axis ($\alpha > 80°$). This lack of absorbing particles at these velocities shows that the outflowing cone must have a low density region inside it. We thus developed a partially empty cone model in order to reproduce absorption profiles for the cases where $\alpha > 80°$.

The principle is the same as described in § 4.1.2 except that we only fill the cone with particles from a certain opening angle $\theta_{\rm in}$ to $\theta_{\rm max}$. The inner cone is therefore empty. As mentioned in Schroetter et al. (2016), this empty inner cone could be the signature of a highly ionized gas filled in the inner cone while the low-ionized gas that we are tracing is entrained in the outskirts of the outflowing cone in a manner similar to Fox et al. (2015) for the MilkyWay and to Veilleux & Rupke (2002) for NGC1482. This scenario is also motivated by references cited in Veilleux et al. (2003)

or Bland-Hawthorn et al. (2007).

In addition to this empty cone model, in some cases (for J0131+1303 and J0937+0656 quasar fields), multiple galaxy candidate for the same absorption are assumed to be responsible for the absorption in the quasar spectrum. If the detected galaxies happen to have a geometrical configuration suitable to be wind-pairs, then we need to generate multiple wind models for the same absorption lines (see Figures 4.19 and 4.20). We can differentiate three main models: "classic" wind models, "empty cone" wind models and "multiple contribution" wind models.

"Classic" wind models are processed to wind-pairs for which there is only one galaxy detected around the Mg II absorption redshift in a quasar field and that the corresponding absorption lines in UVES data do not show a lack of absorption in the middle of the profile. These wind-pairs correspond to pairs with Mg II absorptions in the associated quasars at redshifts z =0.8343 for the J0014−0028 quasar field, $z = 0.9340$ for J0937+0656, $z = 0.9495$ for J1039+0714, $z = 0.9867$ for J1314+0657 and $z = 0.6342$ for J1236+0725. These wind-pairs have impact parameters b of 10.8, 38.1, 72.7, 37.9 and 66.3 kpc, azimuthal angles α of 79, 72, 66, 89 and 77° respectively. The outflowing velocities and cone opening angles are $V_{\rm out}= 210 \pm 10$ km s^{-1} with $\theta_{\rm max}= 25 \pm 5°$ for J0014−0028, $V_{\rm out}= 150 \pm 10$ km s^{-1} with $\theta_{\rm max}= 30 \pm 5°$ for J0937+0656, $V_{\rm out}= 65 \pm 10$ km s^{-1} with $\theta_{\rm max}= 30 \pm 5°$ for J1039+0714, $V_{\rm out}= 95 \pm 10$ km s^{-1} with $\theta_{\rm max}= 20 \pm 5°$ for J1314+0657 and $V_{\rm out}= 65 \pm 10$ km s^{-1} with $\theta_{\rm max}= 30 \pm 5°$ for J1236+0725.

"Empty cone" wind models are processed to wind-pairs like the "classic" pairs except that absorption lines in UVES data show a lack of absorption in the roughly middle of the absorption profile. These wind-pairs correspond to pairs with Mg II absorptions in the associated quasars at redshifts $z = 1.1620$ for the J1107+1757 quasar field, $z = 0.9085$ for J1314+0657 and $z = 1.3185$ for J2152+0625. These wind-pairs have impact parameters b of 47.6, 96.2 and 34.0 kpc, azimuthal angles α of 72, 85 and 88° respectively. The outflowing velocities and cone opening angles are $V_{\rm out}= 150 \pm 10$ km s^{-1} with $\theta_{\rm max}= 30 \pm 5°$ and $\theta_{\rm in} = 20 \pm 2°$ for J1107+1757, $V_{\rm out}= 210 \pm 10$ km s^{-1} with $\theta_{\rm max}= 30 \pm 5°$ and $\theta_{\rm in} = 7 \pm 2°$ for J1314+0657 and $V_{\rm out}= 150 \pm 10$ km s^{-1} with $\theta_{\rm max}= 20 \pm 5°$ and $\theta_{\rm in} = 7 \pm 2°$ for J2152+0625.

The remaining wind-pairs are then in the "multiple contribution" wind models category. These are the two cases where we do find two galaxies at very close redshifts that are considered responsible for the Mg II absorption lines in the quasar spectra.

The first two galaxies detected to be responsible for the Mg II absorption lines are from the J0131+1303 quasar field. These galaxies have redshifts $z = 1.0108$ and $z = 1.0106$, impact parameters b of 125.8 kpc and 26.8 kpc, azimuthal angles α of 53° and 76° respectively. Resulting simulated profiles are shown on top panel of Figure 4.19. The outflow in green has a $V_{\rm out}$ of 205 ± 10 km s^{-1} and an opening angle $\theta_{\rm max}$ of $35 \pm 5°$ for the galaxy at redshift $z = 1.0108$. The outflow in black has

a $V_{\rm out}$ of 80 ± 10 km s^{-1} and an opening angle $\theta_{\rm max}$ of $35 \pm 5°$ and $\theta_{\rm in}$ of $8 \pm 2°$ for the galaxy at redshift $z = 1.0106$.

The last two galaxies detected to be responsible for the Mg II absorption lines are from the J0937+0656 quasar field. These galaxies have redshifts $z = 0.7022$ and $z = 0.7024$, impact parameters b of 67.8 kpc and 37.5 kpc, azimuthal angles α of 84° and 55° respectively. Resulting simulated profiles are shown on top panel of Figure 4.20. The outflow in green has a $V_{\rm out}$ of 100 ± 10 km s^{-1} and an opening angle $\theta_{\rm max}$ of $30 \pm 5°$ for the galaxy at redshift $z = 0.7022$. The outflow in black has a $V_{\rm out}$ of 120 ± 10 km s^{-1} and an opening angle $\theta_{\rm max}$ of $35 \pm 5°$ and $\theta_{\rm in}$ of $8 \pm 2°$ for the galaxy at redshift $z = 0.7024$.

Figures 4.14, 4.19, 4.20, 4.15, 4.16, 4.21, 4.18, 4.22, 4.15 and 4.23 (Figures 4.19 and 4.20 shows results for two wind-pairs each) show the UVES absorption lines centered at the galaxy redshift for every wind-pair as well as corresponding simulated profiles on top. As in § 4.2.3, we derive outflow velocities as well as cone opening angles for each wind-pair. For simplicity, results on outflows are listed in Table 4.5.

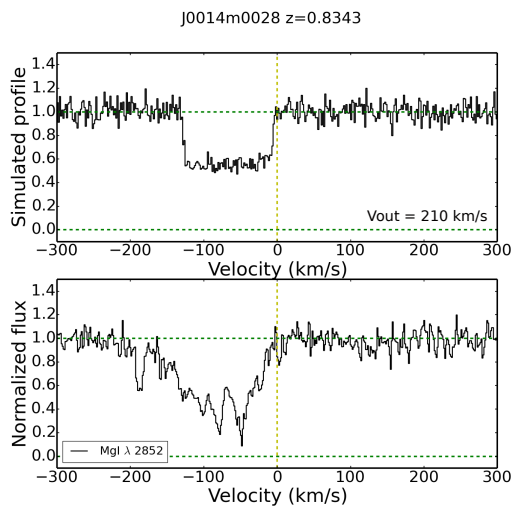

Figure 4.14: Representation of simulated profile and quasar spectrum associated with the J0014−0028 galaxy. Simulated wind profile (top) reproducing the Mg I absorption profile (centered at $z = 0.8343$) from UVES (bottom). This outflow has a $V_{\rm out}$ of 210 ± 10 km s^{-1} and an opening angle $\theta_{\rm max}$ of $25 \pm 5°$.

In summary of this chapter, we managed to put further constraints on galactic outflows thanks to the background quasar technique. Before showing our results on loading factors as a function of the galaxy halo mass, further investigations on relations between galactic winds and galaxy properties are needed.

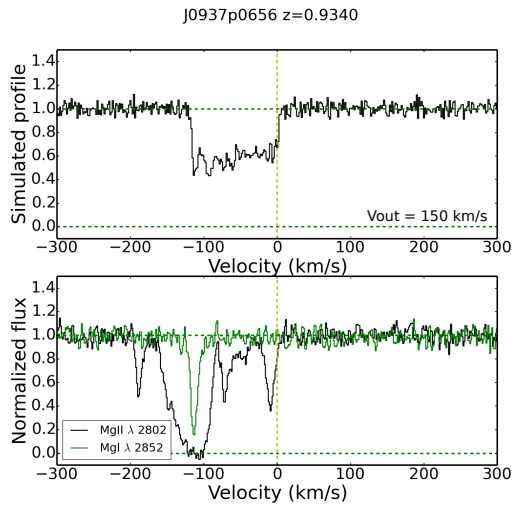

Figure 4.15: Same as Figure 4.14 but for the J0937+0656 galaxy at redshift $z \approx 0.9340$. This outflow has a $V_{\rm out}$ of 150 ± 10 km s^{-1} and an opening angle $\theta_{\rm max}$ of $30 \pm 5°$ for the galaxy at redshift $z = 0.9340$.

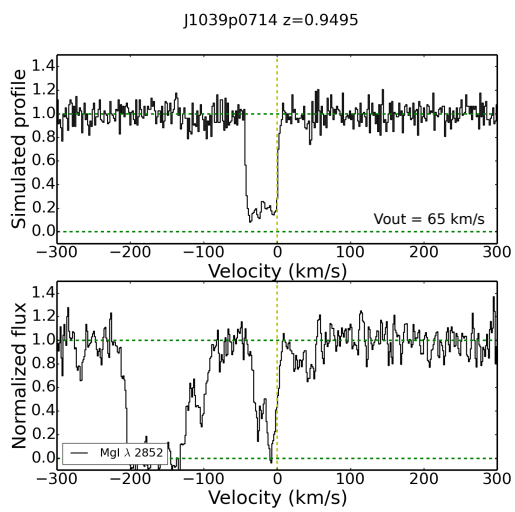

Figure 4.16: Same as Figure 4.14 but for the J1039+0714 galaxy at redshift $z \approx 0.9495$. This outflow has a $V_{\rm out}$ of 65 ± 10 km s^{-1} and an opening angle $\theta_{\rm max}$ of $30 \pm 5°$ for this galaxy.

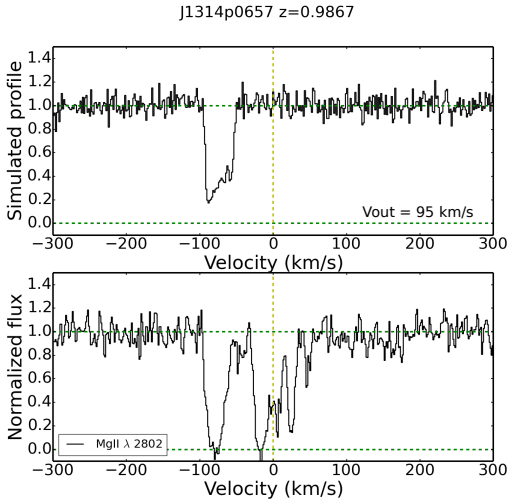

Figure 4.17: Same as Figure 4.14 but for the J1314+0657 galaxy at redshift $z \approx 0.9867$. This outflow has a $V_{\rm out}$ of 95 ± 10 km s^{-1} and an opening angle $\theta_{\rm max}$ of $20 \pm 5°$ for this galaxy.

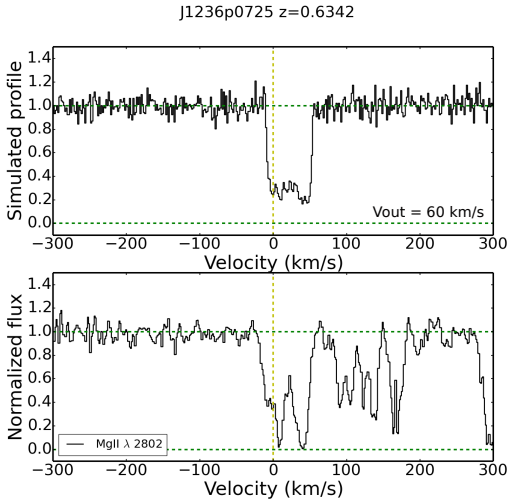

Figure 4.18: Same as Figure 4.14 but for the J1236+0725 galaxy at redshift $z \approx 0.6342$. This outflow has a $V_{\rm out}$ of 60 ± 10 km s^{-1} and an opening angle $\theta_{\rm max}$ of $35 \pm 5°$ for this galaxy.

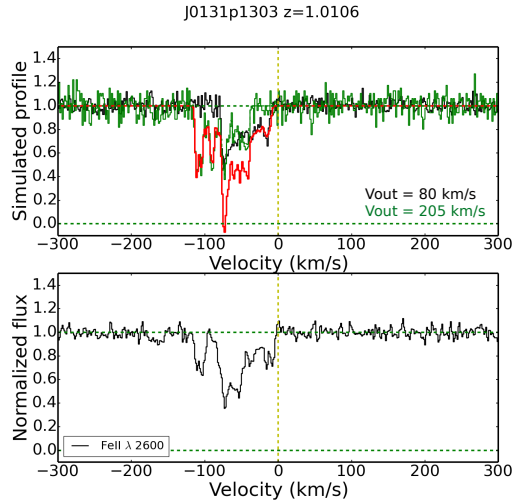

Figure 4.19: Same as Figure 4.14 but for the J0131+1303 galaxies at redshift $z \approx 1.0106$. For this case, because two galaxies were detected at the absorber redshift, we needed to run wind models for both of them (at redshift 1.0106 and 1.0108) in order to reproduce the absorption lines in red. The outflow in green has a $V_{\rm out}$ of 205 ± 10 km s^{-1} and an opening angle $\theta_{\rm max}$ of $35 \pm 5°$ for the galaxy at redshift $z = 1.0108$. The outflow in black has a $V_{\rm out}$ of 80 ± 10 km s^{-1} and an opening angle $\theta_{\rm max}$ of $35 \pm 5°$ and $\theta_{\rm in}$ of $8 \pm 2°$ for the galaxy at redshift $z = 1.0106$.

Table 4.5: Results on outflow properties for MEGAFLOW galaxies.

Galaxy (1)	$z_{\rm gal}$ (2)	b (kpc) (3)	$\log(N_{\rm H}(b))$ (4)	$V_{\rm out}$ (5)	$\theta_{\rm max}$ (6)	SFR (7)	$\dot{M}_{\rm out}$ (8)	$\frac{V_{\rm out}}{V_{\rm esc}}$ (9)	η (10)
J0014m0028	0.8343	10.8	20.08±0.13	210 ± 10	25 ± 5	2.0±0.1	$2.3^{+2.3}_{-1.2}$	8.20	2.21
J0131p1303	1.0106	26.8	19.60±0.05	80 ± 10	35 ± 5	3.4±0.3	$1.0^{+0.6}_{-0.4}$	0.24	0.58
J0131p1303	1.0108	125.8	19.60±0.05	205 ± 10	35 ± 5	2.2±0.1	$11.9^{+4.5}_{-3.6}$	0.70	10.93
J0937p0656	0.7024	37.5	19.90±0.10	120 ± 10	35 ± 5	7.6±0.9	$4.2^{+2.7}_{-1.8}$	0.24	1.11
J0937p0656	0.7022	67.8	19.90±0.10	100 ± 10	30 ± 5	4.6±0.4	$5.4^{+3.7}_{-2.3}$	0.24	2.38
J0937p0656	0.9340	38.1	19.79±0.08	150 ± 10	30 ± 5	7.5±0.9	$3.6^{+2.1}_{-1.4}$	0.56	0.95
J1107p1757	1.1620	47.6	19.98±0.11	150 ± 10	30 ± 5	13.4±2.0	$6.9^{+4.7}_{-3.0}$	1.59	1.03
J1039p0714	0.9495	72.7	19.63±0.06	65 ± 10	30 ± 5	2.4±0.2	$2.0^{+1.2}_{-0.8}$	0.18	1.71
J1314p0657	0.9085	96.2	19.40±0.04	210 ± 10	30 ± 5	0.9±0.0	$5.1^{+1.9}_{-1.5}$	0.51	11.09
J1314p0657	0.9867	37.9	19.47±0.04	95 ± 10	20 ± 5	8.0±1.0	$0.7^{+0.4}_{-0.3}$	0.12	0.18
J1236p0725	0.6342	66.3	19.74±0.08	60 ± 10	35 ± 5	3.8±0.3	$2.5^{+1.6}_{-1.1}$	0.18	1.34
J2152p0625	1.3184	34.0	19.70±0.07	150 ± 10	20 ± 5	4.6±0.4	$1.7^{+1.1}_{-0.8}$	0.54	0.74

(1) Galaxy name; (2) Galaxy redshift; (3) Impact parameter (kpc); (4) Gas column density at the impact parameter (cm^{-2}); (5) Wind velocity (km s^{-1}); (6) Cone opening angle (degrees) (7) Star Formation Rate (M$_\odot$ yr^{-1}); (8) Ejected mass rate for one cone (M$_\odot$ yr^{-1}); (9) Ejection velocity divided by escape velocity; (10) Mass loading factor: ejected mass rate divided by star formation rate (for both cones);

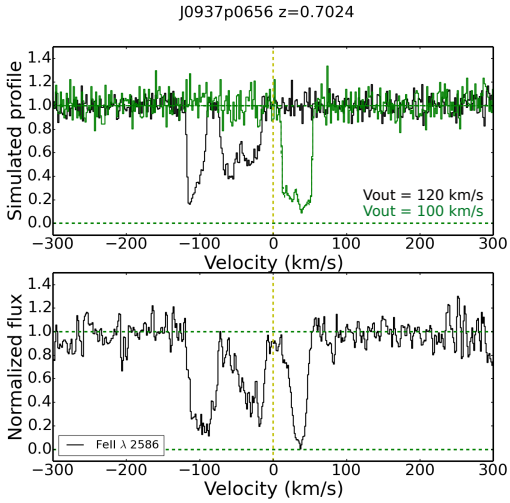

Figure 4.20: Same as Figure 4.19 but for the J0937+0656 galaxies at redshift $z \approx 0.7024$. The outflow in green (the positive absorption component) has a $V_{\rm out}$ of 100 ± 10 km s^{-1} and an opening angle $\theta_{\rm max}$ of $30 \pm 5°$ for the galaxy at redshift $z = 0.7022$ (this pair has an azimuthal angle α of 55°). The outflow in black (the negative absorption components) has a $V_{\rm out}$ of 120 ± 10 km s^{-1} and an opening angle $\theta_{\rm max}$ of $35 \pm 5°$ and $\theta_{\rm in}$ of $8 \pm 2°$ for the galaxy at redshift $z = 0.7024$ (his pair has an azimuthal angle α of 84°). Results on these two pairs are shown in Tables 4.4 and 4.5.

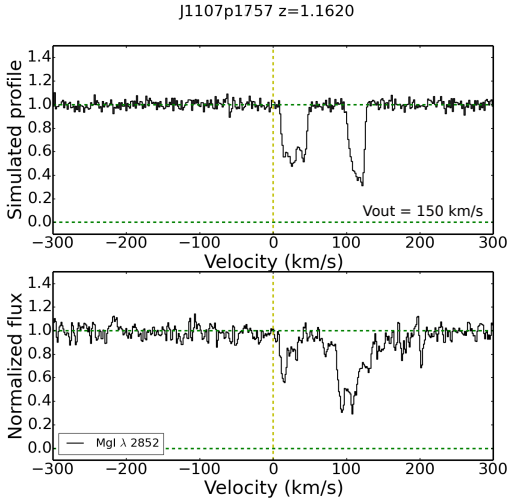

Figure 4.21: Same as Figure 4.14 but for the J1107+1757 galaxy at redshift $z \approx 1.1620$. This outflow has a $V_{\rm out}$ of 150 ± 10 km s^{-1} and an opening angle $\theta_{\rm max}$ of $30 \pm 5°$ and $\theta_{\rm in}$ of $20 \pm 2°$ for this galaxy.

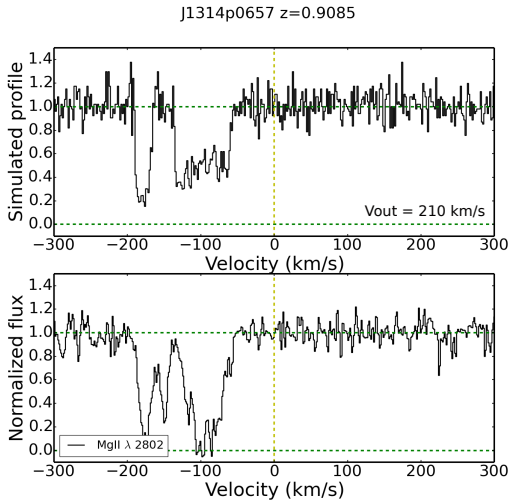

Figure 4.22: Same as Figure 4.14 but for the J1314+0657 galaxy at redshift $z \approx 0.9085$. This outflow has a $V_{\rm out}$ of 210 ± 10 km s^{-1} and an opening angle $\theta_{\rm max}$ of $30 \pm 5°$ and $\theta_{\rm in}$ of $7 \pm 2°$ for this galaxy.

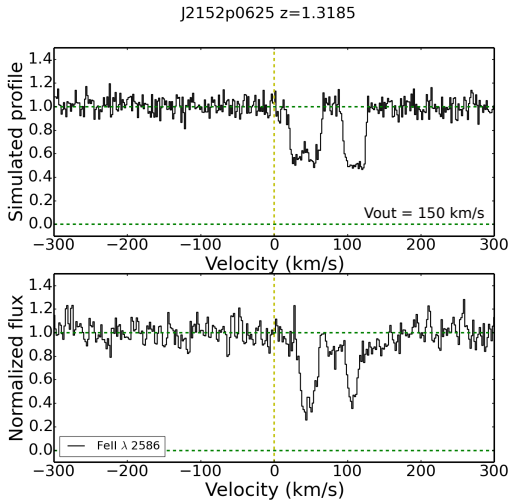

Figure 4.23: Same as Figure 4.14 but for the J2152+0625 galaxy at redshift $z \approx 1.3185$. This outflow has a $V_{\rm out}$ of 150 ± 10 km s^{-1} and an opening angle $\theta_{\rm max}$ of $20 \pm 5°$ and $\theta_{\rm in}$ of $7 \pm 2°$ for this galaxy.

Chapter 5

Combining both samples: galactic wind properties as a function of galaxy properties

Contents

5.1 Basic properties of the sampled galaxies 76
5.1.1 Galaxy redshift distribution 76
5.1.2 Galaxy stellar mass measurement 77
5.2 How far do winds go? 81
5.3 Do winds escape? 83
5.4 Wind scaling relations 85
5.4.1 Previous studies on galactic winds 85
5.4.2 Scaling relations involving $V_{\rm out}$ 88
5.4.3 Scaling relations involving $\dot{M}_{\rm out}$ 89
5.4.4 Scaling relations on loading factor η 92
5.5 What mechanisms drive galactic winds? 94

In this chapter, we combine our two samples (SIMPLE and MEGAFLOW) to characterize galactic winds as a function of galaxy properties. In section 5.1, we present the main properties of all the galaxies in the two samples and compare them to the general underlying galaxy population. In section 5.2, we investigate the spatial extent of galactic winds. In section 5.3, we investigate whether galactic wind material (traced by low-ionization lines) escape the gravitational potential wells of the host. In section 5.4, we investigate relations, if any, between galactic winds and galaxy properties. Finally, in section 5.5, we conclude on mechanisms that drive galactic outflows.

5.1 Basic properties of the sampled galaxies

In this section, we present some basic properties of our sample galaxies to be compared with the general galaxy population. Star-forming galaxies are known to follow fundamental scaling relations such as the SFR-$M_\star$ main-sequence (e.g. Tacconi et al., 2013) and the $M_\star$-$V_{\rm max}$ or Tully-Fisher (TF) relation (Tully & Fisher, 1977; Miller et al., 2011, 2014; Vergani et al., 2012; Simons et al., 2015, to cite a few). Rotational velocity, dispersion velocity, stellar mass, SFR and redshift are fundamental galaxy properties.

5.1.1 Galaxy redshift distribution

We first need to see where our galaxies are located in look-back-time, i.e. in redshift space. Figure 5.1 shows the redshift distribution of both surveys.

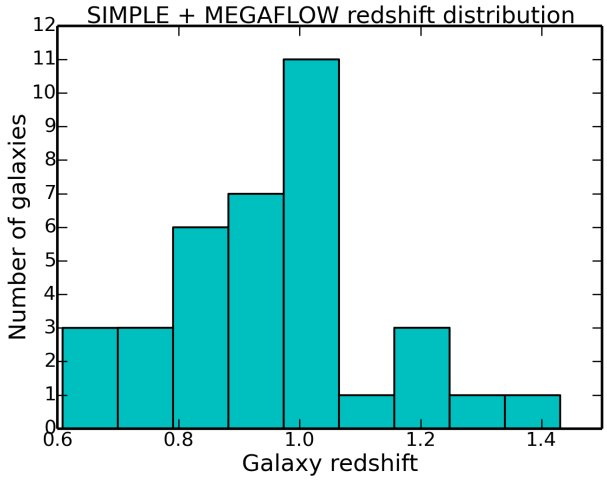

Figure 5.1: Redshift distribution of the 36 galaxies from SIMPLE and MEGAFLOW.

This distribution clearly peaks around $z \sim 1$ with a tail toward lower redshifts but with a few galaxies only extending up to $z \sim 1.4$, reflecting our selection of Mg II absorbers. This figure shows that our sample is representative of galaxies forming stars at around the peak of the cosmic star-formation density, which occurs at $z \approx 1.5$ (Lilly et al., 1996; Madau et al., 1996; Behroozi et al., 2013a).

5.1.2 Galaxy stellar mass measurement

In order to place our sample onto the SFR$-M_\star$ diagram, the two fundamental properties for star-forming galaxies are their SFRs and stellar masses. Indeed, whether our galaxies (selected from the gaseous halo properties via our Mg II criteria) lie on, above or below, the main sequence will shed light on the connection between the circum-galactic medium properties and the star-formation activity. For instance, are galaxies producing winds starbursting, i.e. with a high SFR by surface area $\Sigma_{\rm SFR}$ and above the main-sequence?

In order to address these questions, we thus need SFR and stellar mass measurements. Contrary to the SFR, which can be derived directly from our data using the Hα or [O II] luminosities (see discussion in section § 4.1.1.), the stellar masses cannot be measured directly as our IFU observations are typically too shallow to detect the stellar continuum. Hence, we need an indirect indicator of galaxy (stellar) mass and the kinematics properties (such as the rotational maximum velocity) of our galaxies (see § 2.1.4 for more details) can be used to this purpose.

Indeed, the kinematics properties of galaxies tightly correlate with their stellar mass as demonstrated by the existence of the TF scaling relation (e.g. Miller et al., 2011, 2014; Simons et al., 2015; Contini et al., 2016). The TF relation, traditionally between $M_\star$ and $V_{\rm max}$ is, however, valid only for galaxies that are rotation-dominated ($V/\sigma > 1$). The galaxies in our samples are mostly rotation-dominated, but Figure 5.2 shows that about 10 % are dispersion-dominated.

As described in § 1.2.3, the S_K factor should be a better mass estimator for our galaxies as it includes the dispersion velocity (disordered motion) contribution. Looking at the V/σ distribution of our galaxies we see that about 50% have $V/\sigma < 5$. This motivates us to include disordered motions in estimating our galaxy dynamical masses. For disk galaxies ($V/\sigma > 1$) with exponential $M_\star$ profiles, an approximation of $K = 1/2$ or $K = 1/3$ is adopted by Kassin et al. (2007). Moreover, as argued by Weiner et al. (2006), real galaxies at, or beyond, the peak of baryonic contribution to the rotation curve have $\alpha = 2 - 3$ (if we assume that $\sigma = V/\alpha$) for a spheric mass distribution, and thus adopting $K = 1/3 - 1/2$ is reasonable.

Because, most of the literature on S_K (as in Kassin et al. (2007)) use kinematics measurements from long-slit spectroscopy, where the slit could be mis-aligned with the galaxy kinematic major-axis, we choose to calibrate the S_K-$M_\star$ relation on a

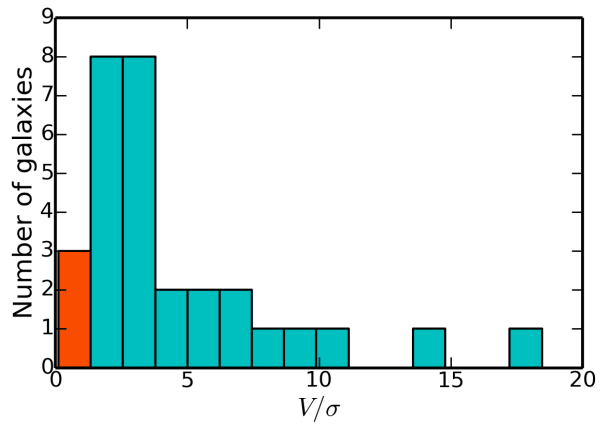

Figure 5.2: V/σ distribution of all the galaxies from both surveys. Orange colored bar represents dispersion-dominated galaxies ($V/\sigma < 1$).

sample observed with an IFU instrument. To date, the deepest MUSE field with the most exquisite kinematic data-set is the Hubble-Deep-Field South (HDFS; Bacon et al., 2015). Contini et al. (2016) presented the kinematic analysis of that sample, extending the TF relation to the low mass regime $M_\star = 10^8$-10^9, and we choose to use this sample as reference. In addition, we used the galaxies from SINS (Cresci et al., 2009) and MASSIV (Epinat et al., 2009; Contini et al., 2012) surveys to sample the high-mass regime as well. Figure 5.3 shows the correlation between $M_\star$ and $S_{0.5}$ for these samples. A fit of these data yields the relation:

$$M_\star \propto S_{0.5}^b \tag{5.1}$$

where $b = 4.75 \pm 0.39$. The fitted coefficients are estimated from the orthogonal distance regression (ODR) module of scipy taking into account the errors in $S_{0.5}$ and $M_\star$ and are shown in Figure 5.3. This dynamical estimator $S_{0.5}$ together with Equation 5.1 yield estimate of stellar masses of our galaxies.

For a rotation-dominated galaxy, the dynamical mass of the galaxy, inside a radius r, $M_{\rm dyn}(r)$ is proportional to $V^2 \times r$:

$$M_{\rm dyn}(r) = \frac{V^2 \times r}{G} \propto V^2 \times r \tag{5.2}$$

where V is the rotational velocity of the galaxy and G is the gravitational constant. As mentioned before, our galaxies have non-negligible dispersion velocities

and we therefore use the $S_{0.5}$ parameter. The dynamical mass of our galaxies becomes:

$$M_{\rm dyn}(r) \propto S_{0.5}^2 \times r \tag{5.3}$$

The surface density is defined by:

$$\Sigma M_{\rm dyn}(r) = \frac{M_{\rm dyn}(r)}{\pi \times r^2} \tag{5.4}$$

thus:

$$\Sigma M_{\rm dyn}(r) \propto \frac{S_{0.5}^2 \times r}{\pi \times r^2} \propto \frac{S_{0.5}^2 \times r}{r^2} \tag{5.5}$$

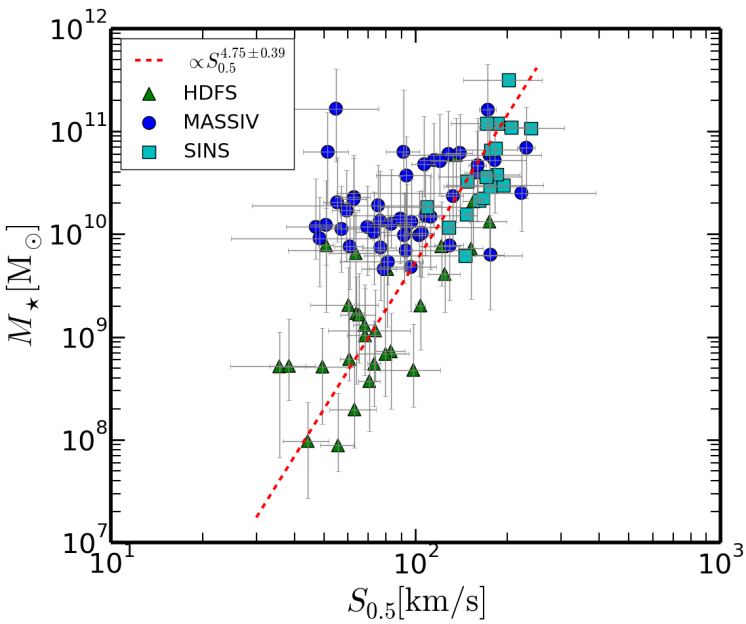

Figure 5.3: Galaxy stellar mass as a function of the $S_{0.5}$ parameter for HDFS, SINS and MASSIV data. The dashed red line represent a fit with coefficients shown in the legend.

Figure 5.4 shows SFR as a function of the galaxy stellar mass $M_\star$ (bottom x-axis) and $S_{0.5}$ (top x-axis) from Eq. 5.1. We added galaxies from Hubble Deep Field South (HDFS) (Contini et al., 2016) to better see where our galaxies are placed in a larger mass/SFR range. We can see on this figure that most of our galaxies have a stellar mass larger than 10^9M$_\odot$. This is not surprising as all our fields only have one or two hours exposure time (compared to 27 hours for HDFS) and thus only

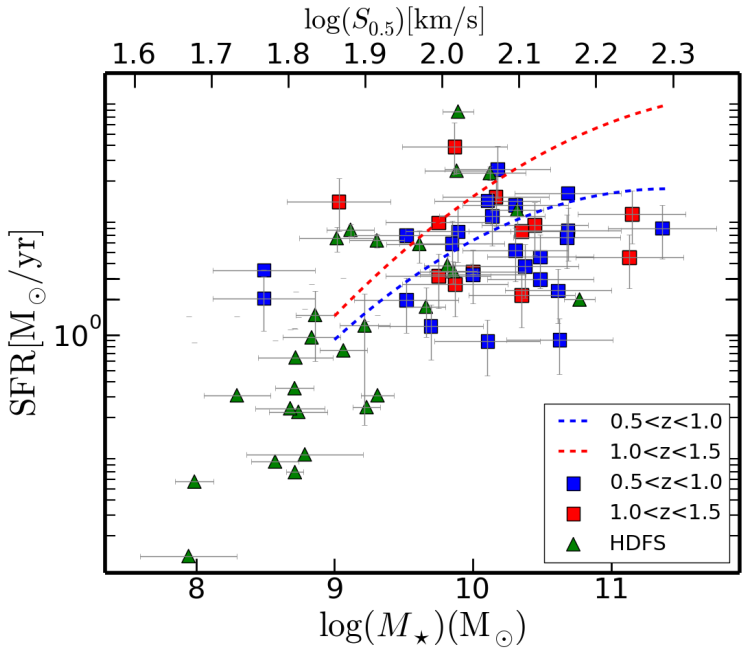

Figure 5.4: Star formation rate as a function of galaxy stellar mass (bottom x-axis) and $S_{0.5}$ (top x-axis) for our surveys. MUSE-HDFS observation from Contini et al. (2016) has been added in order to place our survey in a more general context. Galaxies with $1.0 < z < 1.5$ are represented in red for our surveys. The two dashed lines represent the empirical relations between SFR and stellar mass for different redshifts between $0.5 < z < 1.5$ from Whitaker et al. (2014).

bright/luminous galaxies (and thus massive) are detected.

We note also that above a stellar mass of $\sim 10^{10}$M$_\odot$, our galaxies do not follow the "main-sequence" relations calibrated at different redshifts (dashed curves from Whitaker et al. (2014)). Our galaxies mostly have a lower SFR or/and a larger stellar mass. These differences may come from two major points. We estimate the SFR from the galaxy emission lines (Hα or [O II]) compared to most of other studies which estimate their SFRs from SED fitting. This may lead to biases in our SFR estimates. The other point concerns the stellar mass estimations. To compute the galaxy stellar mass, we use the $S_{0.5}$ which is a combination of rotational and dispersion velocities whereas, as for SFR, $M_\star$ is usually estimated from SED fitting. Because we are using assumptions which include large uncertainties, we should note that derived stellar masses for our galaxies are mostly indicative. However, we can argue that, except for two cases, our galaxies are not starbursts as they seem to land below the galaxy "main sequence". Our galaxies have, on average, low SFRs compared to galaxies with similar stellar masses.

We showed that our galaxies are not starburst and that they are estimated to have stellar masses between $10^{8.5}$ and $10^{11.5}$. This thesis aims to answer several questions about galactic winds. Based on detection, azimuthal angles and impact parameters, we can now answer the first question which is: how far do winds go?

5.2 How far do winds go?

In order to address this question, we need to select only galaxy-quasar pairs with suitable geometrical configuration for wind study (see § 2.1.3 for more details). Figure 5.5 shows the distribution of azimuthal angles for both SIMPLE and MEGAFLOW surveys. We can clearly see the bimodal distribution between inflow-pairs ($\alpha < 40°$) and wind-pairs ($\alpha > 55°$). Because we select Mg II absorption in quasar spectra, it is intuitive to have this kind of distribution but this also indicates that the surrounding gas of galaxies is predominantly located either along the galaxy major or minor axes. Indeed, because outflowing (inflowing) gas is likely to be ejected (accreted) along the minor (major) axis of the galaxy, galaxy-quasar pairs are likely to have azimuthal angles $> 55°$ ($< 40°$). Hence, we selected our quasar fields from Mg II absorption lines in quasar spectra, so a selection effect on azimuthal angle exists. In total, we have 16 wind-pairs out of 30 galaxy quasar pairs (≈50%).

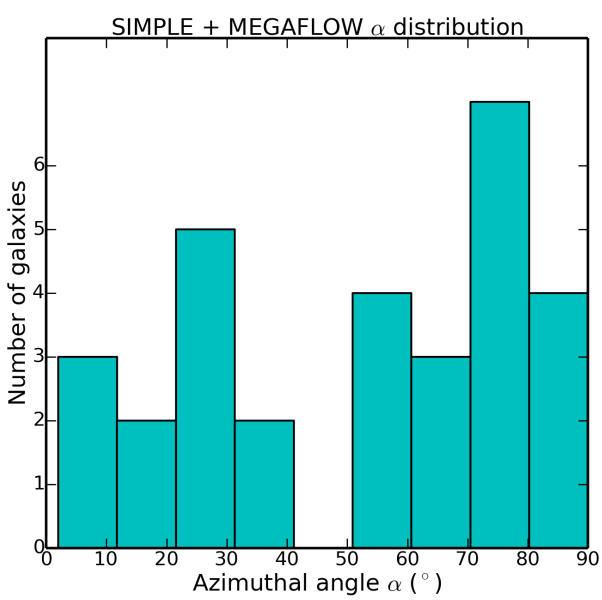

Figure 5.5: Azimuthal angle distribution of all the galaxies from SIMPLE and MEGAFLOW. We note the bimodal distribution of the whole survey.

If we take all the wind-pairs, we can investigate the behavior of the REW as a function of impact parameter b like in Figure 2.3. Figure 5.6 shows the Mg II REW as a function of impact parameter for all the wind-pairs of both our surveys (SIMPLE and MEGAFLOW). We can see a fit of these data showing that the anti-correlation between these two parameters changes from $W_r^{\lambda 2796} \propto b^{-1}$ to $W_r^{\lambda 2796} \propto b^{-0.5}$. Because of the selection we make on the REW ($W_r^{\lambda 2796} > 0.8$ Å), the fit could be biased since more points could be missing at lower REW.

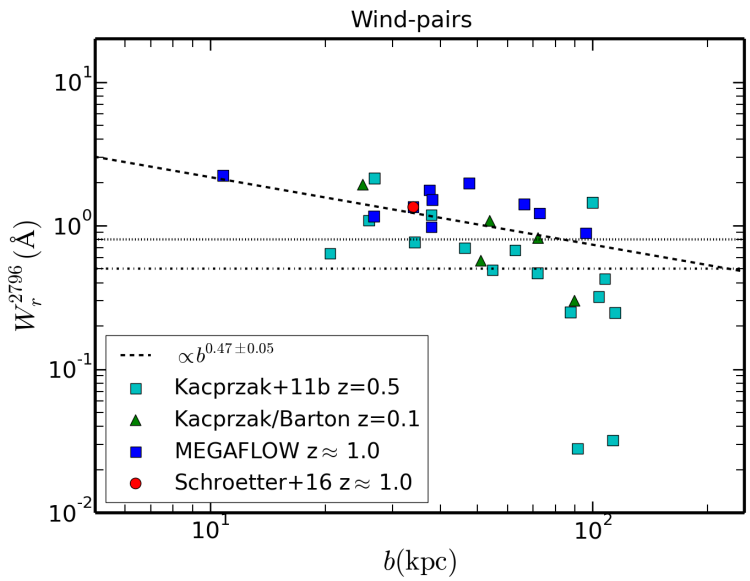

Figure 5.6: Mg II (λ2796) rest equivalent width as a function of impact parameter b for galaxy-quasar pairs classified as wind-pairs. Horizontal dashed black lines shows the $W_r^{\lambda 2796} > 0.5$Å and $W_r^{\lambda 2796} > 0.8$Å selection criteria. The thick black dashed line represent a fit to the data. Fitting coefficients are shown in the legend. Errors on $W_r^{\lambda 2796}$ are typically $\sim 10^{-3}$ Å and ~ 0.5 kpc for b.

In addition to the previous Figure 5.6, we can investigate the same relation for inflow-pairs. Figure 5.7 shows the Mg II REW as a function of impact parameter for all the inflow-pairs (left) and Mg II REW corrected for the LOS path length X as in Bouché et al. (2012). This correction lowers the scatter as it corrects for the galaxy inclination. Indeed, the equivalent width is related to the path length X intercepted by the quasar LOS. This path length is $X \propto 1/\cos(i)$ where i is the galaxy inclination. The normalization of this correction is taken to be 0.5 (see the appendix in Law et al. (2009)). Again, this figure shows an anti-correlation between these two parameters for inflow-pairs. The fit indicates that $W_r^{\lambda 2796} \propto b^{-1}$ for inflow pairs. The difference between the anti-correlations $W_r^{\lambda 2796} \propto b^{-0.5}$ for wind-pairs and $W_r^{\lambda 2796} \propto b^{-1}$ for inflow-pairs could lead to the conclusion that the outflowing gas

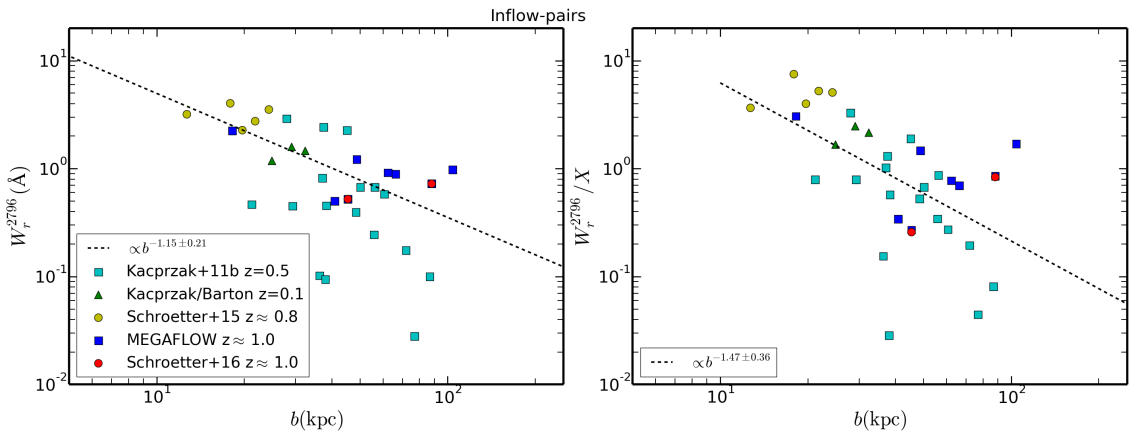

Figure 5.7: *Left:* Mg II (λ2796) rest equivalent width as a function of impact parameter b for galaxy-quasar pairs classified as inflow-pairs. *Right:* same as left panel with the $W_r^{\lambda 2796}$ normalized by the disk path length $X = X_0/\cos(i)$ where i is the galaxy inclination and X_0 is a normalization factor, taken as $X_0 = \cos(60°)$. The thick black dashed line represent a fit to the data. Fitting coefficients are shown in the legend. Errors on $W_r^{\lambda 2796}$ are typically $\sim 10^{-3}$ Å and ~ 0.5 kpc for b.

has larger REW than the inflowing gas at the same distance (i.e. the slope is flatter for wind-pairs). This could support the idea that largest REW are likely to come from outflowing materials.

So far, we can argue that galactic outflows can travel at least up to 80−100 kpc away from their host galaxy leading to the following question: are galactic winds able to escape the gravitational well of their host galaxy?

5.3 Do winds escape?

To estimate the escape velocity of our galaxies, we used the escape velocity relation for an isothermal sphere given by the following Eq. 5.6 (Veilleux et al., 2005b):

$$V_{\rm esc} = V_{\rm max} \times \sqrt{2\left[1 + \ln\left(\frac{R_{\rm vir}}{r}\right)\right]} \tag{5.6}$$

where $V_{\rm max}$ is the maximum rotation velocity of the galaxy and $R_{\rm vir}$ is the virial radius. The virial radius is approximately $R_{\rm vir} \approx V_{\rm max}/10H(z)$ where $H(z)$ is the Hubble constant at redshift z.

Figure 5.8 shows the ratio between the outflow velocity and the escape velocity ($V_{\rm out}/V_{\rm esc}$) as a function of $S_{0.5}$[1] (and thus the galaxy stellar mass on top x-axis).

[1]this parameter is described in § 5.1

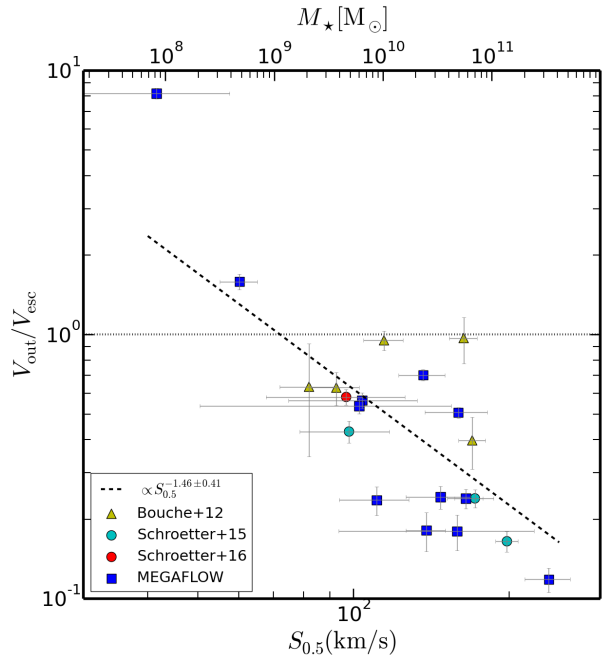

Figure 5.8: $V_{\rm out}/V_{\rm esc}$ as a function of $S_{0.5}$ (bottom x-axis) and $M_\star$ (top x-axis). Yellow triangles are from Bouché et al. (2012), cyan and red circles are from Schroetter et al. (2015) and Schroetter et al. (2016) respectively. The horizontal line corresponds to $V_{\rm out} = V_{\rm esc}$. The dashed black line corresponds to a fit with coefficients shown in the legend.

Different samples using the background quasar technique are shown in this figure. Yellow triangles are from Bouché et al. (2012) (survey from a combination of LRIS and SDSS data), cyan and red circles are from Schroetter et al. (2015) (SIMPLE) and Schroetter et al. (2016) (the only wind-pair within 2 fields of MEGAFLOW) respectively. Again, blue squares are from MEGAFLOW (not published at the time of writing) survey. We can see that in two cases only, the gas is able to reach the escape velocity of the galaxy. These two points are for the lowest mass galaxies. The ability of the gas to leave the gravitational well of the galaxy is, as one can expect, proportional to $S_{0.5}$ (see the fit coefficients in the figure). It is thus easier for an outflow from a low-mass galaxy ($M_\star \leq 10^9$ M$_\odot$ at redshift $z = 1$) to escape the gravitational well of the host, whereas outflows from high-mass galaxies have difficulties leaving their host as the well is too deep.

One of the most important question about galactic winds is what drives these outflows out of the galactic disk. To answer this question, one need to first look for scaling relations between outflow and galaxy properties.

5.4 Wind scaling relations

This section is an attempt to look for scaling relations between properties of galactic winds and host galaxies. Because galaxy properties like SFR and mass appear to be directly linked with properties of galactic winds, we will investigate the relation, if any, between outflow properties like their velocity $V_{\rm out}$, their ejected mass rate $\dot{M}_{\rm out}$ and their loading factors η with these main galaxy properties. We need to keep in mind that our sample is limited in term of wind case number. However, this unique sample has a real interest as it probes a large range of galaxy stellar masses (from $\sim 10^{8.5}$M$_\odot$ to $\sim 10^{11.5}$M$_\odot$). Before going further in investigating wind relations, we first need to describe previous studies on galactic winds that we will use for comparison.

5.4.1 Previous studies on galactic winds

As in § 1.3, we will briefly describe two previous galactic outflow studies from Arribas et al. (2014) and Heckman et al. (2015). We choose to compare our results with these two studies for several reasons. As we can see in Table 5.1, (1) these two studies focus on low-redshift galaxies ($z < 0.2$) and are thus complementary to our $0.6 < z < 1.4$ sample. (2) The stellar mass range probed by these studies is similar to ours and (3) their galaxies are mostly starbursts, and thus complementary to our more "normal" star-forming galaxies. In addition, these two papers are using two different methods to derive outflow properties: from absorption and emission lines (as described in § 1.3). We however choose to include the results from Heckman et al. (2015) only. Indeed, their method to derive outflow properties is similar to ours as they use the absorptions produced by outflows. Finally, Heckman et al. (2015) sample includes both SFGs and starbursts, which allow for a comparison with our "normal" SFGs.

Because Arribas et al. (2014) use the emission line method to derive outflow properties, we decided to exclude their sample of the comparison. Indeed, because their method is completely different from ours, systematic biases can exist.

Table 5.1: Summary of other wind studies

Paper	$N_{\rm gal}$	$z_{\rm gal}$	SFRs	Galaxy type	$V_{\rm out}$	$\log(M_\star)$
(1)	(2)	(3)	(4)	(5)	(6)	(7)
A14	58	$0.01 < z < 0.2$	Hα	U/LIRGs	Emission	$9.5 - 11.8$
H15	40	$z < 0.2$	SED	SFGs and Starbursts	Absorption	$7 - 11$
Our sample	16	$0.6 < z < 1.4$	Hα and [O II]	SFGs	Absorption	$8.5 - 11.5$

(1) Study, A14 for Arribas et al. (2014) and H15 for Heckman et al. (2015); (2) Sample size. (3) Redshift range; (4) Method to estimate galaxy SFR; (5) Type of galaxies; (6) Method to estimate $V_{\rm out}$, "emission" stands for broad blue-shifted emission lines, "absorption" stands for absorption lines in the galaxy spectrum; (7) Galaxies stellar mass range.

Even if we do not include galaxies from Arribas et al. (2014), we will still consider the relations they found to see if there are significant differences between SFGs and U/LIRGs outflow properties. We briefly described the results of Arribas et al. (2014) in § 1.3 but give here a more detailed description.

Work of Arribas et al. (2014) summary

Arribas et al. (2014) focus on 58 local (low-z) (U/LIRGs) using the Visible Multi Object Spectrograph (VIMOS, Le Fèvre et al., 2003) and INTEGRAL (Arribas et al., 1998) instruments. Their galaxies have redshifts between $z \approx 0.01$ and $z \approx 0.2$, and dynamical masses between $10^{9.5}\mathrm{M}_\odot$ and $10^{11.8}\mathrm{M}_\odot$. They derived SFRs from Hα fluxes using Kennicutt (1998) calibration adapted for Chabrier (2003) IMF. In their work, they do not use absorption lines in galaxy spectra but rather study outflows using the blue-shifted broad component of several emission lines like Hα and [N II]. Outflow velocities are derived by fitting a Gaussian profile to this blue-shifted broad component (see Figure 1.15). They define the outflow velocity as follows:

$$V_{\mathrm{out}} = |\Delta V - \mathrm{FWHM}/2| \tag{5.7}$$

where ΔV is the shift in velocities of the broad component with respect to the systemic velocity and FWHM is the full width half maximum of this blue-shifted broad component.

As mentioned in § 1.3.2, their main result is that the outflow velocity correlates with the galaxy SFR ($V_{\mathrm{out}} \propto \mathrm{SFR}^{0.24}$). They also find that the ejected mass rate $\dot{M}_{\mathrm{out}}$ correlates with SFR. For non-AGN-LIRGs, they derive $\dot{M}_{\mathrm{out}} \propto \mathrm{SFR}^{1.11}$.

Work of Heckman et al. (2015) summary

In the study of Heckman et al. (2015), they combined two samples of low-z starburst galaxies: 19 from FUSE and 21 from COS. Their galaxies have redshifts $z < 0.2$ and stellar masses between $10^7\mathrm{M}_\odot$ and $10^{11}\mathrm{M}_\odot$. Their stellar masses were estimated by SED fitting using near-IR or multiband optical photometry. SFRs were derived using a combination of *GALEX* FUV, IRAS and *Herschel* far-IR, and *WISE* and *Spitzer* mid-IR photometry. In all their cases, a Kroupa/Chabrier (Kroupa, 2000; Chabrier, 2003) IMF was adopted to estimate masses and SFRs. As mentioned previously, these galaxies are starburst galaxies, which means that they have high SFRs. In order to derive outflow velocities, they used the absorption lines produced by the outflowing gas but without stacking different galaxy spectra as they have enough SNR to analyze almost each galaxy individually. A representation of the two techniques (wind absorption in galaxy spectrum and absorption using background quasar) is represented in Figure 5.9. In this figure, we mainly show the difference

between absorption profiles depending on used LOS. Because of their technique, they have a selection effect on galaxy inclination. Indeed, in order to detect absorption, the outflowing gas must be between the galaxy and the observer. Because the galaxy is ejecting the gas perpendicular to its plane, galaxies must be roughly face-on and therefore have low inclinations. As a reminder of § 1.3.3, to estimate V_{out}, they used the value corresponding to 80% of the absorption profile in order to avoid instrumental noise seen in the galaxy continuum.

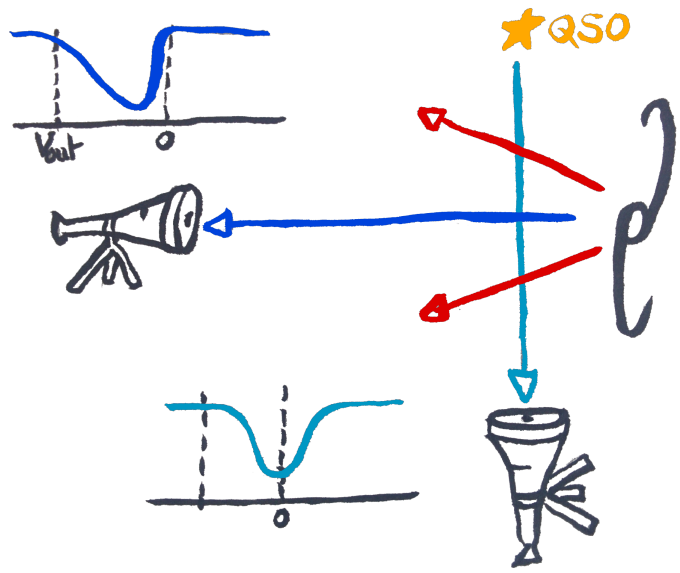

Figure 5.9: Scheme of the two main technique to study outflowing materials in absorption. On the right part of this scheme, we can see a star-forming galaxy (in black) ejecting gas in a cone (represented by the two red arrows). The horizontal dark blue arrow represents the LOS as used in Heckman et al. (2015). In this LOS type observation, the galaxy is face-on and the outflowing gas creates blue-shifted absorption lines in the galaxy spectrum. This absorption profile is represented on top of the telescope on the left in dark blue. We can see that this absorption profile is asymmetric, only blue-shifted (on the left of the systemic velocity, represented by the 0 vertical dashed line) and with an outflow velocity corresponding to where the absorption crosses the galaxy continuum. On the right part of this figure, the light blue vertical arrow represent a quasar (the yellow star labeled "QSO") LOS crossing the outflowing material of the same galaxy. This configuration represent our background quasar technique and the galaxy is seen as edge-on. The projected velocities onto this LOS creates an absorption profile represented in light blue at the bottom of the figure. This absorption profile is symmetric and centered on the galaxy systemic velocity.

Concerning the estimate of V_{out}, we tried building a wind model with the configuration of a galaxy with 0° inclination and a LOS crossing this galaxy (impact

parameter $b = 0$ kpc). With a constant outflow velocity, the simulated absorption profile has an inverse asymmetry compared to what we observe. However, since the LOS is crossing all the outflowing gas from the galaxy, the accelerated phase of the gas is also probed. We thus simulated an absorption profile using an accelerated wind model like in Schroetter et al. (2015). This simulated profile reproduces the right asymmetry. Hence, the input outflow velocity is indeed found to be where the absorption crosses the continuum. For this reason, we find it relevant to use results from Heckman et al. (2015) as their outflow velocities seem not to be over or under-estimated.

From their outflow velocities estimates, they derive the ejected mass rate using the following equation:

$$\dot{M}_{\rm out} = \Omega \times N_{\rm out} \times < m > \times V_{\rm out} \times r_{\rm out} \tag{5.8}$$

where Ω is the solid angle occupied by the outflow $\Omega = 4\pi$, $N_{\rm out}$ is the total column density of the outflow along the LOS, $< m >$ is the mean mass per particle and $r_{\rm out}$ is the characteristic radius of the location of the absorbing material in the outflow (corresponding to the impact parameter, and taken to be 5 kpc).

In their paper, Heckman et al. (2015) mentioned that their outflow rates are uncertain and must be taken as roughly indicative. They found that the outflow velocity correlates weakly with the galaxy stellar mass but strongly with SFR and $\Sigma_{\rm SFR}$. They also find that the loading factor is not correlated with the outflow velocity and conclude that outflowing gas should be accelerated by combined forces of gravity and momentum flux from starburst.

Now that we rapidly described two recent studies on galactic winds, we can begin our investigation on wind relations adding observations from Heckman et al. (2015).

5.4.2 Scaling relations involving $V_{\rm out}$

The most direct property we can derive for galactic outflows is their velocity $V_{\rm out}$. Indeed, for this parameter, we do not necessary need a background quasar as many previous studies derived outflow velocity with enough accuracy (e.g Martin, 2005; Genzel et al., 2011a; Newman et al., 2012; Arribas et al., 2014; Heckman et al., 2015, to cite a few).

These studies found a significant, but scattered, correlation between the outflow velocity and galaxy SFRs at low redshift (Heckman et al., 2000; Martin, 2005; Rupke et al., 2005; Martin et al., 2012; Arribas et al., 2014; Heckman et al., 2015). Martin (2005) even defined an upper limit of $V_{\rm out}$ as a function of SFR. This limit corresponds to the upper envelop of the outflow velocity distribution at a given SFR.

Figure 5.10 shows the outflow velocity ($V_{\rm out}$) as a function of SFR for MEGAFLOW and SIMPLE as well as observations from Bouché et al. (2012) and Heckman et al. (2015)[2]. We can see on this figure that our observations fill the gap of outflowing velocities between 50 km s^{-1} and 200 km s^{-1}. The positive correlation found by Heckman et al. (2015) is thus confirmed, even with the large scatter. For a star-forming galaxy, kinetic and momentum energy are injected when supernovae explode. These injected energies should contribute to the acceleration of the outflowing gas and thus allow it to have a higher outflow velocity. This result suggests that a galaxy with high SFR is likely to have outflows with higher velocity than a galaxy with lower SFR. In addition, on this figure, the dashed black line represents the upper velocity distribution found by Martin (2005). Except for a few objects from Heckman et al. (2015), we clearly see that most of galaxies are above the limit defined by Martin (2005). It is worth mentioning that Martin (2005) used only few galaxies to derive this upper limit. However, they found that $V_{\rm out}$ increases with SFR and their upper limit seems to be in agreement with low-SFR galaxies but is clearly under-estimating $V_{\rm out}$ for SFRs$\geq 4-5$ M$_\odot$ yr^{-1}. From SFR$\geq 4-5$ M$_\odot$ yr^{-1}, it appears that their is an increase of the slope between $V_{\rm out}$ and SFR.

Concerning the correlation between $V_{\rm out}$ and the SFR by surface area ($\Sigma_{\rm SFR}$), there has been disagreements about its existence (e.g. Chen et al., 2010; Rubin et al., 2014) but galaxies from these studies only have small range of SFRs. As mentioned before, Heckman et al. (2015) found a strong correlation between the outflow velocity and $\Sigma_{\rm SFR}$. Adding our observations to their sample we do not find such a correlation.

The next obvious step is to investigate whether the outflow velocity depends on the host galaxy mass. Following the SFR-$M_\star$ relation and the tendency of $V_{\rm out}$ to increase with the host galaxy star formation rate, we could naively expect that the outflow velocity correlates also with the host galaxy mass. However, a more massive galaxy has a deeper gravitational well, and thus it is more difficult for a gas to accelerate. We investigated the relation between $V_{\rm out}$ and $S_{0.5}$ ($M_{\rm dyn}(r)$ and $\Sigma M_{\rm dyn}(r)$) but found no correlation between these properties.

To summarize, we confirm that $V_{\rm out}$ correlates with the SFR but not with $\Sigma_{\rm SFR}$.

5.4.3 Scaling relations involving $\dot{M}_{\rm out}$

Other wind properties are derived from outflow velocities, namely the outflow rate and the loading factor. The ejected mass rate usually has lots of uncertainties as one need to make assumption on the location of the probed outflowing gas.

From the previous result on the relation between the outflow velocity and SFR, $\dot{M}_{\rm out}$ being directly derived from $V_{\rm out}$, it is interesting to investigate whether the

[2]We note that we do not include observations from other previously cited paper as they either use stacked galaxy spectra and/or their galaxies are only starbursts.

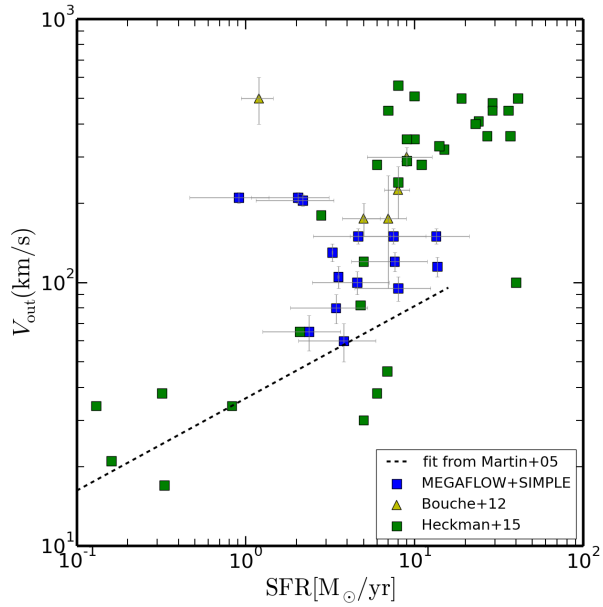

Figure 5.10: $V_{\rm out}$ as a function of SFR for both surveys (MEGAFLOW and SIMPLE) as well as observations from Bouché et al. (2012) and Heckman et al. (2015). The dashed black line show a fit ($\log V = (0.35 \pm 0.06)\log(\mathrm{SFR}) + (1.56 \pm 0.13)$) from Martin (2005). Errors on Heckman et al. (2015) observations are 0.2 dex for SFR and 0.05 dex for $V_{\rm out}$.

ejected mass rate correlates with the galaxy SFR as well. Hopkins et al. (2012) predicted a dependency of the ejected mass rate $\dot{M}_{\rm out} \propto \mathrm{SFR}^{0.7}$ whereas Arribas et al. (2014) derived a stepper index $\dot{M}_{\rm out} \propto \mathrm{SFR}^{1.11}$. Even if the uncertainty on the ejected mass rate is larger without knowing exactly where we trace the outflowing gas, we choose to continue adding observations from Heckman et al. (2015). We recall here that they used Equation 5.8 to estimate the ejected mass rate assuming an impact parameter of 5 kpc for their galaxies.

Figure 5.11 represents the ejected mass rate ($\dot{M}_{\rm out}$) as a function of SFR (left panel), and $\Sigma_{\rm SFR}$ (right panel). Not surprisingly, we see a strong correlation between the outflow mass rate and the SFR, hence, this correlation has a scatter much lower than the one between the outflow velocity and SFR. Because the SFR is directly linked with the amount of ejected mass by supernova explosions, it is then intuitive that SFR correlates with $\dot{M}_{\rm out}$. Like in Heckman et al. (2015), we added a line corresponding to a constant loading factor $\eta = 2$ (dotted blue line) showing that a constant loading factor is consistent with the results. Because results from Heckman et al. (2015) are only indicative, we did not try to fit all the galaxies together. Both relations from Hopkins et al. (2012) and Arribas et al. (2014) are represented on left panel of this figure. We will see in § 5.4.4 that the prediction from Hopkins et al.

(2012) is in better agreement with the observations than Arribas et al. (2014) for SFGs.

The previous attempt to see a correlation between $V_{\rm out}$ and $\Sigma_{\rm SFR}$ failed. But, because SFR and $\dot{M}_{\rm out}$ are correlated, it is interesting to investigate whether the ejected mass rate depends on SFR by surface area. On right panel of Figure 5.11, we can see a weak correlation between the ejected mass rate and $\Sigma_{\rm SFR}$. We note that our galaxies allow to probe for low $\Sigma_{\rm SFR}$ and thus can confirm the (scattered) correlation between the two quantities. From this result, we can argue that mechanisms impacting the amount of ejected mass are acting more on local (SFR, $\Sigma_{\rm SFR}$) than global galaxy scales like their masses. Indeed, comparison between the ejected mass rate and the $S_{0.5}$ factor (and thus its stellar mass) show no obvious correlation. This would mean that a massive galaxy does not necessary eject more mass than a less massive one.

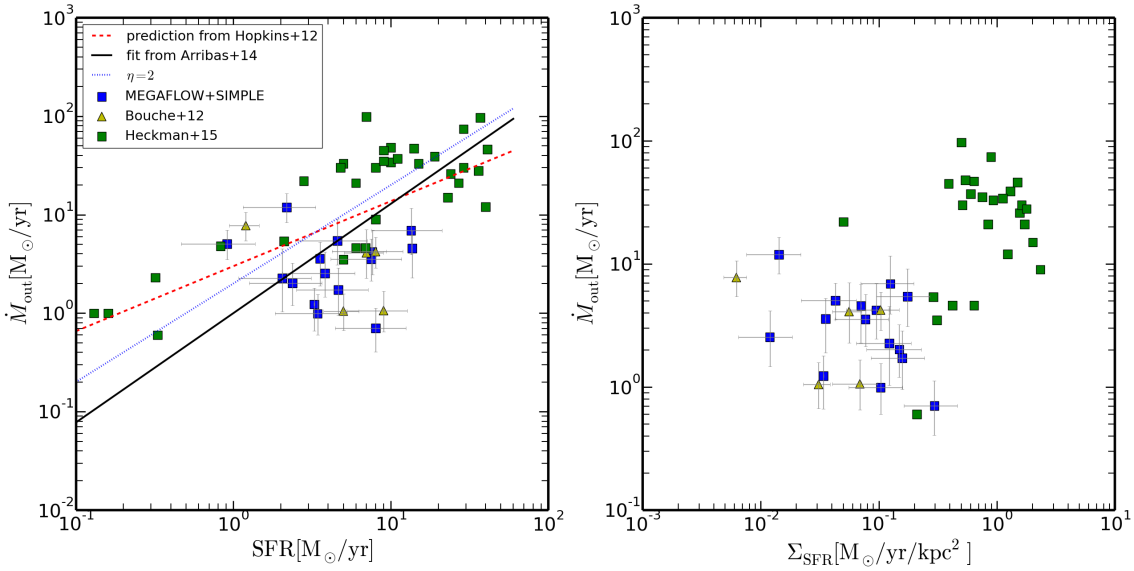

Figure 5.11: Ejected mass rate as a function of star formation rate (left) and star formation rate by surface area ($\Sigma_{\rm SFR}$, right) for both surveys (MEGAFLOW and SIMPLE) as well as observations from Bouché et al. (2012). On left panel, the dashed red line shows a prediction $\dot{M}_{\rm out} \propto {\rm SFR}^{0.7}$ from Hopkins et al. (2012) model. On left panel, the black line shows $\dot{M}_{\rm out} \propto {\rm SFR}^{1.11}$ from Arribas et al. (2014). the blue dotted line correspond to a loading factor ($\dot{M}_{\rm out}$/SFR) equals 2. Errors for Heckman et al. (2015) are 0.25 dex for $\dot{M}_{\rm out}$ and 0.2 dex for SFR and $\Sigma_{\rm SFR}$.

5.4.4 Scaling relations on loading factor η

The last but maybe the most important parameter concerning galactic outflows is the loading factor η. This loading factor is the ratio between the ejected mass rate $\dot{M}_{\rm out}$ and the SFR of the galaxy. This parameter is popular as it represents what fraction of gas, used in the formation of stars, is actually ejected out of the galactic disk.

We previously found that the ejected mass rate correlates with the galaxy SFR. If :

$$\dot{M}_{\rm out} \propto {\rm SFR}^{\alpha} \tag{5.9}$$

then

$$\eta = \frac{\dot{M}_{\rm out}}{\rm SFR} \propto {\rm SFR}^{\alpha-1} \tag{5.10}$$

Depending on the value of α in Equations 5.9 and 5.10, correlation between the mass loading factor and SFR can be positive ($\alpha > 1$), negative ($\alpha < 1$) or η can be constant ($\alpha = 1$). These three possibilities are represented by the curves in Figure 5.11 with $\alpha = 0.7$ (Hopkins et al., 2012), $\alpha = 1.11$ (Arribas et al., 2014) and $\alpha = 1$ (a constant loading factor $\eta = 2$).

Left panel of Figure 5.12 shows the mass loading factor as a function of SFR. We can see a scattered anti-correlation between these two properties. This means that $\eta \propto {\rm SFR}^{\alpha-1}$ with $\alpha < 1$. As on Figure 5.11, we added curves from Hopkins et al. (2012) and Arribas et al. (2014) (red dashed line and black line respectively). Because we found a negative correlation ($\alpha < 1$) between η and SFR, we can say that our observations are in good agreement with predictions from Hopkins et al. (2012). Hence, we can argue that there is an upper limit of $\alpha < 1$ for star-forming galaxies and thus $\eta \propto {\rm SFR}^{\beta}$ with $-1 < \beta < 0$. A direct consequence is that the correlation found by Arribas et al. (2014) does not apply for "normal" star-forming galaxies like ours but rather apply to extreme starbursts galaxies such as (U)LIRGs. Indeed, as mentioned in § 5.1.2, our galaxies tend to lie bellow the galaxy "main sequence". This result leads to the conclusion that galactic winds launched from "normal" star-forming galaxies have different properties than outflows from starbursts.

Because, like other wind properties, we want to know whether the mass loading factor depends on global or local galaxy properties, we investigate relations between the mass loading factor and SFR by surface area. Other wind studies like Genzel et al. (2011b), Newman et al. (2012) and Heckman et al. (2015) found that the loading factor is strongly correlated with $\Sigma_{\rm SFR}$. On right panel of Figure 5.12, we show the mass loading factor as a function of $\Sigma_{\rm SFR}$. Prediction and observations from Hopkins et al. (2012) and Arribas et al. (2014) are represented by red-dashed and black lines respectively. Restricting to loading factors from Heckman et al. (2015) only, there is a clear correlation with $\Sigma_{\rm SFR}$. However, our results clearly question

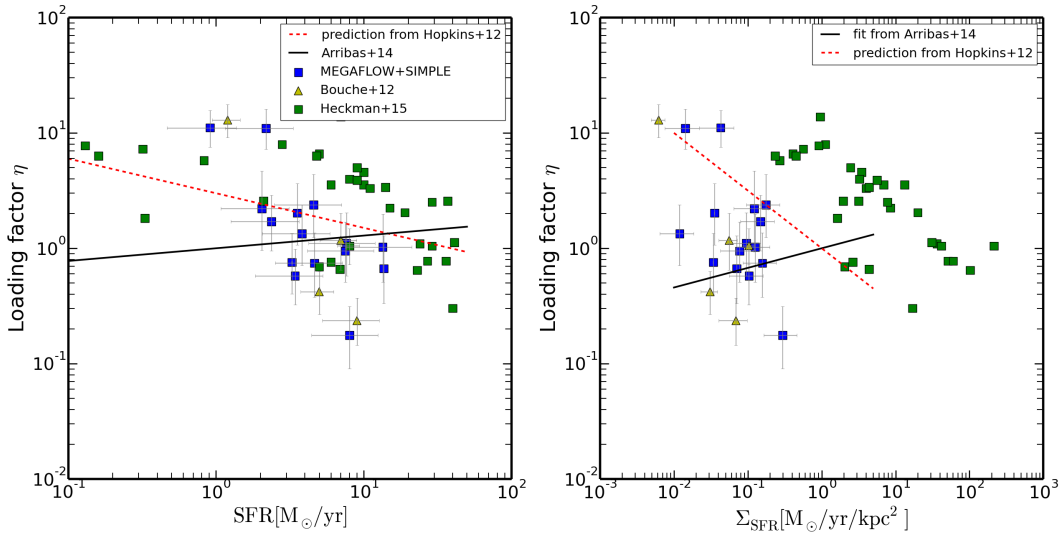

Figure 5.12: η as a function of SFR (left) and $\Sigma_{\rm SFR}$ (right) for both surveys (MEGAFLOW and SIMPLE) as well as observations from Bouché et al. (2012) and Heckman et al. (2015). On left panel, the dashed red line shows a fit $\eta \propto {\rm SFR}^{-0.3}$ from Hopkins et al. (2012) and the black line shows a fit $\eta \propto {\rm SFR}^{0.11}$ from Arribas et al. (2014). On right panel, the dashed red line shows a fit $\eta \propto \Sigma_{\rm SFR}^{-1/2}$ from Hopkins et al. (2012) and the black line shows a fit $\eta \propto \Sigma_{\rm SFR}^{0.17}$ from Arribas et al. (2014). Again, errors for Heckman et al. (2015) are 0.2 dex for SFR (and $\Sigma_{\rm SFR}$) and 0.45 dex for η.

this correlation. Thus, we can argue that, including "normal" SFGs to the extreme starbursts sample of Arribas et al. (2014), the mass loading factor does not correlate with $\Sigma_{\rm SFR}$.

It is also important to remind the reader that as mentioned in § 1.3, Arribas et al. (2014) and Newman et al. (2012) found that galaxies (low-z galaxies from Arribas et al. (2014) and high-z galaxies from Newman et al. (2012)) require a $\Sigma_{\rm SFR}$ larger than 1 ($\Sigma_{\rm SFR} > 1$) for launching strong outflows. This statement is not supported by our galaxies since all of them have winds and a $\Sigma_{\rm SFR}$ below 1.

Another aspect about the loading factor is its redshift dependency. Indeed, as mentioned in § 1.3, as there is a peak in star-formation density at redshift 2-3 (Lilly et al., 1996; Madau et al., 1996; Behroozi et al., 2013a), if η correlates with SFR (which appears to be the case), one can expect a correlation between η and redshift. We thus investigated on this relation but the loading factor does not appear to be redshift dependent (compared to Muratov et al. (2015)).

As a last investigation, we looked for a relation between η and the outflow velocity. We mentioned in § 1.3 that their is no reason for a galaxy to eject more gas if the outflow velocity is larger and their is indeed no correlation between the mass loading factor and the outflow velocity. This is in agreement with results from Heckman

et al. (2015) who find no correlation between η and $V_{\rm out}$.

5.5 What mechanisms drive galactic winds?

We will now try to answer the last and most important question of what mechanisms drive galactic winds out of the galaxy. There are two major mechanisms which could be responsible for driving materials out of the galaxy: energy-driven and momentum-driven.

The momentum-driven wind scenario considers that the two primary sources of momentum deposition in driving galactic winds are supernovae and radiation pressure from the central starburst (i.e. Murray et al., 2005). This model assumes that the wind speed scales as the galaxy velocity dispersion (e.g. Martin, 2005; Oppenheimer & Davé, 2006; Davé et al., 2011). This implies that the mass loading factor must be inversely proportional to the outflow velocity (Oppenheimer & Davé, 2008). In summary, momentum conservation implies $\eta \propto V_{\rm max}^{-1}$.

Energy-driven wind model assumes that when stars evolve, they put energy into the ISM. The amount of gas blown out of the disk is assumed to be proportional to the total energy given by supernovae and inversely proportional to the escape velocity squared. In energy-driven scenario, energy conservation implies $\eta \propto V_{\rm max}^{-2}$ (e.g. van den Bosch, 2001).

One of the most popular relation is the loading factor as a function of galaxy stellar mass. It is indeed crucial to look for dependences between these two properties if we want to step forward in understanding the role of galactic winds concerning the lack of observed baryons (see § 1.2.6). Figure 5.13 shows the mass loading factor as a function of galaxy maximum rotational velocity (bottom x-axis) and galaxy stellar mass (top x-axis). This figure is almost the same as Figure 5.14 but with added observations from Heckman et al. (2015) and without simulation predictions (apart from Hopkins et al. (2012)).

We find a weak correlation between η and $S_{0.5}$. This correlation is in good agreement with the prediction of Hopkins et al. (2012) where $\eta \propto S_{0.5}^{-1.2\pm0.2}$. However, we also show $\eta \propto V^{-2}$ (the black line) in order to see if we could disentangle between the two mechanisms which could explain what drives outflows (see above). We can see that due to the large scatter of our sample, it is not possible to conclude on which curve best fits the data.

As a final result, we need to compare our results with simulations like we did in Schroetter et al. (2015, 2016). We can now show the loading factor η as a function of galaxy halo mass. The results are shown in Figure 5.14.

On this Figure, the first thing to note is the number of gray squares, which correspond to galaxy-quasar pairs having an impact parameter larger than 60 kpc.

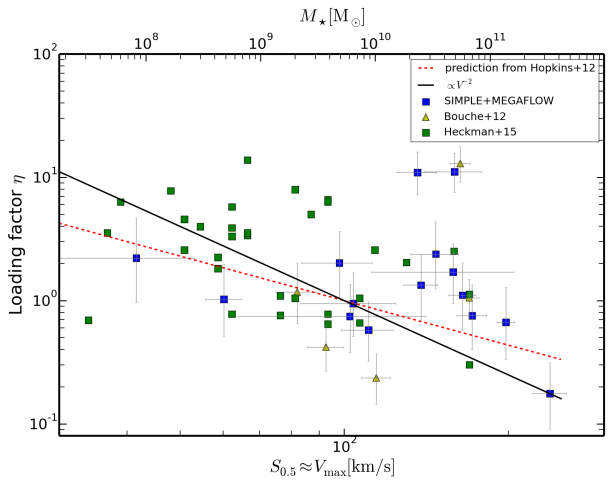

Figure 5.13: η as a function of $S_{0.5}$ for both surveys (MEGAFLOW and SIMPLE) as well as observations from Bouché et al. (2012) and Heckman et al. (2015). The dashed red line shows a fit $\eta \propto S_{0.5}^{-1.2}$ from Hopkins et al. (2012). The black line shows $\eta \propto V^{-2}$. Errors on Heckman et al. (2015) are 0.45 dex for η and 0.1 dex for $V_{\rm max}$.

But, since all these gray squares have large loading factors, this indicates that the ejected mass rate is larger than the SFR of the galaxy. This can mean that the outflowing gas probably quenched the SFR of the host galaxy. Indeed, we derive the SFR from the galaxy [O II] emission lines at the time we observe ($\sim$ 10Myrs). Because the distance b is large, the ejected gas needed a long time (several 100 Myrs) to get to the quasar LOS at an outflow velocity of $\sim$ 200 km s^{-1}. The SFR of the host galaxy was different at the time when the gas was ejected and if a galaxy eject gas, that means ejecting a part of the gas reservoir that could form stars and thus lower or even quench the SFR.

We can, however, focus on the blue squares which are close to unity. Loading factors of these wind pairs have their component on almost same time scales and are thus more comparative with simulations.

Among simulations represented on this figure, three of them clearly do not fit the data for low mass galaxies. Hence, they are roughly one order of magnitude above the observations. These three simulations are the ones from Okamoto et al. (2010); Puchwein & Springel (2013) and Vogelsberger et al. (2014). These curves correspond to loading factors applied in theoretical models and not empirical. In these simulations, they assume a similar wind modeling and try to fit the observed stellar mass function for low mass galaxies. They only assume energy-driven feedback and do not explore momentum-driven winds. In order to reproduce the baryonic mass distribution of galaxies, they need massive outflows. Considering observational

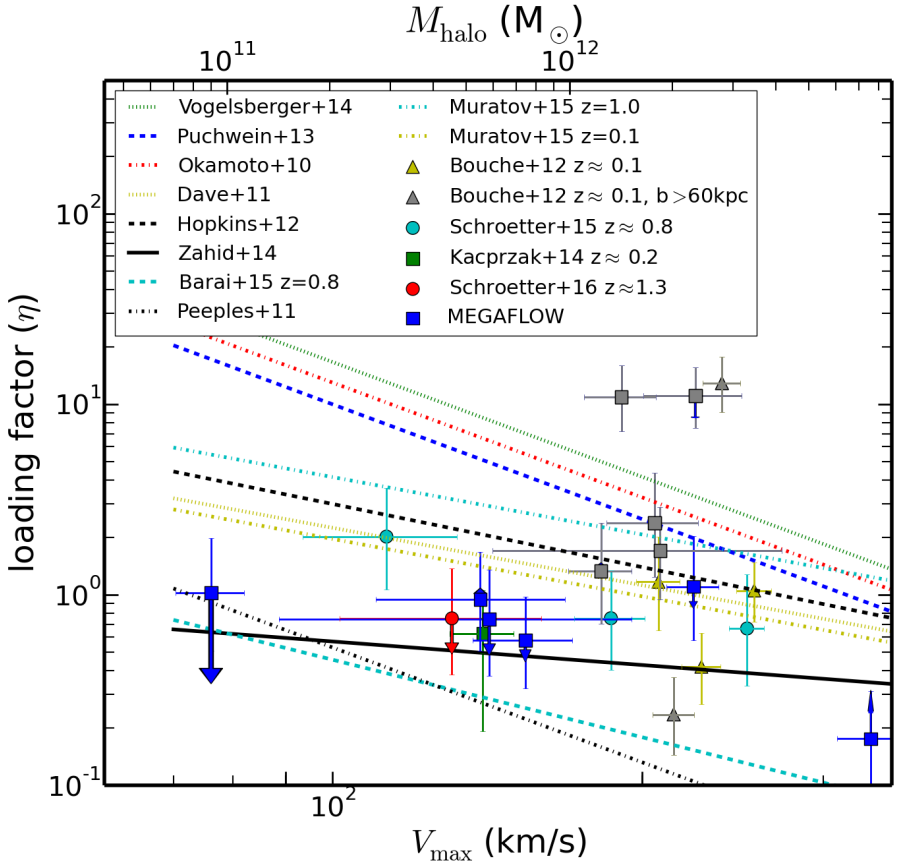

Figure 5.14: Comparison of mass loading factors assumed by theoretical/empirical models (curves) with values derived from background quasar observations (dots and triangles) as a function of the maximum rotational velocity. MEGAFLOW results are represented by the blue squares. The result from Schroetter et al. (2016) is represented by the red circle. Arrows represent the loading factors of the galaxies with the subtracted mass from the inner cone models. The cyan circles show the results for galaxies at $z \approx 0.8$ from Schroetter et al. (2015). The green square shows the mass loading factor for a $z \approx 0.2$ galaxy (Kacprzak et al., 2014). The triangles show the results for $z \approx 0.2$ galaxies from Bouché et al. (2012). The gray triangles and squares show the galaxies with quasars located at >60kpc where the mass loading factor is less reliable due to the large travel time needed for the outflow to cross the quasar LOS (several 100 Myr) compared to the short time scale of the Hα derived SFR ($\sim$ 10Myr). The upper halo mass axis is scaled on $V_{\rm max}$ at redshift 0.8 from Mo & White (2002).

constraints, these needed massive outflows are unrealistically large. These theoretical wind models are therefore over-estimated for low-mass galaxies.

The other wind models (theoretical and empirical), however, are in agreement with

the observational constraints. Even if the theoretical models from Davé et al. (2011); Hopkins et al. (2012); Muratov et al. (2015) and Barai et al. (2014) also try to fit the stellar mass function, they do not appear to over-estimate the mass loading. These models assume momentum-driven outflows but as seen in Figure 5.13, we cannot favor one of the two proposed mechanisms to drive galactic winds (energy-driven or momentum-driven).

At the sight of the previous section, we investigated if any relation exist between different galaxy and winds properties. This investigation was motivated by previous works on observations and theoretical predictions. Some correlations were confirmed (i.e. $V_{\rm out}$ vs SFR, $\dot{M}_{\rm out}$ vs SFR or η vs SFR, $S_{0.5}$) and some were refuted (i.e. $V_{\rm out}$ vs $M_\star$ or η vs redshift).

The most important figures that allows to conclude on what mechanism drives winds are Figure 5.13 and 5.14 showing the loading factor as a function of the galaxy stellar and halo mass respectively. These figures tell us that we can not disentangle between momentum and energy-driven winds due to the large scatter. However, this is also showing that a combination of the two mechanisms could be the best assumption for driving outflows out of the galactic disk.

Chapter 6

Conclusions and perspectives

Contents

6.1 French version 100

6.1.1 Conclusions de thèse 100

6.1.2 Perspectives 102

6.2 English version 103

6.2.1 Thesis conclusions 103

6.2.2 Perspectives 105

6.1 French version

6.1.1 Conclusions de thèse

Dans le contexte de la formation et de l'évolution des galaxies, et plus particulièrement celui des flots de matière autour des galaxies de faibles masses, d'importantes questions se posaient. Des questions comme "quelle quantité de matière est éjectée par les vents galactiques? A quelle vitesse?", ou encore "est-ce que le gaz est capable de quitter le halo gravitationnel de la galaxie et ainsi enrichir le milieu inter-galactique ou aurait-il tendance à retomber sur celle-ci et apporter du combustible permettant la formation de futures étoiles?" Nous nous sommes éfforcés de répondre à ces questions du mieux possible. Il est important de rappeler que l'observation du gaz éjecté en émission est très difficile car ce gaz a une brillance de surface très faible par rapport à celle de la galaxie hôte. Ce gaz éjecté est donc détecté principalement en absorption. C'est à dire qu'il va absorber une partie de la lumière émise par l'objet en arrière plan (dans notre cas le quasar) et pour pouvoir quantifier les propriétés de ce gaz, il va falloir essayer de reproduire cette absorption. La technique que nous utilisons fait appel à des quasars en arrière plan.

Au début de cette thèse, nous avions déjà accès à de nombreuses données acquises avec SINFONI et UVES nécessitant d'être analysées. Le premier échantillon de données (SIMPLE) fût analysé et publié dans Schroetter et al. (2015) (voir Appendice A). Nous avons obtenu les caractéristiques de vents galactiques pour 3 paires galaxie-quasar. Pour une de ces trois paires, nous avons complexifié le modèle de vent afin de reproduire les données. Cette complexification correspond à l'implémentation d'une composante d'accélération pour les paires ayant un faible paramètre d'impact afin de reproduire l'assymétrie du profil d'absorption (voir les détails au § 4.2.3 et dans Schroetter et al. (2015)). Combinant notre analyse à ceux de la littérature (voir Figure 4.8), nous avons vu que le facteur de charge avait tendance à être de l'ordre de l'unité, ce qui correspond à une quantité de matière éjectée équivalente au taux de formation stellaire de la galaxie. Mais il y avait trop peu d'observations pour pouvoir conclure sur des propriétés générales des vents galactiques. Nous avions donc besoin d'observations supplémentaires.

Pendant ce temps, la construction de l'instrument MUSE était en chemin et nous avions déjà commencé à établir notre stratégie d'observation afin d'augmenter le nombre de paires galaxie-quasar d'un ordre de grandeur. Pour atteindre cet objectif, nous avons utilisé la stratégie décrite en détail dans la section § 2.3.1. Cette stratégie consiste à chercher plusieurs absorbants Mg II (au moins 3) dans le spectre de quasars contenus dans la base de donnée SDSS. Ces absorbants devaient avoir une largeur équivalente au repos ($W_r^{\lambda 2796}$) suppérieure à 0.8 Å (comparé à 2 Å pour SIMPLE), ainsi qu'un redshift compris entre 0.4 et 1.4 afin de pouvoir détecter l'émission [O II]

des galaxies potentiellement responsables de ces absorptions.

Lorsque cet instrument a ouvert ses yeux vers le ciel pour la première fois le 5 Mars 2014, MUSE fût un véritable succès et commença à collecter de nombreuses observations. Nous avons aussi obtenu des données complémentaires de nos champs de quasar avec le spectrographe à haute résolution UVES afin d'avoir la résolution spectrale nécessaire dans les profils d'absorptions détectés dans les spectres des quasars. Contrairement au temps MUSE, le temps d'observation avec l'instrument UVES ne nous était pas garanti.

Etant les premiers à avoir des observations MUSE, un travail intensif sur la réduction des données brutes était nécessaire afin de pouvoir travailler avec les meilleurs données possibles pour atteindre nos objectifs scientifiques (voir § 3.2). Suite à ce travail de réduction, nous avons réussi à détecter 85% des galaxies que nous qualifions être à l'origine des absorptions Mg II dans les spectres des quasars. Ceci nous a amené à multiplié par 2-3 l'échantillon que nous avions ainsi que les contraintes sur les propriétés physiques des vents galactiques (dont une paire est décrite dans Schroetter et al. (2016), accessible à l'Apendice B). Ces contraintes sont présentées sur la Figure 5.14.

Nous en avons conclu que si nous voulions mesurer un facteur de charge qui ait une signification, il fallait que la quantité de masse éjectée et le taux de formation d'étoiles de la galaxie soient estimés sur des échelles de temps similaires afin de pouvoir être comparé avec les simulations. Ceci donna lieu à une discussion sur la pertinence de ce paramètre. D'autres paramètres étaient donc nécéssaires si nous voulions en déduire des propriétés entre les vents galactiques et les paramètres des galaxies hôtes (voir § 5.4).

Un résumé des résultats obtenus durant cette thèse est la suivante:

- Les facteurs de charge ont tendance à êtrent proches de l'unité ($\eta \sim 1$), ce qui veut dire que le taux de matière éjecté est de l'ordre du taux de formation stellaire de la galaxie.
- Le gaz faiblement ionisé que nous détectons semble retomber sur la galaxie à partir du moment où la galaxie possède une masse stellaire d'environ $10^9 M_\odot$ (voir § 5.3).
- Nous avons montré que les vents ont une phase d'accélération jusqu'à environ 10 kpc de la galaxie.
- Nous avons aussi développé un modèle de cône creux afin de pouvoir reproduire le profil d'absorption créé par les vents et nous avons trouvé cette configuration dans 5 cas de l'échantillon MEGAFLOW.
- En combinant nos observation avec d'autres travaux sur les vents, nous avons confirmé certaines corrélations entre différentes propriétés des vents et de leurs

galaxies hôtes comme la vitesse d'éjection des vents et le SFR de la galaxie, le taux de masse éjectée et le SFR ou bien le facteur de charge et la masse de la galaxie.

- Certaines corrélations comme la dépendance entre la vitesse d'éjection des vents et la masse de la galaxie ou bien celle entre le facteur de charge et le redshift furent, quand à elles, infirmées.

- Les vents galactiques semblent être entraînés par une combinaison des mécanismes de transfert de moment cinétique et d'énergie cinétique (voir dernier chapitre).

6.1.2 Perspectives

Les observations MEGAFLOW sont extrèmement riches. Si elles nous permettent d'explorer des galaxies ayant des vents galactiques, chaque champ contient aussi de nombreuses autres galaxies dont les vents n'ont pas été détectés dans le spectre du quasar. Par exemple, nous avons détecté environ 40 galaxies en émission ayant un redshift entre 0.4 et 1.4 (voir Figure 5 dans Schroetter et al. (2016)). Celles-ci sont seulement les galaxies ayant une forte raie d'émission (principalement le doublet de [O II]) et d'autres galaxies détéctées par leur continuum n'ont pas été prises en compte. Il serait intéressant de regarder le spectre de ces galaxies (ayant un redshift suppérieur à 0.8) afin de chercher la signature de vents ou non (forte absorption Mg II λ2796) et de caractériser les vents détectés. Cette analyse pourrait permettre de rechercher les propriétés des galaxies pouvant être responsables de la présence ou non de vents galactiques.

Afin de pouvoir mettre de meilleurs contraintes sur les phénomènes de rétro-action des galaxies, il est nécéssaire d'avoir des mesures de $\dot{M}_{\rm out}$ et SFR sur des échelles de temps similaires. Pour calculer le SFR sur une plus longue période de temps, l'ultraviolet est le traceur de choix, étant sensible aux étoiles vivant jusqu'à quelques 100 millions d'années. Malheureusement, les méthodes simplistes permettant de mesurer le SFR peuvent être affectées par des dégénérescences (e.g. est-ce que la galaxie est rouge parce qu'elle forme des étoiles et contient de la poussière ou parce qu'elle a cessé de former des étoiles?) et peut être contaminée par des étoiles vivant très longtemps (e.g. Boquien et al., 2014). De nouveaux modèles utilisant des données de l'ultraviolet lointain (FUV) à l'infrarouge lointain (FIR), tel que CIGALE (Noll et al. (2009a), Boquien et al. in prep.) permettent désormais d'accéder à de meilleures estimations du SFR sur des échelles de temps de 100 Myrs. Ceci impliquerait donc l'observation de suivi de galaxies sélectionnées avec d'autres instruments afin d'avoir une couverture de longueurs d'ondes très large (du FUV au FIR).

De plus, des données de l'observatoire du Keck ont été analysées et des modèles de vents lancés sur une paire galaxie-quasar (Kacprzak et al., 2014) ainsi que sur 5 autres paires. Ces dernières nécéssitent du travail supplémentaire afin d'obtenir leur facteur de charge et autres propriétés qui nous permettront d'augmenter le nombre de contraintes sur le gaz autour des galaxies (Bouché, Schroetter et al, in prep.).

6.2 English version

6.2.1 Thesis conclusions

In the context of galaxy formation and evolution, and in particular about the gas flows around low-mass galaxies, important questions remained. Questions like "what is the amount of ejected mass by galactic winds? how fast are these winds?" or even "is the gas able to escape the gravitational well of the host galaxy to enrich the interstellar medium or is it likely to fall back onto the galaxy and fuel future star formation?" During this thesis, we tried to answer these questions as best as we could. It is important to remind that it is difficult to directly observe the outflowing gas in emission as the surface brightness of this gas is negligible compared to the host galaxy's. This outflowing gas is therefore detected in absorption. It will absorb a part of the background object light (in our case the quasar) and to quantify this gas properties, one needs to reproduce this absorption. The technique we are using implies background quasars.

When starting this thesis, we already had a lot of available data from UVES and SINFONI that needed to be analyzed. The first sample (SIMPLE) was analyzed and published in Schroetter et al. (2015) (see Appendix A). We obtained galactic wind properties for 3 galaxy-quasar pairs. For one of these three pairs, our wind model has been modified in order to reproduce the data. This modification corresponds to an implementation of an acceleration component for pairs with low impact parameter in order to fit the absorption profile asymmetry (see details in § 4.2.3 and in Schroetter et al. (2015)). Combining our analysis with other works in the literature (see Figure 4.8), we first saw that the loading factor had a tendency to be around unity (which corresponds to an ejected mass rate equivalent to the star formation rate of the galaxy) but had too few observations in order to derive general outflow properties. We thus needed lots of additional observational constraints.

In the mean time, MUSE was building up and we already began to establish our observational strategies in order to increase the number of galaxy-quasar pairs by one order of magnitude. To do so, we proceeded as described in § 2.3.1. This strategy consists in searching for multiple Mg II absorptions (3 at least) in quasar spectra from SDSS database. These absorbers needed to have a rest equivalent width ($W_r^{\lambda 2796}$) larger than 0.8 Å (compared to 2 Å for the SIMPLE sample) and redshift between

0.4 and 1.4 in order to detect the [O II] emission lines of the galaxies assumed to be responsible for these absorptions.

When the instrument had its first light in March 5th 2014, MUSE was successful in all aspects so we began gathering lots of observations. We also acquired follow up observations of our quasar fields with the high resolution spectrograph UVES in order to have the necessary spectral resolution of absorption lines seen in the quasar spectra. Contrary to MUSE, observing time with UVES was not guaranteed.

Being the first to have MUSE observations, we needed to work on data reduction in order to have the best data reduced to achieve our science goals (see § 3.2). After intensive data reductions, we analyzed our quasar fields to look for wind-pairs. Our observational strategy was successful as we detected 85% of the galaxies we assumed responsible for the Mg II absorption lines in quasar spectra. This, in turn, led to multiply by 2-3 our sample as well as physical constraints on galactic outflows (one is described in Schroetter et al. (2016), added in Appendix B). These constraints are shown in Figure 5.14.

We then concluded that if we wanted to estimate meaningful loading factors, the ejected mass rate and the star formation rate of the galaxy needed to be estimated on similar time scales in order to be comparable with simulation results. This opened a discussion on the pertinence of our loading factors. New parameters needed to be used in order to put real constraints on galactic winds as a function of galaxy properties (see § 5.4).

A summary of our results is as follow:

- Loading factors tend to be $\eta \sim 1$, which means that the ejected mass rate is of the same order as the galaxy SFR.
- The low-ionization gas we are tracing is likely to fall back onto the galaxy for galaxies with stellar mass larger than $10^9 M_\odot$ (see § 5.3).
- We found that galactic winds should be accelerated until 10 kpc away from the host galaxy.
- We also needed to develop an empty inner cone model to fit the data and this configuration is found for 5 cases in the MEGAFLOW sample.
- Combining our observations with previous works, we confirmed some correlations between outflow and galaxy properties such as the outflowing velocity and the SFR of the galaxy, the ejected mass rate and the galaxy SFR or between the loading factor and the galaxy stellar mass.
- Some correlations like the one between the outflow velocity and the galaxy stellar mass or between the loading factor and the galaxy redshift were, however, refuted.

- Galactic winds seem to have a tendency to be driven by a combination of momentum and kinetic energy mechanisms (see the last chapter).

6.2.2 Perspectives

MEGAFLOW observations are exquisitely rich. If they allow us to explore galaxies with outflows, each field also contains many more galaxies without detected outflows. For instance, we detected around 40 galaxies in emission with redshifts between 0.4 and 1.4 (see Figure 5 from Schroetter et al. (2016)). These are just the galaxies with strong emission lines (mainly the [O II] 3727,3729 doublet), other galaxies detected from their continuum were not taken into account. It would be of interest to look at these galaxy spectra (with redshift larger than 0.8) in order to search for galactic winds signature or not (strong Mg II λ2796 absorption) and characterize the detected outflow properties. This analysis could allow to look for galaxy properties responsible for the presence or absence of galactic winds.

In order to put better constraints on galaxy feedback, one needs to have measures of $\dot{M}_{\rm out}$ and SFR on roughly similar timescales. To measure the SFR over longer periods of time, the ultraviolet is the tracer of choice as it is sensitive to stars living up to a few 100 Myrs. Unfortunately, simple recipes to measure the SFR from the UV can be severely affected by degeneracies (e.g., is a galaxy red because it is star-forming but dusty, or is it rather because it has stopped forming stars?) and contamination by long-lived stars (e.g. Boquien et al., 2014). New models using data from the far-ultraviolet (FUV) to the far-infrared (FIR), such as CIGALE (Noll et al. (2009a), Boquien et al. in prep.) now allow us to have more reliable measurements of the SFR over timescales of 100 Myr. This should implies follow up from other instruments to have a very large wavelength coverage (from FUV to FIR) of selected galaxies.

Hence, data from Keck observatory had to be processed and wind models lunched on one galaxy-quasar pair (Kacprzak et al., 2014) and 5 additional wind pairs have results from wind models. These latter data still need additional work in order to derive loading factors and other outflow properties to increase the number of constraints on gas around galaxies (Bouché, Schroetter et al, in prep.).

Bibliography

Abuter, R., Schreiber, J., Eisenhauer, F., et al. 2006, New Astronomy Review, 50, 398

Alam, S., Albareti, F. D., Allende Prieto, C., et al. 2015, ArXiv e-prints, arXiv:1501.00963

Alexandroff, R. M., Heckman, T. M., Borthakur, S., Overzier, R., & Leitherer, C. 2015, ApJ, 810, 104

Arribas, S., Colina, L., Bellocchi, E., Maiolino, R., & Villar-Martín, M. 2014, A&A, 568, A14

Arribas, S., del Burgo, C., Carter, D., et al. 1998, in Astronomical Society of the Pacific Conference Series, Vol. 152, Fiber Optics in Astronomy III, ed. S. Arribas, E. Mediavilla, & F. Watson, 149

Bacon, R., Bauer, S., Boehm, P., et al. 2006, in Society of Photo-Optical Instrumentation Engineers (SPIE) Conference Series, Vol. 6269, Society of Photo-Optical Instrumentation Engineers (SPIE) Conference Series, 0

Bacon, R., Brinchmann, J., Richard, J., et al. 2015, A&A, 575, A75

Barai, P., Monaco, P., Murante, G., Ragagnin, A., & Viel, M. 2014, ArXiv e-prints, arXiv:1411.1409

—. 2015, MNRAS, 447, 266

Behroozi, P. S., Wechsler, R. H., & Conroy, C. 2013a, ApJ, 762, L31

—. 2013b, ApJ, 770, 57

Bland-Hawthorn, J., Veilleux, S., & Cecil, G. 2007, Ap&SS, 311, 87

Bohlin, R. C., Savage, B. D., & Drake, J. F. 1978, ApJ, 224, 132

Boquien, M., Buat, V., & Perret, V. 2014, A&A, 571, A72

Boquien, M., Kennicutt, R., Calzetti, D., et al. 2016, A&A, 591, A6

Bordoloi, R., Lilly, S. J., Knobel, C., et al. 2011, ApJ, 743, 10

Bordoloi, R., Lilly, S. J., Hardmeier, E., et al. 2014, ApJ, 794, 130

Bouché, N., Carfantan, H., Schroetter, I., Michel-Dansac, L., & Contini, T. 2015, GalPaK 3D: Galaxy parameters and kinematics extraction from 3D data, Astrophysics Source Code Library, ascl:1501.014

Bouché, N., Hohensee, W., Vargas, R., et al. 2012, MNRAS, 426, 801

Bouché, N., Murphy, M. T., Péroux, C., Csabai, I., & Wild, V. 2006, MNRAS, 371, 495

Bouché, N., Murphy, M. T., Péroux, C., et al. 2007, ApJ, 669, L5

Chabrier, G. 2003, PASP, 115, 763

Charlot, S., Kauffmann, G., Longhetti, M., et al. 2002, MNRAS, 330, 876

Chen, H.-W. 2012, MNRAS, 427, 1238

Chen, H.-W., Wild, V., Tinker, J. L., et al. 2010, ApJ, 724, L176

Contini, T., Garilli, B., Le Fèvre, O., et al. 2012, A&A, 539, A91

Contini, T., Epinat, B., Bouché, N., et al. 2016, A&A, 591, A49

Cresci, G., Hicks, E. K. S., Genzel, R., et al. 2009, ApJ, 697, 115

Davé, R., Oppenheimer, B. D., & Finlator, K. 2011, MNRAS, 415, 11

Davies, R. 2007, MNRAS, 375, 1099

Dekel, A., & Silk, J. 1986, ApJ, 303, 39

Dekker, H., D'Odorico, S., Kaufer, A., Delabre, B., & Kotzlowski, H. 2000, in Society of Photo-Optical Instrumentation Engineers (SPIE) Conference Series, Vol. 4008, Optical and IR Telescope Instrumentation and Detectors, ed. M. Iye & A. F. Moorwood, 534–545

Epinat, B., Contini, T., Le Fevre, O., et al. 2009, A&A, 504, 789

Förster Schreiber, N. M., van Dokkum, P. G., Franx, M., et al. 2004, ApJ, 616, 40

Förster Schreiber, N. M., Genzel, R., Bouché, N., et al. 2009, ApJ, 706, 1364

Fox, A. J., Bordoloi, R., Savage, B. D., et al. 2015, ApJ, 799, L7

Genzel, R., Newman, S., Jones, T., et al. 2011a, ApJ, 733, 101

—. 2011b, ApJ, 733, 101

Grimes, J. P., Heckman, T., Aloisi, A., et al. 2009, ApJS, 181, 272

Heckman, T. M., Alexandroff, R. M., Borthakur, S., Overzier, R., & Leitherer, C. 2015, ApJ, 809, 147

Heckman, T. M., Lehnert, M. D., Strickland, D. K., & Armus, L. 2000, ApJS, 129, 493

Heckman, T. M., Sembach, K. R., Meurer, G. R., et al. 2001, ApJ, 554, 1021

Hopkins, P. F., Kereš, D., Oñorbe, J., et al. 2014, MNRAS, 445, 581

Hopkins, P. F., Quataert, E., & Murray, N. 2012, MNRAS, 421, 3522

Jenkins, E. B. 2009, ApJ, 700, 1299

Kacprzak, G. G., Churchill, C. W., Evans, J. L., Murphy, M. T., & Steidel, C. C. 2011, MNRAS, 416, 3118

Kacprzak, G. G., Muzahid, S., Churchill, C. W., Nielsen, N. M., & Charlton, J. C. 2015, ApJ, 815, 22

Kacprzak, G. G., Martin, C. L., Bouché, N., et al. 2014, ApJ, 792, L12

Kassin, S. A., Weiner, B. J., Faber, S. M., et al. 2007, ApJ, 660, L35

Kennicutt, Jr., R. C. 1998, ApJ, 498, 541

Keres, D., Yun, M. S., & Young, J. S. 2003, ApJ, 582, 659

Kewley, L. J., Geller, M. J., & Jansen, R. A. 2004, AJ, 127, 2002

Koribalski, B. S., Staveley-Smith, L., Kilborn, V. A., et al. 2004, AJ, 128, 16

Kroupa, P. 2000, in Astronomische Gesellschaft Meeting Abstracts, Vol. 16, Astronomische Gesellschaft Meeting Abstracts, ed. R. E. Schielicke

Lan, T.-W., Ménard, B., & Zhu, G. 2014a, ApJ, 795, 31

—. 2014b, ApJ, 795, 31

Lanzetta, K. M., & Bowen, D. 1990, ApJ, 357, 321

Law, D. R., Steidel, C. C., Erb, D. K., et al. 2007, ApJ, 669, 929

—. 2009, ApJ, 697, 2057

Le Fèvre, O., Saisse, M., Mancini, D., et al. 2003, in Proc. SPIE, Vol. 4841, Instrument Design and Performance for Optical/Infrared Ground-based Telescopes, ed. M. Iye & A. F. M. Moorwood, 1670–1681

Lilly, S. J., Le Fevre, O., Hammer, F., & Crampton, D. 1996, ApJ, 460, L1

Madau, P., & Dickinson, M. 2014, ARA&A, 52, 415

Madau, P., Ferguson, H. C., Dickinson, M. E., et al. 1996, MNRAS, 283, 1388

Martin, C. L. 2005, ApJ, 621, 227

Martin, C. L., Shapley, A. E., Coil, A. L., et al. 2012, ApJ, 760, 127

Ménard, B., & Chelouche, D. 2009, MNRAS, 393, 808

Miller, S. H., Bundy, K., Sullivan, M., Ellis, R. S., & Treu, T. 2011, ApJ, 741, 115

Miller, S. H., Ellis, R. S., Newman, A. B., & Benson, A. 2014, ApJ, 782, 115

Mo, H. J., & White, S. D. M. 2002, MNRAS, 336, 112

Muratov, A. L., Keres, D., Faucher-Giguere, C.-A., et al. 2015, ArXiv e-prints, arXiv:1501.03155

Murray, N., Quataert, E., & Thompson, T. A. 2005, ApJ, 618, 569

Nestor, D. B., Turnshek, D. A., & Rao, S. M. 2005, ApJ, 628, 637

Newman, S. F., Genzel, R., Förster-Schreiber, N. M., et al. 2012, ApJ, 761, 43

Noll, S., Burgarella, D., Giovannoli, E., et al. 2009a, A&A, 507, 1793

—. 2009b, A&A, 507, 1793

Okamoto, T., Frenk, C. S., Jenkins, A., & Theuns, T. 2010, MNRAS, 406, 208

Oke, J. B., Cohen, J. G., Carr, M., et al. 1995, PASP, 107, 375

Oppenheimer, B. D., & Davé, R. 2006, MNRAS, 373, 1265

—. 2008, MNRAS, 387, 577

Oppenheimer, B. D., Davé, R., Kereš, D., et al. 2010, MNRAS, 406, 2325

Papastergis, E., Cattaneo, A., Huang, S., Giovanelli, R., & Haynes, M. P. 2012, ApJ, 759, 138

Peebles, P. J. E. 1980, The large-scale structure of the universe

Peeples, M. S., & Shankar, F. 2011, MNRAS, 417, 2962

Price, S. H., Kriek, M., Shapley, A. E., et al. 2016, ApJ, 819, 80

Puchwein, E., & Springel, V. 2013, MNRAS, 428, 2966

Puech, M., Flores, H., Hammer, F., et al. 2008, A&A, 484, 173

Ross, N. P., Myers, A. D., Sheldon, E. S., et al. 2012, ApJS, 199, 3

Rubin, K. H. R., Prochaska, J. X., Koo, D. C., et al. 2014, ApJ, 794, 156

Rupke, D. S., Veilleux, S., & Sanders, D. B. 2005, ApJS, 160, 115

Salpeter, E. E. 1955, ApJ, 121, 161

Schaye, J., Dalla Vecchia, C., Booth, C. M., et al. 2010, MNRAS, 402, 1536

Schaye, J., Crain, R. A., Bower, R. G., et al. 2015, MNRAS, 446, 521

Schreiber, J., Thatte, N., Eisenhauer, F., et al. 2004, in ASP Conf. Ser. 314: Astronomical Data Analysis Software and Systems (ADASS) XIII, ed. F. Ochsenbein, M. G. Allen, & D. Egret, p.380

Schroetter, I., Bouché, N., Péroux, C., et al. 2015, ApJ, 804, 83

Schroetter, I., Bouché, N., Wendt, M., et al. 2016, ApJ, 833, 39

Sérsic, J. L. 1963, Boletin de la Asociacion Argentina de Astronomia La Plata Argentina, 6, 41

Shapiro, K. L., Genzel, R., Quataert, E., et al. 2009, ApJ, 701, 955

Simons, R. C., Kassin, S., Trump, J., et al. 2015, IAU General Assembly, 22, 2257477

Soto, K. T., Lilly, S. J., Bacon, R., Richard, J., & Conseil, S. 2016, ZAP: Zurich Atmosphere Purge, Astrophysics Source Code Library, ascl:1602.003

Steidel, C. C. 1995, in QSO Absorption Lines, ed. G. Meylan, 139

Steidel, C. C., Erb, D. K., Shapley, A. E., et al. 2010, ApJ, 717, 289

Tacconi, L. J., Neri, R., Genzel, R., et al. 2013, ApJ, 768, 74

Tully, R. B., & Fisher, J. R. 1977, A&A, 54, 661

van den Bosch, F. C. 2001, MNRAS, 327, 1334

van Dokkum, P. G. 2001, PASP, 113, 1420

Veilleux, S., Cecil, G., & Bland-Hawthorn, J. 2005a, ARA&A, 43, 769

—. 2005b, ARA&A, 43, 769

Veilleux, S., & Rupke, D. 2002, Anglo-Australian Observatory Epping Newsletter, 99, 6

Veilleux, S., Shopbell, P. L., Rupke, D. S., Bland-Hawthorn, J., & Cecil, G. 2003, AJ, 126, 2185

Vergani, D., Epinat, B., Contini, T., et al. 2012, A&A, 546, A118

Vogelsberger, M., Genel, S., Sijacki, D., et al. 2014, MNRAS, 438, 3607

Weiner, B. J. 2009, in American Institute of Physics Conference Series, Vol. 1201, American Institute of Physics Conference Series, ed. S. Heinz & E. Wilcots, 142–145

Weiner, B. J., Willmer, C. N. A., Faber, S. M., et al. 2006, ApJ, 653, 1027

Whitaker, K. E., Franx, M., Leja, J., et al. 2014, ApJ, 795, 104

Zahid, H. J., Torrey, P., Vogelsberger, M., et al. 2014, Ap&SS, 349, 873

Zhu, G., & Ménard, B. 2013, ApJ, 770, 130

Zwaan, M. A., Staveley-Smith, L., Koribalski, B. S., et al. 2003, AJ, 125, 2842

Appendix A

Schroetter et al. 2015: The SINFONI Mg II Program for Line Emitters (SIMPLE) II: background quasar probing z∼1 galactic winds

The Astrophysical Journal, 804:83 (18pp), 2015 May 10 doi:10.1088/0004-637X/804/2/83
© 2015. The American Astronomical Society. All rights reserved.

THE VLT SINFONI Mg II PROGRAM FOR LINE EMITTERS (SIMPLE). II. BACKGROUND QUASARS PROBING $Z \sim 1$ GALACTIC WINDS*

Ilane Schroetter[1,2], Nicolas Bouché[1,2], Céline Péroux[3], Michael T. Murphy[4], Thierry Contini[1,2], and Hayley Finley[1,2]
[1] CNRS/IRAP, 14 Avenue E. Belin, F-31400 Toulouse, France
[2] University Paul Sabatier of Toulouse/ UPS-OMP/ IRAP, F-31400 Toulouse, France
[3] Aix Marseille Université, CNRS, LAM (Laboratoire d'Astrophysique de Marseille) UMR 7326, F-13388, Marseille, France
[4] Centre for Astrophysics and Supercomputing, Swinburne University of Technology, Hawthorn, Victoria 3122, Australia
Received 2014 November 18; accepted 2015 February 26; published 2015 May 5

ABSTRACT

The physical properties of galactic winds are of paramount importance for our understanding of galaxy formation. Fortunately, they can be constrained using background quasars passing near star-forming galaxies (SFGs). From the 14 quasar–galaxy pairs in our Very Large Telescope (VLT)/SINFONI Mg II Program for Line Emitters sample, we reobserved the 10 brightest galaxies in Hα with the VLT/SINFONI with 0.″7 seeing and the corresponding quasar with the VLT/UVES spectrograph. Applying geometrical arguments to these 10 pairs, we find that four are likely probing galactic outflows, three are likely probing extended gaseous disks, and the remaining three are not classifiable because they are viewed face-on. In this paper we present a detailed comparison between the line-of-sight kinematics and the host galaxy emission kinematics for the pairs suitable for wind studies. We find that the kinematic profile shapes (asymmetries) can be well reproduced by a purely geometrical wind model with a constant wind speed, except for one pair (toward J2357−2736) that has the smallest impact parameter $b = 6$ kpc and requires an accelerated wind flow. Globally, the outflow speeds are $\sim$100 km s^{-1} and the mass ejection rates (or $\dot{M}_{\rm out}$) in the gas traced by the low-ionization species are similar to the star formation rate (SFR), meaning that the mass loading factor, $\eta = \dot{M}_{\rm out}/{\rm SFR}$, is $\approx$1.0. The outflow speeds are also smaller than the local escape velocity, which implies that the outflows do not escape the galaxy halo and are likely to fall back into the interstellar medium.

Key words: galaxies: evolution – galaxies: formation – galaxies: kinematics and dynamics – intergalactic medium – quasars: absorption lines

1. INTRODUCTION

Currently, under the cold dark matter scenario, galaxies form via the growth of initial density fluctuations. This scenario is very successful because the observed large-scale structure is well matched by the clustering of halos in *N*-body simulations (e.g., Springel et al. 2006). With the help of state-of-the-art hydrodynamical simulations (Genel et al. 2014; Muratov et al. 2015; Schaye et al. 2015), this scenario has recently successfully reproduced more complex observables such as the galaxy morphologies (Genel et al. 2014; Vogelsberger et al. 2014).

A major success of these recent hydro-simulations is a better understanding of disk formation at high redshifts $z > 1$. Indeed, these simulations (Genel et al. 2012, 2014) are in good agreement with the morphologies and kinematics observed for Lyman break galaxies, which appear to be dominated by gas-rich rotating disks, based on data from deep *Hubble Space Telescope* (*HST*) observations (Elmegreen et al. 2007; Wuyts et al. 2011) and large Integral Field Units (IFU) surveys like SINS (Förster Schreiber et al. 2006, 2009; Genzel et al. 2008) and MASSIV (Contini et al. 2012; Epinat et al. 2012).

One major problem remains, however, namely, that the luminosity function for low-mass galaxies ($L < L_*$) is difficult to reproduce. For instance, the Illustris simulations (Genel et al. 2014) overpredict the number of $z = 0$ low-mass galaxies despite implementing strong galactic outflows (but see Schaye et al. 2015). This tension can be recast in terms of the "galaxy formation efficiency" (Behroozi et al. 2010; Moster et al. 2010; Leauthaud et al. 2011, 2012; Papastergis et al. 2012), which is maximal for $\sim L_*$ galaxies and steeply decreases in the low-mass regime ($L < L_*$). In the low-mass regime, galactic winds, created by accumulated supernova explosions, are commonly invoked to expel baryons back into the intergalactic medium (Dekel & Silk 1986; White & Frenk 1991) since baryons in these galaxy halos are expected to cool rapidly (White & Rees 1978; White & Frenk 1991; Kereš et al. 2005; Dekel et al. 2009).

Although galactic winds seem to occur in every star-forming galaxy, their properties remain poorly constrained despite many attempts at characterizing them (Lehnert & Heckman 1996; Martin 1998, 1999; Heckman et al. 2000; Rupke et al. 2005; Rubin et al. 2010; Martin et al. 2012). This lack of knowledge prevents us from correctly modeling galaxies in numerical simulations, which often require ad hoc recipes (Oppenheimer and Davé 2006; Dubois & Teyssier 2008; Oppenheimer et al. 2010; Shen et al. 2012, 2013; Rosdahl et al. 2013; Dekel et al. 2013; Roškar et al. 2014). In particular, the best estimates for the ejected mass rate ($\dot{M}_{\rm out}$) using standard galaxy absorption lines are uncertain by orders of magnitude (e.g., Heckman et al. 1990, 2000; Martin et al. 2002, 2012, 2013; Pettini et al. 2002; Martin 2005).

The main reason for the large uncertainties is that traditional spectroscopy does not give information of the material physical location because the gas could be at a

* Based on observations made at the ESO telescopes under program 080.A-0364(A) 080.A-0364(B) and 079.A-0600(B).

Table 1
Summary of SINFONI 080.A-0364(B) Observations

Field (1)	z_{qso} (2)	$W_r^{\lambda 2796}$(Å) (3)	PSF(″) (4)	T_{exp}(s) (5)	Date (6)
J0147+1258	1.503	4.025	0.6	9600	2007 Oct 12 2008 Jan 03, 04, 09
J0226–2857	2.171	4.515	0.6	9600	2007 Oct 06 2008 Jan 03, 05
J0302–3216	0.898	2.27	0.7	7200	2007 Oct 02
J0448+0950	2.115	3.169	0.8	4800	2007 Dec 04, 16
J0822+2243	1.620	2.749	0.8	4800	2007 Dec 18 2008 Jan 03
J0839+1112	2.696	2.316	0.8	4800	2007 Dec 14, 15, 23 2008 Jan 01
J0943+1034	1.239	3.525	0.6	7200	2007 Dec 22 2008 Jan 06
J1422–0001	1.083	3.185	0.7	9600	2008 Feb 15, 25 2008 Mar 14
J1441+0443	1.112	2.223	0.6	12000	2008 Mar-14, 15, 25
J2357–2736	1.732	1.940	0.6	7200	2007 Oct 02

Notes:
(1) Quasar name; (2) quasar emission redshift; (3) Mg II rest equivalent width; (4) FWHM of the seeing PSF; (5) exposure time; (6) dates of observations.

distance of 100 pc, 1 kpc, or 10 kpc from the galaxy. Indeed, the standard method usually uses the galaxy spectrum and in some cases stacked galaxy spectra, to obtain the absorption lines corresponding to the outflowing materials. However, background quasars have been recently used to constrain the properties of winds (Bouché et al. 2012; Kacprzak et al. 2014) using low-ionization absorption lines, like Mg II $\lambda\lambda$2796, 2803. Indeed, when the quasar apparent location is close to the galaxy minor axis, the line of sight (LOS) is expected to intercept the wind. Thus, background quasars give us the three main ingredients necessary for determining accurate ejected mass rates: the gas localization (impact parameter), the gas column density, and the wind radial (deprojected) velocity, provided that the galaxy inclination is known.

The background quasar technique also provides the ability to better constrain the ejected mass outflow rate and its relation to the galaxy star formation rate (SFR) via the so-called mass loading factor $\eta \equiv \dot{M}_{\rm out}/{\rm SFR}$, which is a critical ingredient for numerical simulations (Oppenheimer and Davé 2006; Oppenheimer et al. 2010; Dekel et al. 2013). As opposed to relying only on the galaxy spectra to study outflows, the background quasar method has several advantages: it gives us a more precise location of the absorbing gas relative to the galaxy and, because the quasar is seen as a point source, it also provides us with a good characterization of the point-spread function (PSF), an important ingredient for deriving the intrinsic galaxy properties from IFU data.

Recently, there has been progress in this field with low-redshift $z \sim 0.1$ star-forming galaxies (SFGs) (Bouché et al. 2012; Kacprzak et al. 2014) applying this technique. In this paper, we use the sample of 14 intermediate-redshift $z \sim 1$ galaxy–quasar pairs from the SINFONI Mg II Program for Line Emitters (SIMPLE, Bouché et al. 2007, hereafter Paper I) to constrain the outflow properties (e.g., mass ejection rate, outflow velocity) of SFGs when the quasar is suitably located relative to the foreground galaxy.

The outline of this paper is as follows: Section 2 describes the sample and the new Very Large Telescope (VLT) SINFONI/UVES data acquired. In Section 3, we present the analysis of the SINFONI and UVES data together with the selection of pairs suitable for wind studies (wind-pairs). In Section 4, we describe our wind model and the derived outflow rates for the wind-pairs. We end with our conclusions and discussions in Section 5. In this study we used the following cosmological parameters: $H_0 = 70\,{\rm km\,s^{-1}}$, $\Omega_\Lambda = 0.7$, and $\Omega_M = 0.3$.

2. THE SIMPLE SAMPLE

Because the probability of finding galaxy–quasar pairs is very low, one must employ targeted strategies for gathering a suitable sample of galaxy–quasar pairs to study the properties of circumgalactic gas (Péroux et al. 2013; Tumlinson et al. 2013; Werk et al. 2014) around galaxies, which can lead to constraints on outflows (Bouché et al. 2012; Kacprzak et al. 2014) or inflows (Bouché et al. 2013). We thus designed the SIMPLE survey to build a sample of intermediate-redshift $z \sim 1$ quasar–galaxy pairs (Paper I).

The SIMPLE sample (Bouché et al. 2007) was selected with the following criterion: the rest-frame equivalent width of intervening Mg II ($W_r^{\lambda 2796}$) absorptions detected in background quasar spectra had to be at least 2 Å. This criterion ensures that the associated galaxies will be at small impact parameters ($b < 3''$), given the W_r-impact parameter anti-correlation (e.g., Steidel 1995; Bouché et al. 2006; Ménard and Chelouche 2009; Chen 2012), and thus that they will be located within the field of view (FOV) of the IFU SINFONI (8″ each side). Moreover, the absorber's redshift must be $0.8 < z < 1.0$ so that the Hα emission line falls inside the SINFONI J band. These criteria led to the detection of 14 galaxies out of 21 (70% success rate) (Bouché et al. 2007).

The SINFONI data presented in Bouché et al. (2007) were shallow with exposure times $\leqslant$40 minutes and seeing conditions $>0\overset{''}{.}8$. Since we aim to precisely compare the host galaxy kinematics (derived from the Hα emission line) with the kinematics of the absorbing material measured in the quasar LOS, we acquired new VLT/SINFONI and VLT/UVES data. From the sample of 14 galaxies in Bouché et al. (2007), we re-observed a sub-sample of 10 galaxies (Table 1), those with the highest initial Hα fluxes, with longer integration times (2–3 hr), and in better seeing conditions ($<0\overset{''}{.}8$).

The SINFONI observations, done in service mode, were optimized by adopting an "on-source" dithering strategy designed to ensure a continuous integration at the host location.

The UVES (Dekker et al. 2000) data were taken in both visitor mode and service mode.

2.1. SINFONI Data Reduction

The data reduction was performed as in Bouché et al. (2007, 2012) and Förster Schreiber et al. (2009), using the SINFONI pipeline (SPRED, Schreiber et al. 2004; Abuter et al. 2006) complemented with custom routines such as the OH sky line removal scheme of Davies (2007) and the Laplacian edge cosmic-ray removal technique of van Dokkum (2001).

Regarding the wavelength calibration, we emphasize that we applied the heliocentric correction to the sky-subtracted frames, and each frame was associated with a single reference frame by cross-correlating each of the science frames spectrally against the reference frame (the first science exposure). For each observing block, we use the quasar continuum to spatially register the various sets of observations. Finally, we created a co-added cube from all the individual sky-subtracted 600 s exposures using a median clipping at 2.5σ.

Flux calibration was performed on a night-by-night basis using the broadband magnitudes of the standards from the Two Micron All Sky Survey. The flux calibration is accurate to ~15%. Finally, the atmospheric transmission was calibrated out by dividing the science cubes by the integrated spectrum of the telluric standard.

In Figures 1 and 2 we present the flux, velocity, and dispersion maps for each galaxy.

2.2. UVES Observations

The UVES data were taken during two distinct observing runs: 13 hr in Service Mode (ESO 79.A-0600) and 1.5 n in Visitor Mode (ESO 80.A-0364). We used a combination of 390 + 564, 390 + 580, and 390 + 600 nm central wavelength settings appropriate to the range of wavelengths for the lines we were seeking. The total exposure time for each object was split into two or three equal observing blocks to minimize the effect of cosmic rays. The slit width was $1\farcs2$, yielding a spectral resolution $R = \lambda/\Delta\lambda \sim 45{,}000$. A 2 × 2 CCD binning was used for all observations. The observational setups are summarized in Table 2.

The data were reduced using version 3.4.5 of the UVES pipeline in MIDAS. Master bias and flat images were constructed using calibration frames taken closest in time to the science frames. The science frames were extracted with the optimal option. The blue portion of the spectra was checked order by order to verify that all were properly extracted. The spectra were then corrected to the vacuum heliocentric reference frame. The resulting spectra were combined, weighting each spectrum with its signal-to-noise ratio (S/N). To perform absorption line analysis, the spectra were normalized using cubic spline functions of the orders of 1–5 as the local continuum. In this paper, we present the UVES data for the four pairs that will be classified as pairs suitable for wind studies, hereafter wind-pair. The remainder will be presented in subsequent papers. We find it important to mention that UVES and SINFONI data have their wavelength calibrations made in vacuum.

2.3. Ancillary Data

For all of the galaxy–quasar pairs, we checked for ancillary data and found two pairs with available *HST* observations imaging. The first one is J0448+0950, which has *HST*/WFPC2 (F555W filter) data from Lehnert et al. (1999, *HST* proposal ID 5393). The second one is J0839+1112, which has *HST*/WFPC2 (F702W filter) data from *HST* proposal ID 6557 (PI: Steidel), first published in Kacprzak et al. (2010). These *HST* data are discussed later and shown in Figure 1.

3. RESULTS

3.1. Galaxy Emission Kinematics

In most cases, the PSF cannot be estimated from the data themselves given the small SINFONI IFU FOV (8×8 arcsec^2). Here, one advantage of using galaxy–quasar pairs is that the knowledge of the PSF can be determined from the quasar continuum in the data cube. This information is crucial for deriving intrinsic values of host galaxy parameters. Moreover, fitting a disk model to seeing-limited data requires good knowledge of the PSF (see Cresci et al. 2009; Epinat et al. 2012).

From IFU data, it is customary to extract moment maps (e.g., flux, velocity, and dispersion maps) from the emission line spectra. This is usually done on a pixel-by-pixel basis, as most algorithms treat the spaxels to be independent (e.g., Law et al. 2007, 2009; Cresci et al. 2009; Epinat et al. 2009; Förster Schreiber et al. 2009), a condition that requires high-quality data with a high S/N in each spaxel, in order to constrain the width and centroid of the emission lines. Here, we avoid shortcomings of the traditional techniques by comparing the three-dimensional (3D) data cubes directly to a 3D galaxy disk model using the GalPak^{3D} tool (Bouché et al. 2015). The algorithm models the galaxy directly in 3D (x, y, λ), and the model is then convolved with the atmospheric PSF and the instrumental line-spread function. The (intrinsic) model parameters are optimized using Monte Carlo Markov Chains (MCMC), from which we compute the posterior distributions on each of the parameters. The form of the rotation curve $v(r)$ is given by an arctangent profile with $v(r) = V_{\max}\ 2/\pi\ \arctan(r/r_t)$, where r_t is the turnover radius and $V_{\max}$ the maximum rotation velocity. The algorithm has several advantages: (i) the dynamical center does not need to be fixed spatially, and (ii) the supernova remnant (SNR) required per spaxel for the creation of 2D velocity maps is relaxed. In addition, since the actual PSF is well known from the quasar continuum, the returned parameters, including the galaxy position angle (PA, which is defined by the angle between the celestial north and the galaxy major axis, anticlockwise), inclination (i), size, and maximum rotation velocity ($V_{\max}$)[6], are intrinsic (or deconvolved) galaxy parameters. Extensive tests presented in Bouché et al. (2015) show that the algorithm requires data with a SNR $_{\max} > 3$ in the brightest pixel. For high SNR, all parameters can be well recovered, but in low SNR data, degeneracies can appear: for instance, between the turnover radius r_t and the maximum rotation velocity $V_{\max}$.

In order to first assess the flux profile properties, exponential versus Gaussian surface brightness profile, and

[6] Since the three-dimensional disk model is inclined, the value $V_{\max}$ is the deprojected maximum velocity, corrected for inclination.

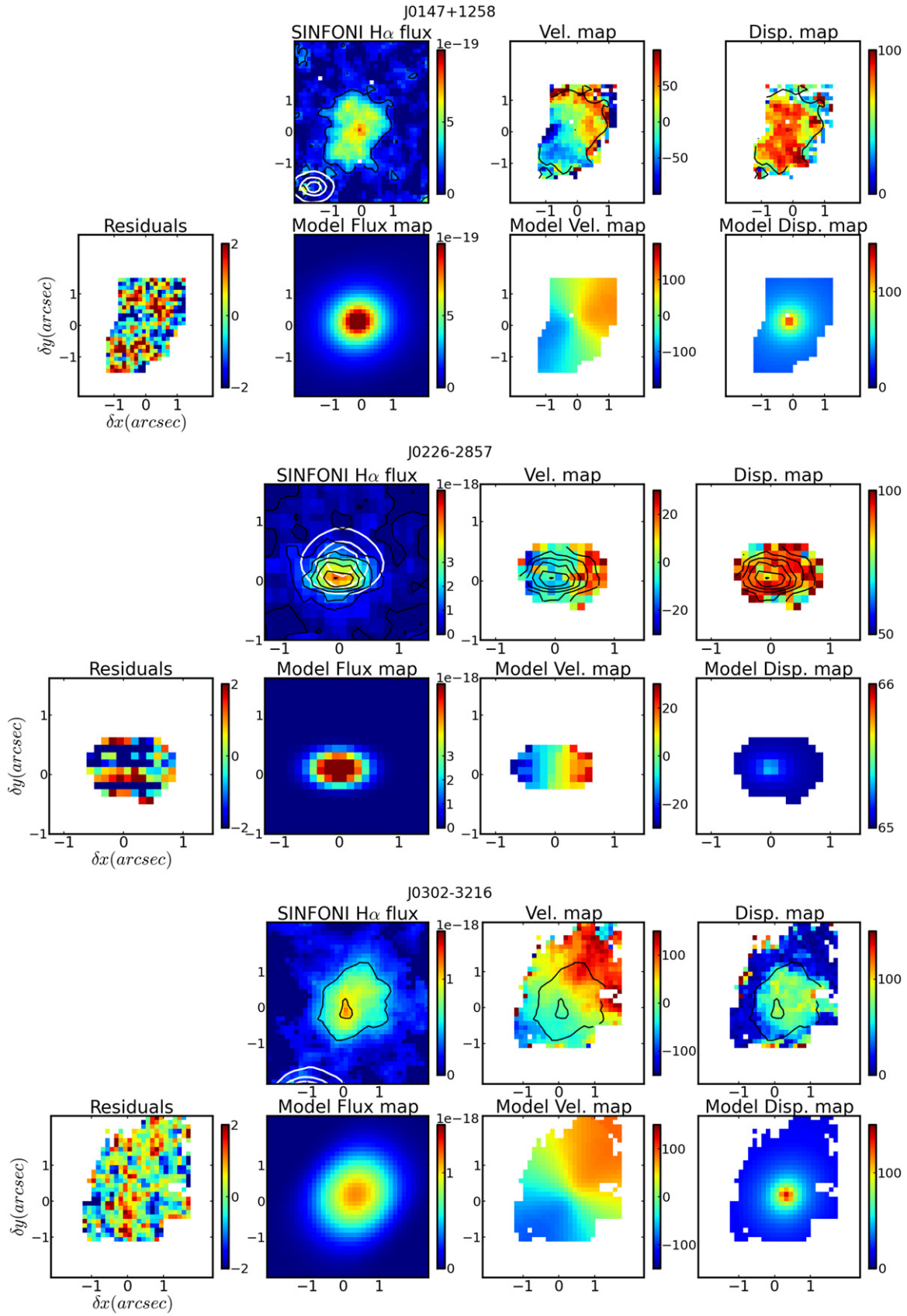

Figure 1. *From left to right:* top: the *HST*/WFPC2 image (when available), the Hα *J*-band SINFONI flux (erg s^{-1} cm^{-2}), the velocity map (in km s^{-1}) derived from the SINFONI data, and the dispersion map (in km s^{-1}). Bottom: the residuals cube represented in 2D (in σ), the intrinsic reconstructed galaxy with GalPaK^{3D} (deconvolved from the PSF given by the quasar), its velocity map, and the dispersion map. The quasar position is represented by the white contours on the observed flux maps when present in the map. In each panel, north is up and east is to the left.

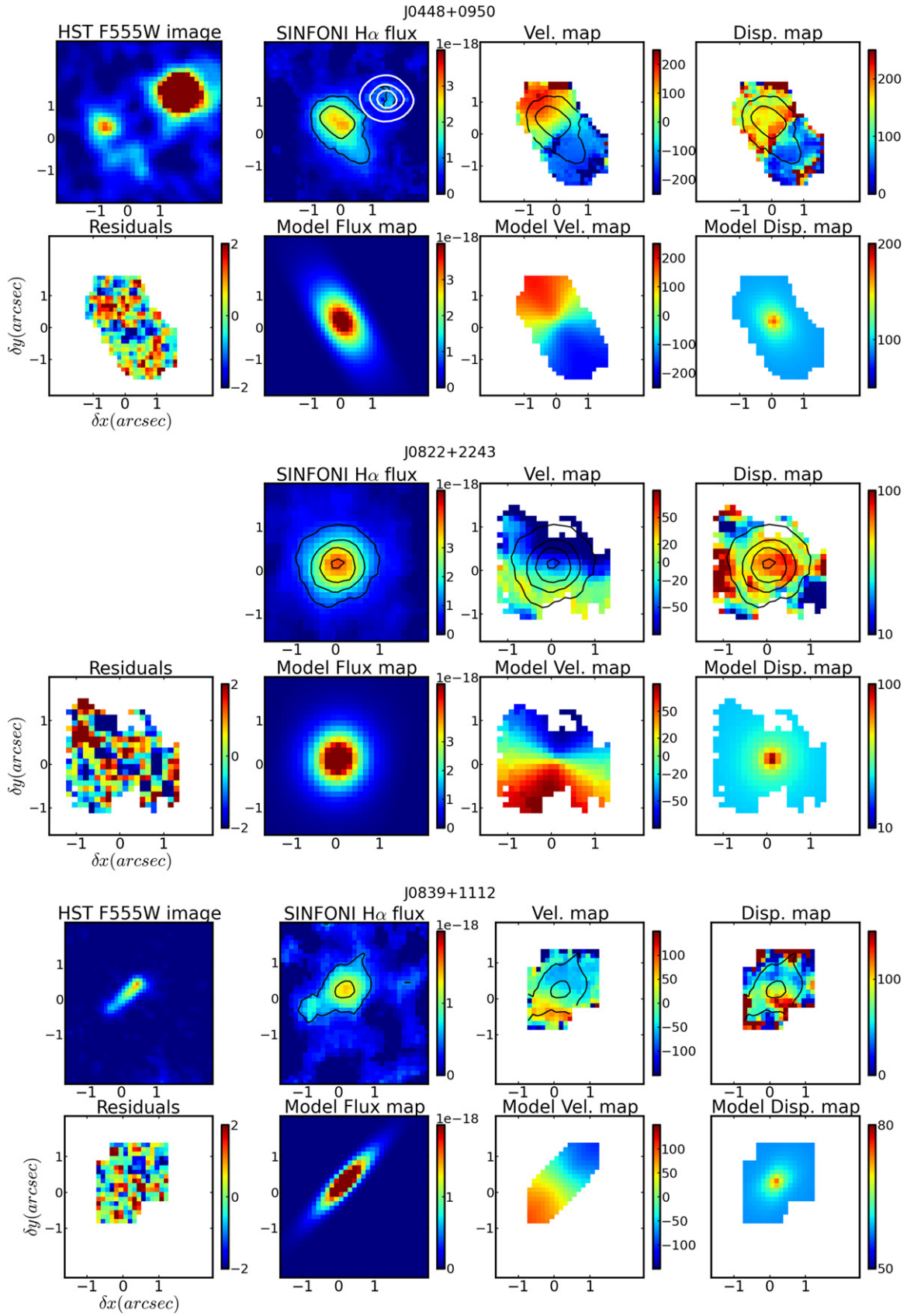

Figure 1. (Continued.)

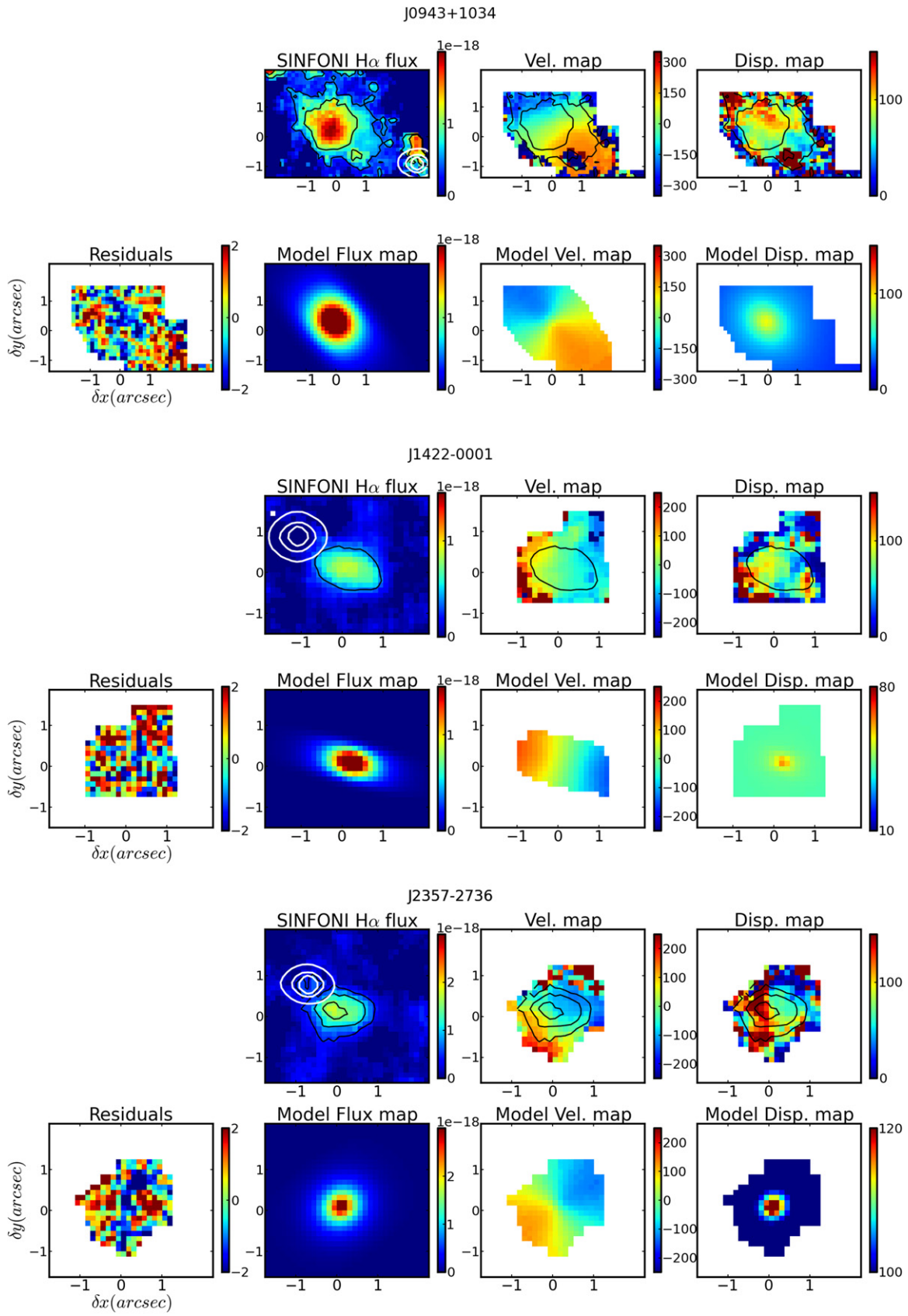

Figure 1. (Continued.)

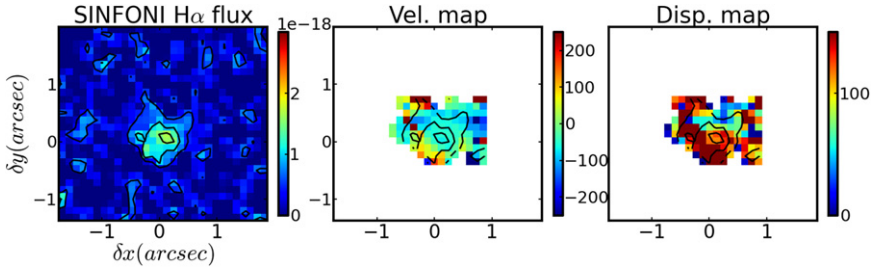

Figure 2. Same as Figure 1 but for the J1441+0443 galaxy. This galaxy has the lowest SNR, below the threshold where we can trust the GalPaK^{3D} results. Even if this galaxy is classified as wind-pair from its apparent PA, the low SNR does not allow us to build a wind model.

Table 2
Summary of UVES Observations

Target	Setting λ_c (nm)	$T_{\rm exp}$ (s)	Run ID[a]	Date
J0147+1258	390+580	4440	SM/079.A-0600(B)	2007 Jul 23 2007 Aug 14
J0226–2857	390+580	9000	SM/079.A-0600(B)	2007 Jul 24, 27 2007 Sep 04
J0302–3216	390+564	5430	SM/079.A-0600(B)	2007 Aug 02
J0448+0950	390+564	13200	VM/080.A-0364(A)	2008 Jan 28, 29
J0822+2243	390+564	7200	VM/080.A-0364(A)	2008 Jan 29
J0839+1112	390+564	13200	VM/080.A-0364(A)	2008 Jan 28
J0943+1034	390+580	9000	SM/079.A-0600(B)	2007 Apr 18, 22
J1422–0001	390+564	9000	SM/079.A-0600(B)	2007 Apr 12, 14
J1441+0443	390+600	8100	VM/080.A-0364(A)	2008 Jan 28, 29
J2357–2736	390+564	4440	SM/079.A-0600(B)	2007 May 15

Note:
[a] SM stands for Service Mode and VM for Visitor Mode.

Table 3
Kinematic and Morphological Parameters

Galaxy (1)	b(kpc) (2)	α (°) (3)	Inclination (°) (4)	PA (°) (5)	Flux (6)	$V_{\rm max}$ (7)	Redshift (8)	$r_{\frac{1}{2}}$ (9)	Profile (10)	Class (11)
J0147+1258	17.9 ± 1.02	30 ± 30	24.4 ± 3.3	-69 ± 3	$1.63 \cdot 10^{-16}$	241 ± 38	1.0389	7.11 ± 0.20	EXP	Face-on
J0226–2857	$\leqslant 2.0 \pm 1.01$	56 ± 3.0	47.9 ± 1.0	91 ± 1	$2.01 \cdot 10^{-16}$	50 ± 12	1.0223	2.69 ± 0.04	EXP	Ambig.
J0302–3216	19.7 ± 0.95	16 ± 15	30.4 ± 1.5	-37 ± 3	$2.70 \cdot 10^{-16}$	180 ± 15	0.8223	8.99 ± 0.31	EXP	Face-on
J0448+0950	13.7 ± 0.96	79 ± 3.0	52.0 ± 1.2	31 ± 1	$5.03 \cdot 10^{-16}$	253 ± 10	0.8391	7.85 ± 0.07	EXP	Wind-pair
J0822+2243	21.8 ± 0.95	32 ± 30	17.9 ± 0.7	168 ± 1	$5.04 \cdot 10^{-16}$	328 ± 14	0.8102	4.14 ± 0.06	EXP	Face-on
J0839+1112	26.8 ± 0.94	59 ± 6.0	72 ± 5[a]	139 ± 4	$1.53 \cdot 10^{-16}$	113 ± 20	0.7866	5.65 ± 0.29	EXP	Wind-pair
J0943+1034	24.3 ± 1.01	32 ± 3.0	43 ± 5[b]	140 ± 1	$3.81 \cdot 10^{-16}$	327 ± 10	0.9956	8.73 ± 0.21	EXP	Inflow-pair
J1422–0001	12.7 ± 0.98	17 ± 5.0	55 ± 5	81 ± 3	$8.93 \cdot 10^{-17}$	130 ± 20[c]	0.9096	4.30 ± 0.16	GAU	Inflow-pair
J1441+0443[b]	10.1 ± 1.02	90 ± 6.0	⋯	87 ± 4	$6.62 \cdot 10^{-17}$	⋯	1.0384	2.99 ± 0.18	GAU	Wind-pair
J2357–2736	6.7 ± 0.95	68 ± 4.0	51.6 ± 2.2	109 ± 2	$1.29 \cdot 10^{-16}$	187 ± 15	0.8149	5.53 ± 0.14	GAU	Wind-pair

Notes:
(1) Quasar name; (2) impact parameter; (3) azimuthal angle α (Section 3.3); (4) galaxy inclination (degrees); (5) position angle (degrees); (6) integrated Hα flux of the galaxy (erg s^{-1} cm^{-2}); (7) maximum rotation velocity (km s^{-1}); (8) Hα redshift (see Section 3.2); (9) half-light radius (kpc); (10) assumed flux profile (Exp. or Gau.); (11) class (inflow-pair/wind-pair) based on α selection.
[a] The inclination is determined from the *HST* data.
[b] Galaxy parameters are derived from 2D fitting (galfit2D).
[c] Turn-over radius is fixed to $r_t/r_{1/2} = 0.25$.

axis ratios, we analyzed the collapsed cubes (i.e., line integrated, continuum-subtracted) with the galfit2D tool. This tool is our custom 2D version of GalPak^{3D}, an equivalent to Galfit (Peng et al. 2010), which fits isophotes to the images (with the PSF convolution) and then uses these isophotes to compute the radial surface brightness profile. With the results from the 2D algorithm, we obtain an initial indication of the galaxy inclination from the axis ratio and the profile shape (exponential versus Gaussian), before analyzing the kinematics in the 3D data. We find that seven galaxy surface

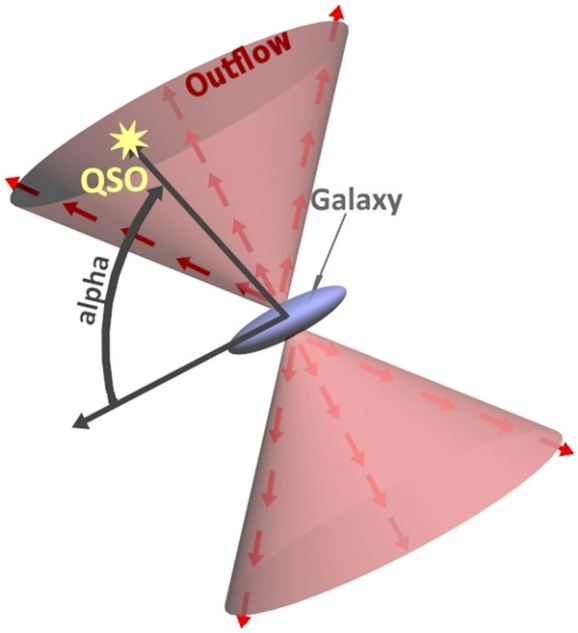

Figure 3. Scheme showing the alpha angle, corresponding to the angle between the galaxy major axis and the quasar position.

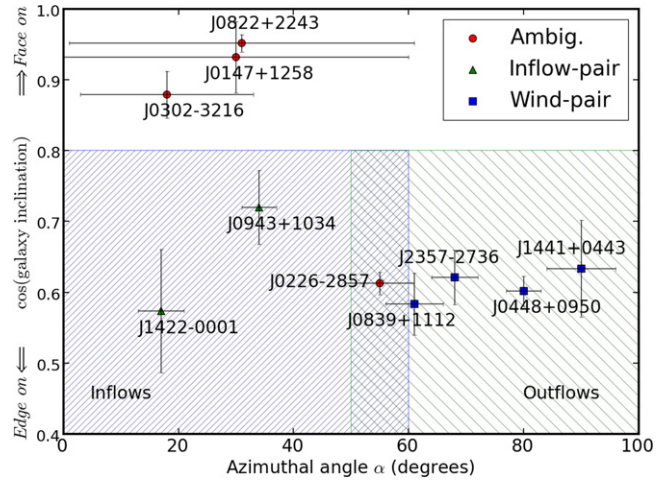

Figure 4. Galaxy inclinations for the SIMPLE sample as a function of the azimuthal angle α. Note there are three types of galaxies in this sample: the wind-pairs, which have an azimuthal angle larger than $60° \pm 10°$; the inflow-pairs, with α lower than $60° \pm 10°$; and pairs that are ambiguous due to uncertainty on α. It is difficult to derive the azimuthal angle for a nearly face-on galaxy. The wind-pair and inflow-pair classes describe the fact of having the quasar absorptions tracing outflows and inflows, respectively.

brightness profiles can be described by exponential profiles, while three are best described by a Gaussian profile (e.g., J1422–0001).

Using the GalPaK^{3D} tool, we fit the kinematics directly to the data cubes. The results are shown in Table 3. We emphasize that the surface brightness profile breaks the common inclination-V_{max} degeneracy in kinematic analysis. For every galaxy, we ran the algorithm for 10,000 iterations and checked that the MCMC converged for each of the parameters and estimated the uncertainties from the last 60% of the iterations. For J1422−0001, some of the kinematic parameters remain unconstrained, because the rotation curve appears shallow such that the turnover radius r_t and the circular velocity V_{max} are degenerate. The parameters relevant for this study for defining the kinematic major axis (PA) are well constrained, however.

As we will see in Section 4 (also illustrated in Figure A1), galaxy inclination is a critical parameter for the wind model. We cross-check the inclination measured using various methods (mainly galfit2D and GalPaK^{3D}) and from the SINFONI and *HST* data sets when present. In particular, for J0943+1034, the galaxy's inclination is set to the value obtained from the 2D profile fitting since GalPaK^{3D} did not converge for the turnover radius parameter. For J0839+1112, the galaxy's inclination is set to the value obtained from the archival *HST* image. For J0448+0950, the galaxy's inclination obtained from the SINFONI and *HST* data is consistent.

In Figure 1 we present the data, i.e., the observed flux and kinematics maps, and the fitted model. For each galaxy, the SINFONI data are shown in the first row, along with the *HST* image when available. In the second row, we present the results from the 3D kinematic fitting with the GalPaK^{3D} algorithm, where we show the dispersion, velocity, flux, and residual maps, from right to left. The residuals maps are generated from the residual cubes, which are just the difference between the data and the model normalized by the pixel noise. The 2D maps show the mean of the residuals in each spaxel normalized by its standard error. All the panels have north up and east to the left.

3.2. Redshifts

An accurate systemic redshift is crucial to characterize the outflow velocity and ultimately the outflow mass loading factor. The GalPaK^{3D} algorithm outputs the wavelength of the Hα emission line from the axisymmetric disk model. Since the galaxy distribution may be somewhat asymmetric, this sometimes lead to a redshift bias.

Therefore, we use two different methods. First, we determine the redshift from the mean of the wavelength of the reddest and the bluest (Gaussian) Hα emission lines along the kinematic major axis. As a second check, we create a pseudo-longslit along the kinematic major axis and determine z_{sys} from the sharp transition in the p–v diagram. We find that both methods yield consistent results. These redshifts are listed in Table 3.

The resulting intrinsic galaxy parameters will now allow us to build a cone model in order to reproduce the data for galactic outflows.

3.3. Azimuthal Dependence

In order to begin the wind modeling, we must first select galaxy–quasar pairs for which the quasar LOS intercepts the galactic winds. This can be achieved using the quasar azimuthal angle α between the galaxy major axis and the quasar (Figure 3), because the presence of strong Mg II absorbers is a strong function of α as demonstrated by numerous recent studies (Bohlin et al. 2011; Bouché et al. 2012; Bordoloi et al. 2014; Lan et al. 2014). Hence, we use the quasar position relative to the associated galaxy major axis, using the inclination and major-axis determined from the SINFONI data (Figure 1), to classify the different galaxy–quasar pairs in two main categories: pairs suitable for wind studies (wind-pair) for likely outflows and pairs suitable for accretion studies (inflow-pair) for likely inflows.

Figure 4 shows the azimuthal angles α versus the galaxy's inclinations for our SIMPLE sample of 10 galaxy–quasar pairs. Pairs with $60° \leqslant \alpha \leqslant 90°$ are selected to be wind-pairs. Pairs with $0° \leqslant \alpha \leqslant 30°$ correspond to the cases where the quasar LOS does not probe outflows but rather probes the extended parts of gaseous disks, where the gas can potentially (or is likely) to be inflowing (inflow-pair) as in Bouché et al. (2013).

Naturally, the azimuthal angle for galaxies with low inclinations, corresponding to face-on cases, is very difficult to constrain. These are then indexed as "face-on" cases. Pairs with $\alpha \sim 45°$ correspond to ambiguous cases where it is difficult to argue for outflows or inflows. For instance, J0226–2857 falls into that category with the additional difficulty that this galaxy has a very low impact parameter ($b = 0\farcs3$ or <2.0 kpc), i.e., the LOS is likely dominated by absorption from the galaxy interstellar medium.

Figure 4 shows that four galaxies are favorable to study galactic wind properties: J0448+0950, J2357–2739, J0839+1112, and J1441+0443 these are classified as wind-pairs in Table 3. J1441+0443 is excluded from subsequent analysis because our SINFONI data do not meet the requirement of SNR ~ 3 imposed by our intensive tests of the GalPaK^{3D} algorithm.

4. WIND PROPERTY ANALYSIS

4.1. Wind Sub-sample Analysis

For each galaxy–quasar pair, we have the quasar spectrum for all the SIMPLE galaxies taken with the VLT/UVES instrument. In these spectra, we identified three main absorption features: the Mg II ($\lambda\lambda$2796, 2803) doublet and the Mg I λ2852 absorption line. Because of our selection in $W_r^{\lambda 2796}$ of 2 Å (to ensure that the host was within the SINFONI FOV), the Mg II doublet is saturated. Hence, we use the Mg I absorption line, which is not saturated and in most cases shows an asymmetric profile. This asymmetry can sometimes be seen in the Mg II doublet, but less clearly. We center the spectrum on every absorption line using the derived redshifts. For each absorption line, we transform wavelength to velocity, using the reference wavelengths in the vaccum. From the absorption system kinematics and geometrical properties of the galaxy, we can now build the wind model for the three galaxies.

4.1.1. Cone Wind Modeling

We follow Bouché et al. (2012) and Kacprzak et al. (2014) in modeling the wind as a bi-conical outflow using the geometric parameters (inclination, α) set by the SINFONI data. The principle is to create a cone perpendicular to the galactic plane, fill it with uniformly distributed particles, and assume that the mass flux is conserved. The particles represent cold gas clouds entrained in the wind, since the equivalent width of the absorption lines is the sum/combination of several individual components (Ménard and Chelouche 2009), each of which corresponds to a "cold" gas cloud (10^4 K) entrained by supernova-heated hot winds ($T > 10^6$ K). Since the galaxy inclination, PA, and azimuthal angle are previously determined from observations using GalPaK^{3D} and other methods, the only free parameters are $V_{\rm out}$ and the cone opening angle $\theta_{\rm max}$. For simplicity, we assign the clouds a constant radial velocity $V_{\rm out}$, i.e., we assume that the LOS intercepts the clouds far from the acceleration region.

The cone is built along the x-, y-, and z-axes: x and y represent the sky plane, and z corresponds to the cone height. For a galaxy with 0° inclination, the cone direction will be along the LOS. We then rotate the cone along the y-axis to match the galaxy's inclination derived from our SINFONI data and create a simulated absorption profile from the distribution of cloud velocities projected along the quasar LOS (z-axis).

We generate $\sim 10^6$ particles in a cone, which are grouped by bins of projected velocities. The quasar LOS is set by the impact parameter (b) and α, both of which are derived from the SINFONI data cubes. Due to the Monte Carlo generation of particles, stochastic effects create fluctuations in the simulated profiles. This noise does not impact the resulting equivalent widths and thus the derived outflow velocities.

We then convolve the particle velocity distribution with the UVES instrument resolution. Additionally, in order to simulate the instrument noise, we add Poisson noise to the simulated profile. This random Poisson noise has the same S/N as the data and provides for a more meaningful comparison. In order to give an intuitive feel for this geometric model, we show in the Appendix examples of simulated profiles using different galaxy inclinations, outflow velocities, and opening angles.

4.1.2. Galaxy Contribution Model

Since our sample consists of pairs with small impact parameters ($b < 20$ kpc) and with inclined galaxies (from $\sim 18°$ to $\sim 55°$), we improve our model by adding the galaxy contribution for the quasar–galaxy pairs with the lowest impact parameters ($b \leqslant 10$ kpc) such as J2357–2736 (Section 4.2.3). The procedure is nearly the same as the cone model: we generate particles in a disk with an exponential distribution from the center to the edge. We take the galaxy half-light radius derived with GalPaK^{3D} to estimate a realistic contribution from the disk. The thickness of the disk is set to be 0.15 times this radius. We assign the particles a constant circular velocity corresponding to the maximum velocity of the galaxy. The velocity distribution of the disk is naturally strongly dependent on the azimuthal angle with a maximum offset at $\alpha = 0°$ and a distribution centered around 0 km s^{-1} at $\alpha = 90°$.

4.2. Comments on Individual Wind-pairs

4.2.1. J0448+0950

The galaxy near the quasar J0448+0950 has an impact parameter $b = 13.7$ kpc and an Hα flux of 5.03×10^{-16} erg s^{-1} cm^{-2}. Its azimuthal angle α of $\sim 79°$ and inclination i of $\sim 52°$ make it a wind-pair (Figure 4). This galaxy has an SFR of $\sim 13\ M_\odot$ yr^{-1} (see Section 4) and a redshift of 0.8390.

In addition to our SINFONI data, we retrieved ancillary data from *HST*/WFPC2 (F555W filter). These *HST* data allow us to compare the morphology of the galaxy (see Figure 1) with the SINFONI one. In both data sets, one sees that the galaxy has an asymmetric flux distribution (Figure 1) with a brighter area somewhat offset with respect to the kinematic center. Comparing the *HST* image and SINFONI flux map (the quasar was subtracted in SINFONI Hα flux), the PA and inclination of the galaxy are in good agreement.

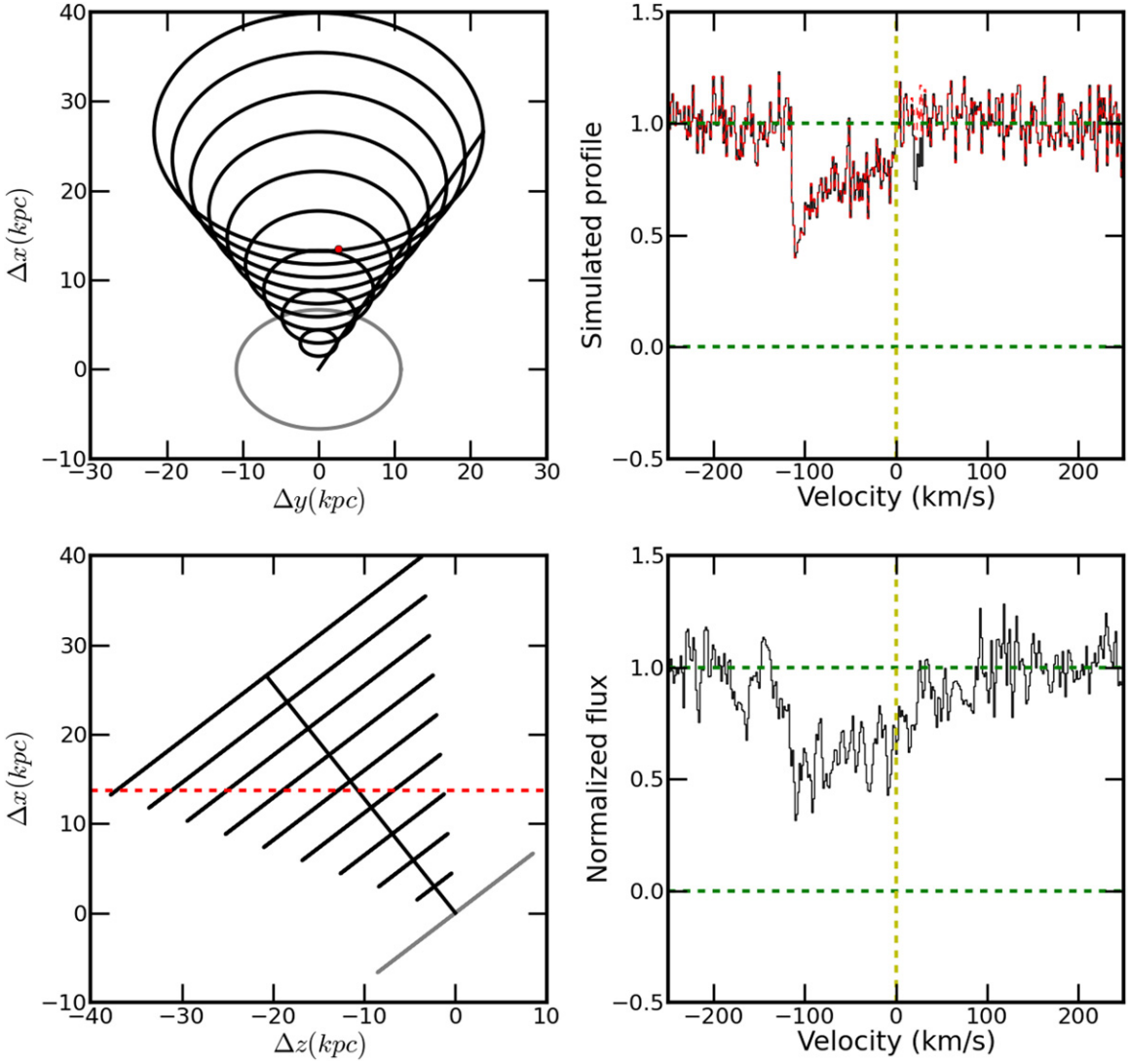

Figure 5. Representation of the cone model and quasar spectrum associated with the J0448+0950 galaxy. *Left:* the cone model seen in the sky plane where the *y*-axis corresponds to the galaxy major axis and *x* to its minor one. The gray circle represents the inclined galaxy disk, and the black circles illustrate the gas outflow cone. *Bottom left:* a side view of the cone where the *z*-axis corresponds to the quasar LOS direction with the observer to the left. *Right:* normalized flux for the Mg I λ2852 absorption line observed with UVES (bottom) where we can see an outward asymmetry, and the reconstructed profile (top). The red dashed line gives the simulated profile without taking into account the galaxy contribution. The black line does take into account this contribution. Note that this model does not reproduce the depth of the absorption line.

After determining the geometrical parameters for this galaxy, we can build a cone model as described in Section 4.1.1. In Figure 5, we compare the simulated profile for Mg I λ2852 [7] to the observed absorption in the UVES data (right column of the figure). To generate this simulated profile,[8] we adjusted the outflow speed $V_{\rm out}$ and the cone opening angle θ, while keeping the geometrical parameters fixed. The best values are an outflow speed $V_{\rm out}$ of $115 \pm 10\,{\rm km\,s^{-1}}$ and a cone opening angle $\theta_{\rm max}$ of $40° \pm 5°$. The errors represent the maximum allowed range values for $V_{\rm out}$ and $\theta_{\rm max}$.

We note that our simulated profile reproduces the asymmetry and equivalent width of the observed profile. Note, our model does not attempt to reproduce the depth of the profile since it is arbitrarily normalized. The fluctuations in the simulated profile are due to stochastic effects from the Monte Carlo particle distribution.

Outflow rates and mass loading factors for each galaxy identified as wind-pairs are detailed in Section 4.3.

4.2.2. J0839+1112

In our sample, the galaxy toward J0839+1112 has the largest impact parameter *b* 26.8 kpc. With an Hα flux of 1.53×10^{-16} erg s^{-1} cm^{-2}, an inclination *i* of ~72°, and an azimuthal angle α of ~59°, this galaxy also belongs to the wind-pair subsample defined in Section 3.3. Its SFR is ~3.4 $M_\odot$ yr^{-1}, and it has a redshift of $z = 0.7866$.

In Figure 1 we compare archival *HST*/WFPC2 (F702W filter) images to our SINFONI Hα data. Both data sets show a slight asymmetry in the galaxy flux distribution and a similar PA. For the galaxy inclination, we used galfit2D on the *HST*

[7] We use Mg I λ2852 since Mg II λ2796 is saturated.

[8] The galaxy contribution is also considered in the simulated profile (the redshifted contribution in upper right of Figure 5).

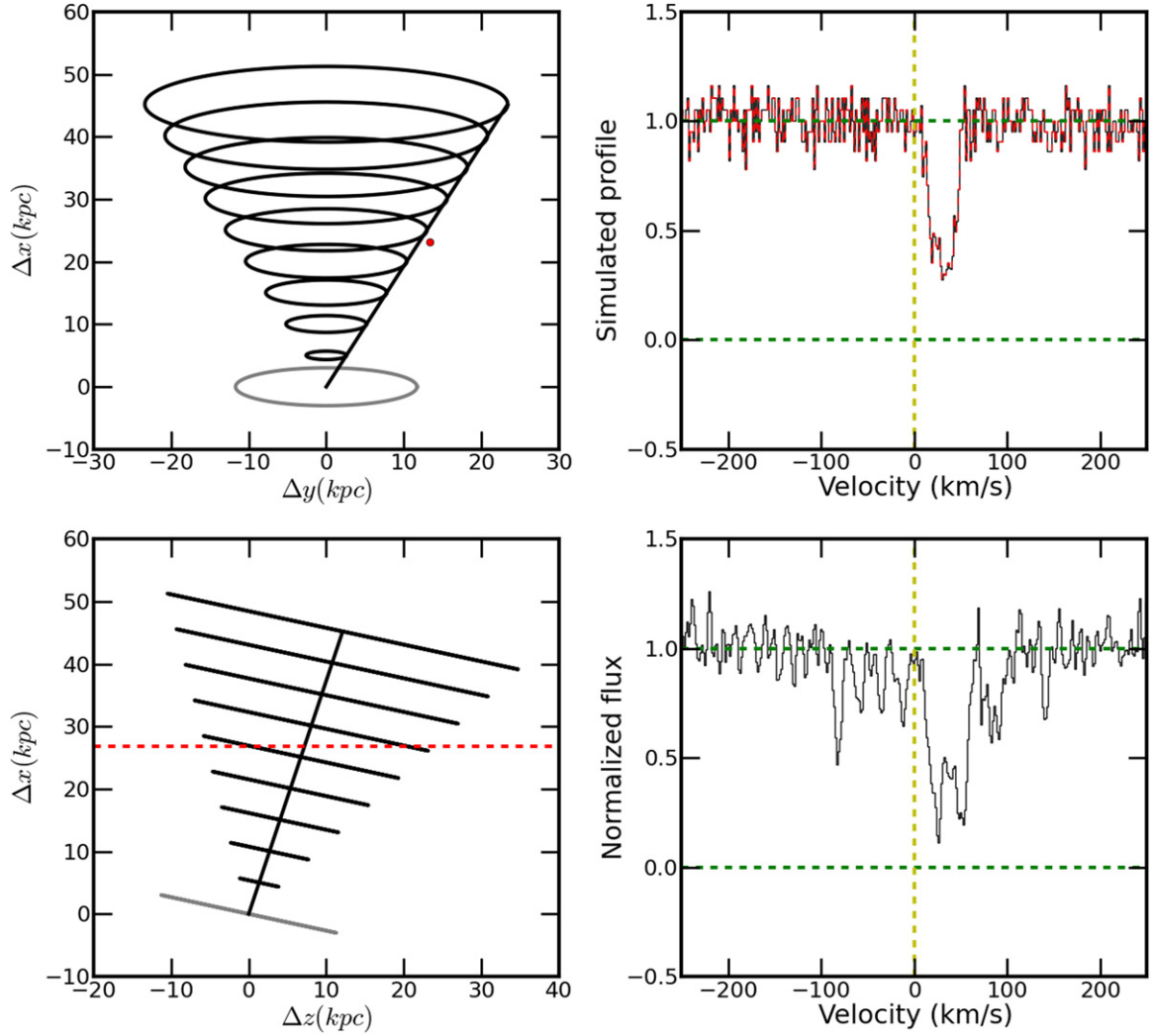

Figure 6. Same as Figure 5 for the J0839+1112 galaxy where no galaxy contribution can be seen.

image to cross-check the results from the 3D fitting and found good agreement (within $\pm 15°$) between the two methods.

As for J0448+1112, we generated a simulated profile from the wind cone model using the geometrical parameters from the SINFONI+*HST* data and adjusted the outflow speed $V_{\rm out}$ and the cone opening angle θ, while keeping the geometrical parameters fixed. Figure 6 shows the simulated profile and the Mg I absorption from the UVES data (right column of the figure). We constrained an outflow speed $V_{\rm out}$ of 105 ± 10 km s^{-1} and a cone opening angle of $\theta_{\rm max}$ of $30° \pm 5°$. The impact parameter b is too high to consider any contribution from the galaxy.

4.2.3. J2357−2736

The last individual case from our wind subsample is the galaxy along the J2357−2736 LOS. The host galaxy has the smallest impact parameter b to the quasar LOS with b of 6.7 kpc. This galaxy has an Hα flux of 1.29×10^{-16} erg s^{-1} cm^{-2} and an SFR of $\sim$3.3 $M_\odot$ yr^{-1}. Its inclination i is $\sim 52°$, and it is classified as wind-pair because of its azimuthal angle α of $\sim 68°$.

As in the previous two cases, we generated a simulated UVES profile using the wind model described in Section 4.1. Figure 7 (bottom) shows the UVES Mg I λ2852 absorption profile, whose asymmetry is reversed compared to the two other cases with a maximum optical depth at $V \sim 0$ km s^{-1}. However, any constant wind speed model will have an outward asymmetry (Figure A1), and the data clearly show the opposite, an inward asymmetry. For a profile with inward asymmetry, the strongest part of the absorption profile is located closer to the systemic velocity (e.g., bottom left of Figure 7). An outward asymmetry profile has the opposite behavior (e.g., Figure 5). This inward asymmetry is seen in the other non-saturated transitions (Zn IIλ2026, Mg I λ2026, Mn II ($\lambda\lambda$2576, 2594, 2606)) present in the UVES data (Figure 8).

Contrary to the other two cases, this galaxy has a very low impact parameter ($b \sim 6.7$ kpc), where the assumption of constant wind speed might break down. Indeed, the low-ionization material in momentum-driven winds and energy-driven winds is thought to be accelerated (e.g., Murray et al. 2005; Steidel et al. 2010) by the hot gas, by the radiation pressure, or both.

Therefore, instead of using a constant wind speed, we added a generic velocity profile such as $V(r) = V_{\rm out}\ 2/\pi \arctan(r/r_0)$,

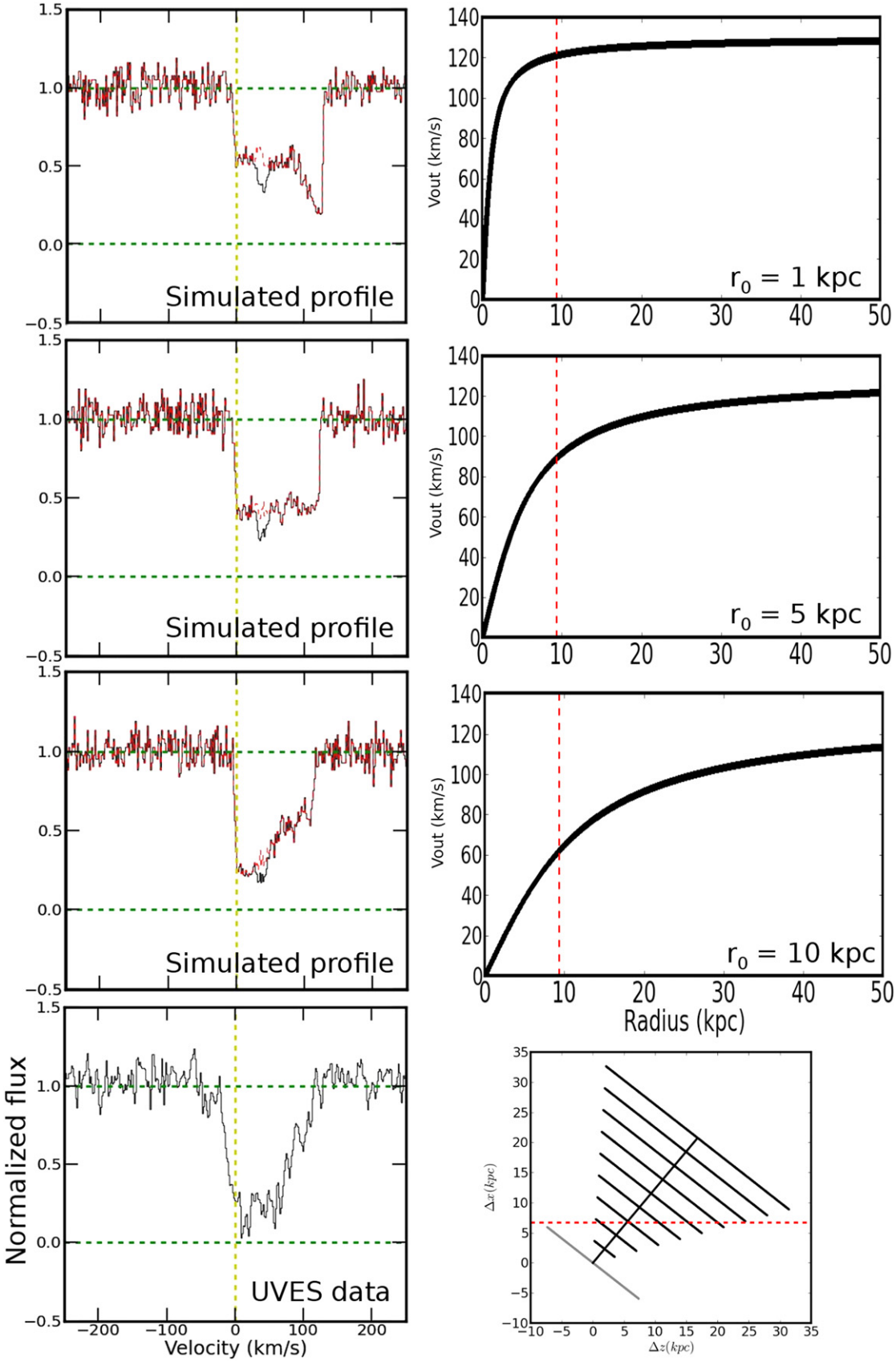

Figure 7. Left column: Mg I absorption from the J2357−2736 galaxy indicating that the model must include accelerating winds, from top to bottom: simulated absorption profiles with $r_0 = 1$, 5, 10 kpc, and the UVES data centered on Mg I λ2852. Notice that the asymmetry changes as r_0 increases; it goes from outward to inward asymmetry. Right column: the velocity profile corresponding to the associated simulated profile to the left where the turnover radius of the velocity profile (r_0) varies, from top to bottom: $r_0 = 1$, 5, 10 kpc. The red dashed line represents the distance between the galaxy and the quasar LOS ($b/\sin(\alpha)/\sin(i)$), corrected for the inclination i. The final simulated profile is the one directly above the data, with $r_0 = 10$ kpc.

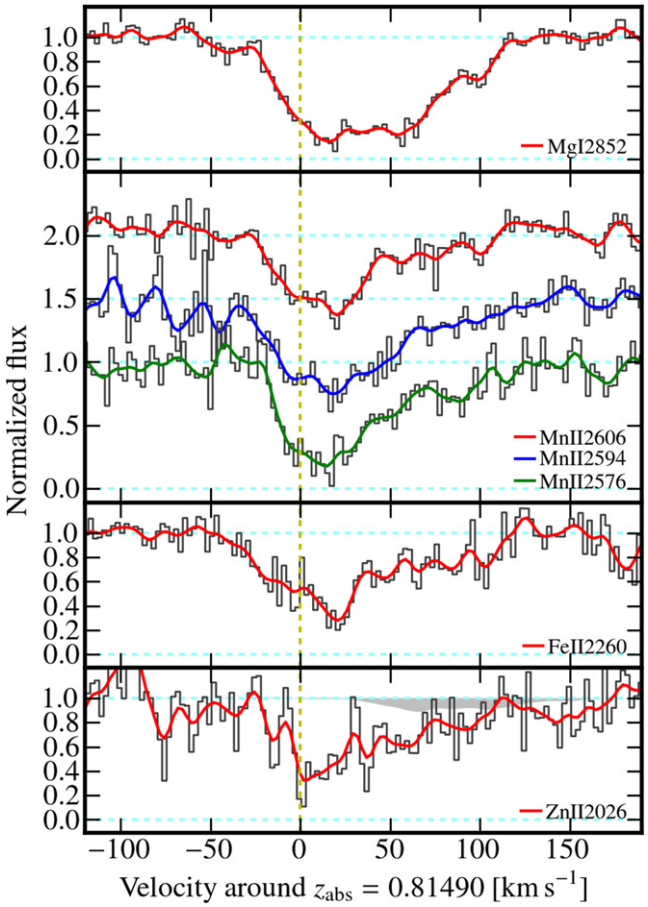

Figure 8. Absorption lines observed with UVES for J2357–2736. The solid lines are a Gaussian smoothing of the data (with a sigma of 1 pixel) to aid the eye. The gray shaded area in the Zn II (λ2026) panel is the absorption expected from the Mg I λ2026 line (derived by scaling the observed optical depth of the Mg I λ2852 line, ignoring potential saturation effects).

where r is the distance from the galaxy and r_0 is the characteristic turnover radius. Figure 7 shows the behavior of this model (dashed line) on the profile asymmetry for different values of r_0, illustrating that the asymmetry reverses as r_0 increases. The accelerated wind model that best describes the data is the one with $r_0 = 10$ kpc shown above the UVES spectrum in Figure 7. Similar to J0448+0950, we also included a contribution from the galaxy that appears to account for the bluest components.

For this case, we found an outflow speed $V_{\rm out}$ of 130 ± 10 km s^{-1} using a cone opening angle $\theta_{\rm max}$ of $45° \pm 5°$. Note that there is no degeneracy between $V_{\rm out}$ and r_0 as the various simulated profiles shown in Figure 7 are for the same outflow velocity. In other words, $V_{\rm out}$ is set by the reddest part of the profile, whereas r_0 is constrained by the profile shape.

Having determined outflow velocities for the three wind-pairs, we now focus on deriving the ejected outflow rates $\dot{M}_{\rm out}$ together with the mass loading factors η.

4.3. Outflow Rate

As discussed in Section 4.2.3, the equivalent width of the Mg I λ2852 absorption lines depends only on $\theta_{\rm max}$ and $V_{\rm out}$ from the cumulated distribution of projected velocities of gas cloud intercepted along the LOS, while the profile asymmetry depends on the system geometry, the particle density, and the outflow velocity ($V_{\rm out}$). From these constraints, we can constrain the total mass flux of this material traced by the low-ionization lines following Bouché et al. (2012) using the following equation:

$$\dot{M}_{\rm out} \approx \mu \cdot N_{\rm H}(b) \cdot b \cdot V_{\rm out} \cdot \frac{\pi}{2} \cdot \theta_{\rm max},$$
$$\frac{\dot{M}_{\rm out}}{0.5\,M_\odot\,{\rm yr}^{-1}} \approx \frac{\mu}{1.5} \cdot \frac{N_{\rm H}(b)}{10^{19}\,{\rm cm}^{-2}} \cdot \frac{b}{25\,{\rm kpc}} \times \frac{V_{\rm out}}{200\,{\rm km\,s}^{-1}} \cdot \frac{\theta_{\rm max}}{30°}, \quad (1)$$

where μ is the mean atomic weight, b the impact parameter, $\theta_{\rm max}$ the cone opening angle,[9] and $N_{\rm H}(b)$ the gas column density of hydrogen at the b distance.

The only parameter that remains to be constrained is the column density $N_{\rm H}(b)$. In order to determine the gas column density $N_{\rm H}$, we use the empirical relation of Ménard and Chelouche (2009) between neutral gas column density and Mg II equivalent width $W_r^{\lambda 2796}$:

$$N_{\rm HI} = \log\left[(3.06 \pm 0.55) \times 10^{19} \times \left(W_r^{\lambda 2796}\right)^{1.7\pm 0.26}\right]. \quad (2)$$

This relation, together with the tight correlation between Mg II equivalent width and dust content (as determined statistically from quasar extinction) from Ménard and Chelouche (2009), leads to a gas-to-dust ratio slightly smaller than that of the Milky Way H I column densities of $\log(N_{\rm HI}) = 19.5$ and above. Furthermore, the redshift evolution of the dust content of Mg II absorbers extrapolated to $z = 0$ shows that Mg II–selected aborbers extend the local relation between visual extinction A_V and the total hydrogen column $N_{\rm H}$ of Bohlin et al. (1978). This in turn indicates that the ionized gas contribution is negligible in regions with H I columns above $\log(N_{\rm HI}) = 19.5$, as also argued by Jenkins (2009), and that one can use the correlation between Mg II equivalent width and $N_{\rm HI}$ as a proxy for the $N_{\rm H}$ gas column density.

Given our selection criteria of $W_r^{\lambda 2796} > 2$ Å, we are very likely in a regime where the gas is mostly neutral. For our three wind-pair sight lines, the H I column densities are $\log(N_{\rm HI}) \approx 20.3$ for J0448+0950, $\log(N_{\rm HI}) \approx 20.1$ for J0839+1112, and $\log(N_{\rm HI}) \approx 19.9$ for J2357–2736. The rest equivalent widths $W_r^{\lambda 2796}$ determined from the UVES data and the corresponding $N_{\rm H}$ column densities for the wind-pair galaxies are listed in Table 4. In future work, we will be able to measure $N_{\rm HI}$ directly from UV spectroscopy with *HST*/Cosmic Origins Spectrograph (COS).

Figure 9 shows the Mg II rest equivalent width $W_r^{\lambda 2796}$ as a function of impact parameter b for quasar–galaxy pairs where the quasar is aligned with the minor axis (wind-pairs) from various literature samples (Kacprzak et al. 2011a, 2011b) and this paper. This figure shows that the tight anti-correlation between impact parameter b and W_r (Bouché et al. 2012) is confirmed at $b < 30$ kpc. The solid line traces the fiducial $1/b$ relation for mass-conserved bi-conical outflows (see Bouché et al. 2012).

[9] $\theta_{\rm max}$ is defined from the central axis, and the cone subtends an area Σ of $\pi \cdot \theta_{\rm max}^2$.

Table 4
Results for Galaxies J0448+0950, J2357–2736, J0839+1112 together with Literature Results

Galaxy (1)	b (kpc) (2)	$\log(N_{\rm H}(b))$ (3)	$V_{\rm max}$ (4)	$V_{\rm out}$ (km s^{-1}) (5)	$\theta_{\rm max}$ (6)	SFR (7)	$\dot{M}_{\rm out}$ (8)	$\frac{V_{\rm out}}{V_{\rm esc}}$ (9)	η (10)	Reference (11)
J0448+0950	13.7	20.30 ± 0.3	253 ± 10	115 ± 10	40 ± 5.0	13.6 ± 0.3	$4.6\ ^{+4.9}_{-3.2}$	0.16	0.70	This work
J0839+1112	26.8	20.10 ± 0.3	115 ± 8	105 ± 10	30 ± 5.0	3.4 ± 0.2	$3.6\ ^{+3.4}_{-2.2}$	0.43	2.11	This work
J2357–2736	6.7	19.92 ± 0.2	186 ± 15	130 ± 10	45 ± 5.0	3.3 ± 0.2	$1.2\ ^{+1.1}_{-0.7}$	0.24	0.75	This work
J081420G1	51.1	19.07 ± 0.2	131 ± 10	175 ± 25	30 ± 5.0	5.0[a]	$1.0\ ^{+1.4}_{-0.7}$	0.63	0.42	B2012
J091119G1	71.2	19.34 ± 0.2	231 ± 10	500 ± 100	30 ± 5.0	1.2[a]	$7.8\ ^{+12.2}_{-4.5}$	0.97	12.9	B2012
J102847G1	89.8	18.60 ± 0.2	162 ± 10	300 ± 25	30 ± 5.0	9.0[a]	$1.1\ ^{+1.5}_{-0.7}$	0.95	0.23	B2012
J111850G1	25.1	19.97 ± 0.2	116 ± 10	175 ± 80	30 ± 5.0	7.0[a]	$4.1\ ^{+10.0}_{-1.1}$	0.63	1.17	B2012
J225036G1	53.9	19.54 ± 0.2	240 ± 10	225 ± 50	30 ± 5.0	8.0[a]	$4.2\ ^{+7.3}_{-2.2}$	0.40	1.06	B2012
J1659+3735	58.0	18.89 ± 0.15	140 ± 10	40–80	40 ± 5.0	4.6–15	1.6–4.2	0.12–0.27	0.1–0.9	K2014

Notes:
(1) Galaxy name; (2) impact parameter (kpc); (3) gas column density at the impact parameter (cm^{-2}); (4) maximum rotational velocity of the galaxy (km s^{-1}); (5) wind velocity (km s^{-1}); (6) cone opening angle (degrees); (7) star formation rate ($M_\odot$ yr^{-1}); (8) ejected mass rate for one cone ($M_\odot$ yr^{-1}); (9) ejection velocity divided by escape velocity; (10) mass loading factor: ejected mass rate divided by star formation rate (for both cones); (11) references: B2012: Bouché et al. (2012), K2014: Kacprzak et al. (2014).
[a] SED-derived SFRs.

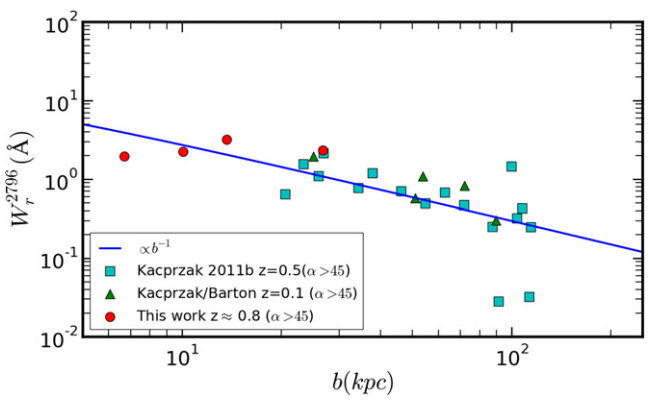

Figure 9. $W_r^{\lambda 2796}$ as a function of impact parameter b for galaxy–quasar pairs classified as wind-pairs.

Table 4 lists our estimated outflow rates determined using Equation (1). In order to determine the error bars for $\dot{M}_{\rm out}$, we take the maximum error of every parameter used to derive it. We thereby objectively determine the maximum uncertainty on the ejected mass rate. We also note that the errors on $\dot{M}_{\rm out}$ are dominated by the errors on $N_{\rm HI}$.

From the outflow rates, we compute the mass loading factor η by comparing it to the SFR. We derived the SFR from Hα using the Kennicutt (1998) calibration, which assumes a Salpeter (1955) initial mass function (IMF):

$$\mathrm{SFR}\left(M_\odot\ \mathrm{yr}^{-1}\right) = 7.9 \times 10^{-42} L_{\mathrm{H}\alpha}, \tag{3}$$

where $L_{\mathrm{H}\alpha}$ is the Hα luminosity in erg s^{-1} cm^{-2}. We note that the SFRs for the Salpeter IMF with no extinction correction are identical to using a dust correction of 1 mag (Zahid et al. 2013) with the Chabrier (2003) IMF, as the two IMFs are offset by −0.25 dex (see Table 2 in Bernardi et al. 2010).

The results for the three galaxies are shown in Table 4. If we assume that galactic winds are symmetric with respect to the galactic plane (Figure 3), the total ejected mass rate for a galaxy must be increased by a factor of 2, which gives $\dot{M}_{\rm out} \approx 9\ M_\odot\ \mathrm{yr}^{-1}$ for J0448+0950, $\dot{M}_{\rm out} \approx 2\ M_\odot\ \mathrm{yr}^{-1}$ for J2357–2736, and $\dot{M}_{\rm out} \approx 7\ M_\odot\ \mathrm{yr}^{-1}$ for J0839+1112.

Considering the ejection velocity of the winds (115, 105, and 130 km s^{-1} for J0448+0950, J0839+1112, and J2357–2736, respectively), it is interesting to test whether this velocity is large enough for the gas to leave the galaxy halo or if it will end up falling back onto the galaxy. The escape velocity $V_{\rm esc}$ for an isothermal sphere is given by the following equation (Veilleux et al. 2005):

$$V_{\rm esc} = V_{\rm max} \cdot \sqrt{2\left[1 + \ln\left(\frac{R_{\rm vir}}{r}\right)\right]}, \tag{4}$$

where $V_{\rm max}$ is the maximum rotation velocity of the galaxy and $R_{\rm vir}$ is the virial radius. Given that our galaxies' halos have a mass close to $10^{12}\,M_\odot$, their virial radius is approximately $R_{\rm vir} \approx V_{\rm max}/10\,H(z)$, where $H(z)$ is the Hubble constant at redshift z. For the wind-pairs, their virial radii are 225 kpc for J0448+0950, 103 kpc for J0839+1112, and 168 kpc for J2357–2736. We give these results in Table 4, along with the results on mass loading factors $\eta = \dot{M}_{\rm out}/\mathrm{SFR}$.

The ratio $V_{\rm out}/V_{\rm esc} < 1$ shows that the ejected gas does not escape from the galaxy halo and should therefore fall back into the galaxy. This gas contributes to the regulation of star formation in the galaxies.

5. CONCLUSIONS AND DISCUSSIONS

In this paper, we studied gas flows around SFGs using the SIMPLE sample of galaxy–quasar pairs (Paper I). The galaxies in this sample are located within $\leqslant 3''$ ($\leqslant 20$ kpc) of the background quasar sightlines due to the selection of absorption with rest equivalent width $\geqslant 2$Å. Thanks to the SINFONI IFU on the VLT and the new algorithm GalPaK^{3D}, we were able to recover the intrinsic morphological and kinematic properties of the galaxies from their Hα emission (Figure 1). The galaxies in our sample can be classified as wind-pairs or inflow-pairs according to the apparent

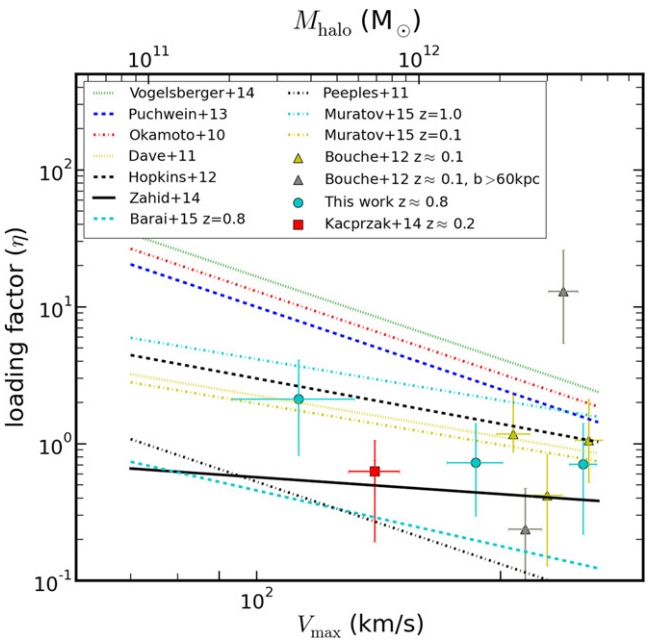

Figure 10. Comparison of predicted mass loading factors from theoretical/empirical models (curves) with values derived from observations (dots and triangles) as a function of the maximum rotational velocity. The results from this work are represented by the cyan circles. The red square shows the mass loading factor for a $z \sim 0.2$ galaxy (Kacprzak et al. 2014). The triangles show the results for $z \sim 0.2$ galaxies from Bouché et al. (2012). The gray triangles show the galaxies with quasars located at >60 kpc where the mass loading factor is less reliable due to the large travel time needed for the outflow to cross the quasar LOS (several 100 Myr) compared to the short timescale of the Hα-derived SFR (~10 Myr). The upper halo mass axis is scaled on V_{max} at redshift 0.8 from Mo & White (2002).

location of the quasar with respect to the galaxy major axis (Figure 4).

With this classification, we focused the analysis on the properties of galactic winds for the sub-sample of four suitable wind-pairs, although one galaxy has an SNR too low for a robust morphological (inclination) measurement. The wind properties are constrained from the high-resolution UVES spectra of the minor-axis quasars. We show that an simple cone model for galactic winds (Section 4.1.1) can reproduce the morphology of the UVES Mg I absorption profiles. The wind properties can be summarized as follows:

1. Like other recent works (e.g., Chisholm et al. 2014; Rubin et al. 2014), outflow velocities are smaller than the escape velocities, so the gas traced by low-ionization lines does not escape the galaxy halo.
2. At the lowest impact parameter ($b \sim 6$ kpc), one quasar–galaxy pair (J2357−2736) has an absorption profile consistent with an accelerated wind (Section 4.2.3).
3. Loading factors η vary between ~0.65 for the two massive galaxies and ~2 for the galaxy with the lowest mass (Figure 10). Our results indicate that the mass loading factors tend to be higher for smaller galaxies, in agreement with theoretical expectations (e.g., Murray et al. 2011; Hopkins et al. 2012).

Figure 10 also includes observational constraints on the mass loading factor from the $z \sim 0.1$ survey of Bouché et al. (2012) (triangles) and $z \sim 0.2$ pair of Kacprzak et al. (2014) (square). For the Bouché et al. (2012) sample, we used spectral energy distribution (SED) derived SFRs (Table 4) given their larger impact parameters and longer travel times ($b/V_{out} > 100$ s of Myr) compared to the timescale for Hα-derived SFRs (few Myr). The SED-derived SFRs are computed from the UV-to-IR photometry (using Galex +SDSS+Wise surveys) with the Code Investigating GALaxy Emission software (Noll et al. 2009). The pairs with the largest impact parameters (>60 kpc) are shown in gray, since these mass loading factors can suffer strong biases due to even larger travel times (~300 Myr). Other measurements at higher redshift from stacked spectra of SFGs (Weiner et al. 2009; Newman et al. 2012) indicate an average mass loading factor of ~2 (Newman et al. 2012).

The different lines in Figure 10 represent various theoretical (Okamoto et al. 2010; Davé et al. 2011; Hopkins et al. 2012; Puchwein & Springel 2013; Vogelsberger et al. 2014; Barai et al. 2015; Muratov et al. 2015) and empirical models (Peeples & Shankar 2011; Zahid et al. 2014).[10] In comparing observations and models, it is important to bear in mind that some are fiducial scaling relations put in the sub-grid physics (e.g., Davé et al. 2011; Puchwein & Springel 2013; Vogelsberger et al. 2014), while others are from more complex numerical approaches (e.g., Hopkins et al. 2012, 2013; Barai et al. 2015; Muratov et al. 2015)[11] and thus are more directly comparable with observations.

Currently our data do not allow us to discriminate between energy- and momentum-driven winds, but thanks to ongoing work at redshift $z \sim 0.2$ with Keck/LRIS (N. Bouché et al. 2015, in preparation; C. L. Martin et al. 2015, in preparation) and to the new-generation IFU Multi Unit Spectroscopic Explorer (MUSE) on the VLT (Bacon et al. 2010, 2015), we will be able to significantly increase the sample size and put tight constraints on the wind scaling relations.

We would like to thank the referee for his/her thorough read of the manuscript and for the useful suggestions and comments. This work is based on observations taken at ESO/VLT in Paranal and partially from the data archive of the NASA/ESA *HST*, which is operated by the Association of Universities for Research in Astronomy, Inc. We would like to thank the ESO staff. N.B. acknowledges support from a Carreer Integration Grant (CIG) (PCIG11-GA-2012-321702) within the 7th European Community Framework Program. M.T.M. thanks the Australian Research Council for *Discovery Project* grant DP130100568 which supported this work. C.P. thanks the Agence Nationale de la Recherche for support (contract ANR-08-BLAN-0316-01). This research made use of Astropy, a community-developed core PYTHON package for astronomy (Astropy Collaboration et al. 2013), NumPy and SciPy (Oliphant 2007), Matplotlib (Hunter 2007), IPython (Perez& Granger 2007), and of NASA's Astrophysics Data System Bibliographic Services.

[10] The parameters of some of these models are listed in Table 1 of Zahid et al. (2014). We also took the values of the corrected version of Vogelsberger et al. (2014).

[11] Note that the outflow rate from Barai et al. (2015) only includes gas particles with velocities greater than the escape velocity.

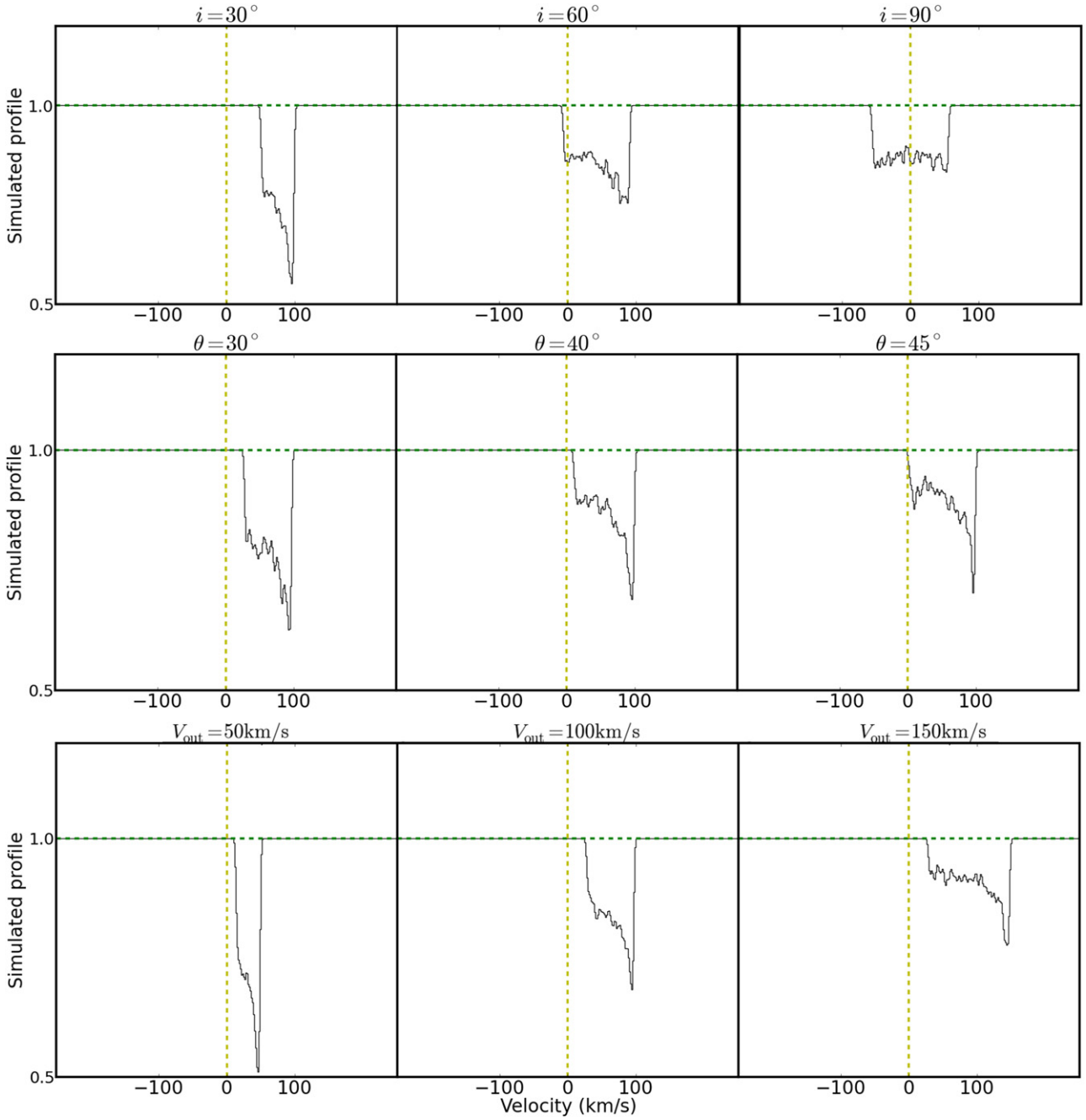

Figure A1. Examples of simulated absorption profiles with different galaxy inclinations (i), opening angle (θ), and wind velocities (V_{out}): while each of the simulated profiles has the same number of particles, the apparent depth decreases as each parameter increases due to larger velocity projections for i and θ and larger range of velocities for V_{out}. *Top row*: absorption profiles for galaxies inclined at 30°, 60°, and 90° with $V_{out} = 100$ km s^{-1}and $\theta = 30°$. The noise effect is due to the Monte Carlo distribution of particles. *Middle row*: absorption profiles for wind cones with opening angles of 30°, 40°, and 45° with $V_{out} = 100$ km s^{-1}and $i = 45°$. *Bottom row*: absorption profiles with wind velocities of 50, 100, and 150 km s^{-1}with $i = 45°$ and $\theta = 30°$. Each simulated profile has the same amount of particles but shows a larger velocity range due to the increasing gas speed, hence the varying apparent depths.

APPENDIX
UNDERSTANDING THE GEOMETRIC WIND MODEL

In this appendix we demonstrate how varying different parameters within the cone model impacts the simulated absorption profile. For the cone model (Section 4.1.1), we change three parameters in order to investigate the behavior of the simulated profile: for different galaxy inclinations (i), cone opening angles (θ), and wind outflow velocities (V_{out}) (Figure A1). The general trends are as follows. The different inclinations and cone opening angles change the left portion of the simulated absorption profile, while the wind velocity extends the right portion. Note that, except for the case of 90° galaxy inclination, all the simulated absorption profiles in Figure A1 present an outward asymmetry.

We also present in Figure A2 the UVES Mg I λ2852 absorption lines of our SIMPLE sample galaxies.

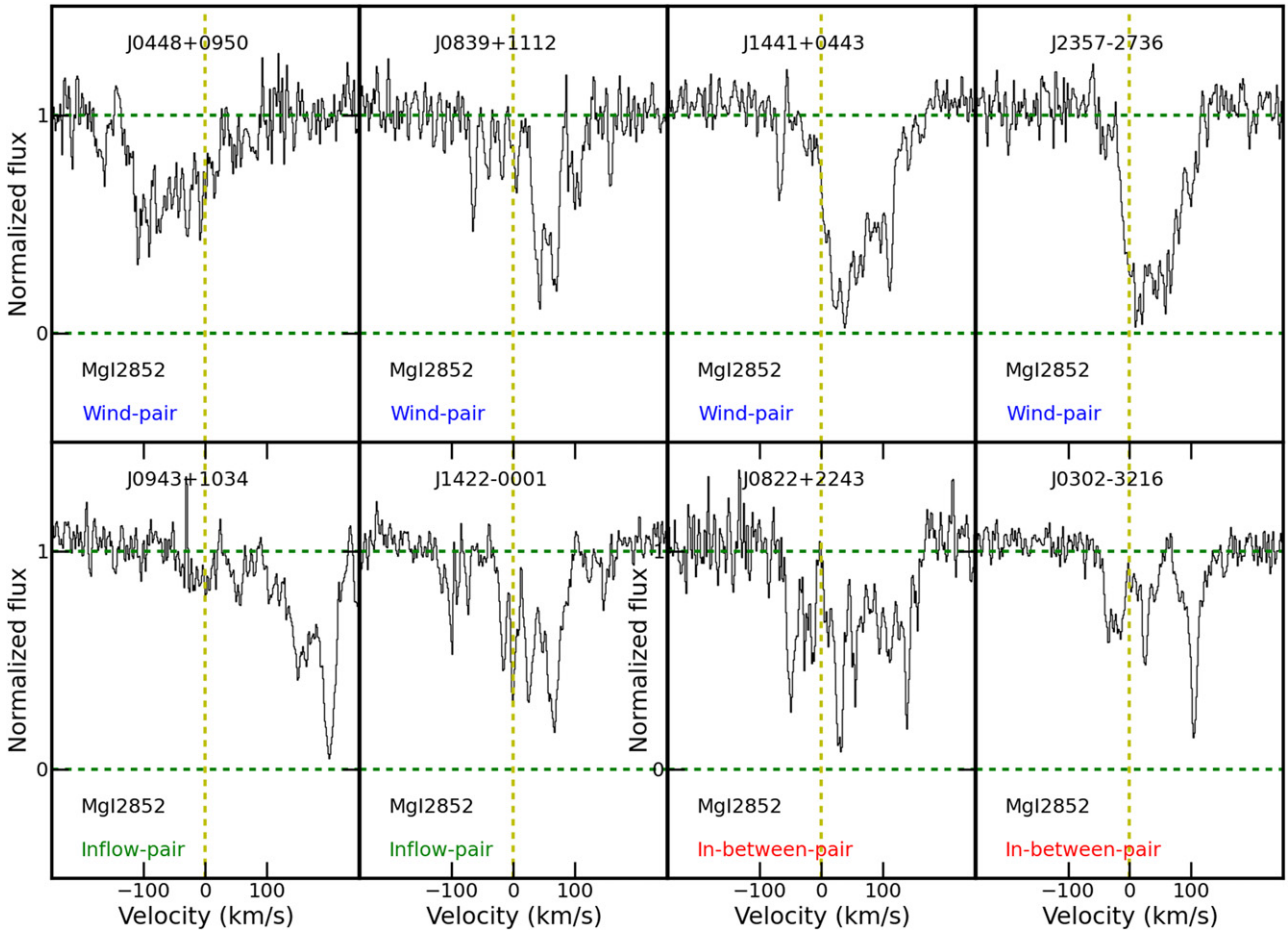

Figure A2. Here we present the UVES Mg I λ2852 absorption lines for 8 out of 10 galaxies. We do not have these absorption lines for J0147+1258 and J0226−2857 as they fall in the gap of UVES data. The top row corresponds to UVES Mg I centered data of the four wind-pairs. The bottom row presents the UVES Mg I centered data of the two inflow-pairs and the two ambiguous cases from left to right.

REFERENCES

Abuter, R., Schreiber, J., Eisenhauer, F., et al. 2006, NewAR, 50, 398
Bacon, R., Accardo, M., Adjali, L., et al. 2010, Proc. SPIE, 7735, 8
Bacon, R., Brinchmann, J., Richard, J., et al. 2015, A&A, 575, A75
Barai, P., Monaco, P., Murante, G., Ragagnin, A., & Viel, M. 2015, MNRAS, 447, 266
Behroozi, P. S., Conroy, C., & Wechsler, R. H. 2010, ApJ, 717, 379
Bernardi, M., Shankar, F., Hyde, J. B., et al. 2010, MNRAS, 404, 2087
Bordoloi, R., Lilly, S. J., Hardmeier, E., et al. 2014, ApJ, 794, 130
Bohlin, R. C., Savage, B. D., & Drake, J. F. 1978, ApJ, 224, 132
Bohlin, R. C., Savage, B. D., & Drake, J. F. 2011, ApJ, 743, 10
Bouché, N., Carfantan, H., Schroetter, I., Michel-Dansac, L., & Contini, T. 2015, arXiv:1501.06586
Bouché, N., Hohensee, W., Vargas, R., et al. 2012, MNRAS, 426, 801
Bouché, N., Murphy, M. T., Kacprzak, G. G., et al. 2013, Sci, 341, 50
Bouché, N., Murphy, M. T., Péroux, C., Csabai, I., & Wild, V. 2006, MNRAS, 371, 495
Bouché, N., Murphy, M. T., Péroux, C., et al. 2007, ApJL, 669, L5
Chabrier, G. 2003, PASP, 115, 763
Chen, H.-W. 2012, MNRAS, 427, 1238
Chisholm, J., Tremonti, C. A., Leitherer, C., et al. 2014, arXiv:1412.2139
Contini, T., Garilli, B., le Fèvre, O., et al. 2012, A&A, 539, A91
Cresci, G., Hicks, E. K. S., Genzel, R., et al. 2009, ApJ, 697, 115
Davé, R., Oppenheimer, B. D., & Finlator, K. 2011, MNRAS, 415, 11
Davies, R. 2007, MNRAS, 375, 1099
Dekel, A., & Silk, J. 1986, ApJ, 303, 39
Dekel, A., Sari, R., & Ceverino, D. 2009, ApJ, 703, 785
Dekel, A., Zolotov, A., Tweed, D., et al. 2013, MNRAS, 435, 999
Dekker, H., D'Odorico, S., Kaufer, A., Delabre, B., & Kotzlowski, H. 2000, Proc. SPIE, 4008, 534
Dubois, Y., & Teyssier, R. 2008, A&A, 477, 79
Elmegreen, D. M., Elmegreen, B. G., Ravindranath, S., & Coe, D. A. 2007, ApJ, 658, 763
Epinat, B., Contini, T., Le Fèvre, O., et al. 2009, A&A, 504, 789
Epinat, B., Tasca, L., Amram, P., et al. 2012, A&A, 539, A92
Förster Schreiber, N. M., Genzel, R., Bounché., et al. 2009, ApJ, 706, 1364
Förster Schreiber, N. M., Genzel, R., Eisenhauer, F., et al. 2006, Msngr, 125, 11
Genel, S., Naab, T., Genzel, R., et al. 2012, ApJ, 745, 11
Genel, S., Vogelsberger, M., Springel, V., et al. 2014, MNRAS, 445, 175
Genzel, R., Burkert, A., Bouché, N., et al. 2008, ApJ, 687, 59
Heckman, T. M., Armus, L., & Miley, G. K. 1990, ApJS, 74, 833
Heckman, T. M., Lehnert, M. D., Strickland, D. K., & Armus, L. 2000, ApJS, 129, 493
Hopkins, P. F., Kereš, D., Murray, N., et al. 2013, MNRAS, 433, 78
Hopkins, P. F., Quataert, E., & Murray, N. 2012, MNRAS, 421, 3522
Jenkins, E. B. 2009, ApJ, 700, 1299
Kacprzak, G. G., Churchill, C. W., Barton, E. J., & Cooke, J. 2011a, ApJ, 733, 105
Kacprzak, G. G., Churchill, C. W., Ceverino, D., et al. 2010, ApJ, 711, 533
Kacprzak, G. G., Churchill, C. W., Evans, J. L., Murphy, M. T., & Steidel, C. C. 2011b, MNRAS, 416, 3118
Kacprzak, G. G., Martin, C. L., Bouché, N., et al. 2014, ApJL, 792, LL12
Kennicutt, R. C., Jr. 1998, ApJ, 498, 541
Kereš, D., Katz, N., Weinberg, D. H., & Davé, R. 2005, MNRAS, 363, 2
Lan, T.-W., Ménard, B., & Zhu, G. 2014, ApJ, 795, 31
Law, D. R., Steidel, C. C., Erb, D. K., et al. 2007, ApJ, 669, 929
Law, D. R., Steidel, C. C., Erb, D. K., et al. 2009, ApJ, 697, 2057
Leauthaud, A., George, M. R., Behroozi, P. S., et al. 2012, ApJ, 746, 95
Leauthaud, A., Tinker, J., Behroozi, P. S., Busha, M. T., & Wechsler, R. H. 2011, ApJ, 738, 45
Lehnert, M. D., & Heckman, T. M. 1996, ApJ, 472, 546
Lehnert, M. D., van Breugel, W. J. M., Heckman, T. M., & Miley, G. K 1999, ApJS, 124, 11

Martin, C. L. 1998, ApJ, 506, 222
Martin, C. L. 1999, ApJ, 513, 156
Martin, C. L. 2005, ApJ, 621, 227
Martin, C. L., Kobulnicky, H. A., & Heckman, T. M. 2002, ApJ, 574, 663
Martin, C. L., Shapley, A. E., Coil, A. L., et al. 2012, ApJ, 760, 127
Martin, C. L., Shapley, A. E., Coil, A. L., et al. 2013, ApJ, 770, 41
Ménard, B., & Chelouche, D. 2009, MNRAS, 393, 808
Mo, H. J., & White, S. D. M. 2002, MNRAS, 336, 112
Moster, B. P., Somerville, R. S., Maulbetsch, C., et al. 2010, ApJ, 710, 903
Muratov, A. L., Keres, D., Faucher-Giguere, C.-A., et al. 2015, arXiv:1501.03155
Murray, N., Ménard, B., & Thompson, T. A. 2011, ApJ, 735, 66
Murray, N., Quataert, E., & Thompson, T. A. 2005, ApJ, 618, 569
Newman, S. F., Genzel, R., Förster-Schreiber, N. M., et al. 2012, ApJ, 761, 43
Noll, S., Burgarella, D., Giovannoli, E., et al. 2009, A&A, 507, 1793
Okamoto, T., Frenk, C. S., Jenkins, A., & Theuns, T. 2010, MNRAS, 406, 208
Oppenheimer, B. D., & Davé, R. 2006, MNRAS, 373, 1265
Oppenheimer, B. D., Davé, R., Kereš, D., et al. 2010, MNRAS, 406, 2325
Papastergis, E., Cattaneo, A., Huang, S., Giovanelli, R., & Haynes, M. P. 2012, ApJ, 759, 138
Peeples, M. S., & Shankar, F. 2011, MNRAS, 417, 2962
Peng, C. Y., Ho, L. C., Impey, C. D., & Rix, H.-W. 2010, AJ, 139, 2097
Péroux, C., Bouché, N., Kulkarni, V. P., & York, D. G. 2013, MNRAS, 436, 2650
Pettini, M., Rix, S. A., Steidel, C. C., et al. 2002, ApJ, 569, 742
Puchwein, E., & Springel, V. 2013, MNRAS, 428, 2966
Rosdahl, J., Blaizot, J., Aubert, D., Stranex, T., & Teyssier, R. 2013, MNRAS, 436, 2188
Roškar, R., Teyssier, R., Agertz, O., Wetzstein, M., & Moore, B. 2014, MNRAS, 444, 2837
Rubin, K. H. R., Prochaska, J. X., Koo, D. C., et al. 2014, ApJ, 794, 156
Rubin, K. H. R., Weiner, B. J., Koo, D. C., et al. 2010, ApJ, 719, 1503
Rupke, D. S., Veilleux, S., & Sanders, D. B. 2005, ApJS, 160, 115
Salpeter, E. E. 1955, ApJ, 121, 161
Schaye, J., Crain, R. A., Bower, R. G., et al. 2015, MNRAS, 446, 521
Schreiber, J., Thatte, N., Eisenhauer, F., et al. 2004, in ASP Conf. Ser. 314: Astronomical Data Analysis Software and Systems (ADASS) XIII, ed. F. Ochsenbein, M. G. Allen, & D. Egret (San Francisco, CA: ASP), 380
Shen, S., Madau, P., Aguirre, A., et al. 2012, ApJ, 760, 50
Shen, S., Madau, P., Guedes, J., et al. 2013, ApJ, 765, 89
Springel, V., Frenk, C. S., & White, S. D. M. 2006, Natur, 440, 1137
Steidel, C. C. 1995, in QSO Absorption Lines, ed. G. Meylan (Berlin: Springer), 139
Steidel, C. C., Erb, D. K., Shapley, A. E., et al. 2010, ApJ, 717, 289
Tumlinson, J., Thom, C., Werk, J. K, et al. 2013, ApJ, 777, 59
van Dokkum, P. G. 2001, PASP, 113, 1420
Veilleux, S., Cecil, G., & Bland-Hawthorn, J. 2005, ARA&A, 43, 769
Vogelsberger, M., Genel, S., Sijacki, D., et al. 2014a, MNRAS, 438, 3607
Vogelsberger, M., Genel, S., Springel, V., et al. 2014b, Natur, 509, 177
Weiner, B. J., Coil, A. L., Prochaska, J. X., et al. 2009, ApJ, 692, 187
Werk, J. K., Prochaska, J. X., Tumlinson, J., et al. 2014, ApJ, 792, 8
White, S. D. M., & Frenk, C. S. 1991, ApJ, 379, 52
White, S. D. M., & Rees, M. J. 1978, MNRAS, 183, 341
Wuyts, S., Förster Schreiber, N. M., van der Wel, A., et al. 2011, ApJ, 742, 96
Zahid, H. J., Torrey, P., Vogelsberger, M., et al. 2014, Ap&SS, 349, 873
Zahid, H. J., Yates, R. M., Kewley, L. J., & Kudritzki, R. P. 2013, ApJ, 763, 92

Appendix B

Schroetter et al. 2016: MusE GAs FLOw and Wind (MEGAFLOW): first MUSE results on background quasars

Draft version August 7, 2016
Preprint typeset using LaTeX style emulateapj v. 12/16/11

MUSE GAS FLOW AND WIND (MEGAFLOW) I: FIRST MUSE RESULTS ON BACKGROUND QUASARS [1]

I. Schroetter[2,4], N. Bouché[3], M. Wendt[5,6], T. Contini[2,4], H. Finley[2,4], R. Pelló[2,4], R. Bacon[7], S. Cantalupo[9], R. A. Marino[9], J. Richard[7], S. J. Lilly[9], J. Schaye[8], K. Soto[9], M. Steinmetz[5], L. A. Straka[8], L. Wisotzki[5]

Draft version August 7, 2016

Abstract

The physical properties of galactic winds are one of the keys to understand galaxy formation and evolution. These properties can be constrained thanks to background quasar lines of sight (LOS) passing near star-forming galaxies (SFGs). We present the first results of the MusE GAs FLOw and Wind (MEGAFLOW) survey obtained of 2 quasar fields which have 8 Mg II absorbers of which 3 have rest-equivalent width greater than 0.8 Å. With the new Multi Unit Spectroscopic Explorer (MUSE) spectrograph on the Very Large Telescope (VLT), we detect 6 (75%) Mg II host galaxy candidates withing a radius of 30″ from the quasar LOS. Out of these 6 galaxy–quasar pairs, from geometrical arguments, one is likely probing galactic outflows, two are classified as "ambiguous", two are likely probing extended gaseous disks and one pair seems to be a merger. We focus on the wind−pair and constrain the outflow using a high resolution quasar spectra from Ultraviolet and Visual Echelle Spectrograph (UVES). Assuming the metal absorption to be due to gas flowing out of the detected galaxy through a cone along the minor axis, we find outflow velocities of the order of ≈ 150 km s^{-1} (i.e. smaller than the escape velocity) with a loading factor, $\eta = \dot{M}_{\rm out}/{\rm SFR}$, of ≈ 0.7. We see evidence for an open conical flow, with a low-density inner core. In the future, MUSE will provide us with about 80 multiple galaxy−quasar pairs in two dozen fields.

Subject headings: galaxies: evolution — galaxies: formation — galaxies: intergalactic medium — quasars: individual: SDSSJ213748+001220, SDSSJ215200+062516

1. INTRODUCTION

In spite of the successes of the ΛCDM cosmological model (i.e. Springel et al. 2005), a major discrepancy remains between the predicted number density of dark matter halos and the observed number density of galaxies in the low-mass regime ($L < L_*$) (i.e. Guo et al. 2010; Papastergis et al. 2012; Moster et al. 2010, 2013; Behroozi et al. 2013). This behavior is usually explained by supernova(SN)-driven outflows (Dekel & Silk 1986) which expel baryons from the galactic disk. Indeed, these galactic outflows are observed in almost every star-forming galaxy (SFG) (Veilleux et al. 2005, for a review) and are likely to enrich the inter-galactic medium (e.g. Dekel & Silk 1986; Aguirre et al. 2001; Oppenheimer & Davé 2006).

The physical mechanisms for driving galactic winds are complex and the cold gas could be accelerated by thermal energy injection (Springel & Hernquist 2003), by momentum injection from radiation pressure (e.g. Murray et al. 2005), by cosmic ray pressure (e.g. Booth et al. 2013; Salem & Bryan 2014) or by a combination of these mechanisms (e.g. Hopkins 2015) The wide range physical scales that describe SN explosions from Astronomical Unit (AU) to tens of kiloparsecs (kpc), are beyond the capabilities of cosmological simulations.

Hence, in most of these simulations, outflows are usually implemented with sub-grid prescriptions (e.g. Schaye et al. 2010; Oppenheimer et al. 2010; Vogelsberger et al. 2014). A popular sub-grid recipe is to let the loading factor η, i.e. the ratio between the outflow rate $\dot{M}_{\rm out}$ and the star-formation rate (SFR), be a function of galaxy (halo) mass or circular velocity V_c (Oppenheimer et al. 2010) such as $\eta \propto V_c^{-1}$ for momentum-driven winds and $\eta \propto V_c^{-2}$ for energy-driven winds. An alternative way to implement the collective effect of SN explosions is the (stochastic) implementation of thermal feedback, where galactic winds develop without imposing any input outflow velocity nor mass loading factor such as in the EAGLE simulations (e.g. Schaye et al. 2015), the FIRE simulations (Hopkins et al. 2014; Muratov et al. 2015), and the multi-phase scheme of Barai et al. (2015).

Given the high impact of SN feedback on galaxy formation and the wide range of mass loading factors used in numerical simulations (see the compilations in Zahid et al. 2014; Torrey et al. 2014; Schroetter et al. 2015), observational constraints are of paramount importance. Unfortunately, our knowledge on the loading factor or the mass outflow rate $\dot{M}_{\rm out}$ is incomplete despite of the

[1] Based on observations made at the ESO telescopes under programs 094.A-0211(B) and 293.A-5038(A).

[2] IRAP, Institut de Recherche en Astrophysique et Planétologie, CNRS, 14, avenue Edouard Belin, F-31400 Toulouse, France
[3] IRAP/CNRS, 9, avenue Colonel Roche, F-31400 Toulouse, France
[4] University Paul Sabatier of Toulouse/ UPS-OMP/ IRAP, F-31400 Toulouse, France
[5] AIP, Leibniz-Institut für Astrophysik Potsdam, An der Sternwarte 16, D-14482 Potsdam, Germany
[6] Institut für Physik und Astronomie, Universität Potsdam, D-14476 Golm, Germany
[7] Univ Lyon, Univ Lyon1, Ens de Lyon, CNRS, Centre de Recherche Astrophysique de Lyon UMR5574, F-69230, Saint-Genis-Laval, France
[8] Leiden Observatory, Leiden University, PO Box 9513, 2300 RA Leiden, The Netherlands
[9] ETH Zurich, Institute of Astronomy, Wolfgang-Pauli-Str. 27, 8093 Zurich, Switzerland
[10] AIG, Institut für Astrophysik, Universität Göttingen, Friedrich-Hund-Platz 1, D-37077 Göttingen, Germany

many efforts made in the past decades (i.e. Lehnert & Heckman 1996; Heckman et al. 2000; Martin 1998, 1999; Rupke et al. 2005; Rubin et al. 2010; Martin et al. 2012). Indeed, estimates of the ejected mass flux $\dot{M}_{\rm out}$ using standard galaxy absorption lines (e.g. Heckman et al. 1990, 2000; Pettini et al. 2002; Martin et al. 2002; Martin 2005; Martin et al. 2012, 2013) are uncertain by orders of magnitude mainly due to the difficulty in constraining the location of the probed outflowing gas [1]. Indeed, the gas responsible for the blue shifted absorption lines in galaxies could be 0.1, 1 or 10 kpc away from the host. Some recent studies have made serious attempts at determining the scaling of outflow rates with galaxy properties by setting the absorbing gas at a fixed distance (Heckman et al. 2015; Chisholm et al. 2015; Wood et al. 2015).

Background quasars can give us the minimum distance of the gas from the impact parameter b and thereby potentially yield more accurate outflow rates (Bouché et al. 2012; Kacprzak et al. 2014; Schroetter et al. 2015; Muzahid et al. 2015). One difficulty is that it is rare for the LOS to a background quasar to pass near a star-forming galaxy. Hence, one needs to devise strategies to build large samples of galaxy-quasar pairs. Another difficulty is that background quasars can probe not only the circum-galactic medium but also the outer regions of gaseous disks and the gas near other, undetected galaxies.

In order to obtain large samples of galaxy-quasar pairs, one can select quasars around galaxies or galaxies around quasars with absorption systems. The former requires quasar follow-up observations, while the latter requires one to detect the associated galaxies. In the era of large quasar catalogs from Sloan Digital Sky Survey (SDSS), we favor the absorption selection technique combined with integral field unit (IFU) observations. Indeed, from Mg II absorption−selected quasar spectra, because we know the host galaxy redshift without knowing its position, IFUs can detect galaxies at previously unknown impact parameters. This kind of instrument also allows us to determine geometrical and kinematic properties of galaxies in the same observation. So far, IFUs such as SINFONI allowed us to probe galaxies within 20 kpc from the quasar line of sight (at redshift around 1). With the new VLT/MUSE instrument (Bacon et al. 2006, 2009), one can now detect galaxies further away ($\sim$250 kpc away at $z = 1$) thanks to its field of view of 1×1 arcmin (compared to $8'' \times 8''$ for SINFONI). The large wavelength coverage of MUSE (4800Å to 9300Å) allows us to target quasar fields with multiple Mg II ($\lambda\lambda 2796, 2802$) absorption lines having redshifts from 0.4 to 1.4 for [O II]($\lambda\lambda 3727, 3729$) identification. We complement the VLT/MUSE IFU observations (which have a resolution $R \sim 2000$ or 150 km s^{-1}) with VLT/UVES follow-up high-resolution spectra of the quasars in order to study the line-of-sight kinematics with the resolution (< 10 km s^{-1}) necessary for obtaining accurate constraints on outflow properties.

In this paper, we present the first results on galactic outflows from our MUSE survey. In § 2 we present the survey, the MUSE+UVES data and the data reduction. § 3 describes the sample results while § 4 presents our wind model as well as individual galaxy properties. Conclusions are then discussed in § 5.

We use the ΛCDM standard cosmological parameters: H_0=70 km s^{-1}, Ω_Λ=0.7 and Ω_M=0.3.

2. THE MEGAFLOW SURVEY

2.1. *Target selection strategy*

Current samples of galaxy−quasar pairs for strong Mg II absorbers, as in Bouché et al. (2012); Schroetter et al. (2015); Muzahid et al. (2015) and Bouché et al. (2016), are made of a dozen pairs. Here, we seek to increase the sample size by almost an order of magnitude in order to allow for statistical analysis of the relation between the absorption properties (and ultimately wind properties such as outflow rates and loading factors) and the galaxy properties. Thanks to the multiplexing capabilities of MUSE, having a sample 80—100 pairs is now within reach using 20–25 quasar fields.

As in our previous surveys, we first select background quasar spectra with Mg II $\lambda 2796$ absorption lines. For our MusE GAs FLOw and Wind (MEGAFLOW) survey, our strategy consists in selecting multiple Mg II absorbers (three, four or five) in quasar spectra from the Zhu and Ménard catalog[2] (Zhu & Ménard 2013) based on the SDSS survey (Ross et al. 2012; Alam et al. 2015). These Mg II absorptions should have redshifts between 0.4 and 1.4 such that the [O II] $\lambda\lambda 3727, 3729$ galaxy emission lines fall into the MUSE wavelength range (4800Å to 9300Å).

To restrict the impact parameter range, we constrain the rest equivalent width (REW) of these absorptions $W_r^{\lambda 2796}$ to $W_r^{\lambda 2796}$ >0.5 Å because of the well-known anti-correlation between impact parameter and $W_r^{\lambda 2796}$ (Lanzetta & Bowen 1990; Steidel 1995; Chen et al. 2010; Kacprzak et al. 2011b; Bordoloi et al. 2011; Werk et al. 2013; Nielsen et al. 2013). Also the largest $W_r^{\lambda 2796}$ tend to be associated with outflows (e.g. Kacprzak et al. 2011b; Lan et al. 2014). We define a strong absorber an absorber with $W_r^{\lambda 2796} > 0.3 - 0.5$ Å as in Nestor et al. (2005). This limit of 0.5 Å corresponds to $b \lesssim$100 kpc. We also need to pay attention to where the galaxy emission lines will appear in the spectrum and try to avoid bright sky emission lines as much as possible.

The MEGAFLOW survey will consist of 20–25 quasar fields and the MUSE observations started in September 2014. In October 2014, we obtained UVES observations on the first two fields (Table 1)[3]. In this paper, we present the first results on these two fields towards SDSSJ213748+0012 and SDSSJ215200+0625, which have 4 Mg II absorption systems each.

2.2. *Observations and data reduction*

2.2.1. *MUSE observations*

MUSE data were taken in September 2014 in visitor mode during the first Guaranteed Time Observations

[1] Furthermore, outflow rates from these low-ionization metal lines also require uncertain ionization corrections (e.g. Chisholm et al. 2016).

[2] This catalog can be found at http://www.pha.jhu.edu/ gz323/Site/Download_Absorber_Catalog.html

[3] as Director Discretionary Time (DDT) program 293.A-5038(A)

(GTO) run (program ID 0.94A-0211). We first point the telescope towards a quasar and then we offset the first exposure by $\approx 4-5''$ in Right Ascension (RA) and Declination (Dec). This first offset is made to avoid the quasar flux to fall in the same pixels than the first pointing. Each observation was composed of four exposures of 900 seconds with a rotation of 90° between every exposure as well as small dithering ($< 1''$). This observation strategy is used in order to minimize systematics. From each MUSE observation, we obtain a combined cube of 317 × 316 spatial pixels (spaxels). Each spaxel has ~ 3680 spectral pixels ranging from 4750 Å to 9350 Å. With a spectral sampling of 1.25 Å/pixel, the average spectral resolution of the data is ~ 2.4 ÅFWHM. The spatial resolution for the two quasar fields is $\sim 0.8''$ FWHM with spatial sampling of $0.2''$/pixel at 7000 Å. The seeing constraint ($< 0.9''$) is necessary if we want to derive galaxy parameters and detect them. Indeed, galaxies at redshift ~ 1 can be small in size ($< 1.2''$) and we need the seeing to be smaller than the galaxy to better derive its parameters.

2.2.2. *MUSE data reduction*

The data are reduced using version 1.0 of the MUSE data reduction software (DRS) pipeline[4]. We process bias, flat field calibrations and arc lamp exposures taken during the night of the observations. Following calibration processing, raw science frames are bias subtracted and flat-fielded using master bias and master flat fields respectively. The flat-fielding is renormalized in each slice to account for slight changes due to temperature variations using a single flat field exposure taken hourly before the science observation or when the instrument temperature changes by more than 0.5° C. An additional flat-field correction was performed using the twilight sky exposures taken at the beginning of each night to correct for slight optical path differences between sky and calibration unit. Geometrical calibration and astrometric solution are then applied. The wavelength solution is obtained from the arc lamps and calibrated in air. Wavelengths are also corrected for the heliocentric velocity. The flux calibration is obtained from a spectrophotometric star observed for each night.

On each individual exposure, we use the default configuration of the DRS recipe and with the sky removal method turned off. This produces, for the 4 individual exposures, a large table called the "pixel-table". For each individual exposure, star positions were registered in order to have accurate relative astrometry as shifts can occur between exposures due to the derotator wobble ($< 0.3''$). The "pixel-tables" were then combined into a single data cube using the previously calculated offsets. The sky-subtraction was performed on this combined data cube with ZAP (Zurich Atmosphere Purge), an algorithm developed by Soto et al. (2016a,b). ZAP operates by first subtracting a baseline sky level, found by calculating the median per spectral plane and then uses principal component analysis and determines the minimal number of eigenspectra that can reconstruct the residual emission features in the data cube. Absolute astrometry is obtained by matching the positions of point sources in the data cube against the SDSS astrometry.

Finally, we cross−checked the flux calibration of these point sources against the SDSS magnitudes in the r and i filter bands (the central wavelengths are $\lambda_r = 6165$Å and $\lambda_i = 7481$Å for r and i filters respectively) whose bandpass are within the MUSE wavelength coverage. Using the r and i images obtained from the MUSE data cube convolved with the SDSS filters, we fitted a Moffat profile on each of the stars to calculate their total flux in each filter and then compare them with the SDSS ones. SDSS filters are design to be in AB magnitudes, but there are still corrections needed for some filters. Given that for the r and i filters, the AB to SDSS magnitudes correction is negligible, we can correct fluxes into AB magnitudes directly using the following relation:

$$AB = -2.5\log_{10}(f) - 5\log_{10}(<\lambda>) - 2.406 \qquad (1)$$

where f is the flux in $\mathrm{erg\,s^{-1}\,cm^{-2}\,Å^{-1}}$ and $<\lambda>$ the filter central wavelength in Å.

The comparison between MUSE and SDSS magnitudes is shown in Table 2. For both fields (J2137+0012 and J2152+0625), the agreement is around 1/10th of a magnitude. In addition, another data reduction was performed using CubeFix and CubeSharp (Cantalupo, in prep) in order to show cleaner images of the fields in the Appendix (Fig A.1 and A.2).

2.2.3. *UVES observation and reduction*

The high resolution spectra for J213748+0012 and J215200+0625 were taken with UVES mounted on the 8.2m VLT at Paranal, Chile (Dekker et al. 2000). These two fields were observed in DDT time under the program 293.A-5038(A). UVES is a cross-dispersed echelle spectrograph with two arms that are functionally identical: one covers the wavelengths in the range 3000-5000 Å(Blue) and the other covers the range 4200-11000 Å(Red). The details of the observational campaigns are presented in Table 3. The slit width of 1.2 arcsec and a CCD readout with 2x2 binning used for all the observations resulted in a spectral resolution power R $\approx$ 38000 dispersed on pixels of $\sim$1.3 $\mathrm{km\,s^{-1}}$. The settings were chosen in order to have a maximum of absorptions from host galaxies (from Fe II λ2586 to Mg I λ2852). The Common Pipeline Language (CPL version 6.3) of the UVES pipeline was used to bias correct and flat field the exposures and then to extract the wavelength and flux calibrated spectra. After the standard reduction, the custom software UVES popler[5] (version 0.66) was used to combine the extracted echelle orders into single 1D spectra. The continuum was fitted with low-order polynomials.

3. MEGAFLOW SAMPLE FIRST RESULTS

3.1. *Galaxy detections*

As we mentioned, the two fields (SDSSJ213748+0012 and SDSSJ215200+0625) were selected to each have at least 3 absorbing systems with $W_r > 0.5$ Å (see Table 4).

In each MUSE field, we search for [O II] $\lambda\lambda 3727, 3729$ emission lines corresponding to the Mg II absorption redshifts seen in the quasar spectrum. However, the MUSE

[4] A short description of the pipeline is given in Weilbacher et al. (2014).

[5] http: //astronomy.swin.edu.au/ ∼mmurphy/UVES_popler/

TABLE 1
Summary of MUSE 094.A-0211(B) observations.

Field (1)	$z_{\rm qso}$ (2)	PSF($''$) (3)	$T_{\rm exp}$(s) (4)	Date (5)
J213748+0012	1.668	0.8	3600	2014-09-23
J215200+0625	2.409	0.7	7200	2014-09-24

(1) Quasar name; (2) Quasar emission redshift; (3) FWHM of the seeing PSF (at ≈7000 Å); (4) Exposure time; (5) Date of observations.

TABLE 2
Magnitude differences between MUSE and SDSS for J213748+0012 and J215200+0625 fields.

Field (1)	object (2)	Instrument (3)	RA (4)	DEC (5)	mag_r (6)	mag_i (7)	Difference (8)
J213748+0012	QSO	MUSE	21:37:48.41	+00:12:20.49	18.33	18.19	−0.13
		SDSS	21:37:48.44	+00:12:20.00	18.20	18.05	
	Star	MUSE	21:37:47.65	+00:12:21.29	19.71	19.55	−0.09
		SDSS	21:37:47.65	+00:12:20.89	19.61	19.46	
J215200+0625	QSO	MUSE	21:52:00.05	+06:25:17.26	19.42	19.44	−0.07
		SDSS	21:52:00.03	+06:25:16.36	19.42	19.30	
	Star	MUSE	21:51:59.84	+06:25:05.48	16.71	16.47	−0.17
		SDSS	21:51:59.83	+06:25:04.72	16.53	16.29	

(1) Field; (2) Object type; (3) Instrument (MUSE or SDSS); (4) Right Ascension (RA); (5) Declination (DEC); (6) Magnitude in r filter (central wavelength $\lambda_r = 6165$Å); (7) Magnitude in i filter (central wavelength $\lambda_i = 7481$Å); (8) Average difference SDSS−MUSE (mag).

TABLE 3
Summary of UVES 293.A-5038(A) observations.

Target	setting λ_c (nm)	$T_{\rm exp}$ (s)	Date
J213748+0012	390+580	5970	2014-10-19
J215200+0625	390+580	9015	2014-10-21,24 2014-11-18

field of view of $1' \times 1'$ allows us to search for other companions in the fields, giving insight into the environment related to the host. We allow the potential host galaxies to have a redshift difference within a velocity interval of ≈ 1000 km s^{-1} with respect to the absorber redshift ($z_{\rm gal} = z_{\rm abs} \pm 0.01$ for a $z \approx 1$ galaxy). This velocity interval is set to prevent selection effects on surrounding gas velocities and thus not rejecting gas able to escape the gravitational well of the host galaxy in case of outflowing gas (more details on escape velocity in § 4.2). In the case where there are multiple galaxy candidates for a single Mg II line, we select the galaxy with the smallest impact parameter from the quasar LOS. Table 4 shows the detection rates for each field. For one of the undetected galaxies the expected emission line falls near a sky emission line at 7618 Å (the $z \approx 1.0437$ absorber in SDSSJ213748+0012) and the other line is too faint to be detected. For the reader interested in all of the galaxies detected in these MUSE data, we provide in the appendix a catalog with all the galaxies for which a redshift could be determined.

We detect galaxies at redshifts of three of the four Mg II absorbers for the SDSSJ213748+0012 quasar field (see Table 4). For the Mg II absorber at $z = 0.8063$, we find one [O II] emission-line galaxy at a distance b of 88 kpc. For the $z = 1.1890$ Mg II absorber, we also find one galaxy at an impact parameter of 63 kpc. For the last $z = 1.2144$ Mg II absorber, we find three [O II] emitters, at impact parameters of 87, 212 and 246 kpc. Given the large impact parameters of the latter two galaxies compared to the typical galaxy halo at these redshifts, and given the large Mg II REW of 1 Å, we assume the galaxy with the smallest impact parameter to be the host galaxy.

TABLE 4
Summary of MUSE galaxy detection.

Field name (1)	$z_{\rm absorber}$ (2)	$W_r^{\lambda 2796}$ (3)	$N_{\rm det}$ (4)	b (5)
J213748+0012	0.8063	0.724±0.09	1	88
	1.0437	0.767±0.08	0[a]	···
	1.1890	0.308±0.06	1	63
	1.2144	1.144±0.06	3	87, 212, 246
J215200+0625	1.0534	0.522±0.14	2	45, 189
	1.1761	0.526±0.15	0	···
	1.3190	1.347±0.12	1	34
	1.4309	1.152±0.11	4	62, 78, 184, 211

(1) Quasar field name; (2) Mg II absorption lines redshift; (3) Mg II (λ2796) REW (Å); (4) Number of detected galaxies near absorber redshift; (5) Impact parameter(s) of the detected galaxy(ies) (kpc);

[a]Affected by OH emission line at 7618Å.

For the SDSSJ215200+0625 field, we also detect galaxies at the redshifts of three out of the four Mg II absorbers (see Table 4). Two galaxies are identified for the first Mg II absorber at $z = 1.0534$, at impact parameters of 45 and 189 kpc. The host of the second absorber at $z = 1.1761$ is not detected in spite of the wavelength for the expected [O II] line being clear of OH lines. The third Mg II absorption has a redshift of 1.3190 and has only one galaxy corresponding to that redshift at an impact parameter of 34 kpc. The last Mg II absorption is at $z = 1.4309$ and we found 4 [O II] emitters at that redshift, which have impact parameters of 62, 78, 184 and 211 kpc (see Figure 7). This might be indicative of a group environment. Among, two have impact parame-

ters very close to each other (62 and 78 kpc). We choose to assume that the closest galaxy (at 62 kpc) should be responsible for the Mg II absorption because it is the most massive and the brightest ($V_{\rm max}$ = 298 km s^{-1}and 200 km s^{-1}, [O II] fluxes being 5.05×10^{-17}erg s^{-1} cm^{-2} and 1.38×10^{-17}erg s^{-1} cm^{-2}, respectively).

Using the propagated noise in the MUSE datacube, we can estimate flux (and surface brightness) limits on the expected [O II] emission line for the non-detected host galaxies. For the SDSSJ213748+0012 quasar field, at the first expected [O II] wavelength ($\sim 6730\AA$), with a noise of 2.3×10^{-20} erg s^{-1} cm^{-2} Å^{-1} (1σ), we estimate a surface brightness limit of 1.43×10^{-18} erg s^{-1} cm^{-2} arcsec^{-2} (1σ) for emission line objects (assuming a FWHM = 2.48 Å). This corresponds to a flux limit of 1.04×10^{-18} erg s^{-1} cm^{-2} (1σ) for an unresolved emitter at 0.82″ seeing. The flux limit is $\sqrt{2}$ times for the [O II] doublet (assuming a resolved doublet), or 1.47×10^{-18} erg s^{-1} cm^{-2} (1σ), which corresponds to a SFR of 0.13 M$_\odot$ yr^{-1} at $z = 1$, typical of our sample. Surface brightness and flux limits are shown in Table 5.

3.2. *SFR determination*

We use the $L_{\rm O\,II}$ ($\lambda\lambda3727, 3729$) luminosity to estimate the SFR as follows. We use the Kennicutt (1998) calibration, which assumes a Salpeter (1955) Initial Mass Function (IMF):

$$SFR(\mathrm{M}_\odot\ \mathrm{yr}^{-1}) = (1.4 \pm 0.4) \times 10^{-41}\ \mathrm{L([O\,II])_o(erg\ s^{-1})} \quad (2)$$

Where $L([\mathrm{O\,II}])_o$ is the [O II] observed luminosity. Using a Chabrier (2003) IMF and assuming a mean flux attenuation of $A_V = 1$, which is typical for $z = 1$ galaxies (e.g. Charlot et al. 2002), gives the same results (within 10%) as Equation 2.

Equation 4 in Kewley et al. (2004, hereafter K04) uses also a Salpeter IMF but makes no assumption of reddening. In their paper, they show that using the "average" attenuation correction of 0.3 mag leads to underestimate the high SFR[O II] ($> 1\mathrm{M}_\odot\,\mathrm{yr}^{-1}$) and overestimate the low SFRs. They provide a way of deriving the E(B-V) (Eq.16 and 18 of K04) color excess which leads to a more accurate mean attenuation, assuming that $A_V = 3.1 \times E(B - V)$. We choose to use the following equations (Eq 3 and 4 from K04) to derive our SFRs.

$$SFR(\mathrm{M}_\odot\ \mathrm{yr}^{-1}) = (6.58\pm1.65)\times10^{-42}\ \mathrm{L([O\,II])_i(erg\ s^{-1})} \quad (3)$$

$$L([\mathrm{O\,II}])_i = 3.11 \times 10^{-20}\ L([\mathrm{O\,II}])_o^{1.495} \quad (4)$$

3.3. *Galaxy morpho-kinematic properties*

Before classifying the galaxy−quasar pairs as favorable for gas outflows or inflows based on the azimuthal angle α of the apparent quasar location with respect to the galaxy major axis, we need to determine the galaxy's major axis position angle (PA)[6].

[6] The position angle (PA) of a galaxy is the angle between the galaxy major axis and the celestial north.

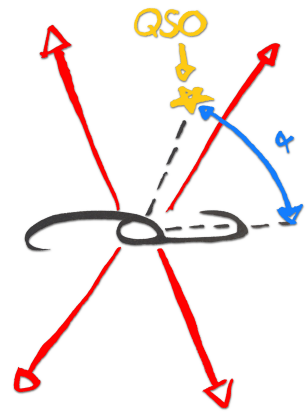

FIG. 1.— Scheme representing the azimuthal angle: The galaxy is represented at the center in black, the red arrows represent the outflowing gas expelled from both side of the galaxy minor axis. The azimuthal angle α is represented by the blue angle between the galaxy major axis and the quasar LOS (in yellow).

We determine the PAs from the morpho-kinematic properties of each galaxy using two approaches. First, we used the 2D fitting tool Camel[7] on the [O II] emission lines to extract velocity and dispersion maps as in Epinat et al. (2012) in order to establish whether the galaxy has a regular velocity field compatible with a disk. Second, we use the GalPaK^{3D} algorithm (Bouché et al. 2015) to derive simultaneously the morphological and kinematic properties of these galaxies using the continuum subtracted sub-cubes extracted around the [O II] emission lines. GalPaK^{3D} uses a disk parametric model with 10 free parameters and a Monte-Carlo Markov Chain (MCMC) algorithm with non-traditional sampling laws in order to efficiently probe the parameter space. Because the algorithm uses a 3-dimensional kernel to convolve the model with the spatial point-spread function (PSF or seeing) and the instrument line spread function (LSF), it returns the intrinsic (free of the PSF) galaxy properties (such as half-light radius, inclination, and maximum velocity). Other parameters include the major-axis position angle, the galaxy flux, position, redshift and intrinsic velocity dispersion. Results on the geometrical and kinematic properties of each galaxy are presented in Table 6.

Figures 2−7 show GalPaK^{3D} reconstructed models as well as Camel velocity maps for the 6 galaxies in the two fields. In Figure 2 (SDSSJ213748+0012 field), the other emission sources are the quasar and a star's residual continuum. In these figures, the left panel corresponds to a narrow band image of 30 pixels (37.5 Å) around the galaxy's [O II] emission lines. The background continuum has been subtracted so that we can only see the galaxy in emission. In each of these Figures, we see the galaxy (inside the white rectangles) within 15″ of the quasar LOS (represented by a white cross). In the two right columns of these Figures, [O II] integrated flux and velocity maps are shown. The top row corresponds to a 2×2 (2 pixels FWHM) spatial Gaussian-smoothed flux map (left) and the Camel velocity map (right). The bottom row shows the GalPaK^{3D} model flux (left) and the PSF-deconvolved velocity (right) maps. We can see

[7] The source code can be found at https://bitbucket.org/bepinat/camel.git

TABLE 5
SURFACE BRIGHTNESS AND FLUX LIMITS.

Quasar field (1)	$z_{\rm absorber}$ (2)	LSF (3)	Noise (4)	PSF (5)	Surface brightness limit (6)	[O II] flux limit (7)
J213748+0012G1	0.8063	2.48	2.3×10^{-20}	0.82	1.43×10^{-18}	1.47×10^{-18}
J213748+0012	1.0437	2.37	3.7×10^{-20}	0.78	2.19×10^{-18}	2.14×10^{-18}
J213748+0012G2	1.1890	2.57	2.4×10^{-20}	0.75	1.54×10^{-18}	1.45×10^{-18}
J213748+0012G3	1.2144	2.43	2.4×10^{-20}	0.76	1.45×10^{-18}	1.39×10^{-18}
J215200+0625G1	1.0534	2.28	2.1×10^{-20}	0.67	1.19×10^{-18}	1.01×10^{-18}
J215200+0625	1.1761	2.60	1.7×10^{-20}	0.66	1.10×10^{-18}	9.14×10^{-19}
J215200+0625G2	1.3190	2.41	3.6×10^{-20}	0.66	2.17×10^{-18}	1.79×10^{-18}
J215200+0625G3	1.4309	2.60	2.1×10^{-20}	0.66	1.36×10^{-18}	1.13×10^{-18}

(1) Quasar field name; (2) Mg II absorption line redshift; (3) Line Spread Function FWHM (LSF) of the MUSE data (Å); (4) Data cube noise at the expected [O II] wavelength ($\rm erg\,s^{-1}\,cm^{-2}\,Å^{-1}$) given at 1 σ; (5) PSF of the data ($''$); (6) Surface brightness limit ($\rm erg\,s^{-1}\,cm^{-2}\,arcsec^{-2}$) given at 1 σ; (7) [O II] flux limit ($\rm erg\,s^{-1}\,cm^{-2}$) given at 1 σ.

that in all cases, except in Figure 3 for the dispersion-dominated SDSSJ213748+0012G2 galaxy, the model flux maps from GalPaK^{3D} is in a good agreement with the observed flux, and that GalPaK^{3D} and Camel velocity maps are consistent. Table 6 lists the resulting parameters for each galaxy.

GalPaK^{3D} results are reliable if the central galaxy pixel has, at minimum, a Signal to Noise Ratio (SNR) pixel^{-1} of 3 (Bouché et al. 2015). For each galaxy, we have SNR pixel^{-1} of 11.0, 11.0, 4.5, 9.3, 4.2, 10.5 for SDSSJ213748+0012G1, G2, G3 and SDSSJ215200+0625G1, G2, G3 respectively. We checked that the parameters have converged for each galaxy as well as cross checked on raw data.

3.4. *Classification and notes on the individual cases*

To put constraints on galactic outflows, we first need to select galaxy−quasar pairs suitable for wind studies (wind pairs). To do so, we measure the angle between the galaxy major axis and the apparent quasar location, which is referred to as the azimuthal angle α (see Figure 1). Depending on this angle, the quasar LOS is likely to probe different phenomena around the galaxy. If $55° \leq \alpha \leq 90°$, the quasar's position on the sky is roughly along the galaxy minor axis and is likely to cross the outflowing material of the galaxy[8] (e.g. Bordoloi et al. 2011, 2014; Kacprzak et al. 2012, 2014). If a pair has such an azimuthal angle, it will be classified as a wind-pair. On the other hand, if the quasar is positioned along the galaxy major axis ($0° \leq \alpha \leq 30°$), the quasar LOS is likely to probe inflowing or circumgalactic gas. With such configuration, we classify the pair as suitable for accretion studies (inflow pair). In between, ($35° \leq \alpha \leq 55°$), we cannot distinguish between these two extreme cases.

In addition to the azimuthal angle, if a galaxy has a low inclination, classification can be ambiguous given that the uncertainty on the position angle will be large. Figure 8 shows galaxy inclination as a function of quasar azimuthal angle. From the 5 detected galaxies in the two quasar fields that are non-mergers, 2 are classified as inflow−pairs, one is an ambiguous case as its azimuthal angle is 47°, one is a face-on galaxy and only 1 (**J215200+0625G2**) can be robustly classified as a wind-pair.

[8] the Bordoloi papers have the definition of azimuthal angle reversed, i.e. their minor axis correspond to an α angle $< 45°$.

3.4.1. *SDSSJ213748+0012G1 galaxy*

The first detected galaxy ('G1') in the SDSSJ213748+0012 quasar field (Figure 2) has an impact parameter $b \approx 88$ kpc and corresponds to the $z_{\rm abs} \approx 0.8063$ Mg II absorption lines with a REW $W_r^{\lambda 2796}$ of 0.789 Å. This J213748+0012G1 galaxy is inclined by $i \approx 49 \pm 1.4°$ and its derived maximum rotation velocity is $V_{\rm max} \approx 127 \pm 5$ km s^{-1}. With an [O II] integrated flux of 8.7×10^{-17}erg s^{-1} cm^{-2}, its SFR is $\approx 6.3 \pm 0.7$ M$_\odot$ yr^{-1}. In Figure 2, we can see that the morphology and the position angle is well reproduced by GalPaK^{3D}. The azimuthal angle α with the quasar LOS is $\alpha = 25$ deg, i.e. the LOS is aligned with the major-axis.

3.4.2. *SDSSJ213748+0012G2 galaxy*

The galaxy J213748+0012G2 (Figure 3) corresponding to the $z_{\rm abs} \approx 1.1890$ Mg II absorption lines with a REW $W_r^{\lambda 2796}$ of 0.308 Å in the J213748+0012 quasar spectrum, has an impact parameter of $b \approx 64$ kpc and a total [O II] doublet flux of 1.47×10^{-16} erg s^{-1} cm^{-2}. From the [O II] integrated flux we derive a SFR of $\approx 41 \pm 8.0$ M$_\odot$ yr^{-1}. This galaxy has a large velocity dispersion $\sigma \approx 114 \pm 2.3$ km s^{-1}, i.e. it is a dispersion dominated system with $V/\sigma \sim 0.2$. Furthermore, the velocity field derived from the line fitting algorithm Camel does not agree with its morphology, i.e. its morphological and kinematic main axes are strongly misaligned, by $\approx 80°$ (Figure 3). This is a strong indication for a merger, and therefore this galaxy will not be considered as a wind case since the position angle of this galaxy is ambiguous.

3.4.3. *SDSSJ213748+0012G3 galaxy*

The other galaxy (J213748+0012G3, Figure 4) from the J213748+0012 field corresponding to the Mg II absorption lines at redshift $z_{\rm abs} \approx 1.2144$ and a REW $W_r^{\lambda 2796}$ of 1.144Å has an impact parameter b of ≈ 87 kpc. This galaxy has an inclination $i \approx 40 \pm 5°$, a maximum rotational velocity $V_{\rm max} \approx 166 \pm 18$ km s^{-1}and an [O II] flux of 4.17×10^{-17} erg s^{-1} cm^{-2}. From this flux we derive a SFR of $\approx 8.9 \pm 1.1$ M$_\odot$ yr^{-1}. Contrary to J213748+0012G2, the kinematic and morphological PAs agree well (Figure 4), hence the 3D GalPaK^{3D} model accounts for the 3D emission of this galaxy. In this case, the quasar LOS is at $\approx 45°$ from the major axis of this galaxy, this pair is thus classified as ambiguous.

3.4.4. *SDSSJ215200+0625G1 galaxy*

The first detected galaxy from the SDSSJ215200+0625 quasar field corresponds to the Mg II absorption lines at redshift $z_{\rm abs} \sim 1.0534$ with a REW $W_r^{\lambda 2796}$ of 0.545 Å. This galaxy (J215200+0625G1) has an impact parameter $b \approx 45$ kpc, a maximum rotational velocity $V_{\rm max} \approx 161 \pm 2$ km s^{-1} and an inclination $i \approx 69 \pm 0.7°$. With an [O II] integrated flux of 1.09×10^{-16} we derive a SFR of $\approx 19.0 \pm 3.1$ M$_\odot$ yr^{-1}. For this galaxy, Figure 5 shows a good agreement between GalPaK^{3D} and Camel flux and velocity maps. We can clearly see that the quasar LOS is aligned with the major axis of this galaxy with $\alpha = 4$ deg and is thus classified as an inflow-pair.

3.4.5. *SDSSJ215200+0625G2 galaxy*

[9] The galaxy (**J215200+0625G2**) corresponding to the redshift $z_{\rm abs} \approx 1.3190$ Mg II absorption lines with a rest equivalent width $W_r^{\lambda 2796}$ of 1.424 Å has an impact parameter $b \approx 34$ kpc. The derived galaxy redshift is 1.31845 with an inclination of $i \approx 59 \pm 11°$ and a maximum rotational velocity $V_{\rm max} \approx 130 \pm 29$ km s^{-1}. With an [O II] flux of $\approx 1.99 \times 10^{-17}$ erg s^{-1} cm^{-2}, we derive a SFR of $\approx 4.6 \pm 0.4$ M$_\odot$ yr^{-1}. Even if this galaxy is faint, as seen in Figure 6, its GalPaK^{3D}-derived morphology and position angle are in good agreement with Camel maps. The quasar LOS is aligned with the minor axis of this galaxy with $\alpha = 88 \pm 5$ deg.

3.4.6. *SDSSJ215200+0625G3 galaxy*

The last galaxy (J215200+0625G3) in the J215200+0625 quasar field has an impact parameter $b \approx 63$ kpc and corresponds to the Mg II absorption lines at redshift $z_{\rm abs} \approx 1.4309$ with $W_r^{\lambda 2796} = 1.152$ Å. The galaxy has an inclination of $i \approx 13 \pm 4°$, a maximum rotational velocity $V_{\rm max} \approx 298 \pm 40$ km s^{-1} and an [O II] integrated flux of $\approx 5.05 \times 10^{-17}$ erg s^{-1} cm^{-2}. With this flux we derive a SFR of $\approx 19 \pm 3.0$ M$_\odot$ yr^{-1}. Figure 7 shows that the morphology is in agreement with Camel but the position angle derived for this galaxy is more uncertain due to the low inclination of this galaxy. With an azimuthal angle of $\alpha = 72 \pm 20$ deg and its low inclination, we cannot determine whether the quasar LOS is aligned with the minor or major axis of the galaxy.

3.5. *Radial dependence of CGM*

For each quasar spectrum, we measure the REW for the Mg II absorption lines ($W_r^{\lambda 2796}$) in the UVES data and compare them with the SDSS values $W_r^{\lambda 2796}$ (see Table 7). We find that the results are consistent with each other. We also calculate REWs of the Mg II $\lambda 2803$, Mg I $\lambda 2852$, Fe II $\lambda 2586$ and Fe II $\lambda 2600$ in UVES quasar spectra. Results are shown in Table 7. Figures 9 and 10 show the UVES MgI $\lambda 2852$, Mg II $\lambda\lambda 2796, 2802$ and Fe II $\lambda\lambda 2586, 2600$ absorption profiles and label the measured REW of each profile for both quasar fields.

One of the first deductions we can make from Figures 9 and 10 is that there is no clear difference (like different asymmetry behavior for instance) between what seems to be outflowing material and circum-galactic or inflowing gas concerning the different absorption lines.

Figure 11 shows the distribution of REW $W_{\rm r}^{\lambda 2796}$ for pairs with an azimuthal angle $\alpha > 45°$ as a function of impact parameter b for this work as well as Kacprzak et al. (2011b,a) and Schroetter et al. (2015). This Figure shows that for wind pairs, as mentioned in Bouché et al. (2012), we clearly see a tight correlation between $W_{\rm r}^{\lambda 2796}$ and b. This $W_{\rm r}^{\lambda 2796} - b$ correlation goes approximatively as b^{-1}. This figure shows that the anti-correlation between impact parameter b and W_r is again confirmed at $b < 100$ kpc. The scatter around the relation in Figure 11 is ≈ 0.3 dex (delineated with the dotted lines). The solid line traces the fiducial $1/b$ relation for mass-conserved bi-conical outflows (see Bouché et al. 2012).

4. WIND MODEL

In this section, we describe the wind modeling. We create a cone having an opening angle corresponding to $\theta_{\rm max}$[10] and fill it randomly with particles representing cold gas clouds being pushed away by a hot medium or radiation pressure. These particles are distributed such that their number goes like $1/r^2$, where r is the distance to the galaxy center. The particle density is normalized arbitrarily to reproduce the optical depth of the absorption profiles.

Such entrained clouds are accelerated to their terminal velocity quickly in a few kpc or < 10 kpc since the pressure from the hot medium or the radiation field scales as $1/r^2$. The range of impact parameters for the galaxy−quasar pair in our sample is always larger than 30 kpc. Hence, we assume, for simplicity, that the particles have a constant radial velocity corresponding to $V_{\rm out}$. In addition, a single LOS probes a rather small range of distances from the host galaxy such that a gradient in the outflow velocity would have no significant impact on our results. So far, only in one LOS with an impact parameter less than 10 kpc in Schroetter et al. (2015), we required an accelerated wind profile.

We then orient the cone following the galaxy inclination and simulate the quasar LOS such that the galaxy−quasar pair matches the geometrical configuration of the MUSE data.

The particle velocities are then projected along the simulated quasar LOS and the distribution of the projected velocities gives us a simulated optical depth $\tau_{\rm v}$, which we turn into an absorption profile $\propto \exp(-\tau_{\rm v})$. In order to facilitate comparison with the data, Poisson noise is added to the simulated absorption profile to simulate the instrumental noise. This noise is chosen to have the same level as the data.

The model has two main free parameters, the wind speed $V_{\rm out}$ and $\theta_{\rm max}$ the wind opening angle. These two parameters are independent for a given galaxy inclination as one can see from the following arguments (see also Schroetter et al. (2015) for more details). The outer edges of the absorption profile (reddest for a cone pointing away from the observer, bluest for a cone pointing towards the observer) depends directly on the wind velocity (Figure A-1 in Schroetter et al. (2015)). The inner edge (towards Vsys) of the absorption profile depends

[9] In all the paper (text, Tables and Figures), the only wind-pair will appear in bold font to help the reader

[10] $\theta_{\rm max}$is defined from the central axis, and the cone subtends an area Σ of $\pi \cdot \theta_{\rm max}^2$.

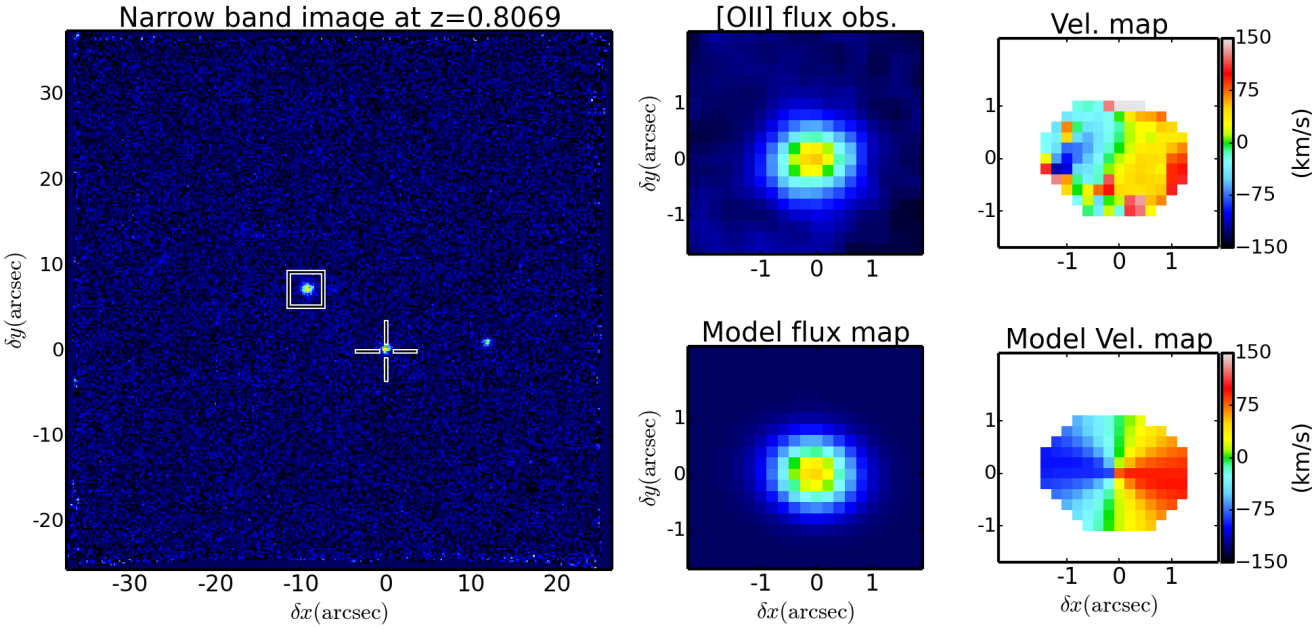

FIG. 2.— GalPaK and Camel results on galaxy J213748+0012G1. *Left:* Narrow band image (30 pixels corresponding to 37.5 Å) for [O II] $\lambda 3727, 3729$ at redshift $z = 0.8069$. The quasar LOS is represented by the white cross and the galaxy is inside the white rectangle. The other spot on the right corresponds to continuum residuals from a star. *Right:* from left to right: [O II] doublet integrated flux and velocity maps. The top row corresponds to a 2×2 Gaussian smoothed flux map (the left panel) and Camel velocity map (top right). The bottom row represents the GalPaK^{3D} model flux (left) and PSF-deconvolved velocity maps (right). Color bars on the right show the velocities of the corresponding Velocity maps, in km s^{-1}. This galaxy has a maximum SNR/pixel of ≈11.

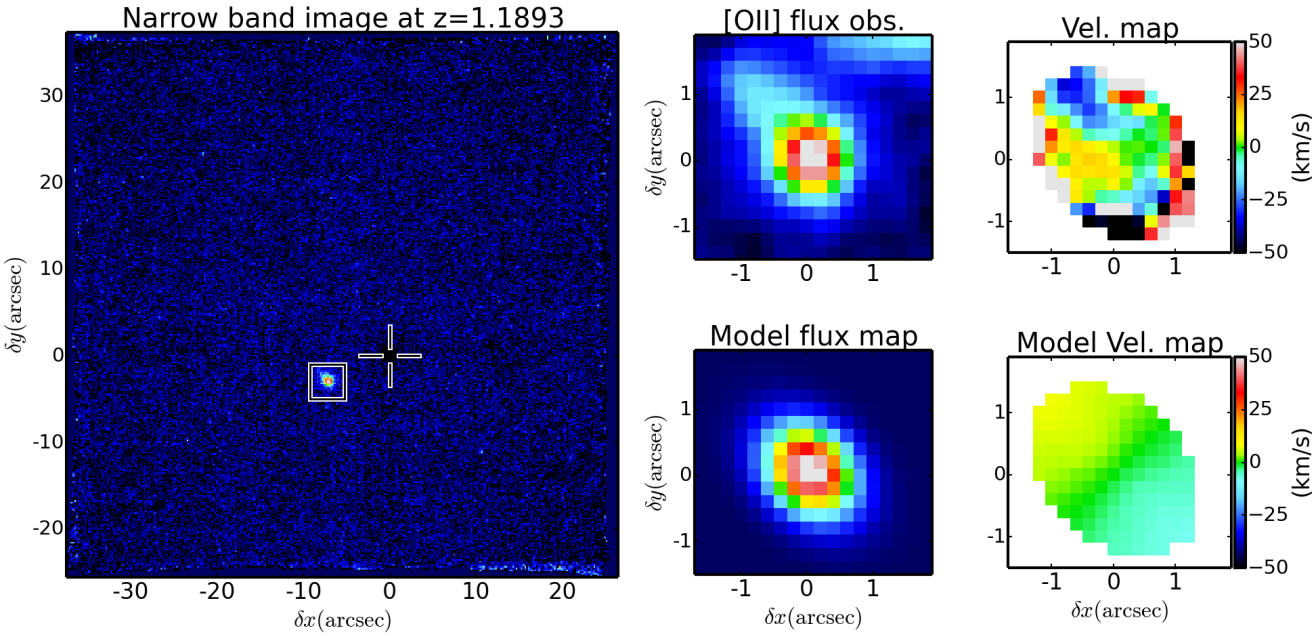

FIG. 3.— Same as Figure 2 but for J213748+0012G2 at redshift $z = 1.1893$. This galaxy has a maximum SNR/pixel of ≈11. For this galaxy, we can see that the velocity maps do not agree with each other. Because one part of the galaxy is not reproduced by our model and clearly has a flux component (top middle panel), this galaxy seems to be a merger and therefore the azimuthal angle of this pair is not reliable.

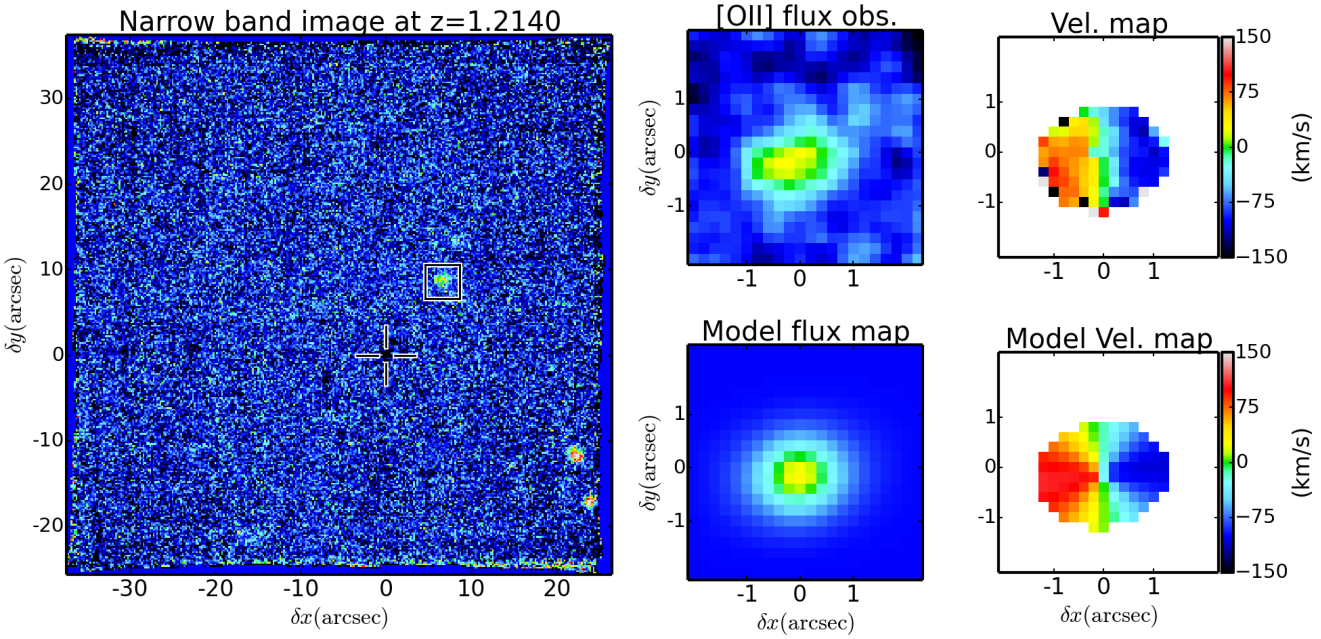

FIG. 4.— Same as Figure 2 but for J213748+0012G3 at redshift $z = 1.2140$. This galaxy has a maximum SNR/pixel of 4.5. The spots located bottom right in the narrow band image corresponds to other galaxies. These galaxy have very low probability to be the host of the Mg II absorption line in the quasar spectrum as they are located further away from the quasar LOS (212 kpc and 246 kpc).

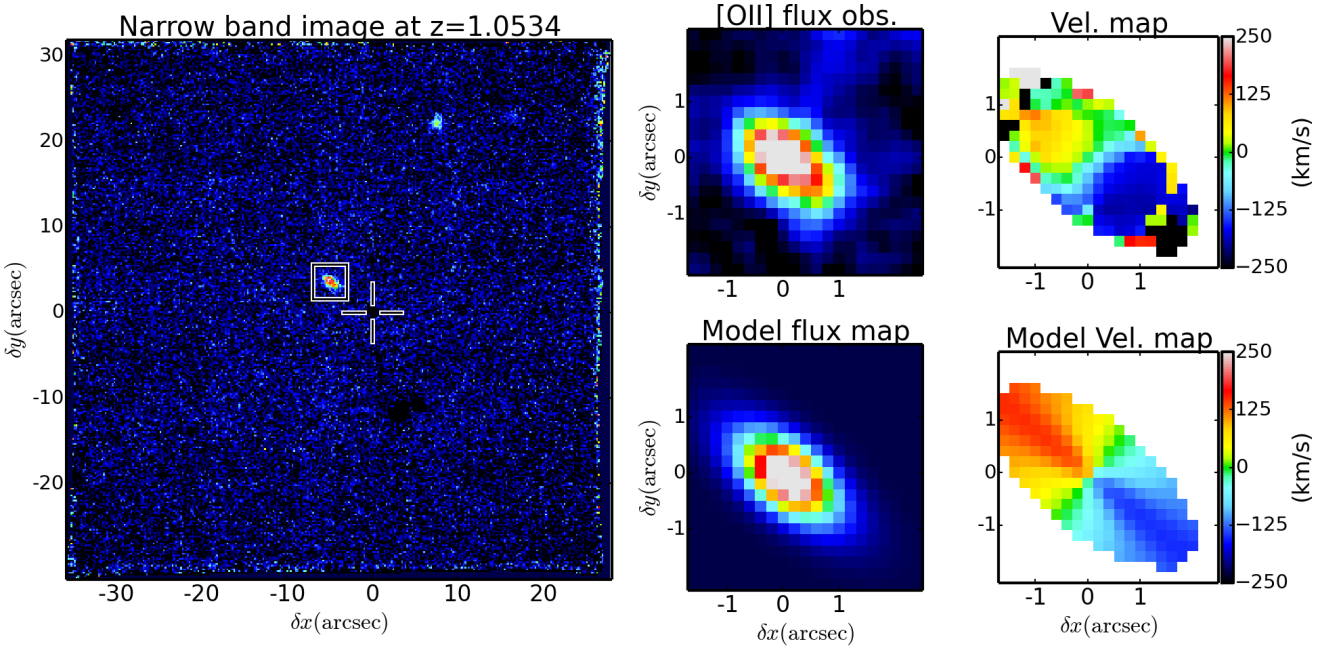

FIG. 5.— Same as Figure 2 but for J215200+0625G1 at redshift $z = 1.0534$. This galaxy has a maximum SNR/pixel of 9.3. The spot located top middle-right in the narrow band image corresponds to another galaxy. Like the one in Figure 4, this galaxy is less likely to be the host of the Mg II absorption line in the quasar spectrum as it is located further away from the quasar LOS (189 kpc).

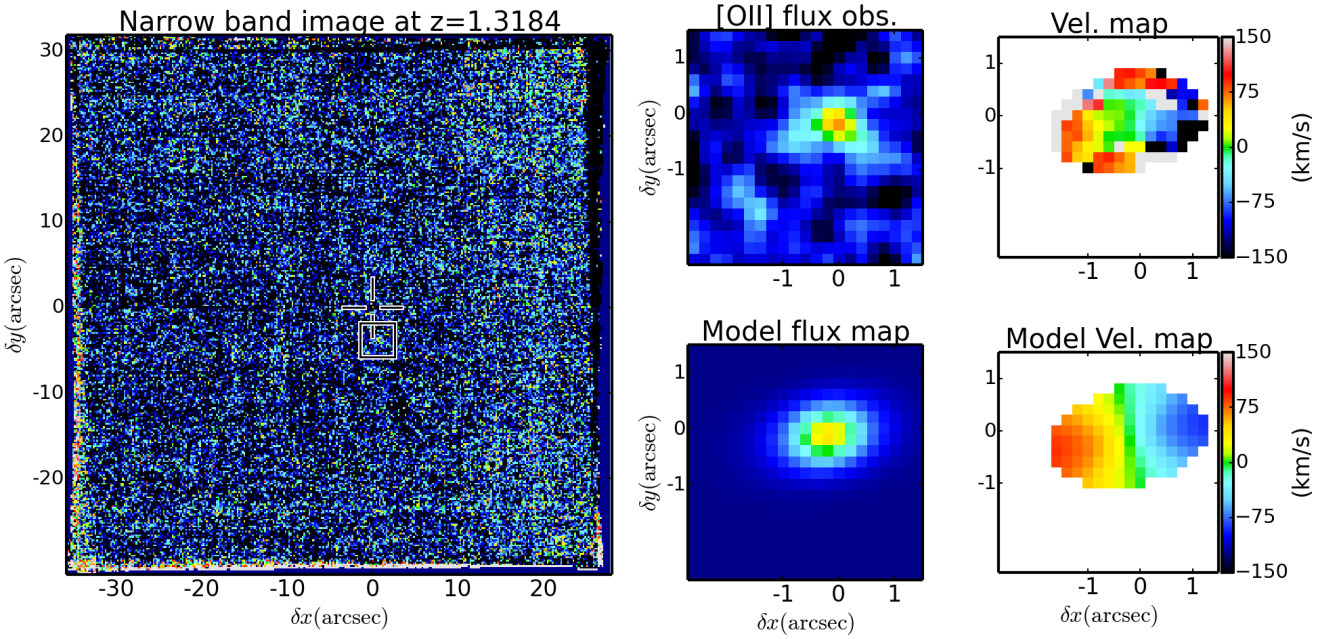

FIG. 6.— Same as Figure 2 but for **J215200+0625G2** at redshift $z = 1.3184$. This galaxy has a maximum SNR/pixel of 4.2 and is thus difficult to see in the left image but can be seen in the smoothed [OII] flux image.

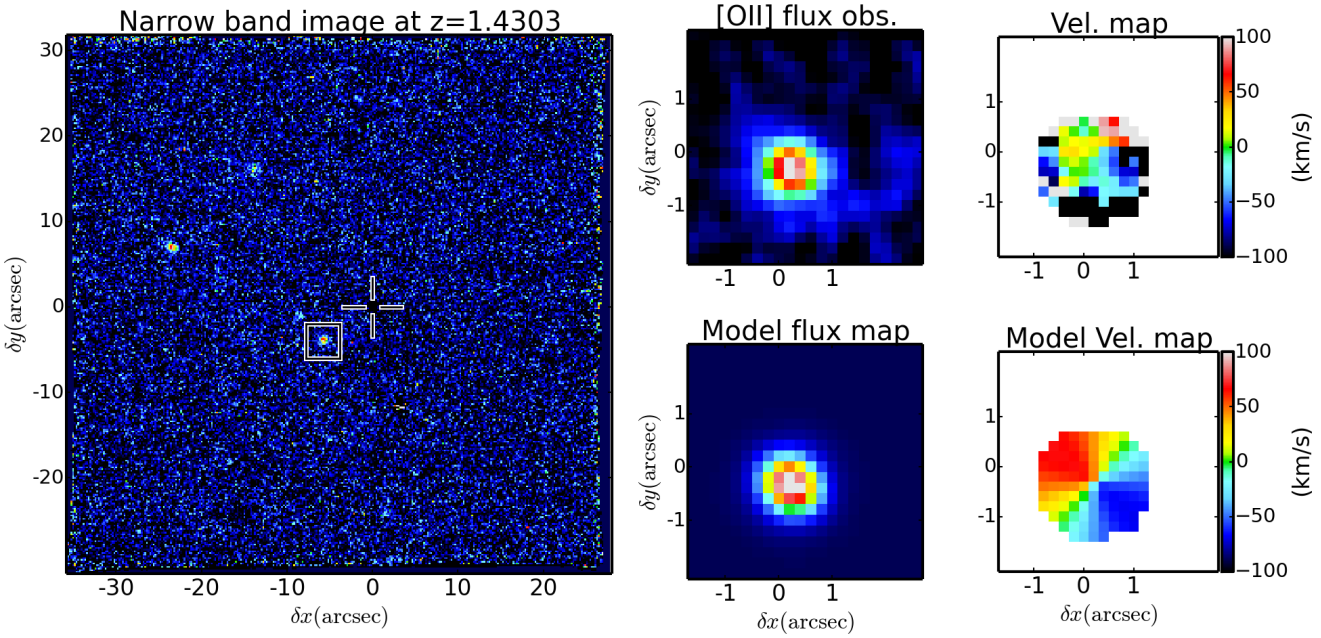

FIG. 7.— Same as Figure 2 but for J215200+0625G3 at redshift $z = 1.4303$. Note that the emissions around the galaxy in the observed [O II] flux panel is noise and not tidal tails. This galaxy has a maximum SNR/pixel of 10.5. Again, as in Figures 4 and 5, residual spots are galaxies further away from the quasar LOS and are thus less likely to be the host of the absorbing materials (78, 184 and 211 kpc). The 78 kpc away galaxy is close enough to be considered as an host galaxy but we choose to ignore it based on impact parameter argument.

TABLE 6
MORPHO-KINEMATICS RESULTS ON HOST GALAXIES.

Galaxy (1)	$z_{\rm abs}$ (2)	$z_{\rm gal}$ (3)	b (4)	SNR (5)	Size (6)	i (7)	$V_{\rm max}$ (8)	Flux (9)	α (10)	Class (11)
J213748+0012G1	0.8063	0.80690±0.00001	88.1±0.2	11	2.43±0.06	49.6±1.4	126.2±5	8.67×10^{-17}	25±1	Inflow
J213748+0012G2	1.1890	1.18925±0.00001	63.7±0.2	11	3.15±0.08	55.6±0.8	15.9±8	1.47×10^{-16}	···	Merger
J213748+0012G3	1.2144	1.21397±0.00003	87.2±0.2	4.5	5.38±0.33	40.4±5.0	166.5±18	4.18×10^{-17}	47±2	Ambig.
J215200+0625G1	1.0534	1.05335±0.00001	45.4±0.2	9.3	5.52±0.09	69.4±0.7	161.4±2	1.09×10^{-16}	4±1	Inflow
J215200+0625G2	1.3190	1.31843±0.00005	34.0±0.2	4.2	3.06±0.51	58.9±10.8	130.6±29	1.99×10^{-17}	88±5	Wind
J215200+0625G3	1.4309	1.43033±0.00004	62.5±0.2	10.5	1.51±0.12	13.3±3.4	298.5±39	5.05×10^{-17}	72±20	Wind/Ambig.

(1) Quasar name; (2) Mg II absorption redshift; (3) Galaxy redshift; (4) Impact parameter (kpc); (5) SNR per pixel; (6) Galaxy half-light radius (kpc); (7) Galaxy inclination (degrees); (8) Galaxy maximum velocity (km s^{-1}); (9) Integrated [O II] flux of the galaxy (erg s^{-1} cm^{-2}); (10) Azimuthal angle (degrees); (11) Class (inflow-pair/wind-pair) based on α selection.

TABLE 7
UVES REST EQUIVALENT WIDTHS.

Galaxy (1)	$W_r^{\lambda2796}$(SDSS) (2)	$W_r^{\lambda2796}$ (3)	$W_r^{\lambda2802}$ (4)	$W_r^{\lambda2852}$ (5)	$W_r^{\lambda2586}$ (6)	$W_r^{\lambda2600}$ (7)	$log(N_{\rm H\,I})$ (8)	Class (9)
J213748+0012G1	0.724±0.09	0.789±0.02	0.572±0.02	0.145±0.02	0.135±0.02	0.309±0.02	19.24	Inflow
J213748+0012G2	0.308±0.06	0.294±0.02	0.155±0.02	0.039±0.02	···	0.058±0.02	18.61	Merger
J213748+0012G3	1.122±0.06	1.132±0.02	1.040±0.02	0.223±0.02	0.707±0.02	0.947±0.02	19.58	Ambig.
J215200+0625G1	0.522±0.14	0.545±0.02	0.460±0.02	0.116±0.02	0.175±0.02	0.271±0.02	19.01	Inflow
J215200+0625G2	1.347±0.12	1.424±0.02	1.065±0.02	0.158±0.02	0.322±0.02	0.709±0.02	19.71	Wind
J215200+0625G3	1.152±0.11	1.157±0.02	···	···	0.122±0.02	0.242±0.02	19.59	Wind/Ambig.

(1) Quasar name; (2) SDSS Mg II $\lambda2796$ rest equivalent width (Å); (3) UVES Mg II $\lambda2796$ rest equivalent width (Å); (4) UVES Mg II $\lambda2803$ rest equivalent width (Å); (5) UVES Mg I $\lambda2852$ rest equivalent width (Å); (6) UVES Fe II $\lambda2586$ rest equivalent width (Å); (7) UVES Fe II $\lambda2600$ rest equivalent width (Å); (8) Gas column density at the impact parameter (cm^{-2}); (9) Class (inflow-pair/wind-pair) based on α selection.

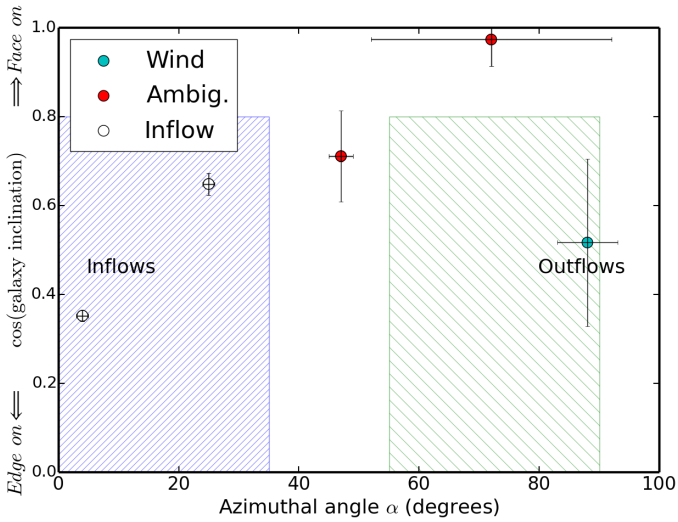

FIG. 8.— Galaxy inclinations as a function of azimuthal angle α for the 5 non-merger galaxies detected in the two fields J213748+0012 and J215200+0625. We note that only one galaxy is classified as a wind-pair. The dashed areas correspond to azimuthal angle ranges for which we classify pairs as inflow-pairs (blue and narrow dashes) or wind-pairs (green and wider dashes). These areas stop for face-on galaxies as uncertainty on position angles are too large and thus difficult to classify pairs.

directly on the wind opening angle $\theta_{\rm max}$ (Figure A-1 in Schroetter et al. (2015)). Note that the galaxy inclination impacts the absorption profiles similarly to the $\theta_{\rm max}$ parameter but since the inclination is determined by our 3D fit with GalPaK^{3D}, there are no degeneracies.

In order to choose which model best reproduces the data, we generate tens of simulated profiles for every set of parameters. The best-fit model is found "by eye" and errors on these parameters are given by the range of values allowed by the data[11]. We proceed as follow: We first generate models changing only one parameter to fit one part of the absorption profile (outer part for $V_{\rm out}$ or inner part for $\theta_{\rm max}$). Then, we change only the other parameter ($\theta_{\rm max}$ or $V_{\rm out}$) generating other models to fit the other part of the absorption. We generate models with range of values of 10 to 500 km s^{-1} (with steps of 10 km s^{-1}) for $V_{\rm out}$ and 20 to 50° (with steps of 5°) for $\theta_{\rm max}$. As mentioned before, these two parameters being independent, there is no degeneracy between generated models.

Examples on how the wind model behaves as we change the different parameters can be seen in the appendix of Schroetter et al. (2015).

4.1. *The wind−pair case of* ***J215200+0625G2***

Figure 10, middle column (b), shows the UVES Mg I λ2852, Mg II $\lambda\lambda$2796, 2802 and Fe II $\lambda\lambda$2586, 2600 absorption lines for this galaxy-quasar pair. From this Figure, we can see that the Mg II $\lambda\lambda$2796, 2802 absorption lines are saturated and thus the need to simulate the absorption from Fe II λ2586 which is the only non-saturated absorption lines in the presented transitions.

The bottom right panel of Figure 12 shows the UVES Fe II λ2586 absorption lines corresponding to the **J215200+0625G2** galaxy redshift of $z = 1.3184$. This absorption is the one we intend to fit in order to constrain outflow properties since other absorption lines like Mg II are saturated (see panel (b) of Figure 10). In this profile, we can see a suppression of absorption around 80 km s^{-1}. We first tried to fit this absorption with our wind model described in § 4 but failed to reproduce this gap, even with stochastic effects. This lack of absorbing particles at these velocities shows that the outflowing cone must have a low density region inside it.

Given that the geometry of this galaxy-quasar system (with a galaxy inclination i of 59°) and that the quasar line of sight is crossing the outflowing cone near its middle ($\alpha = 88°$), we thus developed a partially empty cone model in order to reproduce the absorption profile.

The principle is the same as the wind model described in § 4 except that we only fill the cone with particles from a certain opening angle $\theta_{\rm in}$ to $\theta_{\rm max}$. The inner cone is thus empty. This model should only work if the azimuthal angle α of a galaxy−quasar system is above $\sim 80°$, so the quasar LOS is crossing this empty region and thus creating a gap of velocities in the simulated profile.

This empty inner cone could be the signature of a hotter gas filling the inner cone while the ionized gas traced by our low-ionization lines would correspond to the walls of the outflowing cone in a manner similar to Fox et al. (2015) for the MilkyWay and to Veilleux & Rupke (2002) for NGC1482.

Figure 12 illustrates the resulting wind modeling for this galaxy. The first left column corresponds to the wind model representation. The top left panel shows a [O II] integrated flux, continuum subtracted, image with the orange cross showing the quasar LOS position. The inclined circles represent the outflowing cone. The bottom left panel represents a side view of the cone, the quasar LOS being represented by the dashed red line, the observer being on the left. This representation allows us to see if the outflowing material is ejected toward or away from us, assuming our cone model is representative. The red part of the cone represents the empty inner part.

On the middle column are represented the simulated profiles (top) and UVES spectrum around the absorption line Fe II λ2586 (bottom). The red part of the simulated profile is the profile without instrumental noise and the apparent noise is due to stochastic effects from the Monte Carlo particle distribution. The red simulated absorption profile does not change much for the UVES data as compare to the noise-added one. We also present in Figure 12, top right panel, a similar simulated profile (with the same parameters) but without the empty inner cone model. We clearly see on this Figure that we cannot reproduce the gap shown in the data without an empty region.

The bottom middle panel corresponds to UVES data. It corresponds to the QSO spectrum absorption lines centered at the galaxy systemic velocity. The element Fe II λ2586 corresponding to the absorption lines is shown in the bottom middle column panel.

To reproduce the shape of this absorption profile and generate the simulated profile shown in the top middle panel of Figure 12, we adjust the outflow speed $V_{\rm out}$ and the cone opening angle $\theta_{\rm max}$ while keeping the geometrical parameters of the galaxy fixed as described in § 4.

The best values for reproducing the UVES Fe II λ2586

[11] Thus, errors on $V_{\rm out}$ and $\theta_{\rm max}$ correspond to $\approx 3\sigma$.

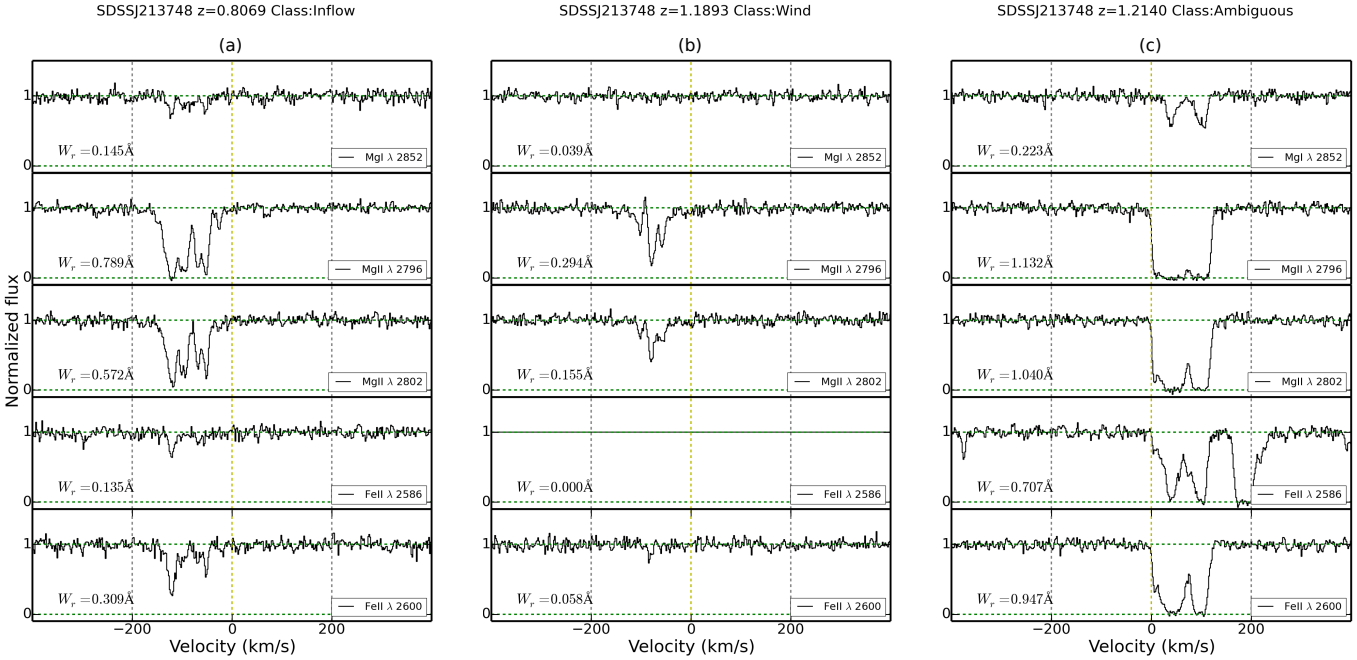

FIG. 9.— UVES Mg I $\lambda 2852$, Mg II $\lambda\lambda 2796, 2802$ and Fe II $\lambda\lambda 2586, 2600$ absorption lines centered at host galaxy systemic velocity for the SDSSJ213748+0012 quasar spectrum. The left panel corresponds to absorption lines from the SDSSJ213748+0012G1 host galaxy (a). The middle panel to the SDSSJ213748+0012G2 host galaxy (b), and right panel to SDSSJ213748+0012G3 (c). Note that in the right column, the Fe II $\lambda 2586$ REW is calculated without the $\approx$200 km s^{-1} absorption component.

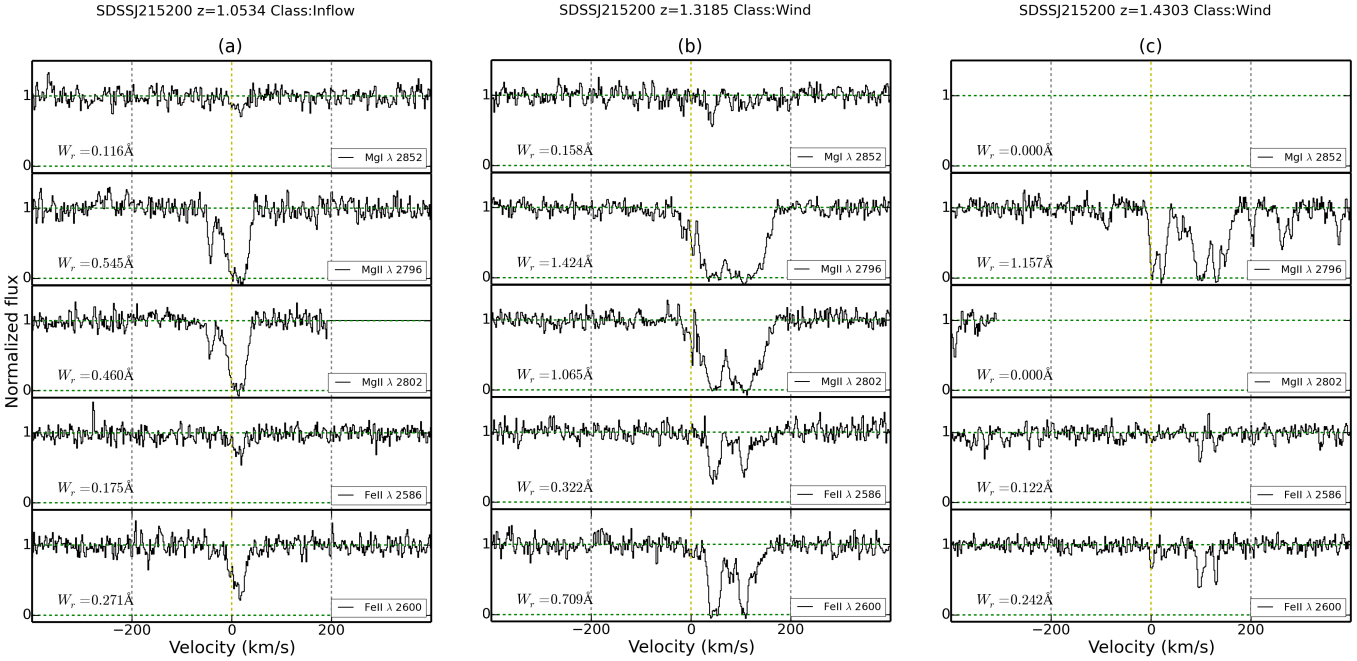

FIG. 10.— UVES Mg I $\lambda 2852$, Mg II $\lambda\lambda 2796, 2802$ and Fe II $\lambda\lambda 2586, 2600$ absorption lines centered at host galaxy systemic velocity for the SDSSJ215200+0625 quasar spectrum. The left panel corresponds to absorption lines from the SDSSJ215200+0625G1 host galaxy (a). The middle panel to the **SDSSJ215200+0625G2** host galaxy (b), and right panel to SDSSJ215200+0625G3 (c).

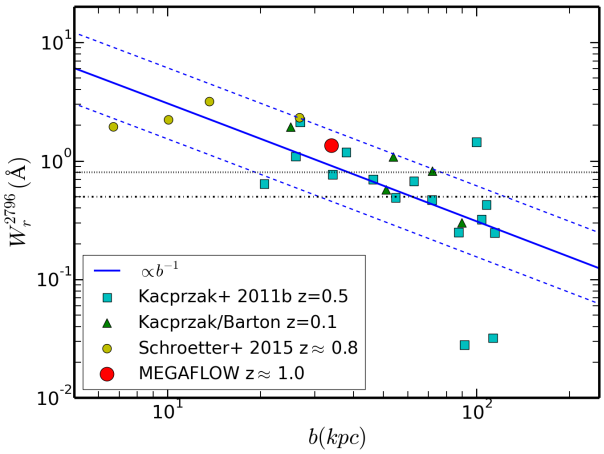

FIG. 11.— $W_r^{\lambda 2796}$ as a function of impact parameter b for galaxy-quasar pairs classified as wind-pairs. The dashed blue lines show the 0.3 dex scatter. The horizontal dotted black lines represent the $W_r^{\lambda 2796}$=0.8 Å and $W_r^{\lambda 2796}$=0.5 Å selection limits.

absorption profile are an outflow velocity $V_{\rm out}$ of 150 ± 10 km s^{-1} and a cone opening angle $\theta_{\rm max}$ of $20 \pm 5°$. For this specific case, we derive an inner opening angle of the cone of $\theta_{\rm in} \approx 7°$.

4.2. *Outflow rates*

Having constrained the outflow velocity and cone opening angle for the wind-pair, we can now derive the ejected mass rate $\dot{M}_{\rm out}$ as well as the loading factor.

For our wind-pair, the equivalent width of the absorption lines only depends on $\theta_{\rm max}$ and $V_{\rm out}$ (see § 4). After testing several opening angles and outflow velocities, we fitted the width of the absorption profile created by gas outflowing from the galaxy. The asymmetry of the profile depends on the system geometry. To constrain the ejected mass rate probed by the quasar LOS, we use relation 5 from Bouché et al. (2012) and Schroetter et al. (2015):

$$\dot{M}_{\rm out} \approx \mu \cdot N_{\rm H}(b) \cdot b \cdot V_{\rm out} \cdot \frac{\pi}{2} \cdot \theta_{\rm max} \qquad (5)$$

$$\frac{\dot{M}_{\rm out}}{0.5 {\rm M}_\odot\,{\rm yr}^{-1}} \approx \frac{\mu}{1.5} \cdot \frac{N_{\rm H}(b)}{10^{19}{\rm cm}^{-2}} \cdot \frac{b}{25{\rm kpc}} \cdot \frac{V_{\rm out}}{200{\rm km\,s}^{-1}} \cdot \frac{\theta_{\rm max}}{30°}$$

μ being the mean atomic weight, b the impact parameter, $\theta_{\rm max}$ the cone opening angle[12], $V_{\rm out}$ the outflow velocity and $N_{\rm H}(b)$ is the gas column density at the b distance.

The only parameter which is yet to be constrained is the gas column density $N_{\rm H}(b)$. To do that, we use the empirical relation 6 between the neutral gas column density and the Mg II λ2796 REW $W_r^{\lambda 2796}$ (Ménard & Chelouche 2009):

$$\log(N_{\rm HI})({\rm cm}^{-2}) = \log[(3.06{\pm}0.55){\times}10^{19}{\times}(W_r^{\lambda 2796})^{1.7\pm0.26}]. \qquad (6)$$

To compute the errors, we assume a gaussian error distribution. As described in Schroetter et al. (2015), for regions with H I column density above $\log(N_{\rm HI}) = 19.5$, the ionized gas contribution is negligible. Also argued by Jenkins (2009), if this column density is above this limit, one can use the correlation between Mg II equivalent width and $N_{\rm HI}$ as a proxy for the $N_{\rm H}$ gas column density. For the wind-pair **J215200+0625G2**, we have a gas column density of $\log(N_{\rm HI}) \approx 19.7 \pm 0.07$.

Another aspect of outflow properties is whether the outflowing gas is able to escape from the galaxy gravitational well. To determine this, we derive the escape velocity $V_{\rm esc}$ for the **J215200+0625G2** galaxy. The escape velocity for an isothermal sphere is defined by Eq. 7 (Veilleux et al. 2005).

$$V_{\rm esc} = V_{\rm max} \cdot \sqrt{2\left[1 + \ln\left(\frac{R_{\rm vir}}{r}\right)\right]} \qquad (7)$$

$V_{\rm max}$ being the maximum rotation velocity of the galaxy and $R_{\rm vir}$ its virial radius. The virial radius of the galaxies can be define as $R_{\rm vir} \approx V_{\rm max}/10H(z)$ where $H(z)$ is the Hubble parameter at redshift z. In Table 8, we compare the outflow velocity with the escape velocity for the wind-pair. This ratio $V_{\rm out}/V_{\rm esc}$ of 0.52 shows that the outflowing material is not able to reach the escape velocity and will thus likely to fall back onto the galaxy, assuming we are tracing the gas going out of the galaxy. One can ask whether we are already tracing the gas falling back onto the galaxy. If this is the case, we should see another opposite component (with respect to the systemic velocity) in the absorption profile corresponding to the outflowing gas.

Table 8 also lists the estimated outflow rate. The errors on the ejected mass rate $\dot{M}_{\rm out}$ are dominated by the ones on the gas column density $N_{\rm HI}$ and the SFR.

From the outflow rate, we compute the mass loading factor η by comparing it to the SFR ($\eta = \dot{M}_{\rm out}/{\rm SFR}$). For our **SDSSJ215200+0625G2** pair, we used the empty cone model to reproduce the absorption profile with an inner cone opening angle $\theta_{\rm in}$ of 7°. To be consistent with the other cases, we give two solutions for this galaxy−quasar pair: one with the filled cone and one with the inner cone subtracted.

Figure 13 shows the loading factor η as a function of halo mass and maximum rotational velocity $V_{\rm max}$ for this work and previous similar studies (Bouché et al. 2012; Kacprzak et al. 2014; Schroetter et al. 2015). The derived loading factor for galaxy **SDSSJ215200+0625G2** follows the same trend as the others. The green arrow shows the loading factor for the subtracted mass from the low-density inner cone.

MUSE allows us to probe galaxies with an impact parameter larger than before with an IFU. But, in Figure 13, we caution the reader that loading factor for galaxies with impact parameters larger than 60 kpc are less reliable because of the time needed for the gas to travel from the galaxy to the quasar LOS ($\sim$ 400 Myr at $V_{\rm out} \approx 150$km s^{-1} with b = 60 kpc). A major limitation for the comparison between data and models in Figure 13, is that η in simulations are usually measured on a scale of a few kpc away from the galaxy, which is one order of magnitude lower than most of the observations (tens of kpc).

5. DISCUSSION AND CONCLUSIONS

We present results on 2 GTO VLT/MUSE fields in which we searched for galaxy-quasar pairs. These fields

[12] We remind the reader that $\theta_{\rm max}$is defined from the central axis, and the cone subtends an area Σ of $\pi \cdot \theta_{\rm max}^2$.

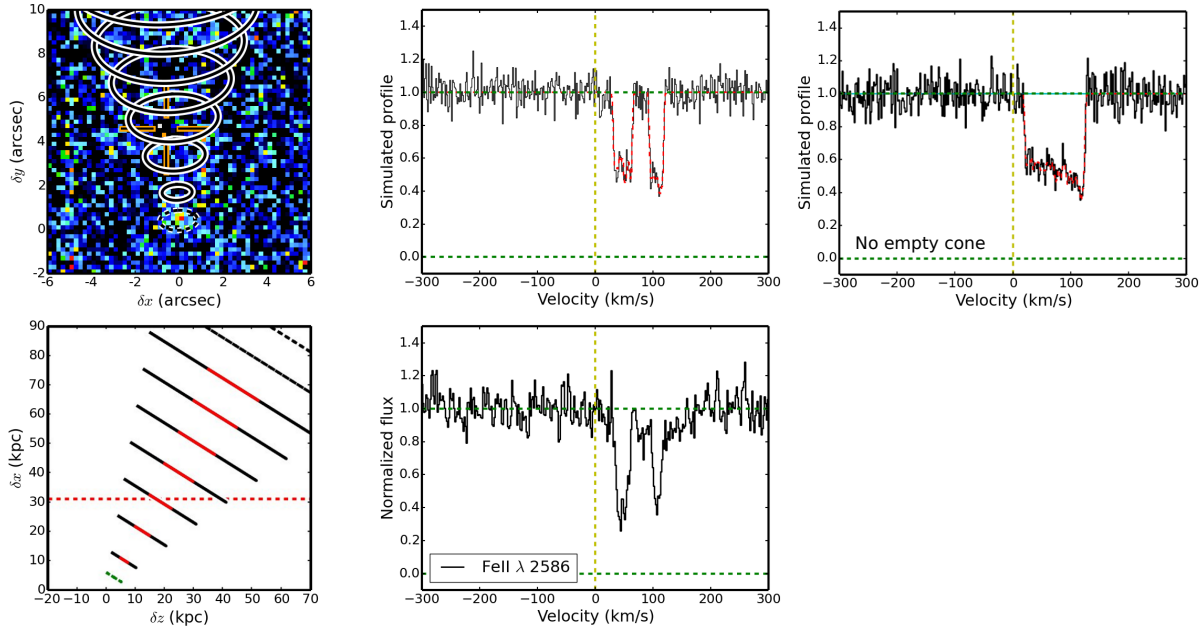

FIG. 12.— Representation of the cone model and quasar spectrum associated with the **J215200+0625G2** galaxy ($z = 1.31845$). *Top left:* the cone model seen in the sky plane (xy). This is a narrow band image centered around the galaxy [O II] emission lines with the continuum subtracted. The dashed circle represents the inclined galaxy disk and the black and white inclined circles illustrate the gas outflow cone. The orange cross represents the position of the quasar LOS. *Bottom left:* a side view of the cone where the z-axis corresponds to the quasar LOS direction with the observer to the left. The red part of the cone represents the empty inner cone. *Middle:* Normalized flux for the Fe II (λ2586) absorption line observed with UVES (bottom) and the reconstructed profile (top). Note that this model does not reproduce the depth of the absorption line. In UVES simulated absorption profile, the red line corresponds to the simulated profile without any instrumental noise. This wind model uses a very low-density inner cone as described in § 4.1. *Right:* same as the top middle panel but with no empty inner cone model. This simulated profile has the same parameters as the empty inner cone one. We can clearly see that we cannot reproduce the gap in absorptions seen in the UVES absorption profile without the empty cone model. This outflow has a $V_{\rm out}$ of 150±10 km s^{-1}, a cone opening angle $\theta_{\rm max}$ of 20±5° and an inner opening angle θ_{in} of 7±2°.

TABLE 8
RESULTS FOR THE GALAXY **J215200+0625G2**.

Galaxy	b (kpc)	$\log(N_{\rm H}(b))$	$V_{\rm max}$	$V_{\rm out}$	$\theta_{\rm max}$	SFR	$\dot{M}_{\rm out}$	$\frac{V_{\rm out}}{V_{\rm esc}}$	η
(1)	(2)	(3)	(4)	(5)	(6)	(7)	(8)	(9)	(10)
J215200+0625G2	34.0	19.7±0.07	140.8 ± 51	150 ± 10	20 ± 5.0	4.6±0.4	$1.7\,^{+1.1}_{-0.8}$	0.52	0.75
							$1.1\,^{+0.9}_{-0.6}$		0.49

(1) Galaxy name; (2) Impact parameter (kpc); (3) Gas column density at the impact parameter (cm^{-2}); (4) Maximum rotational velocity of the galaxy (km s^{-1}); (5) Wind velocity (km s^{-1}); (6) Cone opening angle (degrees) (7) Star Formation Rate (M$_\odot$ yr^{-1}); (8) Ejected mass rate for one cone (M$_\odot$ yr^{-1}); (9) Ejection velocity divided by escape velocity; (10) Mass loading factor: ejected mass rate divided by star formation rate (for both cones). We note that values in row 2 correspond to the empty inner cone model.

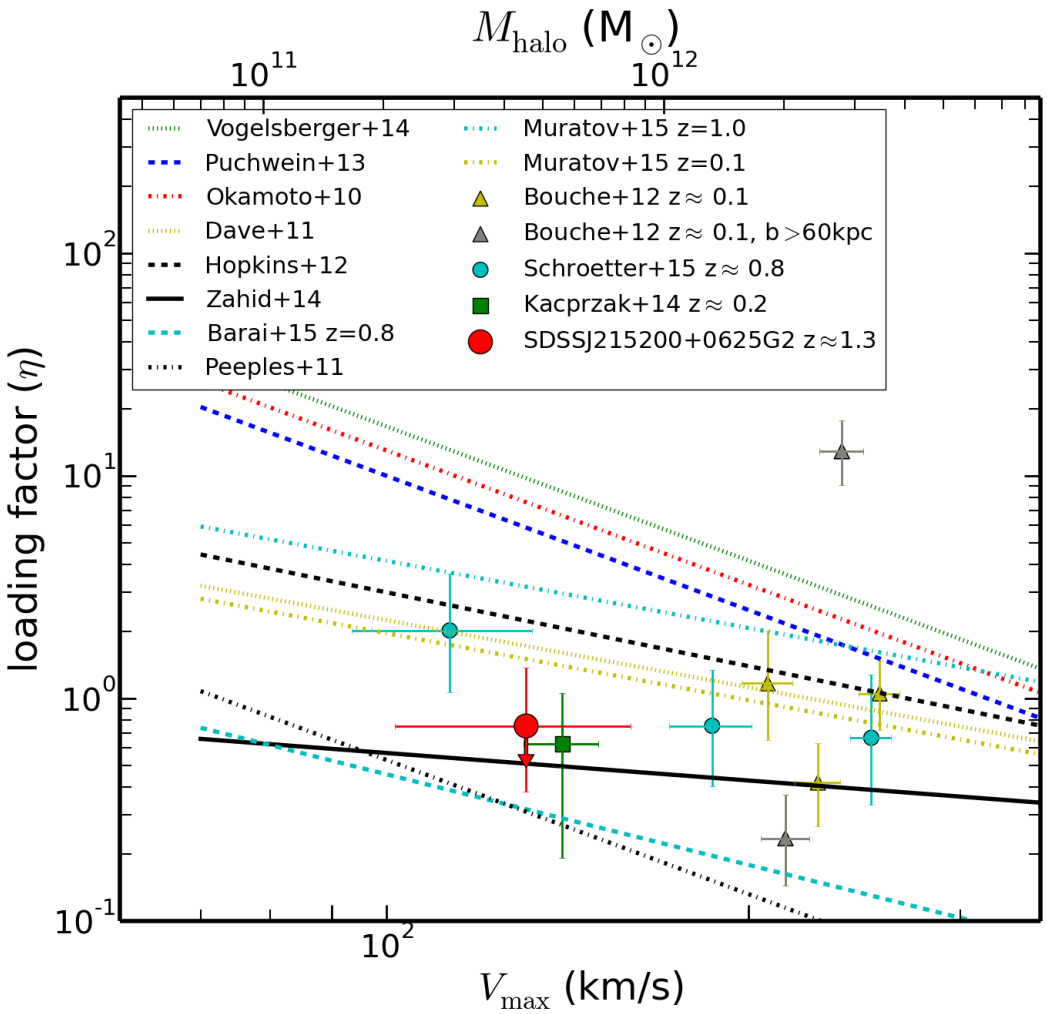

FIG. 13.— Comparison of mass loading factors assumed by theoretical/empirical models (curves) with values derived from **background quasar** observations (dots and triangles) as a function of the maximum rotational velocity. The result from this work is represented by the red circle. The red arrow represents the loading factor of the **SDSSJ215200+0625G2** galaxy with the subtracted mass from the inner cone model. The cyan circles show the results for galaxies at $z \approx 0.8$ from Schroetter et al. (2015). The green square shows the mass loading factor for a $z \approx 0.2$ galaxy (Kacprzak et al. 2014). The triangles show the results for $z \approx 0.2$ galaxies from Bouché et al. (2012). The gray triangles show the galaxies with quasars located at >60kpc where the mass loading factor is less reliable due to the large travel time needed for the outflow to cross the quasar LOS (several 100 Myr) compared to the short time scale of the Hα derived SFR ($\sim$ 10Myr). The upper halo mass axis is scaled on $V_{\rm max}$ at redshift 0.8 from Mo & White (2002).

were selected from the SDSS database where we searched for multiple Mg II absorbers, with $z \approx 0.8 - 1.4$ and $W_r^{\lambda 2796} > 0.5$Å, in the quasar spectra. Out of 8 Mg II absorptions in the quasar spectra of these two fields, we detect 6 redshift-corresponding SFGs. For these 2 fields (J213748+1112 and J215200+0625) we also have high resolution spectra of the quasars from the VLT/UVES instrument. In each of these two fields, we detected more than 40 emitters in the $1' \times 1'$ MUSE field of view (see the Appendix). We focused on galaxies at MgII absorptions redshifts in the quasar spectra and for which the associated quasar LOS is aligned with their minor axis ($\alpha > 55°$) and is thus likely to probe outflowing materials (wind−pairs). Among the 6 detected SFGs, one is likely to be a wind-pair due to its orientation with respect to its relative quasar.

In summary, thanks to our new GTO VLT/MUSE and VLT/UVES data, MUSE allows us to detect galaxies far away from their associated quasar ($\sim$ 100 kpc) as compare to previous similar works (i.e. Bouché et al. 2012; Kacprzak et al. 2014; Schroetter et al. 2015). For the wind-pair **SDSSJ215200+0625G2**, we found that the outflow velocity $V_{\rm out}$ is $\approx$ 150 km s^{-1}. The outflowing gas is likely to stay inside the gravitational well of the galaxy and the loading factor is $\eta \approx 0.7$. We showed a gap in velocities in the absorption profile which led to a low-density inner cone modeling. At this point, we have outflowing constraints for one galaxy but we showed that MUSE is able to provide very good data and will play a fundamental role in this field.

MUSE allowed us to probe multiple galactic wind cases at the same time and enhance the number of cases with only two quasar fields. We also have a case of low-density inner cone which opens discussions on geometrical properties of outflowing materials. The MEGAFLOW sample is currently growing and successful in detecting galaxies in each quasar field ($\approx$84% detection). Future work will be done with a lot more observation with MUSE+UVES, and in a short time, the MEGAFLOW sample should be large enough to produce statistical results on outflow

properties.

Acknowledgments. We would like to thank the referee for his/her thorough read of the manuscript and for the useful suggestions and comments. NB acknowledges support from a Career Integration Grant (CIG) (PCIG11-GA-2012-321702) within the 7th European Community Framework Program. This work has been carried out thanks to the support of the ANR FOGHAR (ANR-13-BS05-0010-02), the OCEVU Labex (ANR-11-LABX-0060) and the A*MIDEX project (ANR-11-IDEX-0001-02) funded by the "Investissements d'Avenir" French government program managed by the ANR. This work received financial support from the European Research Council under the European Union's Seventh Framework Programme (FP7/2007-2013) / ERC Grant agreement 278594-GasAroundGalaxies.

REFERENCES

Aguirre, A., Hernquist, L., Schaye, J., et al. 2001, ApJ, 561, 521
Alam, S., Albareti, F. D., Allende Prieto, C., et al. 2015, ArXiv e-prints, arXiv:1501.00963
Bacon, R., Bauer, S., Boehm, P., et al. 2006, in Society of Photo-Optical Instrumentation Engineers (SPIE) Conference Series, Vol. 6269, Society of Photo-Optical Instrumentation Engineers (SPIE) Conference Series, 0
Bacon, R., Bauer, S., Brau-Nogué, S., et al. 2009, Astrophysics and Space Science Proceedings, 9, 331
Barai, P., Monaco, P., Murante, G., Ragagnin, A., & Viel, M. 2015, MNRAS, 447, 266
Behroozi, P. S., Wechsler, R. H., & Conroy, C. 2013, ApJ, 770, 57
Booth, C. M., Agertz, O., Kravtsov, A. V., & Gnedin, N. Y. 2013, ApJ, 777, L16
Bordoloi, R., Lilly, S. J., Kacprzak, G. G., & Churchill, C. W. 2014, ApJ, 784, 108
Bordoloi, R., Lilly, S. J., Knobel, C., et al. 2011, ApJ, 743, 10
Bouché, N., Carfantan, H., Schroetter, I., Michel-Dansac, L., & Contini, T. 2015, GalPaK 3D: Galaxy parameters and kinematics extraction from 3D data, Astrophysics Source Code Library, ascl:1501.014
Bouché, N., Hohensee, W., Vargas, R., et al. 2012, MNRAS, 426, 801
Bouché, N., Finley, H., Schroetter, I., et al. 2016, ApJ, 820, 121
Chabrier, G. 2003, PASP, 115, 763
Charlot, S., Kauffmann, G., Longhetti, M., et al. 2002, MNRAS, 330, 876
Chen, H.-W., Wild, V., Tinker, J. L., et al. 2010, ApJ, 724, L176
Chisholm, J., Tremonti, C. A., Leitherer, C., Chen, Y., & Wofford, A. 2016, ArXiv e-prints, arXiv:1601.05090
Chisholm, J., Tremonti, C. A., Leitherer, C., et al. 2015, ApJ, 811, 149
Dekel, A., & Silk, J. 1986, ApJ, 303, 39
Dekker, H., D'Odorico, S., Kaufer, A., Delabre, B., & Kotzlowski, H. 2000, in Society of Photo-Optical Instrumentation Engineers (SPIE) Conference Series, Vol. 4008, Optical and IR Telescope Instrumentation and Detectors, ed. M. Iye & A. F. Moorwood, 534–545
Epinat, B., Tasca, L., Amram, P., et al. 2012, A&A, 539, A92
Fox, A., Jenkins, E. B., Hernandez, S., et al. 2015, in American Astronomical Society Meeting Abstracts, Vol. 225, American Astronomical Society Meeting Abstracts, 203.02
Guo, Q., White, S., Li, C., & Boylan-Kolchin, M. 2010, MNRAS, 404, 1111
Heckman, T. M., Alexandroff, R. M., Borthakur, S., Overzier, R., & Leitherer, C. 2015, ApJ, 809, 147
Heckman, T. M., Armus, L., & Miley, G. K. 1990, ApJS, 74, 833
Heckman, T. M., Lehnert, M. D., Strickland, D. K., & Armus, L. 2000, ApJS, 129, 493
Hopkins, P. F. 2015, MNRAS, 450, 53
Hopkins, P. F., Kereš, D., Oñorbe, J., et al. 2014, MNRAS, 445, 581
Jenkins, E. B. 2009, ApJ, 700, 1299
Kacprzak, G. G., Churchill, C. W., Barton, E. J., & Cooke, J. 2011a, ApJ, 733, 105
Kacprzak, G. G., Churchill, C. W., Evans, J. L., Murphy, M. T., & Steidel, C. C. 2011b, MNRAS, 416, 3118
Kacprzak, G. G., Churchill, C. W., & Nielsen, N. M. 2012, ApJ, 760, L7
Kacprzak, G. G., Martin, C. L., Bouché, N., et al. 2014, ApJ, 792, L12
Kennicutt, Jr., R. C. 1998, ApJ, 498, 541
Kewley, L. J., Geller, M. J., & Jansen, R. A. 2004, AJ, 127, 2002
Lan, T.-W., Ménard, B., & Zhu, G. 2014, ApJ, 795, 31
Lanzetta, K. M., & Bowen, D. 1990, ApJ, 357, 321
Lehnert, M. D., & Heckman, T. M. 1996, ApJ, 472, 546
Martin, C. L. 1998, ApJ, 506, 222
—. 1999, ApJ, 513, 156
—. 2005, ApJ, 621, 227
Martin, C. L., Kobulnicky, H. A., & Heckman, T. M. 2002, ApJ, 574, 663
Martin, C. L., Shapley, A. E., Coil, A. L., et al. 2012, ApJ, 760, 127
—. 2013, ApJ, 770, 41
Ménard, B., & Chelouche, D. 2009, MNRAS, 393, 808
Mo, H. J., & White, S. D. M. 2002, MNRAS, 336, 112
Moster, B. P., Naab, T., & White, S. D. M. 2013, MNRAS, 428, 3121
Moster, B. P., Somerville, R. S., Maulbetsch, C., et al. 2010, ApJ, 710, 903
Muratov, A. L., Keres, D., Faucher-Giguere, C.-A., et al. 2015, ArXiv e-prints, arXiv:1501.03155
Murray, N., Quataert, E., & Thompson, T. A. 2005, ApJ, 618, 569
Muzahid, S., Kacprzak, G. G., Churchill, C. W., et al. 2015, ApJ, 811, 132
Nestor, D. B., Turnshek, D. A., & Rao, S. M. 2005, ApJ, 628, 637
Nielsen, N. M., Churchill, C. W., & Kacprzak, G. G. 2013, ApJ, 776, 115
Oppenheimer, B. D., & Davé, R. 2006, MNRAS, 373, 1265
Oppenheimer, B. D., Davé, R., Kereš, D., et al. 2010, MNRAS, 406, 2325
Papastergis, E., Cattaneo, A., Huang, S., Giovanelli, R., & Haynes, M. P. 2012, ApJ, 759, 138
Pettini, M., Rix, S. A., Steidel, C. C., et al. 2002, ApJ, 569, 742
Ross, N. P., Myers, A. D., Sheldon, E. S., et al. 2012, ApJS, 199, 3
Rubin, K. H. R., Weiner, B. J., Koo, D. C., et al. 2010, ApJ, 719, 1503
Rupke, D. S., Veilleux, S., & Sanders, D. B. 2005, ApJS, 160, 115
Salem, M., & Bryan, G. L. 2014, MNRAS, 437, 3312
Salpeter, E. E. 1955, ApJ, 121, 161
Schaye, J., Dalla Vecchia, C., Booth, C. M., et al. 2010, MNRAS, 402, 1536
Schaye, J., Crain, R. A., Bower, R. G., et al. 2015, MNRAS, 446, 521
Schroetter, I., Bouché, N., Péroux, C., et al. 2015, ApJ, 804, 83
Soto, K. T., Lilly, S. J., Bacon, R., Richard, J., & Conseil, S. 2016a, MNRAS, submitted (astro-ph/1602.08037), arXiv:1602.08037
—. 2016b, ZAP: Zurich Atmosphere Purge, Astrophysics Source Code Library, ascl:1602.003
Springel, V., & Hernquist, L. 2003, MNRAS, 339, 289
Springel, V., White, S. D. M., Jenkins, A., et al. 2005, Nature, 435, 629
Steidel, C. C. 1995, in QSO Absorption Lines, ed. G. Meylan, 139
Torrey, P., Vogelsberger, M., Genel, S., et al. 2014, MNRAS, 438, 1985
Veilleux, S., Cecil, G., & Bland-Hawthorn, J. 2005, ARA&A, 43, 769
Veilleux, S., & Rupke, D. 2002, Anglo-Australian Observatory Epping Newsletter, 99, 6
Vogelsberger, M., Genel, S., Springel, V., et al. 2014, Nature, 509, 177
Weilbacher, P. M., Streicher, O., Urrutia, T., et al. 2014, in Astronomical Society of the Pacific Conference Series, Vol. 485, Astronomical Data Analysis Software and Systems XXIII, ed. N. Manset & P. Forshay, 451
Werk, J. K., Prochaska, J. X., Thom, C., et al. 2013, ApJS, 204, 17
Wood, C. M., Tremonti, C. A., Calzetti, D., et al. 2015, MNRAS, 452, 2712
Zahid, H. J., Torrey, P., Vogelsberger, M., et al. 2014, Ap&SS, 349, 873
Zhu, G., & Ménard, B. 2013, ApJ, 770, 130

TABLE 9
MUSE Sources in the SDSSJ213748+0012 field with redshifts. Within these 42 emitters, 36 have identified emission lines.

ID	R.A.	Dec.	redshift	lines
obj001	21:37:48.303	+00:12:21.69	0.132	OIII, H_β, H_α, NII
obj002	21:37:48.757	+00:12:19.29	0.156	OIII, H_β, H_α, NII
obj003	21:37:50.157	+00:12:52.89	0.315	H_β, OIII
obj004	21:37:48.370	+00:12:23.89	0.325	OII, OIII, H_β, H_α, NII
obj005	21:37:48.370	+00:12:24.09	0.325	OII, OIII, H_β, H_α
obj006	21:37:48.930	+00:12:38.69	0.409	OII, OIII, H_α, NII
obj007	21:37:49.223	+00:12:20.09	0.410	OII, OIII, H_β
obj008	21:37:49.810	+00:12:15.69	0.442	OII
obj009	21:37:48.477	+00:12:30.09	0.543	OII, OIII, H_β
obj010	21:37:48.450	+00:12:29.49	0.543	OII, OIII, H_β
obj011	21:37:50.450	+00:12:02.89	0.580	OIII, H_β
obj012	21:37:48.983	+00:12:55.09	0.616	OII, OIII, H_β
obj013	21:37:49.343	+00:12:52.09	0.684	OII, OIII, H_β
obj014	21:37:47.743	+00:12:46.69	0.711	OII
obj015	21:37:49.530	+00:12:14.69	0.766	OII
obj016	21:37:48.317	+00:12:15.69	0.767	OII
obj017	21:37:49.463	+00:12:16.49	0.767	OII, OIII
obj018	21:37:49.023	+00:12:27.29	0.806	OII, OIII, H_β
obj019	21:37:48.823	+00:12:27.49	0.806	OII, OIII
obj020	21:37:50.157	+00:12:30.89	0.806	OII, OIII
obj021	21:37:49.490	+00:12:33.69	···	8281.3
obj022	21:37:50.103	+00:12:53.29	···	6823.
obj023	21:37:49.117	+00:12:11.89	···	6897.
obj024	21:37:47.663	+00:12:12.69	0.900	OII
obj025	21:37:48.930	+00:12:09.49	0.902	OII?
obj026	21:37:48.517	+00:12:05.69	···	7079.69
obj027	21:37:48.063	+00:12:33.69	···	7376.81
obj028	21:37:48.437	+00:12:46.29	1.010	OII
obj029	21:37:48.837	+00:12:42.69	1.010	OII
obj030	21:37:48.970	+00:12:09.49	1.045	OII
obj031	21:37:49.970	+00:12:09.09	1.044	OII
obj032	21:37:49.970	+00:12:15.29	1.122	OII
obj033	21:37:48.903	+00:12:17.69	1.188	OII
obj034	21:37:46.837	+00:12:02.89	1.212	OII
obj035	21:37:47.970	+00:12:29.09	1.213	OII
obj036	21:37:46.943	+00:12:08.89	1.214	OII
obj037	21:37:47.850	+00:12:33.49	1.214	OII
obj038	21:37:50.410	+00:12:20.09	1.257	OII
obj039	21:37:48.370	+00:12:04.69	1.300	OII
obj040	21:37:47.717	+00:12:46.89	···	8569.12
obj041	21:37:48.730	+00:12:15.29	5.941	8434.53 Lyα?
obj042	21:37:48.823	+00:12:27.49	6.442	9043.03 Lyα?

APPENDIX

MUSE FIELDS EMITTERS DETECTION

For completeness we looked for these emitters by visual inspection and found 42 galaxies with emission lines in each of these two fields (see Table 9 for SDSSJ213748+0012 and Table 10 for SDSSJ215200+0625).

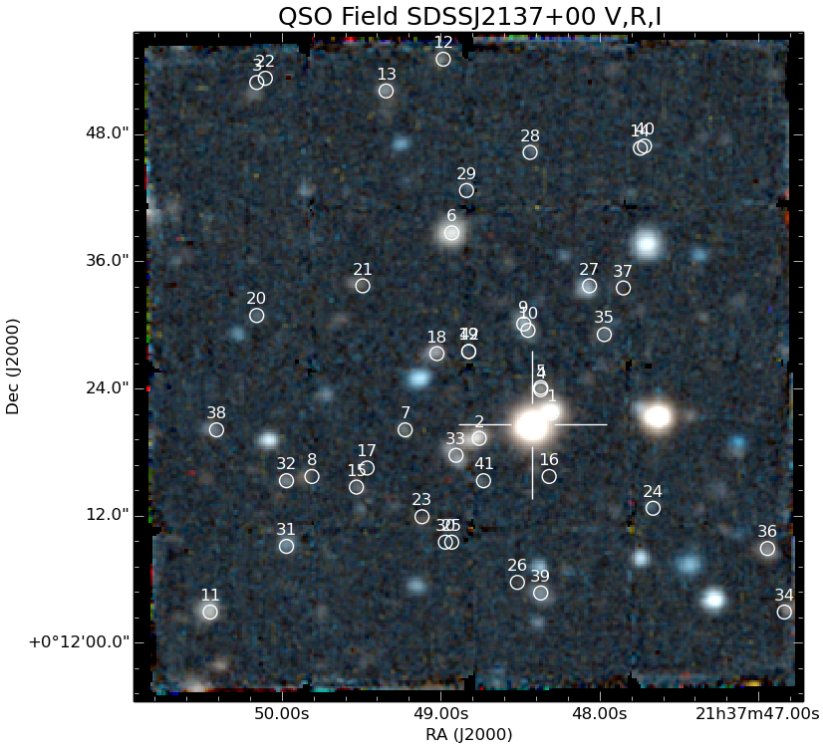

FIG. A.1.— RGB image of the J213748+0012 field with identifications of emission detected galaxies. The white cross points the quasar location. Circles represent emission detected galaxies corresponding to Table 9. Not all the galaxy-like spots are circled on the image. These spots are either stars or galaxies with a continuum but without obvious emission line.

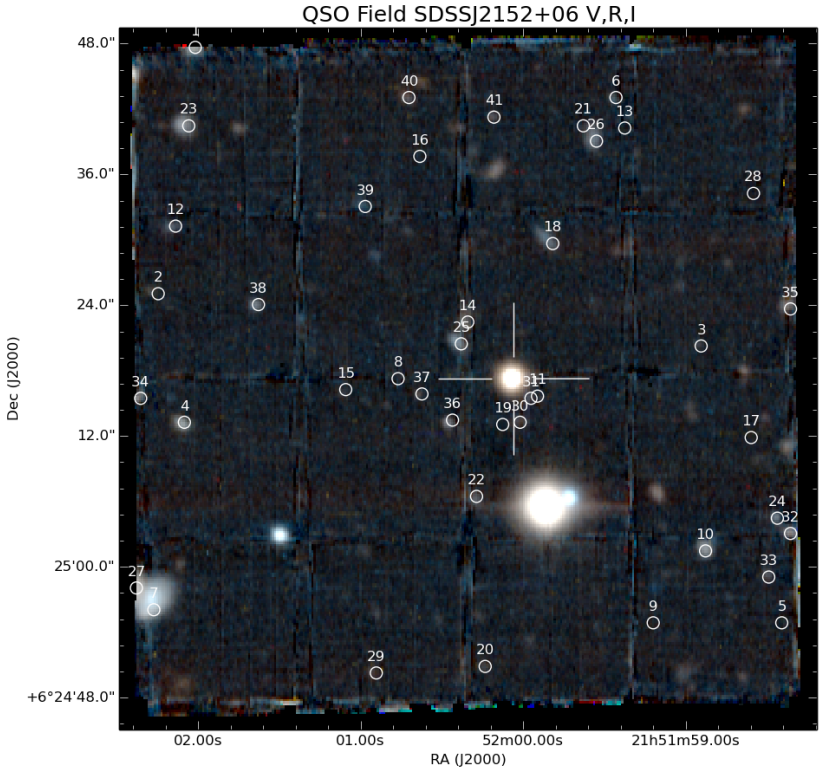

FIG. A.2.— Same as Figure A.1 but for the J215200+0625 quasar field. Again, the white cross shows the quasar location and galaxies with emission lines are circled and listed in Table 10.

TABLE 10
MUSE Sources in the SDSSJ215200+0625 field with redshifts. We found 40 galaxies out of 41 having identified emission lines

ID	R.A.	Dec.	redshift	lines
obj001	21:52:02.018	+06:25:47.66	0.433	OII, OIII, H_β
obj002	21:52:02.246	+06:25:25.06	0.439	OII
obj003	21:51:58.905	+06:25:20.26	0.452	OII, OIII, H_β
obj004	21:52:02.085	+06:25:13.26	0.489	OII, OIII, H_β
obj005	21:51:58.409	+06:24:54.86	0.517	OII
obj006	21:51:59.429	+06:25:43.06	0.554	OII, OIII
obj007	21:52:02.273	+06:24:56.06	0.597	OII, OIII, H_β
obj008	21:52:00.770	+06:25:17.26	3.931?	5992.37 Lyα?
obj009	21:51:59.200	+06:24:54.86	4.196?	6314.05 Lyα?
obj010	21:51:58.878	+06:25:01.46	0.742	OII, OIII, H_β
obj011	21:51:59.912	+06:25:15.66	0.748	OII, H_β
obj012	21:52:02.139	+06:25:31.26	0.770	OII, OIII, H_β
obj013	21:51:59.375	+06:25:40.26	0.786	OII
obj014	21:52:00.341	+06:25:22.46	0.332	OII, OIII, H_α
obj015	21:52:01.092	+06:25:16.26	0.824	OII, OIII
obj016	21:52:00.636	+06:25:37.66	0.289	H_α, NII
obj017	21:51:58.597	+06:25:11.86	0.847	OII?
obj018	21:51:59.818	+06:25:29.66	0.873	OII
obj019	21:52:00.126	+06:25:13.06	0.879	OII, OIII
obj020	21:52:00.234	+06:24:50.86	0.438	OII, OIII, H_β
obj021	21:51:59.630	+06:25:40.46	0.943	OII
obj022	21:52:00.287	+06:25:06.46	0.989	OII
obj023	21:52:02.058	+06:25:40.46	1.013	OII
obj024	21:51:58.436	+06:25:04.46	1.013	OII
obj025	21:52:00.381	+06:25:20.46	1.052	OII
obj026	21:51:59.549	+06:25:39.06	1.053	OII
obj027	21:52:02.380	+06:24:58.06	0.185	OIII, H_β, H_α, NII
obj028	21:51:58.583	+06:25:34.26	···	8413.87
obj029	21:52:00.904	+06:24:50.26	1.302	OII
obj030	21:52:00.019	+06:25:13.26	1.318	OII
obj031	21:51:59.952	+06:25:15.46	1.318	OII
obj032	21:51:58.355	+06:25:03.06	1.349	OII
obj033	21:51:58.489	+06:24:59.06	···	8757.32
obj034	21:52:02.354	+06:25:15.46	1.362	OII
obj035	21:51:58.355	+06:25:23.66	1.403	OII
obj036	21:52:00.435	+06:25:13.46	1.430	OII
obj037	21:52:00.623	+06:25:15.86	1.430	OII
obj038	21:52:01.629	+06:25:24.06	1.431	OII
obj039	21:52:00.972	+06:25:33.06	1.433	OII
obj040	21:52:00.703	+06:25:43.06	1.435	OII
obj041	21:52:00.180	+06:25:41.26	1.432	OII

Last note